Measurements of the mass and width of the W boson from $e^+e^- \rightarrow \mathrm{W^+W^-} \rightarrow (e/\mu)\nu\mathrm{q\bar{q}}$ events with the ALEPH detector

Barbara Maartje Raeven

Department of Physics and Astronomy
University of Glasgow

A thesis submitted for the degree of
Doctor of Philosophy

October 2000

Abstract

In 1998 at CERN (Geneva), 174 pb^{-1} of data was collected with the ALEPH detector, at an e^+e^- centre-of-mass energy of 188.6 GeV. For this dataset, the selection of semi-leptonic decays of W boson pairs ($\mathrm{WW} \to (e/\mu)\nu\mathrm{q\bar{q}}$) is improved. The resulting efficiencies for selecting $e\nu\mathrm{q\bar{q}}$ and $\mu\nu\mathrm{q\bar{q}}$ events are 82.0% and 88.1% respectively, with purities of 92.4% and 93.3%. For the first time in ALEPH, the width of the W boson is measured using a two parameter (mass $\mathrm{M_W}$ and width Γ_W) fit to the reconstructed W mass distribution, yielding:

$$\begin{aligned} \mathrm{M_W} &= 80.313 \pm 0.119(\mathrm{stat.}) \pm 0.052(\mathrm{syst.})\ \mathrm{GeV}/c^2 \\ \Gamma_\mathrm{W} &= 2.17^{+0.29}_{-0.26}(\mathrm{stat.}) \pm 0.11(\mathrm{syst.})\ \mathrm{GeV}/c^2, \end{aligned}$$

for $e\nu\mathrm{q\bar{q}}$ and $\mu\nu\mathrm{q\bar{q}}$ decays combined. The mass value is in good agreement with the world average mass and the width value is in good agreement with Standard Model calculations.

The systematic error includes detector uncertainties as well as uncertainties in the background, the beam energy and the theoretical model. Additional studies are done with respect to previous years to take into account errors in the angular and energy resolutions of the ALEPH detector. The stability of the data fit results is checked as a function of various selection cuts.

A preliminary measurement is performed at centre-of-mass energies ranging from 191.6 to 201.6 GeV. These results are combined with the result above to obtain the preliminary result for a total integrated luminosity of 411 pb^{-1}:

$$\begin{aligned} \mathrm{M_W} &= 80.537 \pm 0.079 \pm 0.052\ \mathrm{GeV}/c^2 \\ \Gamma_\mathrm{W} &= 2.11^{+0.20}_{-0.18} \pm 0.11\ \mathrm{GeV}/c^2. \end{aligned}$$

Author's Declaration

This thesis presents measurements of the mass and width of the W boson in the $W^+W^- \rightarrow (e/\mu)\nu q\bar{q}$ decay channels using data taken in 1998 and 1999 by the ALEPH detector at LEP centre-of-mass energies from E_{cms} = 188.6 to 201.6 GeV. Much of this work has been undertaken within the ALEPH W group at CERN and the results in this thesis reflect the efforts of the ALEPH collaboration over many years.

The author's contributions to the ALEPH measurements include contributions to the preliminary mass results at E_{cms} = 188.6 GeV for the EPS-HEP99 winter conference [1]; the improvement of the selection of W pair decay events with respect to previous years; the implementation of a 2 parameter fit, resulting in the first measurement of Γ_W from the W mass distribution in ALEPH [2, 3]; new studies of systematic uncertainties due to detector resolutions in ALEPH; the evaluation of all systematic uncertainties for the two parameters (M_W,Γ_W) in the fit; extensive checks of the fit method and the stability of the data; comparisons of data distributions to Monte Carlo predictions; contributions to tests of modules of the VDETII sub-detector and regular shifts as data manager to monitor data quality.

Acknowledgements

Many people have contributed to this thesis. I would like to thank Prof. D. Saxon and Andy Halley for giving me the opportunity to study in Glasgow and the University of Glasgow for their financial support. Many thanks to members of the Glasgow group, Jim, Catherine, Stan and others, for making my time in Glasgow enjoyable. Thanks to Jim and Stan for correcting my thesis.

At CERN, I would like to thank Jason Ward for his help with my Ph.D. in general, for correcting this thesis (many times) and for his invaluable moral support. Thanks also to all the members of the ALEPH W group, in particular to Evelyn Thomson, Helenka Przysieniak, Anne Ealet, Rob Edgecock and Alain Blondel.

I would also like to mention the people who helped me to forget about physics from time to time; Paul in St-Genis; Juan and the other l'Athenee'rs in Geneva; George, Ben and frequent visitors to 274, as well as my other flat-mates in Glasgow; Gavin, Dave (×2) and the Glasgow Ph.D. students.

In the Netherlands, I would like to thank Rene Kamermans for the discussions about life in general and particle physics in particular. To my parents, my brother Joost and my sister Femke, thanks for your visits and especially for the KJ and GJ initiative. Pietepaf would like to thank Lou and Joost for their spontaneous decision. And finally, thanks to Matthew for, apart from everything else, properly introducing me to Scottish culture and learning my silly language.

October 2000

Glasgow

Contents

List of Figures

List of Tables

Chapter 1

Introduction

1.1 A short history of particle physics

The concept of particles as basic constituents of matter originated from around 400 BC when Democritus developed the theory that *'The universe consists of empty space and an (almost) infinite number of invisible particles which differ from each other in form, position and arrangement'*. He called these particles atoms, from the Greek $\alpha\tau o\mu o\varsigma$, meaning indivisible. For centuries experiments were not considered an important part of science and it was not until 1808 that the English chemist John Dalton found that many substances can be formed by combining definite quantities of only a few elements [4]. He called the 90 elementary substances that were known at that time *atoms* and in doing so introduced the first modern atomic theory of matter.

Experiments in the last century have shown that atoms are not indivisible. The start of experimental particle physics is usually identified with Röntgen's discovery of X-rays in 1895 [5]. He found that atoms produce highly energetic light that can traverse material. At this time, a proper interpretation was not yet available. A theoretical description of the photon was not possible before 1900 when Max Planck postulated that light is emitted in microscopic packets (*quanta*) of energy [6], or before 1905 when Einstein proposed that light remains in these packets as it travels through space [7].

The discovery of the electron by Thomson in 1897 [8] won him the Nobel prize and as atomic physics progressed, Rutherford [9] and Bohr [10] developed theories to describe the structure of the atom. In 1919 the proton was discovered by Rutherford in an emission experiment using Nitrogen gas [11].

The basis for our present day *Standard Model* of particle physics is the Dirac equation, formulated in 1928, in which Dirac combined quantum mechanics and special relativity to describe the electron [12]. In 1930 Max Born stated that *'Physics as we know it will be over in six months'* when hearing of the Dirac equation.

Three years after the publication of his theory, Dirac realised that his equations implied the existence of anti-matter and he postulated the existence of the positron [13] that was subsequently discovered by Anderson in cosmic rays in 1933 [14].

Electromagnetism has been well described since Maxwell formulated his equations in 1864 [15]. Decades later, the process of β decay puzzled many physicists. The continuous energy spectrum of the emitted electrons seemed to violate energy conservation. In 1930 Pauli proposed the existence of a massless neutral particle to explain the missing momentum and called it the little neutral one, or *neutrino* [16]. In 1934 Fermi introduced a first theory of the weak interaction to explain the process in more detail [17]. The similarities in the coupling strength of β decay, μ decay and μ capture led theorists to postulate in 1949 [18] that one single mediator particle (and its anti-particle) is responsible for these charged interactions. Papers by Glashow [19] motivated Steven Weinberg [20] and Abdus Salam [21] to introduce theories that unify the weak interaction and electromagnetism in 1967. Apart from the photon that was known to mediate electromagnetic interactions, their electroweak theories predicted the existence of three weakly interacting mediator particles, later known as the $W^{\pm}$ and the Z^0 bosons. The existence of an additional heavy boson, known as the Higgs, is also predicted.

From the early 1960s, after the introduction of accelerators in particle physics, experimentalists actively sought for signs of the carriers of the weak interaction. Evidence for the weak neutral current was found at CERN in 1973 [22].

In 1982, the UA1 and UA2 experiments at the CERN super proton synchrotron (SPS) started taking data from $p\bar{p}$ collisions at a centre-of-mass energy of 540 GeV. Subsequently, CERN claimed the discoveries of the Z [23, 24] and the W [25, 26] bosons. The UA2 collaboration reported the first signs of a charged resonance and

UA1 claimed the discovery of the W boson on the basis of six events at the winter meeting of the American Physical Society in January 1983 [27].

Before the introduction of accelerators, the neutron was discovered by Chadwick in 1932 [28] and many particles such as the muon [29] and the pion [30] were discovered in cosmic rays. In 1948 the first artificial pions were produced in an accelerator at Berkeley, USA. With the use of accelerators, higher energies could be reached and the race to find new particles took off. Before 1960, many particles were discovered including the Λ, the Σ and the Ξ, the anti-proton, the anti-neutron and the $\nu_e, \nu_\mu, \rho, \omega, \eta, \phi$. With the discovery of more different particles in the 1960s, a simple model for the structure of matter seemed as remote as ever. A solution was found in the discovery of the substructure of the proton leading to the introduction of quarks [31]. At the linear accelerator facility SLAC in California, this substructure was proven in a similar way to Rutherford's discovery of the nucleus: from the distribution of electrons that scatter off a proton target [32].

In recent decades many different theories have been proposed to describe the basic constituents of our universe. In this thesis, only the present day status of the theory of the Standard Model will be discussed. All particles discovered in the past are implemented in this model as either one of the six leptons $(e, \mu, \tau, \nu_e, \nu_\mu, \nu_\tau)$ or as a structure built from the six elementary quarks (u, d, c, s, t, b). The remaining elements of the model are the objects that describe the interactions between these particles (W, Z, γ, g,H). Today, most experiments are designed to test the predictions or find extensions of the Standard Model, but the question of whether this model is the true description of the elementary building blocks of matter is not answered yet.

1.2 Motivation of the measurements

The Standard Model provides a limited theoretical framework in which our present knowledge of particle physics is defined, but is not complete. Many properties of the elementary particles are not predicted, such as their mass. In the search for answers to the remaining questions, theorists have found a possible explanation for the generation of mass in nature. In this theory an additional field is introduced, resulting in the prediction of an additional object, the Higgs boson, that has not yet been discovered [33]. Experimental and theoretical limits on the Higgs boson mass suggest that, if the Standard Model Higgs exists, the discovery of it may happen in the next few years [34].

The mass of the Z^0 and $W^{\pm}$ bosons are not predicted in the Standard Model. The mass of the Z^0 boson has been measured to very high precision during the first stage of the LEP physics program ($M_Z = 91.1872 \pm 0.0021$ GeV/c^2 for the combined four LEP experiments [34, 35]). The Z boson parameters, including the Z mass, were determined from the measured cross-sections on and near the Z resonance.

Global Standard Model fits to electroweak data, including the LEP1 data, have been used to indirectly determine the W mass. For example, at the time of the ICHEP1996 summer conference, which is close to the time when W pairs were first being produced at LEP, the indirect determination of the W mass using LEP data alone was $M_W = 80.278 \pm 0.049$ GeV/c^2. Using all data including the top quark mass, this was $M_W = 80.352 \pm 0.033$ GeV/c^2 [36].

The first motivation to measure the mass of the W boson directly, with as high a precision as possible, would be to test the consistency of the Standard Model by comparing the direct and the indirect measurements of M_W. This requires that the uncertainties on the direct and indirect determinations are comparable and therefore suggests that the direct reconstruction of M_W from LEP should achieve a precision of around 30 MeV/c^2.

A second motivation to measure the W mass is that precise knowledge of the Standard Model parameters allows predictions for the parameters that are not yet directly measurable. For example, a precise measurement of the mass of the W allows limits to be set on the mass of the Standard Model Higgs boson. The precision on this prediction depends on the measurements of all observables chosen to constrain the model and at present the large errors on the masses of the top quark and the W boson are the main limitations [34].

The width of the W boson is related to its decay and can be calculated from Standard Model parameters as will be described in chapter 2. At present, this result is in agreement with the world average measurement of the W width as will be shown in chapter 8. Other theoretical models with extended sets of elementary particles predict other decay channels of the W and therefore a different value for the W width. However, the measurement of the width described in this thesis assumes the Standard Model to be valid. It is therefore to be used as a cross check of the Standard Model only and not as a model independent measurement of Γ_W.

The resolution of the detector translates directly into the width of the reconstructed mass distribution. Systematic uncertainties are evaluated for both the mass and the width measurements. If the Standard Model is assumed to be valid, agreement between the measured width and the Standard Model prediction ensures that other systematic uncertainties do not significantly affect the the resolution of the constructed mass.

1.3 The LEP2 program

At the LEP collider near Geneva, W bosons are generated in energetic collisions of electrons and positrons. The centre-of-mass threshold for the production of W boson pairs ($\sim$ 161 GeV) was reached by LEP in 1996. The analysis described in this thesis covers centre-of-mass energies from 188.6 to 201.6 GeV, at which the two W bosons are created with a velocity of at least half the velocity of light with respect to the laboratory frame. The size of the ALEPH data samples and the actual mean centre-of-mass energies measured by LEP are shown in table 1.1.

Year	E_{cms}(GeV)	$\mathcal{L}$ (pb^{-1})	N_{WW}
1996	161.3	11.1	$\sim$ 40
	172.1	10.7	$\sim$ 140
1997	182.7	56.8	$\sim$ 900
1998	188.6	174.2	$\sim$ 3000
1999	191.6	28.9	$\sim$ 4100
	195.5	79.9	
	199.5	86.3	
	201.6	41.9	

Table 1.1: ALEPH data samples from W pair production threshold. The last four samples are preliminary. The estimated number of produced W pair decays in ALEPH, N_{WW}, is estimated from the GENTLE [37] cross section.

About 68% of the produced W bosons decay into a quark anti-quark pair ($q\bar{q}$), leaving 32% to decay into a charged lepton and a neutrino ($l\nu$), where the lepton l is either an electron, a muon or a tau. This gives rise to three distinct event topologies: the hadronic channel ($WW \to q\bar{q}q\bar{q}$), the semi-leptonic channel ($WW \to l\nu q\bar{q}$) and the fully leptonic channel ($WW \to l\nu l\nu$), with branching fractions of 47%, 43% and 10% respectively. In this thesis, the analysis of the semi-leptonic decay channel will be described, where the lepton is either an electron or a muon.

Uncertainties in the theoretical description of final state interactions contribute to the systematic error on the measurements of $\mathrm{M_W}$ and Γ_W in the hadronic decay channel. Firstly, the hadronic decay products of the two W bosons can interact through *colour reconnection* [38]. Secondly, pions that are produced in the hadronic jets follow *Bose-Einstein* statistics. The presence of one hadronically decaying W can therefore affect the decay of the other [39]. Decay channels with only one (or no) hadronically decaying W are not sensitive to Bose-Einstein or colour reconnection effects. As a result of this and because of the large branching fraction of the semi-leptonic decay channel, it is referred to as the *golden* channel.

1.4 Outline of the thesis

In the next chapter, the theory of the Standard Model will be described. A theoretical description of the W boson is given in section 2.2. The experimental setup of LEP in general and the ALEPH detector in particular is described in chapter 3. Understanding the detector is vital for the selection of the W pair decays described in chapter 4. The reconstruction of the W mass in each event is explained in section 4.2, and the method to extract the mass and width from the distribution of mass estimators is described in chapter 5.

Expectations for the statistical uncertainty on the measurement are given in section 5.3 and in chapter 6 the systematic errors are evaluated. The data fits are performed in chapter 7. Many checks were done to investigate the performance of the method and the stability of the data fit result as a function of the selection cuts. Checks of the method are described in section 5.4 and 5.6, the stability of the fit to the data is shown in section 7.4. In chapter 8 the results are combined and compared to other measurements and the conclusions of the work described in this thesis are drawn in chapter 9.

Chapter 2

Theory

A general introduction of the Standard Model of particle physics is given in section 2.1. The origin of the terms of the Standard Model Lagrangian is explained. In section 2.1.5 it is shown how Feynman simplified the calculations and how event rates can easily be derived from the Feynman rules. A more detailed description is found in [40, 41, 42].

In section 2.2, the theory is applied to the W boson. The lowest order cross section for W pair production is outlined in section 2.2.1 and the decay of the W is described in sections 2.2.2 and 2.2.3. A more detailed description of W physics is found in [43].

A Monte Carlo method is used to generate large samples of events in order to predict the experimental results. The Monte Carlo generators relevant to the analysis are introduced in section 2.3.

Throughout this thesis, natural units are used: the constants defining the scale in quantum field theories are set to unity ($\hbar = c = 1$). All quantities therefore have dimensions in which the relevant factors of c and $\hbar$ are incorporated (e.g. $\{p\} = \mathrm{GeV}/c$).

2.1 The Standard Model of particle physics

The formalism that describes our present day knowledge of particle physics is known as the *Standard Model*. This theory defines the different elementary particles: the fermions, the basic building blocks of matter, and the gauge bosons, responsible for the interactions between them. The elementary particles are assumed to be point-like because, within the energy regime reachable today, no experimental proof for a sub-structure exists [44]. The characteristics of the fermions are summarised in table 2.1.

Leptons			Quarks		
Flavour	Q (q_e)	m$_l$ (MeV/c^2)	Flavour	Q (q_e)	m$_q$ (bare) (GeV/c^2)
e	-1	0.510999	down	-1/3	~0.006
ν_e	0	<0.000003	up	2/3	~0.003
μ	-1	105.65836	strange	-1/3	~0.13
ν_μ	0	<0.19	charm	2/3	~1.3
τ	-1	1777	bottom	-1/3	4
ν_τ	0	<18.2	top	2/3	174

Table 2.1: The Standard Model fermions [45]. The electric charge Q is defined in units of electron charge, where $q_e = 1.6 \times 10^{-19}$ C. The first elementary particle to be discovered was the electron and its mass is known to better than $4{\times}10^{-6}$ %. The ν_e mass limit from ^{3}H decay is ambiguous, the ν_μ and ν_τ mass limits are 90% and 95% CL respectively. The c and b masses are estimated from meson states. The top quark was discovered in 1995 and its mass, from direct observation of top events, has an uncertainty of the order of 3%.

The four observed forces in nature are the electro-magnetic interaction, the weak interaction, the strong interaction and gravity. The first three are incorporated in the Standard Model, but theorists are still working on a proper implementation of gravity [46]. The interactions are described by mediator particles, known as gauge bosons. Their characteristics are summarised in table 2.2.

Bosons			
	Interaction	Q (q_e)	M (GeV/c^2)
γ	Electro(weak)	0	0
Z	(Electro)weak	0	91.19
W$^\pm$	(Electro)weak	$\pm$1	80.4
g	Strong	0	0

Table 2.2: The Standard Model interactions [45]. The Z mass is known to 2.1 MeV/c^2 and the W mass to 56 MeV/c^2 precision.

The building blocks and their interactions are both described by particles in the Standard Model, but their characteristics differ. Unlike bosons, fermions are sensitive to the Pauli exclusion principle [47]: no two fermions can be in exactly the same state at any one time. Based on quantum field theory, fermions have half-integer internal angular momentum (*spin* $s = \frac{1}{2}, \frac{3}{2}, ...$) while bosons have integer spin ($s = 0,1,2,...$).

The weak and electro-magnetic interactions are combined into one single formalism known as electroweak theory (see section 2.1.2). The ultimate goal of particle physics is to unify all interactions in one Grand Unified Theory (GUT) [48].

2.1.1 Definition of the free Lagrangian

A standard method to calculate the evolution of a particle in space, described by a given equation of motion, is to minimise the *action* $\mathcal{A}$ of the system [41]:

$$\mathcal{A} \equiv \int \mathcal{L} dt, \tag{2.1}$$

where the *Lagrangian* $\mathcal{L}$ satisfies the Euler-Lagrange equation:

$$\frac{\partial}{\partial x_\mu}\left(\frac{\partial \mathcal{L}}{\partial(\partial\psi/\partial x_\mu)}\right) - \frac{\partial \mathcal{L}}{\partial \psi} = 0. \tag{2.2}$$

The Lagrangian is $\mathcal{L} = \mathrm{T} - \mathrm{V}$, where T and V are the kinetic and potential energy of the system respectively. A Lagrangian that is defined in order to describe experimental observations of matter enters in the Standard Model.

Dirac derived the equation of motion for an elementary particle in the absence of any interactions from a relativistic generalisation of the *Schrödinger equation*, the basis for Quantum Mechanics. By introducing four *Dirac γ matrices*, he simplified Einstein's relation between energy and mass, $\mathrm{H}^2\psi = (\mathrm{P}^2 + \mathrm{m}^2)\psi$, to obtain a first order differential equation:

$$(i\gamma^\mu \partial_\mu - \mathrm{m})\psi = 0, \tag{2.3}$$

where $\partial_\mu = (\partial/\partial t, \nabla)$ and $\mu = 1, 4$. H is the Hamiltonian, P is the momentum operator and m is the mass of the particle. Combining the Dirac equation with equation 2.2 results in the free Standard Model Lagrangian:

$$\mathcal{L} = \bar{\psi}(i\gamma^\mu \partial_\mu - \mathrm{m})\psi, \tag{2.4}$$

where $\bar{\psi} \equiv \psi^\dagger \gamma^0$. Any interaction of the free particle with a potential field adds a potential term to the Lagrangian. Terms for the Standard Model interactions are introduced in section 2.1.2.

2.1.2 The interaction Lagrangian

According to Noether's theorem, the conservation of a physical quantity (e.g. energy, momentum) is implied by invariance of the theory under a corresponding transformation. For example, rotation symmetry implies conservation of angular momentum. Standard Model interactions are incorporated in the Lagrangian through their underlying symmetry. The symmetry, or invariance of the Lagrangian, is imposed under a relevant transformation and in order to achieve this invariance, a term is added to the free Lagrangian.

Therefore, each interaction corresponds to a group of transformations under which the Lagrangian is invariant. The electro-magnetic interaction is described by a U(1) gauge group, the weak interaction by an SU(2) gauge group. The number of carriers of the electroweak force SU(2)$\times$U(1) equals four: 3($= n^2$-1) for SU(2) plus 1($= n^2$) for U(1). These force carriers are observed in nature as the gauge bosons of the interaction. In the next sections the implementation of each interaction in the Lagrangian will be described separately.

The electro-magnetic interaction and the covariant derivative

For a wave-function ψ, only the probability $|\psi|^2$ can be observed experimentally. Any theory should therefore be invariant under the U(1) group of local gauge transformations:

$$\psi(x) \to e^{i\alpha(x)}\psi(x). \tag{2.5}$$

The derivative term of the Dirac Lagrangian in equation 2.4 is made gauge invariant by replacing the derivative ∂_μ by the *covariant derivative* D_μ^{EM}, where

$$D_\mu^{EM} = \partial_\mu - ieA_\mu \tag{2.6}$$

and A_μ transforms as $A_\mu \to A_\mu + (\partial_\mu \alpha / e)$. Since D_μ^{EM} transforms like ψ, the new Lagrangian is gauge invariant.

Similarly to classical electrodynamics, where the equation of motion for a particle with charge e in a photon field A is obtained by substituting $p_\mu \to p_\mu + eA_\mu$, the field A in equation 2.6 is the photon acting on the particle wave function. To complete the Lagrangian, the kinetic energy of the photon is added and the Lagrangian becomes:

$$\mathcal{L} = \bar{\psi}(i\gamma^\mu \partial_\mu - \mathrm{m})\psi + e\bar{\psi}\gamma^\mu A_\mu \psi - \frac{1}{4}F^{\mu\nu}F_{\mu\nu}, \tag{2.7}$$

where $F_{\mu\nu} = \partial_\mu A_\nu - \partial_\nu A_\mu$ is chosen to ensure that the last term in the Lagrangian is also invariant. The resulting theory is known as quantum-electro-dynamics (QED). Electromagnetism is an interaction between particles that carry electric charge and electro-magnetic *gauge invariance* implies conservation of charge according to Noether's theorem.

The electroweak interaction

In nature, particles exist in two possible configurations. The spin and velocity vectors can either be parallel (right-handed) or anti-parallel (left-handed). Experiments show that the weak interaction is *chiral* [49]: it only affects left-handed particles and right-handed anti-particles. This can be implemented in the theory by introducing a fifth Dirac matrix:

$$\gamma_5\psi = i\gamma_0\gamma_1\gamma_2\gamma_3\psi = 2\frac{\Sigma \cdot p}{|p|}\psi, \tag{2.8}$$

where $\Sigma = I\vec{\sigma}$, and σ_i are the Pauli spin matrices. The new Dirac matrix projects the particle spin in the direction of motion. The eigenvalues (± 1) are used to define the *helicity* of the particle. The resulting projection operators for the left-handed (ψ_L) and right-handed (ψ_R) components of a wave function ψ are:

$$\begin{aligned} \psi_L &= \frac{1}{2}(1-\gamma_5)\psi \\ \psi_R &= \frac{1}{2}(1+\gamma_5)\psi. \end{aligned} \tag{2.9}$$

Fermions exist in both configurations apart from neutrinos, that have not (yet) been observed in a right-handed state [50]. Left-handed fermions are defined as doublets ($\{e_L, \nu_L\}$ etc.) and right-handed leptons as singlets (e_R, u_R, d_R etc.). A parity transformation changes left-handed particles to right-handed particles, and the lack of right-handed neutrinos in nature is evidence for parity violation in weak interactions.

To obtain a Lagrangian that includes the weak force, the *weak iso-spin* is defined as $T_i = \sigma_i/2$ on the doublet states and 0 on the singlets. To include the electro-magnetic charge operator Q, the *weak hyper-charge* Y is defined as:

$$Y = 2(Q - T_3). \tag{2.10}$$

The covariant derivative for the electroweak interaction is postulated to be:

$$D_\mu^{EW} = \partial_\mu + igT_j \mathrm{W}_\mu^j + \frac{ig'}{2} Y \mathrm{B}_\mu, \tag{2.11}$$

which again results in a gauge invariant Lagrangian. The fields defined in this way are the weak bosons $\mathrm{W}_1, \mathrm{W}_2$ and W_3, that interact with particles with non-zero iso-spin, and a fourth carrier B, that couples to hyper-charge.

Apart from this covariant derivative, a term is added to the Lagrangian for the kinetic energies and self-interactions of the W and B bosons to obtain:

$$\mathcal{L}_{EW} = -\bar{\psi}(g\gamma^\mu T_j \mathrm{W}_\mu^j + \frac{g'}{2} Y \gamma^\mu \mathrm{B}_\mu)\psi - \frac{1}{4}(\mathrm{W}^{\mu\nu}\mathrm{W}_{\mu\nu} + \mathrm{B}^{\mu\nu}\mathrm{B}_{\mu\nu}). \tag{2.12}$$

In nature, the electroweak force is observed as either a charge-exchange ($\mathrm{W}^\pm$) or a neutral current (Z, γ). The observable force carriers are related to W and B according to the *Weinberg mixing angle* θ_W [20]:

$$\begin{aligned} A &= \mathrm{B}\cos\theta_\mathrm{W} + \mathrm{W}_3 \sin\theta_\mathrm{W} \\ \mathrm{Z} &= -\mathrm{B}\sin\theta_\mathrm{W} + \mathrm{W}_3\cos\theta_\mathrm{W} \\ \mathrm{W}^\pm &= (\mathrm{W}_1 \mp \mathrm{W}_2)/\sqrt{2}. \end{aligned} \tag{2.13}$$

As a result, the coupling constants g and g' in equation 2.11 are related to θ_W and the electric charge in equation 2.6 as:

$$e = g\sin\theta_\mathrm{W} = g'\cos\theta_\mathrm{W}. \tag{2.14}$$

The strong interaction

The strong interaction couples to *colour* charge, which is only carried by quarks, and can be either red, blue or green. The mediators of the strong interactions, the gluons, carry colour-anticolour pairs ($r\bar{g}$ etc.). One of the 9 possible combinations turns out to be a singlet ($r\bar{r} + b\bar{b} + g\bar{g}$). Free particles are always singlets, and a singlet gluon would result in a strong interaction that could act between mesons or baryons and have a long range. As there is no experimental evidence for that [51], the gluon singlet is not included in the Standard Model resulting in 8 strong gauge bosons.

The Pauli spin matrices σ_i are used as generators of the electroweak interaction. In a similar way, the coupling to the colour field is described by the *Gell-Mann* λ_a *matrices*. The quantum number $M_a = \lambda_a/2$ is used to define the covariant derivative:

$$D_\mu^S = \partial_\mu + ig_s M_a C_\mu^a, \tag{2.15}$$

where a runs over all 8 colour states. The resulting theory is known as quantum-chromo-dynamics (QCD). The energy of the gluon field adds a term $-(G^{\mu\nu}G_{\mu\nu})/4$ to the Lagrangian, where the strong field strength tensor G is defined as:

$$G_{\mu\nu}^a = \partial_\mu C_\nu^a - \partial_\nu C_\mu^a + g_s f^{abc} C_\mu^b C_\nu^c, \tag{2.16}$$

where f^{abc} is the tensor of quark structure constants. Since the quarks carry colour themselves, they can interact with each other. These interactions appear in the Lagrangian because, unlike for the QED tensor F, the commutator of the strong field strength tensor is non-zero.

2.1.3 The Higgs mechanism and particle masses

The complete electroweak Lagrangian is the sum of equation 2.4 and 2.12 and is only gauge invariant if the masses of the fermions are set to zero. Similar mass terms for the gauge bosons would also violate gauge invariance. However, experiment shows that fermions are not massless and although the photon does not have mass, the electroweak $\mathrm{W}^\pm$ and Z^0 gauge bosons are heavy. A way to introduce mass terms in the Lagrangian without violating gauge invariance is proposed by spontaneous symmetry breaking according to the *Higgs mechanism* [33].

In the Higgs mechanism, four real scalar fields ϕ_i are introduced. The simplest choice is an iso-spin doublet $\phi = (\phi^+, \phi^0)$ with hyper-charge $Y = 1$ (see equation 2.10) defined as:

$$\begin{aligned} \phi^+ &\equiv (\phi_1 + i\phi_2)/\sqrt{2} \\ \phi^0 &\equiv (\phi_3 + i\phi_4)/\sqrt{2}. \end{aligned} \tag{2.17}$$

The scalar fields couple to the electroweak field and give rise to new terms in the Lagrangian related to the Standard Model bosons:

$$\mathcal{L}_{\mathrm{H}b} = (D_\mu^{EW}\phi)^\dagger(D_\mu^{EW}\phi) - \frac{1}{2}\mu^2\phi^\dagger\phi - \frac{1}{4}\lambda(\phi^\dagger\phi)^2, \tag{2.18}$$

where the last two terms are known as the Higgs potential V(ϕ). The first two terms of equation 2.18 describe a scalar field with mass μ in an electroweak field, if $\mu^2 > 0$. The last term corresponds to a four-particle interaction, with coupling λ.

For $\mu, \lambda > 0$, the minimum of the Higgs potential (the vacuum) is at $\phi = 0$, but if $\mu^2 < 0$, the derivative of V(ϕ) is zero at $\phi = \pm\sqrt{-\mu^2/\lambda}$ and the potential has the shape of a Mexican hat in the space spanned by (ϕ^+, ϕ^0). In this case, the Lagrangian should be expanded around the new minimum:

$$\phi(x) = \pm v + \eta(x), \tag{2.19}$$

where $v \equiv \sqrt{-\mu^2/\lambda}$. If 2.19 is substituted for ϕ in the free Lagrangian (equation 2.18 where $D^{EW} \to \partial_\mu$), the amplitude of the η^2 term can be identified with the mass of a scalar particle m_η. The result is [41]:

$$\mathrm{m}_\eta = \sqrt{-2\mu^2}. \tag{2.20}$$

As a result, if the Higgs mechanism is present in nature, there has to exist at least one scalar particle that has not yet been observed, known as the Higgs boson.

The mass terms for the $\mathrm{W}^\pm$ and Z^0 gauge bosons follow if the vacuum expectation value v is substituted for ϕ in the first term of the Higgs Lagrangian 2.18. Any point in space where $|\phi|^2 = v^2$ corresponds to a potential minimum. Choose for instance ϕ_i in equation 2.17 to be zero for $i = 1, 2, 4$. The minimum is then found at $\phi = \sqrt{1/2}(0, v)$. Substituting this in the Lagrangian, terms proportional to $\mathrm{W}^{+\mu}\mathrm{W}^-_\mu$ appear, corresponding to the mass terms of the $\mathrm{W}^\pm$ bosons, and terms proportional to $(a\mathrm{W}^3_\mu + b\mathrm{B}_\mu)$, corresponding to the mass of the Z boson (and the photon) [41]:

$$\begin{aligned} \mathrm{M_W} &= \frac{1}{2}vg \\ \mathrm{M_Z} &= \frac{1}{2}v\sqrt{g^2 + g'^2}. \end{aligned} \tag{2.21}$$

Other terms include linear terms in η, corresponding to the couplings of the Higgs to the W and Z. From equations 2.14 and 2.21 follows the relation between $\mathrm{M_W}$ and $\mathrm{M_Z}$:

$$\mathrm{M_W} = \mathrm{M_Z}\cos\theta_\mathrm{W}. \tag{2.22}$$

The choice of $\phi = (0, \phi^0)$ corresponds to the neutral Standard Model Higgs, but other choices are made for example in super-symmetric models [52]. Its properties are such that the charge symmetry remains unbroken (Q=0) and the photon remains massless. The hyper-charge and the iso-spin are nonzero, resulting in mass terms for the W and Z.

The mass terms for the fermions are introduced by the interaction of the fermions with the Higgs field ϕ:

$$\mathcal{L}_{\mathrm{H}f} = -g_f \bar{\psi}_f \phi \psi_f. \tag{2.23}$$

Substituting 2.19 for ϕ results in mass terms for the fermions, with $\mathrm{m}_f = g_f v/\sqrt{2}$, and a term that describes the interaction of the Higgs with the fermions. The mechanisms for the generation of the masses of the leptons and the quarks are similar, but due to the special properties of the strong interactions the Higgs field needs to be defined slightly differently from equation 2.17 to generate the quark masses [41].

The derivation of the masses of the fermions makes use of the symmetry between left-and right-handed particles. As mentioned in section 2.1.2, right-handed neutrinos are not included in the Standard Model. As a result, the neutrino mass terms are zero. The recent observation of a non-zero neutrino mass [53] could mean that new fields, such as right-handed neutrinos, need to be added to the Standard Model to allow gauge invariant mass terms in the Lagrangian.

2.1.4 The complete Standard Model Lagrangian

The final Lagrangian $\mathcal{L}_{\mathrm{SM}}$ that describes all interactions presently included in the Standard Model is a sum over the following terms:

- $-\frac{1}{4}(\mathrm{W}^{\mu\nu}\mathrm{W}_{\mu\nu} + \mathrm{B}^{\mu\nu}\mathrm{B}_{\mu\nu} + G^{\mu\nu}G_{\mu\nu})$,
  kinetic energies and self-interactions of the bosons,

- $\bar{f}\gamma^\mu(i\partial_\mu - gT_j\mathrm{W}^j_\mu - \frac{g'}{2}Y\mathrm{B}_\mu)f$,
  kinetic energies of the fermions and electroweak interactions between them,

- $-\bar{q}\gamma^\mu g_s M_a C^a_\mu q$,
  strong interactions between quarks,

- $|(i\partial_\mu - gT_j\mathrm{W}^j_\mu - \frac{g'}{2}Y\mathrm{B}_\mu)\phi|^2 - (\frac{1}{2}\mu^2\phi^2 + \frac{1}{4}\lambda\phi^4)$,
  kinetic energy of the Higgs boson, couplings to the W and Z, the boson masses, and the Higgs self-interactions,

- $-\mathrm{m}_f\bar{f}f(1+\frac{\eta}{v})$,
  masses of the fermions and their couplings to the Higgs.

2.1.5 Feynman rules

To calculate observables of a particle interaction, a matrix S is defined that contains all the information of the process. Define two states a and b. S is defined by the probability $\mathcal{P}$ for a transition from a to b:

$$\mathcal{P}(a \to b) \equiv |< b|S|a >|^2 \tag{2.24}$$

and alternatively, interaction probabilities can be calculated for any state a and b if the elements of S are known. The elements can be derived from the Hamiltonian H (or the Lagrangian $\mathcal{L}_{\mathrm{SM}}$) of the system using perturbation theory. The result is an infinite series of terms [42]:

$$\begin{aligned} < b|S|a > &= < b|a > \\ &- i\int dt < b|\mathrm{H}|a > \\ &- \int dt_1 dt_2 < b|T(\mathrm{H}(t_1), \mathrm{H}(t_2))|a > \\ &+ \mathcal{O}(\mathrm{H}^3), \end{aligned} \tag{2.25}$$

where T is the time-ordered product of the Hamiltonian: $T = \mathrm{H}(t_1)\mathrm{H}(t_2)...\mathrm{H}(t_n)$ and $t_1 > t_2 > t_3 > ... > t_n$. The state a can be defined as the sum over all orthogonal states n that span the space: $|a >= \sum_n c_n|n >$, where the amplitudes $c_n(t)$ change with time as a result of particle interactions. The elements of S are related to these amplitudes as $S_{ab} \equiv c_b(\infty)$.

To obtain the elements of S, an integration over the available phase space is performed. The solution for S is the product of this phase space, and an infinite series of terms that contain the characteristics of the fields, known as the *invariant amplitude* $\mathcal{M}$.

Feynman introduced a graphic representation of the infinite series of terms in equation 2.25, known as Feynman diagrams, in 1948 [54]. If a and b are different states, $< b|a >= 0$ due to orthogonality of the base. Therefore, the zeroth order contribution corresponds to the probability that a particle will not interact and is represented by a line. The first order contribution corresponds to a line with a vertex and the second order contribution corresponds to a diagram with two vertices, relevant for processes such as annihilation and pair production. An example of processes with two vertices are the Feynman diagrams for W pair production in figure 2.1.

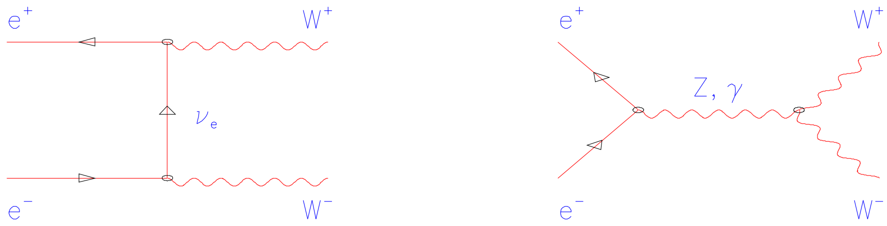

Figure 2.1: Dominant first order W pair production processes at LEP2, referred to as the three charged current (CC03) diagrams. The neutrino exchange process dominates at low velocities of the W bosons.

The expression for the amplitude $\mathcal{M}$ of a specific process can be separated into terms corresponding to the different elements of the appropriate Feynman diagram. Terms for all possible elements of a diagram for which the interaction Hamiltonian H is known can be derived by solving equation 2.25. This derivation is not described in this thesis, but the result of the derivation is a set of *Feynman rules* that can be applied to any process [42].

Once these rules are known, the expression for $\mathcal{M}$ corresponding to a chosen diagram is found by multiplying terms for the incoming wave function(s), the vertex and the outgoing wave function(s). The Feynman rules relevant for lowest order W pair production are summarised in table 2.3 and equation 2.27.

The term corresponding to a particle that propagates between two vertices in a Feynman diagram is known as the propagator term. The spin of such a particle is not an observable and this term therefore includes a summation over all possible

Waves	
Initial (anti-)fermion	$(\bar{v})u$
Final (anti-)fermion	$(v)\bar{u}$
Initial boson	ϵ_μ
Final boson	ϵ^*_μ
Vertices	
$ee\gamma$	$ie\gamma^\mu$
eeZ	$-ie\gamma^\mu(c^e_v - c^e_A\gamma^5)/(2\sin\theta_{\mathrm{W}}\cos\theta_{\mathrm{W}})$
$e\nu$W, $\mu\nu$W	$-ie\gamma^\mu(1-\gamma^5)/(2\sqrt{2}\sin\theta_{\mathrm{W}})$
W$\mathrm{q\bar{q}}$	$-ie\gamma^\mu(1-\gamma^5)V_{\mathrm{q\bar{q}}}/(2\sqrt{2}\sin\theta_{\mathrm{W}})$
$\gamma\mathrm{W^+W^-}$	$-ie[g^{\mu\nu}(p_\gamma - p_{\mathrm{W}^+})^\sigma$ $+g^{\nu\sigma}(p_{\mathrm{W}^+} - p_{\mathrm{W}^-})^\mu$ $+g^{\mu\sigma}(p_{\mathrm{W}^-} - p_\gamma)^\nu]$
$\mathrm{ZW^+W^-}$	$-ie[g^{\mu\nu}(p_{\mathrm{Z}} - p_{\mathrm{W}^+})^\sigma$ $+g^{\nu\sigma}(p_{\mathrm{W}^+} - p_{\mathrm{W}^-})^\mu$ $+g^{\mu\sigma}(p_{\mathrm{W}^-} - p_{\mathrm{Z}})^\nu]/\tan\theta_{\mathrm{W}}$

Table 2.3: Relevant S matrix terms for W pair production [42]. $c^e_A = T^3_e$ and $c^e_v = c^e_A - 2\sin^2\theta_{\mathrm{W}} Q_e$, where e is the electron. $Q_e = \pm 1$, but T^3_e = -1/2 for e_L (and $\bar{e}_R$) and zero for e_R (and $\bar{e}_L$). V is the appropriate element of the CKM mixing matrix [55]. The boson fields entering the $b\mathrm{W^+W^-}$ vertices carry indices μ, ν, σ respectively, and p_b are their momenta. The metric tensor $g^{\mu\nu}$ is defined to allow $g_{\mu\nu}p^\mu q^\nu \equiv p_\mu q^\mu$.

spin states. For instance, the Lagrangian of a W boson in the absence of any other fields is given by:

$$\mathcal{L}_{\mathrm{W}} = -\frac{1}{4}\mathrm{W}^{\mu\nu}\mathrm{W}_{\mu\nu} + \mathrm{m}^2\mathrm{W}^\mu\mathrm{W}_\mu. \tag{2.26}$$

From this Lagrangian, an equation of motion for freely propagating W bosons can be derived. The Fourier transform of a Green's function $G(x, x')$ is used to solve the equation in terms of the momentum p rather than the spatial coordinates x, where $G(x, x')$ is the potential at x due to a source at x'. A detailed derivation is found in [41].

The derivation of the Feynman propagator involves a contour integration of the wave function in the complex momentum plane. The choice of the contour defines the expression for the propagator. To be able to describe unstable particles, the contour is chosen in order to include a small imaginary part $i\epsilon$ in the propagator term. In section 2.2.3, the relation between this term and the decay width of the particle will be illustrated. The propagator for stable particles is described by the same expression, in the limit where $\epsilon \to 0$.

Since fermions and bosons have different spin states, two different propagator expressions P_f and P_b are derived:

$$\begin{aligned} P_f &= \frac{\sum_s \bar{u}^{(s)} u^{(s)}}{p^2 - m^2 + i\epsilon} = \frac{\not{p} + m}{p^2 - m^2 + i\epsilon} \\ P_b &= \frac{\sum_s (\epsilon_\mu^*)^{(s)} \epsilon_\nu^{(s)}}{p^2 - m^2 + i\epsilon} = \frac{-g_{\mu\nu} + (p_\mu p_\nu / m^2)}{p^2 - m^2 + i\epsilon}, \end{aligned} \tag{2.27}$$

where $\not{p} \equiv \gamma^\mu p_\mu$. The boson is not observable in the final state and a different gauge is often chosen to simplify the expression. On the Feynman-'t Hooft gauge that is used for many Standard Model calculations, the boson propagator is defined as [56]:

$$P_b = \frac{-g_{\mu\nu}}{p^2 - m^2 + i\epsilon}. \tag{2.28}$$

2.1.6 Renormalisation and unification

The strength of the interactions included in the Standard Model depends on the values for e and g_s. The weak couplings g and g' are defined by e and the mixing angle θ_W in equation 2.14. Since experimental observables are proportional to $|\mathcal{M}|^2$ (see equation 2.24), the commonly used definition of the coupling strengths are α and α_s:

$$\begin{aligned} 4\pi\alpha &= e^2 \\ 4\pi\alpha_s &= g_s^2. \end{aligned} \tag{2.29}$$

Internal loops in a Feynman diagram cannot directly be observed experimentally: the propagator particle can pair produce and if the pair annihilates again before producing the final state, this cannot be distinguished from the original process. Loops can cause series of Feynman diagrams to diverge, which makes the calculation of observables impossible. The solution to this problem in case of QED was found by Feynman [57], Tomonaga [58] and Schwinger [59] in 1949, in the *renormalisation* of the QED coupling constant in equation 2.29. They proposed a theory in which particle loops that affect the propagator are incorporated in the definition of α.

The renormalisability of more general gauge theories (Yang-Mills theories [60]) was proven by Gerard 't Hooft in 1971 [56] and was an important breakthrough in the general acceptance of the Standard Model. As a result of any renormalisation scheme, the Standard Model couplings become energy dependent and are referred to as a *running couplings* (see appendix A.1). There are indications that the coupling constants converge to the same value at very high energies ($E > 20$ TeV [61]), which leads theoreticians to believe that they originate from one and the same force. The different forces observed in nature are, in that case, the result of a symmetry breaking process at lower energies. Grand unification models such as super-symmetry assume the existence of more particles than presently observed. Many experimental searches are performed to find evidence for physics beyond the Standard Model but, for the analysis described in this thesis, the Standard Model is assumed to be valid.

2.2 The W boson and electroweak physics

In this section, the Standard Model theory described in the previous section is applied to the W boson. In section 2.2.1, the lowest order cross section for W pair production is shown.

In section 2.2.2, the width of the W is introduced and the different final states of W pair decays and their relative importance are shown. In section 2.2.3, the shape of the W mass distribution is described. Radiative corrections are described in section 2.2.4.

2.2.1 W pair production cross section

The transition rate W from an initial state a to a final state b per unit volume v is defined as $W_{ab} = |S_{ab}|^2/(vt)$, where t is the interaction time and S_{ab} is the appropriate element of the S matrix defined in equation 2.25. The *cross section* σ is the commonly used observable for this transition rate:

$$\sigma_{ab} = \frac{N_b W_{ab}}{F_a} = \frac{N_b |S_{ab}|^2}{vtF_a}, \tag{2.30}$$

where N_b is the number of available final states and F_a is the flux of initial states. Both N_b and F_a can be derived in terms of the initial and final state energies and momenta, simply by counting the number of states in the available phase space. N_b, F_a and the phase space normalisation of S are evaluated to express the cross section in terms of the amplitude $\mathcal{M}$ defined in section 2.1.5.

Take a process of two initial state particles with momenta $|p_a|$ and two final state particles with momenta $|p_b|$ in the centre-of-mass frame. The cross section per unit of solid angle equals [41]:

$$\left(\frac{d\sigma}{d\Omega}\right)_{ab} = \frac{1}{64\pi^2 {\mathrm{E_{cms}}}^2}\frac{p_b}{p_a}|\mathcal{M}_{ab}|^2 \approx \frac{\beta_b}{64\pi^2 {\mathrm{E_{cms}}}^2}|\mathcal{M}_{ab}|^2, \tag{2.31}$$

where the approximation is valid if the initial state particles are very relativistic ($\beta_a \approx 1$). With this expression, the relative event rates for different processes occurring in e^+e^- annihilation can be evaluated from the Feynman rules.

W pairs are produced in e^+e^- collisions if the leptons collide head on and the centre-of-mass energy exceeds $\mathrm{E_{cms}} \simeq 2\mathrm{M_W}$. In case of unpolarised lepton beams, they are produced predominantly in the processes shown in figure 2.1 that are referred to as the three charged current (CC03) diagrams. A derivation of $\mathcal{M}$ for these diagrams is shown in appendix A.2, and is valid if [62]:

- the electron mass m_e is neglected and the Higgs exchange diagram is neglected, as it is suppressed by a factor of $\mathrm{m}_e/\mathrm{M_W}$,
- the CP violating phase in the CKM matrix [55] is neglected (the CP violating contributions to the cross section are small),
- the W is a stable particle (its decay width is zero).

Define the momenta of the in-going electron and positron as p and q and the momentum of the outgoing $\mathrm{W}^+$and W^-as k and l. The first diagram in figure 2.1 is a t-channel diagram, the annihilation diagrams are s-channel diagrams, where t and s are the Mandelstam variables and define the momentum exchange in the interaction:

$$\begin{aligned} s &\equiv (p+q)^2 = (k+l)^2 \\ t &\equiv (p-k)^2 = (q-l)^2. \end{aligned} \tag{2.32}$$

Due to the lack of right-handed neutrinos, the neutrino exchange only involves left-handed electrons. If $\mathrm{m}_e = 0$, the electron and positron have opposite helicities ($\equiv \pm h$, where $h = \pm 1/2$). The $\mathrm{W}^\pm$ is a spin-1 particle and occurs in three helicity states $h_\pm$: -1, 0 and 1. As a result, there are 18 different matrix elements.

The $W^{\pm}$ polarisation vectors are, according to table 2.3, $\epsilon^*(k, h_\pm)$ and $\epsilon^*(l, h_\pm)$. The (CP conserving) amplitudes do not change if $h_+ \to -h_-$ and $h_- \to -h_+$ simultaneously. This reduces the number of diagrams to 12. The differential cross section for W pair production of unpolarised W bosons and unpolarised electron beams is derived in appendix A.2. The result of equation 2.31 is [62]:

$$\frac{d\sigma}{d\Omega} = \frac{\beta}{64\pi^2 s} \times \frac{1}{2} \sum_{h,h_+,h_-} |\mathcal{M}(h, h_+, h_-, s, t)|^2, \tag{2.33}$$

where β is the velocity of the W bosons and the factor $(\frac{1}{2})$ originates from the average over the two beam helicity configurations. The terms of $\mathcal{M}$ for the 6 independent polarisations of the W pairs are shown in equation A.14 of the appendix.

Define θ as the scattering angle between the positron and the W^+. The total matrix element $\mathcal{M}$ is the sum over the three individual diagrams and has terms for each of the W polarisations. The W pairs at $\theta = 0$ all have helicities (0,$\pm$1). This is due to the fact that spin and momentum are conserved: the sum of the electron helicities ($\pm$1) has to be equal to the sum of the W helicities if they are moving along the same axis.

For small β, the dominant term of the amplitude is independent of β for the neutrino exchange diagram, but linear with β in case of the s channel. The s channel is therefore negligible at threshold. For small β the result of equation A.14 is [62]:

$$\frac{d\sigma}{d\Omega} \approx \frac{\alpha^2 \beta}{4s \sin^4\theta_W} \left(1 + \frac{3\cos^2\theta_W - 1}{4\cos^2\theta_W - 1} 4\beta \cos\theta + O(\beta^2)\right). \tag{2.34}$$

The first term originates from the t channel diagram, and does not depend on the scattering angle. At threshold, the total angular momentum of the W bosons is given by the sum of their spins ($J = 0$, 1 or 2). $J = 0$ is not possible because of the helicity of the in-going leptons. $J = 1$ violates CP. The s channel mediators have $J < 2$, and their contribution therefore has to vanish at threshold. For the total cross section, the s channel contributions (and the interference terms) are $O(\beta^3)$, and negligible up to a few GeV from threshold:

$$\sigma \approx \frac{\pi\alpha^2\beta}{s \sin^4\theta_W} + O(\beta^3). \tag{2.35}$$

The high energy behaviour follows from substituting $\beta = 1$ and $s \to \infty$ in the equations A.14 and performing the summation. The interference between s

and t channels results in a cancellation of terms and as a result, the cross section decreases with increasing energy. The terms that remain are terms for oppositely polarised W bosons (only t-channel contributes to $h_+ - h_- = 2$) and terms with two longitudinal W bosons ($h_+ - h_- = 0$). At $\theta = 0$ however, all these terms are zero and the contribution of (0,±1) W pairs dominates, even though its amplitude is proportional to $\mathrm{M_W}/\sqrt{s}$.

The importance of the s channel diagrams at higher energies is illustrated in figure 2.2. The figure shows the preliminary results from all four LEP experiments combined at each centre-of-mass energy analysed for the ICHEP 2000 summer conference [63]. The calculation of the cross section according to various Monte Carlo programs [37, 64, 65] is shown. The top curve includes only the t-channel ν_e exchange diagram. The second curve takes into account the two diagrams that do not include a ZWW vertex (plus their interference) and in the third curve all three diagrams are taken into account.

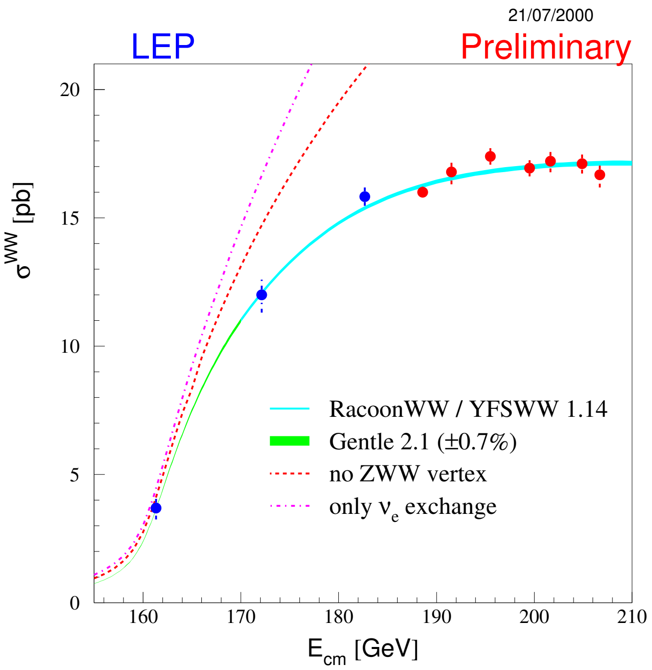

Figure 2.2: Preliminary cross section for W pair production as measured by the four LEP experiments, compared to Standard Model predictions as a function of the LEP centre-of-mass energy. For the full simulation, GENTLE is used near threshold ($\mathrm{E_{cms}} < 170$ GeV) and RacoonWW/YFSWW is used for $\mathrm{E_{cms}} > 170$ GeV [66].

2.2.2 W decay rate

Assume an initial number of W bosons N_{W}, that decay exponentially with a certain lifetime τ: $N_{\mathrm{W}}(t) = N_{\mathrm{W}}(0)\exp\{-t/\tau\}$. Define the decay rate Γ_{W} as:

$$\Gamma_{\mathrm{W}} \equiv \frac{-1}{N_{\mathrm{W}}}\left(\frac{dN_{\mathrm{W}}}{dt}\right) = \frac{1}{\tau}. \tag{2.36}$$

According to Heisenberg's uncertainty principle ($\Delta\mathrm{M} \geq \hbar/\Delta t$), Γ_{W} is directly related to the intrinsic width of a distribution of experimentally measured W masses.

In the Standard Model, the W boson decays into either an $l\nu$ or a $q\bar{q}$ pair. Searches for other decays have not yielded any positive results [45, 67].

Assume one W boson decays into two particles, f_1 and f_2. The decay rate is related to a transition probability and therefore proportional to $|\mathcal{M}|^2$, where $\mathcal{M}$ is the transition amplitude for one in-going particle (W) and two out-going particles ($f_{1,2}$). Other terms originate from phase space factors, and the result is [43]:

$$\frac{d\Gamma_{\mathrm{W}}}{d\Omega} = \frac{|p_f|}{32\pi^2 M_{\mathrm{W}}^2}|\mathcal{M}|^2. \tag{2.37}$$

Since there is no preferred decay direction in the centre-of-mass frame after averaging over the W polarisations, the integration over solid angle is simply a multiplication of the differential width by 4π.

The expression for $\mathcal{M}$ is obtained from the rules in table 2.3 and the result for the width of the W is derived in appendix A.3:

$$\begin{aligned} \Gamma(\mathrm{W} \to l\nu) &= \frac{G_{\mathrm{F}}{\mathrm{M_W}}^3}{2\sqrt{2}\pi} \\ \Gamma(\mathrm{W} \to \mathrm{q\bar{q}}) &= \frac{G_{\mathrm{F}}{\mathrm{M_W}}^3}{\sqrt{2}\pi}\left[1 + \frac{\alpha_s}{\pi} + \mathcal{O}\left(\frac{\alpha_s^2}{\pi^2}\right)\right], \end{aligned} \tag{2.38}$$

where G_{F} is the Fermi coupling constant. The expansion in the case of the hadronic width originates from the QCD corrections for massless quarks. The main electroweak corrections are included in the definition of G_{F} and/or the experimentally measured value of $\mathrm{M_W}$ [68] and the result of equation 2.38 for the total width is:

$$\Gamma_{\mathrm{W}} = \frac{G_{\mathrm{F}}{\mathrm{M_W}}^3}{2\sqrt{2}\pi}\left[3 + 2\frac{\alpha_s}{\pi} + \mathcal{O}\left(\frac{\alpha_s^2}{\pi^2}\right)\right], \tag{2.39}$$

which results in $\Gamma_{\mathrm{W}} = 2.0927 \pm 0.0025$ GeV/c^2 [62, 69]. A Standard Model prediction that takes all known uncertainties into account, including the small electroweak correction δ^{SM} defined in appendix A.3, yields $\Gamma_{\mathrm{W}} = 2.067 \pm 0.021$ GeV/c^2 [45, 70].

The hadronic and leptonic branching ratios have been measured accurately [45]:

$$\begin{aligned} B(\mathrm{W} \to \mathrm{q\bar{q}}) &= 68.5 \pm 0.6\% \\ B(\mathrm{W} \to l\nu) &= 31.7 \pm 0.4\%. \end{aligned} \tag{2.40}$$

Since the three different leptonic branching ratios are in good agreement, lepton universality is assumed. For the semi-leptonic W pair decay channels analysed in this thesis follows:

$$B(\mathrm{WW} \to e\nu\mathrm{q\bar{q}}) = B(\mathrm{WW} \to \mu\nu\mathrm{q\bar{q}}) = 14.5 \pm 0.2\%. \tag{2.41}$$

2.2.3 W decay amplitude

The propagator for the W boson in the 't Hooft gauge (equation 2.28) is derived from the Lagrangian in equation 2.26:

$$P_b = \frac{-g_{\mu\nu}}{p^2 - m^2 + i\epsilon}. \tag{2.42}$$

The pole $i\epsilon$ can be defined in various ways, depending on the renormalisation scheme that is chosen to perform the summation over all possible irreducible loop insertions. A gauge invariant way to define the propagator is by introducing the *fixed width* Γ_{W} in the expression:

$$P_b = \frac{-g_{\mu\nu}}{p^2 - {\mathrm{M_W}}^2 + i\mathrm{M_W}\Gamma_{\mathrm{W}}}. \tag{2.43}$$

Define the matrix elements $\mathcal{M}(h, h_+, h_-, s, t)$ in equation 2.33 as $\mathcal{M}_{\mathrm{prod}}$ and the lowest order (Born level) amplitude for $e^+e^- \to \mathrm{WW} \to 4f$ as $\mathcal{M}_{\mathrm{born}}$. If $\mathrm{W}^+ \to f_1\bar{f}_2$ and $\mathrm{W}^- \to f_3\bar{f}_4$, the amplitude equals:

$$\mathcal{M}_{\mathrm{born}} = \mathcal{M}_{\mathrm{prod}} \times \frac{\bar{u}_1 V^+ v_2 \; \bar{u}_3 V^- v_4}{(l^2 - {\mathrm{M_W}}^2 + i\mathrm{M_W}\Gamma_{\mathrm{W}})(k^2 - {\mathrm{M_W}}^2 + i\mathrm{M_W}\Gamma_{\mathrm{W}})}, \tag{2.44}$$

where $V^\pm$ are the vertex terms for the $\mathrm{W} \to f\bar{f}$ decay vertices defined in table 2.3. k and l are the momenta of the W^- and the W^+ as in the previous section.

The width of the W is small compared to its mass. As a result, the observable mass m_O of the W boson is distributed according to a Breit-Wigner distribution [43]:

$$\sigma(m_O) \propto \frac{\mathrm{M_W}\Gamma_\mathrm{W}}{(m_O^2 - \mathrm{M_W}^2)^2 + \mathrm{M_W}^2\Gamma_\mathrm{W}^2}. \tag{2.45}$$

The same definition applies to the Z propagator, introducing the width of the Z, Γ_Z.

The definition in equation 2.43 is gauge invariant, but does not take the energy dependence of the loop corrections to the propagator into account. To incorporate this energy dependence, the width of the W can be defined in an energy dependent way:

$$i\mathrm{M_W}\Gamma_\mathrm{W} \to i\frac{p^2}{\mathrm{M_W}^r}\Gamma_\mathrm{W}^r, \tag{2.46}$$

where Γ_W^r is called the *running* width. This scheme violates gauge invariance and therefore breaks down in the high energy limit [71].

At LEP energies, both definitions lead to a proper theoretical description of the physics involved. However, it is important to specify what definition is used in the measurement of the mass and width. Near the resonance, they are related to each other via a transformation of variables and will therefore yield different results. This transformation is [72, 73]:

$$O = O^r\left[1 + \left(\frac{\Gamma_\mathrm{W}^r}{\mathrm{M_W}^r}\right)^2\right]^{-1/2} \approx O^r\left[1 - \frac{1}{2}\left(\frac{\Gamma_\mathrm{W}^r}{\mathrm{M_W}^r}\right)^2\right], \tag{2.47}$$

where the observable O is either Γ_W or $\mathrm{M_W}$. In the simulation and the fit described in the next sections, the fixed width convention is used. In order to be consistent with results from other collaborations, the published result uses a running width. Therefore, 27 MeV/c^2 is added to the fitted mass and 0.7 MeV/c^2 to the fitted width, based on the present world average $\mathrm{M_W}$ and the corresponding Standard Model width.

2.2.4 Radiative corrections to W production and decay

The CC03 diagrams in figure 2.1 are the lowest order diagrams contributing to W pair production. Higher order diagrams include particle loops in the propagators or the fermions that are not observable, but affect the calculation of experimental observables. Processes in which additional photons are radiated have a significant effect on the W pair cross section [71]. The mass of the W can be expressed in terms of $G_{\rm F}$, α and $\sin^2\theta_{\rm W}$ in the absence of higher order corrections:

$$
{\rm M_W}^2 = \frac{\pi\alpha}{\sqrt{2}G_{\rm F}\sin^2\theta_{\rm W}}. \tag{2.48}
$$

The effect of radiative corrections from higher order diagrams that contain $\rm q\bar{q}$, $\rm W\gamma$ or WZ loops in the W propagator can be parameterised by the introduction of the correction Δr:

$$
{\rm M_W}^2 = \frac{\pi\alpha}{\sqrt{2}G_{\rm F}\sin^2\theta_{\rm W}(1-\Delta r)}. \tag{2.49}
$$

$G_{\rm F}$ and α are measured to high precision. From equation 2.22, $\sin^2\theta_{\rm W}$ can be expressed as:

$$
\sin^2\theta_{\rm W} = 1 - \left(\frac{\rm M_W}{\rm M_Z}\right)^2. \tag{2.50}
$$

$\rm M_Z$ is measured experimentally with high precision [35]. As a result, the size of Δr can be evaluated from a precise measurement of the W mass.

Apart from loop contributions, photon radiation influences the measurement. Some of these processes can be observed in the final state, including:

- Final State Radiation (FSR) of photons off the charged final state lepton. If the radiated photon carries a significant amount of energy, it can be detected;
- Initial state radiation (ISR) of photons off one (or both) of the incoming beam leptons;
- Bremsstrahlung off the final state lepton. The high energy lepton is decelerated in the detector material.

Identified photons are corrected for in the analysis as described in section 4.1.4. ISR and FSR effects are included in the Monte Carlo simulation described in section 2.3 and Bremsstrahlung is included in the detector simulation (see chapter 3).

2.3 Monte Carlo event generators

The analysis described in this thesis makes use of theoretical predictions for an experimentally observable W mass estimator. Distributions of this observable are calculated from the Standard Model Lagrangian by means of a Monte-Carlo method.

A Monte-Carlo method uses random (or pseudo-random) numbers to perform numerical calculations and is based on the theorem of Monte Carlo [74]:

The average of a function f over a volume V is equal to the average of the set $\{f(x_1), f(x_2), f(x_3), ..., f(x_n)\}$ in the $n \to \infty$ limit, where $(x_i)_n$ are random and independent coordinates from the domain space V.

For each of the processes that contribute to the distribution of the W mass estimator, a large number of events is generated with event topologies distributed according to probabilities derived from Standard Model theory. The uncertainty of Monte Carlo predictions is generally proportional to the square-root of the number of generated events.

The relevant final states that are generated are introduced in chapter 4. The generation of large samples of $q\bar{q}$, Zee, ZZ, $We\nu$ and $\tau\tau$ events is necessary to simulate the background to W pair production. Different programs are used to simulate the different background types and the signal processes: PYTHIA [37] and KORALZ [75] are used to simulate the background distributions, KORALW [76] is used to simulate the $4f$ final states.

e^+e^- annihilation is well described by QED, but QCD is needed to describe the production of two quarks. After the production of a $q\bar{q}$ pair, the confinement of strong interacting particles results in two jets of hadrons. Near the production vertex, the strong coupling constant is large and exact calculations according to perturbation theory are no longer possible. The JETSET [77] program calculates the properties of the final state jet according to a phenomenological model and is used to simulate these processes. To evaluate the uncertainty in the measurement due to the choice of this model, the measurement is repeated with the alternative HERWIG [78] model. The results of this study are shown in chapter 6.

The topology of the final states generated by the Monte Carlo programs is translated into observables by the GALEPH code that uses the simulation package GEANT [79] and includes a detailed description of the ALEPH detector.

Chapter 3

Description of the experiment

The particles produced in collisions of the two LEP beams are detected by four detectors along the LEP ring: ALEPH, DELPHI, OPAL and L3. The analysis in this thesis uses data collected by the ALEPH detector. Understanding of the properties of the detector is vital in the evaluation of the systematic uncertainties on the measurement of the mass and width of the W.

The motivation for choosing a storage ring accelerator is discussed in section 3.1 and the main limitations of the design are mentioned. The generation and acceleration of the LEP beams is described in section 3.2. The ALEPH detector is described in section 3.3. Two main components are used to construct the detector: tracking detectors and calorimetry. The sub-detectors belonging to these two categories are described in section 3.3.1 and 3.3.2 respectively. The detection of muons in ALEPH makes use of both these techniques as is explained in section 3.3.3. The ALEPH trigger system is explained in section 3.4 and the reconstruction of the particles in recorded events is explained in section 3.5.

3.1 Choice of the LEP accelerator

Collisions at energies of the order of the W mass can be produced in either a fixed-target experiment or a storage ring accelerator. The energy available in a collision process is the Lorentz invariant mass, which is equal to the centre-of-mass energy E_{cms}. Assume a set energy is available to accelerate the particles. If this energy is used in a fixed target experiment where the beam particles have a mass m_b and the target particles have a mass m_t, the centre-of-mass energy $\mathrm{E_{cms}}$ is derived from:

$$\begin{aligned} \mathrm{E_{cms}}^2 = p_\mu p^\mu &= (\mathrm{E_b} + m_t)^2 - \beta^2 \mathrm{E_b}^2 \\ &= m_b^2 + 2\mathrm{E_b} m_t + m_t^2. \end{aligned} \tag{3.1}$$

In case of a storage ring accelerator the centre-of-mass energy equals twice the beam energy because the total momentum of the system is zero. If the masses are small compared to the kinetic energy, the energy $\mathrm{E}_{f,s}$ needed to reach a defined centre-of-mass energy is, in case of a fixed target accelerator, $\mathrm{E}_f \simeq \mathrm{E_{cms}}^2/(2m_t)$ and in case of a storage ring $\mathrm{E}_s = \mathrm{E_{cms}} \simeq \mathrm{E}_f \cdot (2m_t/\mathrm{E_{cms}})$. To investigate the properties of the W, centre-of-mass energies of the order of twice the W mass have to be reached. If m_t is much lighter than the W, a fixed target set-up would require too much energy. Therefore, a suitable choice for the large electron-positron collider (LEP) is a storage ring accelerator, or synchrotron.

A synchrotron is a circular accelerator in which the beam is kept in a fixed orbit by use of a series of bending magnets. The magnetic field B needed to keep a particle with momentum p and charge $Q = qe$ in an orbit with a radius of curvature ρ equals $B = p/(Q\rho)$ [80]. The momentum of the leptons increases as they pass through accelerating *cavities* around the ring, each effectively a series of linear accelerators operating on a high frequency voltage produced by a klystron. This frequency is chosen in such a way that the leptons always experience an accelerating force and the magnetic field of the bending magnets is adapted to keep ρ constant. Quadrupole (and higher order) magnets are used to keep the beam focused during the acceleration process.

In a circular accelerator the beam is accelerated repeatedly by the same cavities and higher energies can be reached than in a similar linear accelerator setup. However, the charged particles in the beam change direction in every bending magnet and as a result they radiate photons, known as synchrotron radiation. If Larmor's formula [15] is applied to a relativistic ($\beta \approx 1$) particle with charge e, the energy lost in each revolution due to synchrotron radiation equals [80]:

$$\Delta\mathrm{E} = \frac{4\pi e^2}{3\rho}\beta^3\gamma^4 \approx \frac{4\pi e^2}{3\rho}\left(\frac{\mathrm{E}}{m}\right)^4, \tag{3.2}$$

where β and γ are the Lorentz parameters related to the velocity of the particle, E is the energy of the particle and m is its mass. For electron beams in an ideally circular LEP ring ($\rho = 4.2$ km) this results in ΔE(keV) ≈ 0.02 (E(GeV))^4, or 2 GeV for a 100 GeV beam.

LEP has a circumference of 26.7 km and an electron travelling with the speed of light will experience over 11 thousand revolutions per second. Therefore, the LEP energy is limited by the power of the accelerating cavities needed to compensate for radiation losses.

Lepton collisions result in clean events with a well defined collision energy. This is not the case if composite particles such as protons are used. However, if protons were used instead of electrons, the synchrotron radiation would be reduced by a factor of $(m_p/m_e)^4 \approx 11 \times 10^{12}$ and therefore be negligible up to very high energies. The future LHC collider is a pp accelerator and will therefore be able to look for new physics at the TeV scale [81]. The other option is to use a long linear collider to accelerate the leptons which is the basis of other future projects [82].

3.2 The acceleration process

To create high energy collisions between an electron and a positron in ALEPH, beams are produced and accelerated in the setup shown in figure 3.1. The electrons are produced by a pulsed electron gun before entering a linear accelerator, the LINAC, where they reach an energy of 200 MeV. Some of these electrons are sent through a tungsten converter to create the positron beam.

When light charged particles traverse solid matter they are decelerated significantly due to electromagnetic interactions with the charges in the medium. As a result, they lose energy through photon radiation known as Bremsstrahlung according to Larmor's formula. The resulting energy loss is proportional to the particle's energy E [80]:

$$\frac{d\mathrm{E}}{dx} \equiv \frac{\mathrm{E}}{X_0}, \tag{3.3}$$

defining the *radiation length* of the medium, X_0.

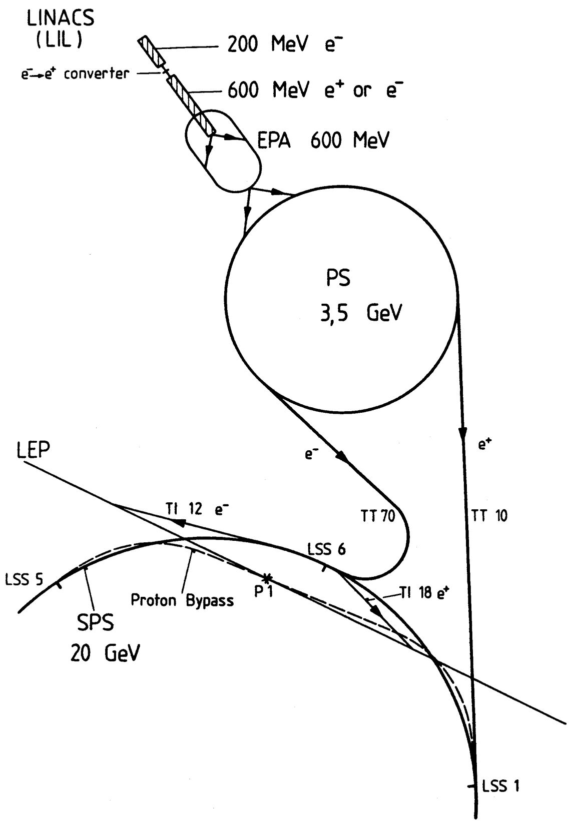

Figure 3.1: Schematic overview of the machines used in the acceleration process. As the beams accelerate they are focused and injected into longer but narrower beam pipes until they reach the energy needed to enter the LEP ring.

The electron mass is small compared to its energy and the dominant cause for Bremsstrahlung in the tungsten are interactions with the tungsten nuclei. Photons created in this process convert into e^+e^- pairs and the produced positrons are extracted for the second beam.

A second LINAC, the LEP linear injector (LIL) accelerates the electrons and positrons to an energy of 600 MeV. The two beams are fed into the electron positron accumulator (EPA) where they are separated into bunches. A series of different accelerators is needed to reach the final collision energy because the changing momentum of the leptons affects the topology of the beam.

From the EPA the electron and positron beams are injected into the proton synchrotron (PS) where they are accelerated to an energy of 3.5 GeV. As the beam energy increases the beams are focused. At this energy they are fed into the super proton synchrotron (SPS) where they reach an energy of 22 GeV and the beams are sufficiently collimated to be injected into LEP.

The LEP ring is built at an angle of $\sim 0.8^\circ$ with respect to the horizontal plane in a seam of soft rock, in a tunnel situated 80 to 150 m below the surface. It consists of 8 straight sections combined with dipole bending magnets that force the beam into a circular orbit. The beam is focused by higher order magnets, mostly quadrupoles. The beams are accelerated by cavities around the ring, most of which are superconducting. Inside the cavities an accelerating field of 6-7 MV/m is reached and the current for each group of 8 cavities is supplied by a radio frequency (RF) klystron.

The available RF voltage is equal to the integral of the accelerating field over the active length of the cavities and is the limiting quantity for the beam energy that can be reached by LEP. At present a voltage of 3650 MV has been reached for centre-of-mass energies up to 208 GeV.

The LEP centre-of-mass energy reached the threshold for W pair production ($\sim$ 161 GeV) in June 1996. During the running of LEP2 the machine has had a series of upgrades, first to reach $\sim$172 GeV in Autumn of the same year, and from 1997 onwards to reach energies ranging from $\sim$183 to 208 GeV. The present goal of LEP is to reach as high a beam energy as possible, so as to discover or to place the highest lower-mass bound on the Higgs boson before the end of LEP data taking. In this thesis, centre-of-mass energies up to 201.6 GeV are included.

3.3 The ALEPH detector

The ALEPH (A detector for LEP PHysics) detector covers a solid angle of $\sim 3.9\pi$ and is shown in figure 3.2. A detailed description is found in [83] and its performance is described in [84]. The emphasis of the design is put on high precision charged particle tracking and efficient lepton and photon identification due to a good spatial resolution of the calorimeters. Track reconstruction very close to the beam pipe enables identification of secondary vertices important for the selection of Higgs candidate events with b quarks in the final state. The combined tracking detectors allow a precise measurement of high energy leptons vital for a good resolution on the W mass in the (semi)-leptonic channel.

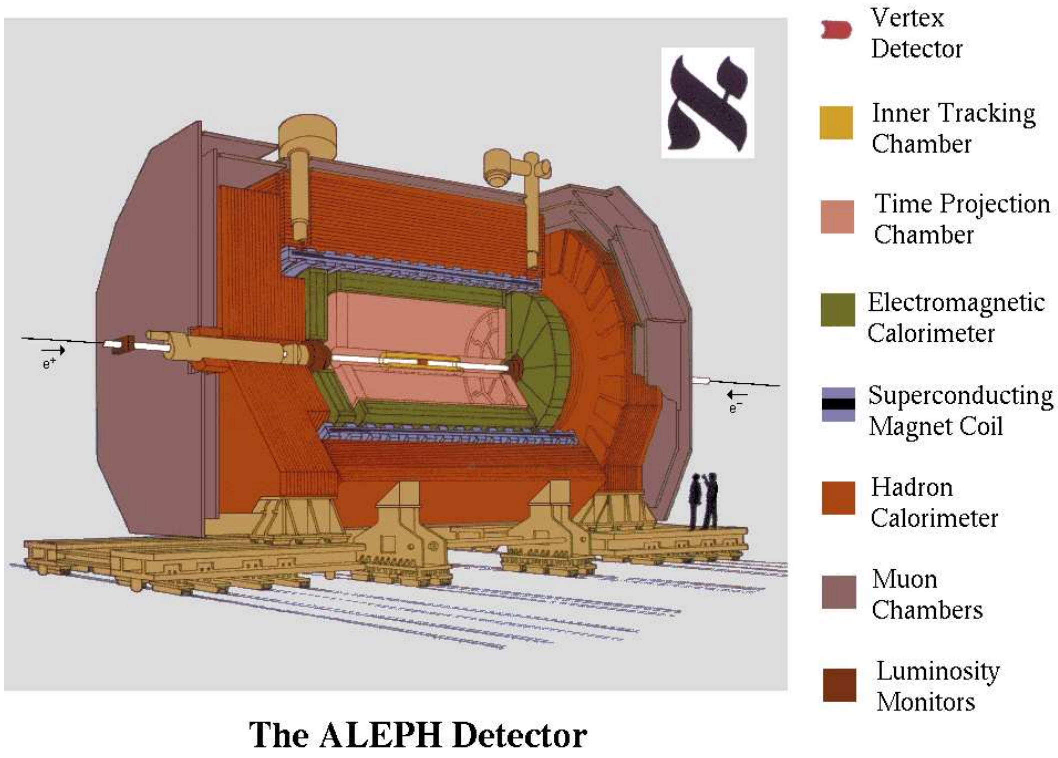

Figure 3.2: Schematic view of the ALEPH detector at CERN, Geneva. ALEPH uses colliding e^+e^- beams from the LEP accelerator and consists of the sub-detectors listed on the right-hand side, in order of their distance from the interaction vertex. The luminosity monitors are located close to the beam pipe, on either side of the interaction point.

Particles that traverse solid matter lose energy through collisions with the atoms and through Bremsstrahlung (see equation 3.3). For light or very relativistic particles (e, γ), Bremsstrahlung and pair production are the main sources of energy loss and the radiation length X_0 is the relevant measure for the thickness of detector material.

For heavy or very low energetic particles, ionisation processes become important. The rate of energy loss is described by the Bethe-Bloch formula [80]:

$$\frac{d\mathrm{E}}{dx} = C_1 \left(\frac{Z}{\beta}\right)^2 [\ln C_2(\beta\gamma)^2 - \beta^2], \tag{3.4}$$

where C_1 contains properties of the electron and the electron density of the gas and C_2 takes into account the mean ionisation potential of the gas atoms. Z is the charge of the incident particle and β and γ are the relativistic parameters describing the particle's velocity. In the case of hadrons, a relevant measure for the thickness of the material is the hadronic interaction length λ_{int}, which is the mean free path between two collisions. Alternatively, the absorption length λ_{abs} can be used, that is defined similarly but does not take into account elastic scattering from the nucleus or quasi-elastic scattering from the nucleons.

Unlike calorimeters that are designed to fully absorb a particle's energy, tracking detectors should reconstruct the path of a particle without slowing it down. They are therefore thin in terms of X_0 and λ. Any dense material found in the tracking region causes radiation losses that need to be corrected for in the analysis.

Starting at the interaction point, the ALEPH sub-detectors are described individually in the following sections. The three charged particle tracking detectors, the super-conducting coil, the two calorimeters and the muon chambers are mentioned, as well as various low angle detectors used for the measurement of the luminosity and the background rates.

3.3.1 Tracking detectors

Tracks are reconstructed in ALEPH using information from three different tracking detectors: the silicon vertex detector (VDETII), the inner tracking chamber (ITC) and the time projection chamber (TPC). A magnet is used to bend the tracks in order to allow a measurement of the particle momentum and the determination of the sign of its electric charge. In this section these three sub-detectors are described and the procedure to reconstruct tracks in ALEPH is outlined.

The silicon vertex detector (VDETII)

A good reconstruction of tracks near the beam pipe allows a precise measurement of the primary vertex and the reconstruction of secondary vertices relevant for Higgs physics. In the W analysis, the VDET is important as it improves the tracking performances of ALEPH as a whole and the resolution on the momentum of charged leptons in particular.

Since its upgrade in 1996 the VDET consists of two concentric layers of silicon wafers at 6.3 and 11 cm from the beam axis with length of 40 cm. A schematic view is shown in figure 3.3. For the inner layer, 9 faces are positioned in a circular way around the beam pipe. Each face consists of 2 modules on different sides of

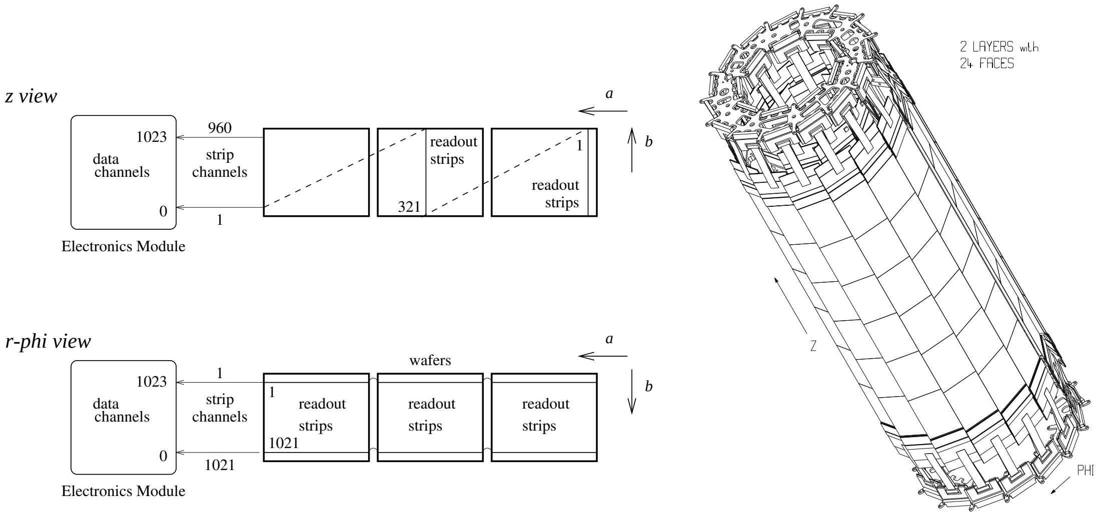

Figure 3.3: Schematic view of the VDETII detector with on the left-hand side a schematic view of both sides of one of the 48 modules.

the interaction point. A total of 15 faces are needed to cover the circumference of the outer layer. All 48 modules are covered with 3 silicon wafers with double sided readout. One side of a module contains 640 read-out strips to determine the z coordinate while the other side contains 1021 strips in the z direction to measure $r\phi$. Since the distance of the faces from the beam pipe is known with high precision, each track that passes both VDET layers is reconstructed from two 3 dimensional points.

The support faces are stable to better than 5 μm. The resolution on the track coordinates is therefore governed by the distance between the strips: 50 μm on the $r\phi$ side and 100 μm on the z side. The resolution is of the order of 10-15 μm in both the $r\phi$ and the z coordinates. The efficiency for reconstructing a hit near the point of impact of a track is 99% for both the z and the $r\phi$ views of the module. However, during the reconstruction of the track a few percent of the hits are lost because the hits on the two different views are occasionally not properly associated to the same track.

The inner tracker chamber (ITC)

The VDET is surrounded by the ITC. Its inner wall is made from polystyrene and carbon fibre with a thickness of 0.3% of a radiation length. The wafers of VDET are

300 μm thick, corresponding to 1.5 % of a radiation length for tracks perpendicular to the beam axis. The Bremsstrahlung off electrons in the region of the VDET and the ITC inner wall is taken into account in the analysis of the $e\nu q\bar{q}$ channel as will be described in chapter 4.

The ITC is a cylindrical drift chamber filled with a 4:1 mixture of argon and CO_2. Between the inner radius at 13 cm from the beam pipe and the outer radius at 29 cm from the beam pipe, 8 layers of sense wires are positioned along the z direction. The gold plated tungsten sense wires are surrounded by gold plated aluminium field wires forming hexagonal cells, as shown in figure 3.4. One field wire per drift cell is used to calibrate the offset of the sense wires. When an ITC calibration is needed, a pulse is sent through these wires and read out on the sense wires. Offsets are compensated for in the readout electronics.

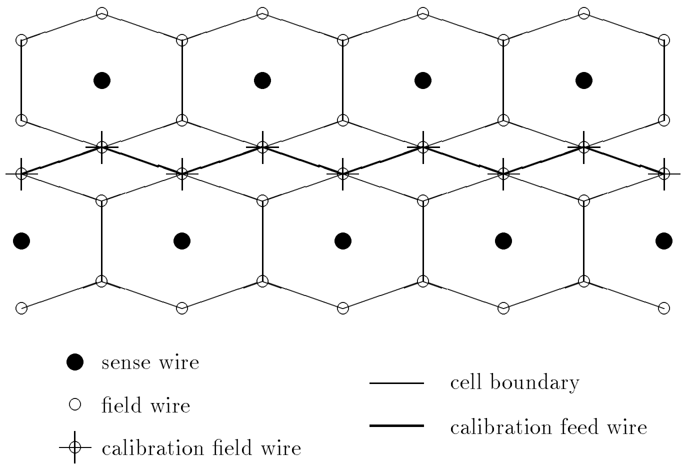

Figure 3.4: Layout of the sense and field wires in the ITC. The drift cells are hexagonal and each sense wire corresponds to four field wires.

The inner four layers have 96 cells each, the outer layers 144. In total 960 sense wires and 3840 field wires are mounted into aluminium alloy end caps on both ends of the ITC with a thickness of 2.5 cm.

A positive voltage of the order of 2 kV is put on the sense wires. When a charged particle passes through the ITC, the gas along the track is ionised and the electrons drift to the nearest wire due to the difference in potential between the anode sense wire and the grounded cathode field wires. The electrons are amplified in the gas as a Townsend avalanche [80] is formed due to the strong electric field very close to the wire. In this avalanche, electrons and positive ions are produced that induce a pulse on the sense wire when they separate in the electric field.

The time it takes for the electron to drift to the region where the field is sufficiently strong for an avalanche to be created is used to derive the $r\phi$ coordinate. The z coordinate is calculated from the time difference between the arrival of the pulse at each of the two end caps. The resolution in the $r\phi$ direction is of the order of 150 μm and in the z direction about 5-10 cm, depending on z. Since the three dimensional information is available in 2 μs, the ITC is used for the first level trigger described in section 3.4.

The alignment of the ITC is important for a proper association of the hits to the tracks in the other sub-detectors. Uncertainties in the alignment are taken into account in the evaluation of the systematic uncertainty on the measurement described in chapter 6. Decays of Z bosons to muon pairs (at $\mathrm{E_{cms}} = \mathrm{M_Z}$) are used to align and calibrate the detector to a precision of the order of 20 μm in $r\phi$.

The time projection chamber (TPC)

Outside the ITC, the time projection chamber is located. Its inner wall has a thickness of 2.3% of a radiation length. The outer wall of the ITC adds about another 1% of a radiation length at perpendicular impact. Bremsstrahlung originating from this boundary is therefore not negligible. The end plates of the TPC have a thickness of about a third of a radiation length and the cables and readout materials create small regions where electrons are slowed down significantly. The algorithms that take these effects into account in the analysis are described in chapter 4.

The TPC is vital for the momentum resolution and the identification of charged particles in ALEPH. The $r\phi$ and z coordinates of a track are reconstructed from the position of hits on wire chambers in the TPC end plates and the drift time of electrons through the TPC volume respectively. Apart from track reconstruction, the TPC also allows a measurement of $d\mathrm{E}/dx$ from wire chambers located in the two end plates.

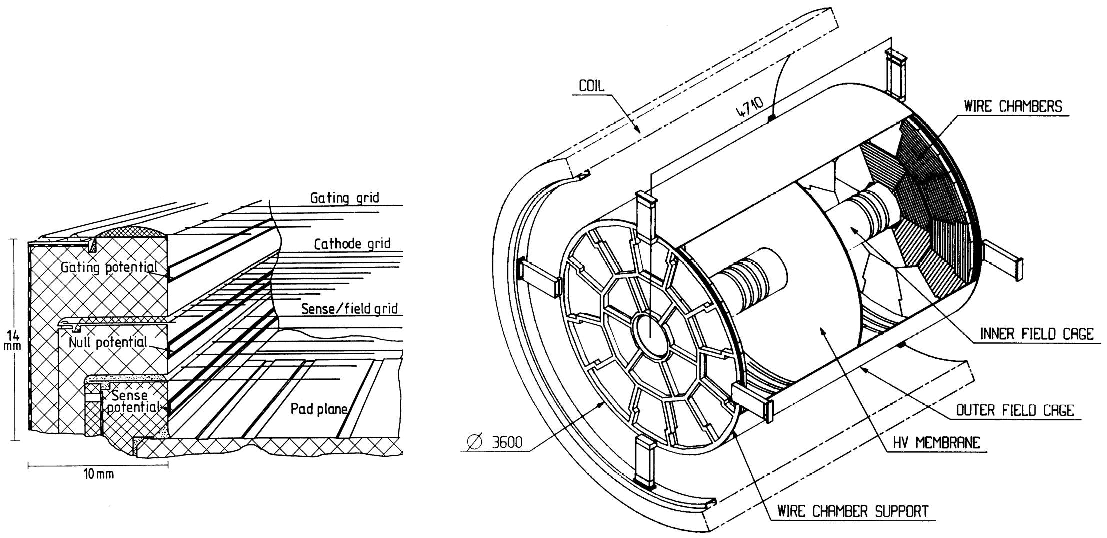

Figure 3.5: Schematic view of the TPC on the right-hand side. On the left-hand side is a schematic view of the wire chamber structure in one of the end caps.

A schematic overview of the TPC is shown in figure 3.5. It consists of a cylindrical volume with a length of 4.7 m located between 31 and 180 cm from the beam pipe. It is filled with argon combined with 9% methane. A graphite coated mylar membrane perpendicular to the beam axis separates the volume into two parts. A potential of -27 kV is applied to the central membrane to create an electric field along the beam axis of about 11 kV/m that causes electrons from ionised gas atoms to drift to the end plates when a charged particle passes through the TPC. The electric field is parallel to the magnetic field produced by the ALEPH solenoid described below. Inner and outer field cages ensure the uniformity of the field.

The end plates of the TPC consist of 18 wire chamber modules each: 6 inner sectors positioned in a circle around the ITC outer wall and 12 outer sectors further away from the beam pipe. Each of the 36 modules is a proportional wire chamber with concentric rows of cathode readout pads. The wires are oriented along the $r\phi$ direction and an electron reaching the end plate encounters the following layers.

Firstly, a grid with a wire spacing of 2 mm is located 1.4 cm from the outer wall. This grid is installed to stop positive ions created in the end caps entering the drift region of the TPC where they could cause distortions in the electric field. These *gating* wires are transparent to electrons originating from physics tracks because the wire potential is fixed to the electric field potential at this point (-67 V) if a first level event trigger occurs. About 2 μs before every bunch crossing the gate is *opened* and if a trigger occurs it remains open for a period of 45 μs. This time period is sufficient for electrons created near the TPC membrane to drift to the end plates and be detected.

If no first level trigger occurs, an alternating voltage of ± 40 V away from the default setting is put on the wires about 4 μs after the bunch crossing, causing a potential difference between each pair of neighbouring wires. As a result, a web of electric field lines is created in which positively charged particles are caught and forced to drift to one of the wires. This setup is referred to as a *closed gate*. Even though the gate is closed for only about two thirds of the time depending on the trigger rate, no positive ions enter the drift region. The 45 μs time period is too short for these slow ions to escape the gating region. Ions that are produced when the gate is open drift to the wires during the 17 μs that the gate is closed before the next bunch crossing occurs.

The second layer of wires is a shielding grid located 0.8 cm from the outer wall. The wires are 1 mm apart and are grounded to create a cathode plane. The third layer of wires located 0.4 cm from the outer wall consists of alternating field and sense wires with a wire spacing of 2 mm. The field wires are kept at a positive potential of the order of 2 kV in order to obtain an amplification of the electrons in the gas before they reach the sense wires and are detected.

The outer wall of the end cap is covered with grounded cathode pads ordered in 21 concentric rows around the beam pipe, 9 per inner sector and 12 per outer sector. The rows are 6.4 cm apart, ranging from 40 to 171 cm from the beam pipe. Each sector has about 100 pads per row resulting in a total of over 41000 pads in the whole TPC. Additionally, each sector has thin rows of 32 pads in total used for the second level trigger only, as described in section 3.4.

Measurement of coordinates and $d\mathrm{E}/dx$ in the TPC

The inner modules of the end caps contain 148 sense wires each, the outer modules 196, resulting in a total of over 6300 channels in the entire TPC. The height of a pulse on one of the wires is a measurement of $d\mathrm{E}/dx$ of the track because they operate in proportional mode: the height is a direct measure of the number of electrons created by the track in the distance that is covered by that wire.

The amount of energy lost through ionisation depends on the velocity and the charge of the incident particle, but not on its mass. It is described by the Bethe-Bloch formula in equation 3.4. At low velocities, the first term in equation 3.4 dominates and the energy loss rapidly decreases with increasing particle velocity. In this region the energy loss as a function of track momentum will be different for particles that differ in mass. This characteristic is used to identify particles according to the value of $d\mathrm{E}/dx$ if their momentum is known. At very high velocities the second term dominates and a plateau is reached known as the region of minimum ionisation.

One track can leave a signal in up to 340 wires, resulting in as many independent measurements of the energy loss. Since measurements of $d\mathrm{E}/dx$ are distributed according to a Landau distribution, this set of measurements is truncated before the mean is evaluated. After omitting the lowest 8% and the highest 40% of the measurements, the mean is used to define the ionisation I of the track. The electron pull R_i is defined as:

$$R_i = \frac{I - < I >}{\sigma}, \tag{3.5}$$

where σ is the resolution on I and $< I >$ is the mean value for electrons. Since electrons are expected to ionise the TPC gas more than most other charged particles in the momentum region above a few GeV, background events are found at negative values for R_i and this variable is used in the rejection of background events from the $e\nu\mathrm{q}\bar{\mathrm{q}}$ selection as described in section 4.1.2.

The concentric rows of readout pads at the outer walls of the end plates are used to determine the $r\phi$ coordinate of the charged particle. They are capacitively coupled to the sense wire. The spatial resolution that can be achieved at perpendicular incidence of the electrons is 180 μm.

The z coordinate is derived from the drift time of the electrons in the TPC. The time between the initial event trigger and the arrival of the electrons at the sense wires is divided by the z component of the drift velocity of electrons in the gas. This velocity is of the order of 5.2 cm/μs and is measured by a complex laser system that is also used for calibration purposes. The result is a spatial resolution of the order of 0.8 - 1.2 mm in z.

The solenoid

To allow a measurement of the momentum of charged particles in ALEPH, the tracks are bent in a magnetic field along the beam direction. This field of 1.5T is generated by a current of ~ 5 kA flowing through a super-conducting coil. The field maps are known to a precision of the order of 0.01%.

The conductor is made of aluminium around a NbTi/Cu core and is cooled by a system of pipes filled with liquid helium. The total setup corresponds to 0.4 absorption lengths or 1.6 radiation lengths. It is therefore located outside the electromagnetic calorimeter but inside the hadron calorimeter. The absorption of the hadron calorimeter is achieved by layers of iron that also serve as yoke for the magnetic flux return.

3.3.2 Calorimetry

When electrons pass through solid matter, they lose energy through Bremsstrahlung much faster than through collision processes. The radiated photons convert to e^+e^- pairs that radiate new photons. In this way an electromagnetic shower is created the size of which scales with the radiation length X_0 of the detector material.

Bremsstrahlung losses are negligible for heavier particles such as hadrons. They lose their energy through ionisation of the atoms in the medium (see equation 3.4). All relativistic particles ($\beta \approx 1$) that are equally charged lose energy through ionisation at an equal rate. The electrons that are created in this process each initiate an electromagnetic shower. Secondary hadrons are created as well that can have a large transverse momentum. Hadronic showers are therefore much longer and wider than showers originating from a single electron or photon, and scale with the interaction length λ of the material. As a result, two separate calorimeters are needed.

Calorimeters can be made from either thick blocks of homogeneous absorbing (high Z) material read out as a whole, or a sandwich of absorbing and detecting layers such as wire chambers. The latter are known as sampling calorimeters and are used in ALEPH. The energy of an incident particle scales with the number of detected electrons and its uncertainty is therefore governed by Poisson statistics ($\sigma_{\mathrm{E}} \propto \sqrt{\mathrm{E}}$).

The electromagnetic calorimeter (ECAL) and the hadron calorimeter (HCAL) are described in this section, as well as the small calorimeters near the beam pipe that are used for the measurement of the luminosity and the radiation levels in ALEPH.

The electromagnetic calorimeter (ECAL)

The ECAL is located outside the TPC but inside the magnetic coil, at a distance of 185 to 225 cm from the beam axis. It is a sampling calorimeter consisting of modules with 45 lead sheets interleaved with wire chambers filled with a 4:1 mixture of xenon and CO_2.

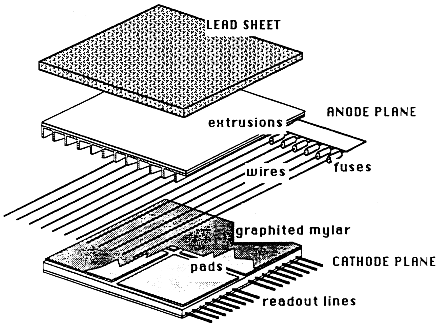

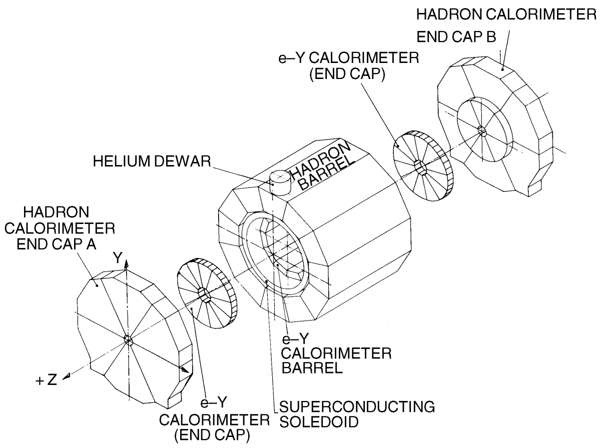

Figure 3.6: Schematic overview of an ECAL layer and the position of ECAL, HCAL and the coil in ALEPH. ECAL is located inside the coil and consists of 45 layers read out in 3 different stacks. The ECAL wires are placed in aluminium extrusions.

A schematic overview of the position of the two calorimeters and the magnetic coil in ALEPH is shown in figure 3.6. The ECAL consists of 12 barrel modules aligned along the z direction, with 12 *petals* on each of the two end caps. Each module is subdivided into towers pointing to the vertex and the towers are read out in three different storeys with a thickness of about 4, 9 and 9 radiation lengths respectively. The total thickness corresponds to about 1.0-1.3 interaction lengths.

Each wire chamber consists of an anode plane, a layer of tungsten wires with a 5 mm separation, and a cathode plane with readout pads as shown in figure 3.6. The pads have a surface area from 3×3 cm and stacks of pads belonging to the same storey are connected to the same readout channel. There are about 4100 towers per module in the barrel, about 1000 towers per module in the end caps and three times as many readout channels.

When a particle creates a shower in ECAL, the generated electrons that enter the wire chambers are amplified as they form an avalanche near one of the wires. The wires are capacitively coupled to the pads and the induced signal on the pads is also read out. The wire signals are used for trigger purposes only, as described in section 3.4.

Strongly interacting particles produce minimum ionising tracks in ECAL and the shape of the shower is therefore used to reduce the background due to misidentified high energy leptons in the $e\nu q\bar{q}$ channel. The relative energy in the each of the three storeys is used as a measure of the longitudinal shower profile. The assumption is made that the longitudinal profile can be parameterised according to the equation:

$$\frac{d\mathrm{E}}{dx} = x^{(\frac{1}{b}-1)} \cdot e^{-ax/b}. \tag{3.6}$$

The shower energy E_s is defined as the sum of the energy deposition in the 3 storeys and 4 stacks centred on the extrapolated track. An estimator for the inverse distance a is defined as [84]:

$$X_{\mathrm{inv}} = \frac{\mathrm{E}_s}{\sum_{i=1}^{4}\sum_{j=1}^{3}\mathrm{E}_i^j S_j}, \tag{3.7}$$

where E_i^j is the energy deposited by the particle in stack i of storey j in depth of ECAL. S_j is the mean depth of the energy deposition in that storey. X_{inv} is measured from the set of $\{\mathrm{E}_i^j\}$ with an iterative procedure, assuming equation 3.6 to be valid, and used to define R_l:

$$R_l = \frac{X_{\mathrm{inv}} - < X_{\mathrm{inv}} >}{\sigma}, \tag{3.8}$$

where σ is the resolution of X_{inv} and $< X_{\mathrm{inv}} >$ is the measured mean value of X_{inv} for electrons.

The fraction of the momentum of the track that is deposited as energy in this region is a measure of the compactness of the shower and the pull R_T is defined as:

$$R_T = \frac{1}{\sigma}\left(\frac{\mathrm{E}_s}{p_l} - \left\langle\frac{\mathrm{E}_s}{p_l}\right\rangle\right), \tag{3.9}$$

where σ is the resolution of E_s/p_l and $< E_s/p_l >$ is the mean value for electrons. For electrons, the distribution of R_T is Gaussian with tails corresponding to badly measured leptons such as leptons near a boundary of ECAL modules (*crack*). Electrons in a crack region deposit less energy in ECAL and are usually found at a pull between -5 and -20.

The resolution of ECAL is measured in test beams and from real data. Bhabha events at the Z resonance produce ~46 GeV electrons and positrons. Results from these beams are combined with measurements of low energy electrons from τ decays and pair production to determine the energy resolution as a function of the particle energy:

$$\frac{\sigma_{\mathrm{E}}}{\mathrm{E}} = \frac{0.18}{\sqrt{\mathrm{E}}} + 0.01, \tag{3.10}$$

where E is the particle energy in GeV. If all angles are defined in mrad, the spatial resolution is:

$$\sigma_\phi = \frac{\sigma_\theta}{\sin\theta} = \frac{2.7}{\sqrt{\mathrm{E}}} + 0.32. \tag{3.11}$$

The hadron calorimeter (HCAL)

The HCAL consists of a 23 layers of iron interleaved with streamer tubes parallel to the beam axis. The tubes are filled with a mixture of argon, CO_2 and isobutane. The HCAL consists of 12 modules rotated by 1.9° with respect to the ECAL modules to ensure that their boundaries do not overlap. A schematic overview of the calorimeter is shown in figure 3.6, the structure of a module is shown in figure 3.7.

The barrel is located between 300 and 468 cm from the beam pipe. At normal incidence, the iron has a thickness of 120 cm corresponding to 7.2 interaction lengths.

The tubes have a square cross section of 1×1 cm each and every 8 tubes in one layer are connected to the same gas supply. The tubes consist of a plastic *comb*, the three internal surfaces of which are coated with graphite. The upper, open side is covered with copper cathode readout pads that are positioned in towers pointing to the interaction vertex. Each of the 4800 towers is divided into three storeys that are read out separately to measure the total energy of a cluster. On the bottom side of the comb, aluminium strips are glued along the length of the tube and supply

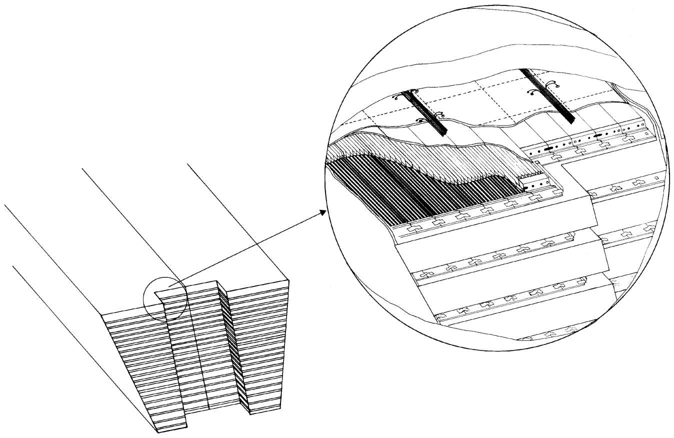

Figure 3.7: Schematic overview of a layer an HCAL module. The streamer tubes are located in gaps in the iron.

information on the profile of the shower. They are 0.4 cm wide and are placed 1 cm apart. Each of the nearly 12×10^4 cells contains a sense wire in the centre that is kept at a high voltage of $\sim$4 kV.

The energy resolution of the calorimeter is tested using pion beams with various energies. Up to a beam energy of 40 GeV, the response of HCAL is found to be linear with the beam energy, and the energy resolution for E in GeV is:

$$\frac{\sigma_{\mathrm{E}}}{\mathrm{E}} = \frac{0.84}{\sqrt{\mathrm{E}}}. \tag{3.12}$$

The luminosity and background monitors (LCAL, SiCAL, BCAL)

If the bunches in LEP contain n particles each, and N collisions between two bunches occur, the number of produced data events $\mathrm{N_d}$ of a process with a cross section σ is given by [41]:

$$\mathrm{N_d} = \frac{n^2 N \sigma}{A} \equiv \mathcal{L}\sigma. \tag{3.13}$$

where A is the area of overlap between two colliding bunches and $\mathcal{L}$ is the integrated luminosity delivered to ALEPH. The value of σ can be calculated from the theory described in chapter 2.

The value of the integrated luminosity is therefore needed to make quantitative predictions about a data sample. It cannot be calculated because the exact properties of the beam in the interaction region are not known. To measure $\mathcal{L}$ directly, calorimeters near the beam pipe are used to count the number of produced Bhabha events.

Bhabha scattering is the process where the e^+e^- pair interacts through the exchange of a photon and scatter with a scattering angle defined by the photon energy. The cross section for these events is well known and the luminosity can be evaluated from this event rate with high precision. In first order, the cross section is a sum of an s and a t channel diagram plus their interference, and can be expressed in the centre-of-mass frame as [43]:

$$\frac{d\sigma}{d\Omega} = \frac{\alpha^2}{4\mathrm{E_{cms}}^2} \left(\frac{3 + \cos^2\theta}{1 - \cos\theta} \right)^2 . \tag{3.14}$$

As a result of the pole at $\theta = 0$ rad, detectors at small angles to the beam pipe are needed.

Three calorimeters are used on either side of the interaction point, namely the solid state calorimeter SiCAL, the luminosity calorimeter LCAL and the very small angle luminosity monitor BCAL. Apart from a measurement of the luminosity, these calorimeters are used as an extension of ECAL near the beam pipe. The positions of these calorimeters are shown in table 3.1.

Detector	z (cm)	Δz (X_0)	r_{in} - r_{out} (cm)	Layers
SiCAL	250	24	6 - 15	12×(W + Si pads)
LCAL	263	25	10 - 52	38×(Pb + wires)
BCAL++	770	22	7 - 9	10×(W + scintillator + Si pads)

Table 3.1: Position and properties of the small angle monitors in ALEPH [85]. z is the distance from the interaction point and Δz is the thickness in radiation lengths. Two modules are located on either side. r_{in} and r_{out} are the inner and outer radii of both modules perpendicular to the beam axis.

High energy e^+e^- pairs originating from Bhabha events deposit most of their energy in LCAL, SiCAL (and BCAL). The luminosity used in the analysis of LEP2 data in ALEPH is evaluated from LCAL information only. BCAL is used to provide an on-line measurement of the luminosity and as a cross check for the SiCAL result.

Bhabha events in LCAL and SiCAL are selected as follows. Hits in the detectors are combined into energy clusters and events with only low energy clusters are removed. A hit on one side of the interaction point is required to coincide with a hit in the opposite direction.

Many physics processes responsible for background to ALEPH analyses peak at low angles to the beam pipe. Therefore, the detectors in table 3.1 supply information on the quality of the data. Other detectors that are specifically designed to measure background levels are the small angle background monitor SAMBA, behind the ITC end caps, and the VDET radiation monitor RADMON, consisting of six silicon pin photo-diodes at z = ± 36 cm from the interaction point. The inner parts of ALEPH can be damaged if the high voltage is switched on when high levels of radiation are present and these photo-diodes are used in a rapid beam dump system ARBLIS vital for a safe running of ALEPH.

3.3.3 Detection of muons

A high energy muon will not be completely absorbed in ALEPH. The muon mass is too large to allow significant Bremsstrahlung in the ECAL but sufficiently small to behave as a minimum ionising particle in HCAL. The signals on the strips along the HCAL tubes, together with hits in two additional double layers of streamer tubes outside the HCAL allow the identification of tracks that are not fully stopped in the ALEPH detector material. The tubes contain the HCAL gas mixture and a schematic overview of the detector and one of the double layers are shown in figure 3.8.

One side of each tube is covered with 4 mm wide strips with a separation of 1 cm that run parallel to the wires. The other side is covered with 1 cm wide strips, separated by 1.2 cm, running perpendicular to the wire direction. Two layers are mounted on top of each other, shifted in both directions by half a strip spacing to improve the spatial resolution. In total, over 1.8×10^4 x strips and 2.5×10^4 y strips are read out from the 94 muon chambers in ALEPH.

A muon is identified if it leaves one or more hits in the muon chambers that can be extrapolated to a charged track, or if the pattern of hits in the HCAL planes is likely to originate from a minimum ionising particle. The latter is true if many subsequent planes are hit and the hits correspond to only a few separate clusters.

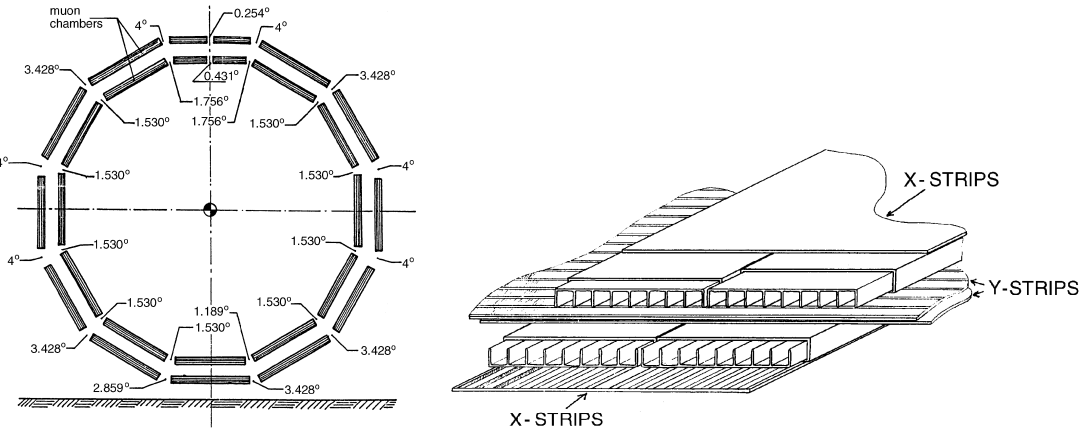

Figure 3.8: Schematic overview of the muon detector in the barrel and one of the double layers. The x strips run parallel to the wires and the y strips are orthogonal to the wires. The two layers are shifted to improve the spatial resolution. Each end cap is divided into four different chambers.

To determine the efficiency of the HCAL planes, $\mu^+\mu^-$ events are selected from information in ECAL and the TPC. The efficiency of each plane is of the order of 73-75%. The efficiency of the muon chambers depends on the point of impact of the track and the average is found to be of the order of 92%.

The spatial resolution of the muon chambers is of the order of 0.35 cm and is directly derived from the separation between the strips. However, before the muons reach the muon chambers they may be displaced due to multiple scattering in the detector material. Hits are only associated to a track if they are within a cone with a radius of 4 times the mean expected displacement. The uncertainty in the position due to multiple scattering is equal to:

$$\sigma(\text{cm}) = \frac{23}{p(\text{GeV}/c)}. \tag{3.15}$$

This uncertainty is added to the spatial resolution of the chambers before searching for the associated track.

The identification of about 90% of the $\mu\nu q\bar{q}$ decays generated in ALEPH is based on the information described in this section. About 1.3% of the $\mu\nu q\bar{q}$ events are rejected as candidates but recovered using ECAL information as described in section 4.1.2. In most of these events, the high energetic muon escapes through a crack region in HCAL or a gap between the muon chambers. The remaining inefficiency is mainly due to the reduced acceptance near the beam pipe.

3.4 Triggers and data taking

The goal of the ALEPH trigger system is to identify (and distinguish between) three different types of events: Bhabha scattering events, $\gamma\gamma$ interactions and other e^+e^- collisions. The frequency of e^+e^- interactions is sufficiently low for all detected collision events to be written to tape. In order to be sensitive to new physics, even events with only one track or energy cluster are written to tape.

$\gamma\gamma$ interactions occur when both beam leptons radiate a photon and these two photons interact to produce final state particles that are detected. The two leptons are scattered with a cross section peaked at small angles. Unlike in Bhabha scattering, charged tracks can be found in the detector even if the leptons escape in the beam pipe. Therefore, 2-photon trigger rates, at LEP centre-of-mass energies away from the Z resonance, are much larger than the rates for other processes. ALEPH is not optimised for 2-photon physics and only a small but well defined fraction of these events is written to tape.

The ALEPH trigger is divided in three levels. The time between two bunch train crossings in ALEPH is 22 μs and the first level trigger is designed to take a decision within 5 μs. If a track is found in the ITC and/or energy is deposited in the calorimeters, the level one trigger is set. The calorimeters are subdivided in trigger segments of solid angle to reduce effects due to noise. Wire information from HCAL, ECAL and LCAL is used, as well as SiCAL information. If the first level trigger is negative, the TPC gate is closed. If not, it is kept open and the TPC is read out. A positive first level trigger occurs with a frequency of 5-10 Hz.

About 50 μs after the beam crossing the second level trigger is set. The ITC information used for the first level trigger is replaced by TPC information, again combined with calorimeter information. The second level trigger is set with a frequency of about 1-2 Hz.

The actual cuts on tracks and energy deposits that are used for the trigger depend on the physics process that is to be selected. A series of trigger bits correspond to the various types of events. The number of events with a certain signature that is written to tape can be scaled down by a factor of up to 2^{16}.

Physics triggers for processes such as neutral energy events, Bhabha events or events with a single muon track do not rely on TPC information and pass the second level trigger automatically if the first level trigger is set.

If a positive second level trigger occurs, the entire detector is read out and an online event reconstruction is done for the third level trigger. This trigger decides if the recorded information is written to tape. The regions of the detector that caused the first and/or second level triggers to be set are analysed until sufficient information is gathered to take a decision. Events are written to tape with a frequency of the order of 1 Hz and the trigger efficiency for most physics processes, including W pair production, is near 100%.

3.5 Event reconstruction

3.5.1 Track reconstruction

The super-conducting coil described in section 3.3.1 bends charged tracks to allow a measurement of their momenta. A helix is fitted to the track coordinates in the TPC and the track is extrapolated into the inner tracking detectors. Hits that are consistent with the helix hypothesis are added to the track and an optimisation procedure known as a Kalman filter [86] is used to find the final track parameters, taking into account the uncertainty in all hits along the track. Examples of fitted tracks are shown in figure 3.9.

The track momentum is derived from its radius of curvature ($p \propto B\rho$). Fast tracks are bent less than slow tracks and it can therefore be shown that:

$$\frac{\sigma_p}{p} = Cp + C', \tag{3.16}$$

where C depends on the detector resolutions and the direction of the track. At low momenta, C' originates from multiple scattering and is of the order of 0.5%. It adds little to the resolution of high energy leptons relevant for this thesis.

In ALEPH, muon pairs originating from Z decays are investigated to evaluate C. The results for different combinations of the three sub-detectors are shown in table 3.2.

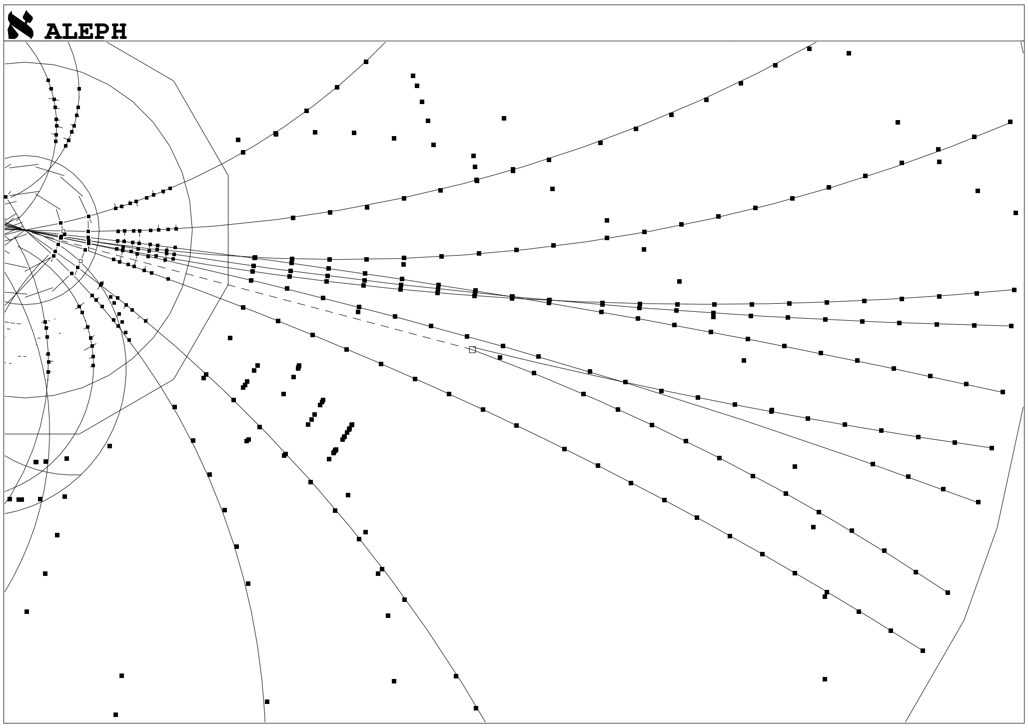

Figure 3.9: Example of track fits in ALEPH. The TPC track is matched to hits in the ITC and VDET. The two layers of VDETII and the 8 wire planes of the ITC are clearly visible. Hits are shown as dots in the figure and the solid lines are the final result of the helix fit.

Detector	C (% per GeV/c)
TPC only	0.12
TPC + ITC	0.08
TPC + ITC + VDET	0.06

Table 3.2: Resolution of the track momentum as defined in equation 3.16. To illustrate, a 45 GeV/c track will have a relative uncertainty in its momentum of 5.4% if only TPC information were used for the reconstruction.

3.5.2 The energy flow algorithm

The analysis described in this thesis is based on identified tracks and calorimeter clusters. A standard ALEPH algorithm is used to combine the tracks and the clusters in order to reconstruct particle candidates referred to as energy flow objects [84].

Firstly, high momentum charged tracks with less than 8 hits in the TPC or no hits in the ITC and low momentum charged tracks with less than 4 hits in the TPC are rejected. Tracks not originating from within a cylinder with a length of 20 cm along the beam direction and a radius of 2 cm around the interaction point are removed as well. A check is done to recover tracks that originate from a secondary vertex.

Noise is removed from the calorimeters if a correlation is found between many consecutive events, or if tower energy is not in agreement with the energy on the calorimeter wires.

The tracks are extrapolated to the calorimeters and calorimeter objects are associated to the tracks. The energy flow objects are created as follows:

- All charged tracks are combined with their associated calorimeter clusters and, in first instance, identified as pions.

- Electron tracks are identified from the shape of the shower in ECAL and $d\mathrm{E}/dx$ in the TPC. The calorimeter objects corresponding to these tracks are removed. If the energy in the calorimeter cluster is more than 3σ larger than the track momentum, the energy is assumed to be a Bremsstrahlung photon and a neutral object with an energy equal to this difference is created.

- Muon tracks are identified from the information described in section 3.3.3 and their energy is removed from the associated calorimeter object. At most 1 GeV of the remaining energy of the associated ECAL cluster is removed together with at most 400 MeV per HCAL plane.

- A photon is created from an ECAL cluster with an energy exceeding 250 MeV if no charged track is found near its centre, and the shape of the shower is in agreement with the photon hypothesis.

- Neutral hadrons are identified from a significant excess in calorimeter energy. If the calorimeter energy that remains after subtraction of the objects above is significantly larger than the energy of any remaining tracks, hadrons are identified if they deposit more than 500 MeV.

The resolution on the total energy in the detector according to the energy flow algorithm is governed by calorimeter information. It is evaluated from hadronic Z decays and found to be:

$$\sigma_{\mathrm{E}} = 0.6\sqrt{\mathrm{E}} + 0.6, \tag{3.17}$$

with the energy E and its resolution defined in GeV.

In a semi-leptonic WW decay, the resolution on the energy of the lepton track originates from the tracking algorithms described in the previous section. The resolution on the energy of the quark pair, in the barrel region, is given by equation 3.17, because the two quarks create two hadronic jets and the jet energy is a sum of the energy of all energy flow objects (see section 4.1.5).

Chapter 4

Event selection and mass reconstruction

From the events that occur in ALEPH and are written to tape, only a small sample originates from W pair decays. The selection of these events and the reconstruction of the mass of the W bosons is described in this chapter, in section 4.1 and 4.2 respectively. Comparisons are made between the ALEPH data and distributions generated using a Monte Carlo technique.

The selection consists of a number of steps each described in a separate section. The pre-selection is introduced in section 4.1.1, the choice of the lepton originating from the leptonically decaying W is explained in section 4.1.2 and radiative corrections to the lepton track are described in 4.1.4. The hadronically decayed W produces two hadronic jets, and the reconstruction of these jets is explained in section 4.1.5. Additional background cuts are described in section 4.1.6, 4.1.7 and 4.1.8.

4.1 Event selection

A typical picture of a semi-leptonic W pair decay in ALEPH is shown in figure 4.1. The isolated, high momentum muon track hits one of the muon chambers on the top of the detector and is clearly visible. The other tracks and calorimeter clusters originate from the hadronically decaying W. The neutrino is not detected in ALEPH but is reconstructed from the centre-of-mass energy and the measured energy in the

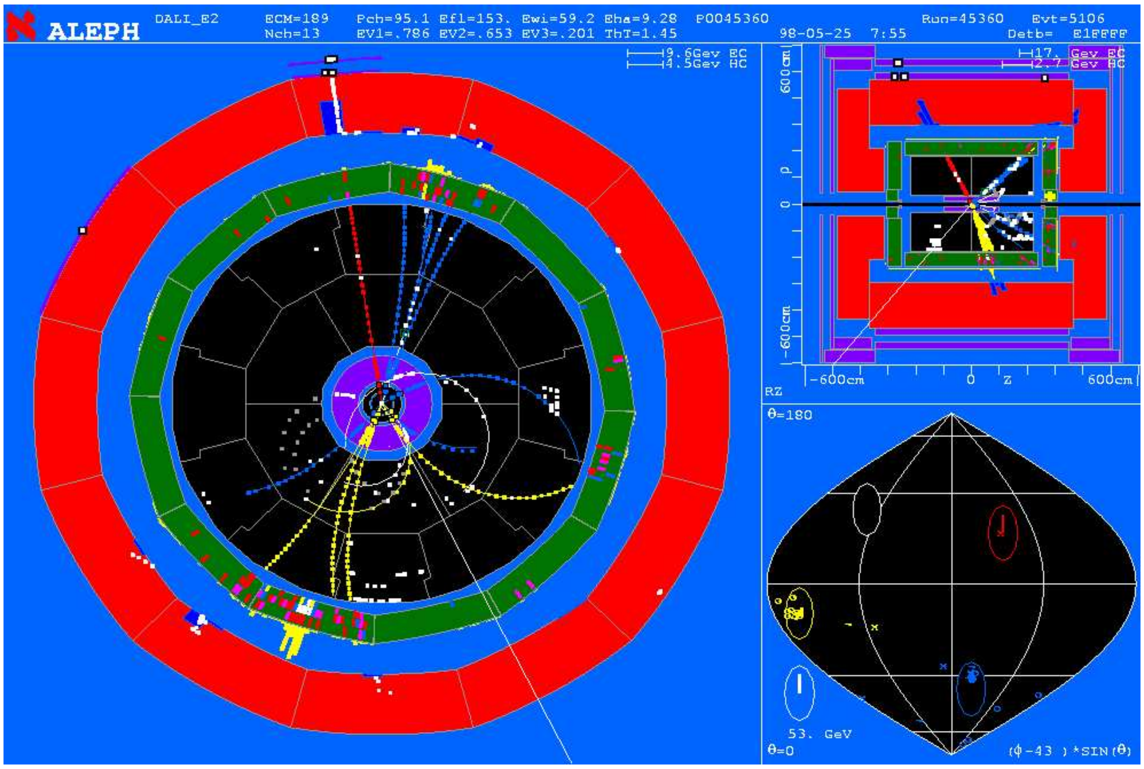

Figure 4.1: The first WW $\rightarrow \mu\nu q\bar{q}$ event observed at E_{cms}= 188.6 GeV. The muon is the high energy track that hits the muon chamber indicated as a thin line outside the calorimeters. The other particles are clustered into two (light gray and dark gray) hadronic jets. The neutrino direction is calculated from momentum conservation in the event.

event. Its direction is indicated in the figure as a line escaping through the lower right quadrant of the detector.

In order to obtain precise measurements of the W characteristics, a pure sample of semi-leptonic W pair decays has to be selected from the collected data without losing too many signal events. The purity ρ and the efficiency ϵ should both be maximal, where ρ is the fraction of signal events in the selected sample and ϵ is defined as the fraction of simulated WW $\rightarrow (e/\mu)\nu q\bar{q}$ events that pass the selection. Both are determined from Monte Carlo simulated samples of signal and background events. The WW $\rightarrow (e/\mu)\nu q\bar{q}$ selection is optimised by maximising the quality Q, where $Q = \sqrt{\epsilon\rho}$.

The selection is an improvement of the selection used by ALEPH in previous years [87]. Changes were needed because of the change in the event topology with increasing centre-of-mass energy. The general selection procedure consists of the following steps. First a pre-selection is applied to reject backgrounds that are easy to identify (e.g. interactions involving the gas in the beam pipe). An isolated high energy lepton is chosen as candidate for the track originating from the leptonically decaying W and detector information is used to identify this lepton as an electron or a muon. The track is corrected for Bremsstrahlung and final state radiation. Specific cuts are applied on the lepton momentum, the number of charged tracks and the transverse momentum in the event to reduce mainly the $\mathrm{q\bar{q}}$ background and radiative Bhabha events in the $e\nu\mathrm{q\bar{q}}$ channel. The objects detected, apart from the selected lepton, are clustered into two hadronic jets originating from the hadronically decaying W. The final step in the selection is to determine the probability for a selected event to be a signal event as a function of three observables: the lepton momentum, the lepton isolation and the transverse momentum of the event. This signal probability is parameterised on Monte Carlo events. Events with a low signal probability are removed. Each of the steps mentioned above is described in sections 4.1.1 to 4.1.8.

To determine the contribution from the different diagrams to the selected data sample, a large set of Monte Carlo events was generated. The size of the samples are shown in table 4.1. All samples were generated at a centre-of-mass energy of $\mathrm{E_{cms}}$= 188.6 GeV, which is the mean LEP centre-of-mass energy in 1998. Samples at higher energies will be described in chapter 5.

W$e\nu$ events in which the electron is visible in the detector are included in the KORALW [76] sample (WW $\rightarrow 4f$). Events in which the electron scattering angle is small are generated as a separate sample by PYTHIA [37], because this generator is more reliable at small angles. The size of this second event sample is shown in table 4.1 ($e^+e^- \rightarrow \mathrm{W}e\nu$).

Processes with a large cross section are $\gamma\gamma$ interactions, radiative Z returns and Bhabha scattering diagrams. These processes can be simulated using a Monte Carlo simulation but in many of these calculations cut-offs have to be used to eliminate infinities such as the radiation probability along the beam direction. Other processes such as beam-gas interactions or cosmic ray events cannot be simulated properly. Comparisons between data and Monte Carlo predictions are therefore vital to ensure that the backgrounds are understood.

Process	$N/10^3$	σ(pb)	$\mathcal{L}/\mathcal{L}_{\mathrm{data}}$
$\mathrm{WW} \to 4f$	1039	16.93	352
$e^+e^- \to \mathrm{W}e\nu$	15	0.66	130
$e^+e^- \to \mathrm{ZZ}$	100	2.76	208
$e^+e^- \to \mathrm{Z}ee$	1957	99.11	113
$e^+e^- \to \mathrm{Z}/\gamma \to \mathrm{q\bar{q}}(\gamma)$	490	99.41	28
$e^+e^- \to \mathrm{Z}/\gamma \to \mu^+\mu^-(\gamma)$	20	8.27	14
$e^+e^- \to \mathrm{Z}/\gamma \to \tau^+\tau^-(\gamma)$	190	8.21	133
$e^+e^- \to e^+e^-(\gamma)$	400	965.7	2.4
$e^+e^- \to \gamma\gamma \to \mathrm{u\bar{u}/d\bar{d}}$	400	487	4.7
$e^+e^- \to \gamma\gamma \to \mathrm{c\bar{c}}$	200	93.2	12
$e^+e^- \to \gamma\gamma \to \mathrm{s\bar{s}}$	40	23.9	10
$e^+e^- \to \gamma\gamma \to \mathrm{b\bar{b}}$	12	0.63	109
$e^+e^- \to \gamma\gamma \to e^+e^-$	500	3800	0.8
$e^+e^- \to \gamma\gamma \to \mu^+\mu^-$	500	3550	0.8
$e^+e^- \to \gamma\gamma \to \tau^+\tau^-$	500	427	6.7

Table 4.1: Size of the generated event samples. The fluctuations in the number of events is negligible only if the luminosity of the sample is much larger than the data luminosity at $\mathrm{E_{cms}} = 188.6$ GeV: $\mathcal{L}_{\mathrm{data}} = 174.2\ \mathrm{pb}^{-1}$.

4.1.1 Pre-selection

The first step in the selection is the pre-selection and is the same as for lower centre-of-mass energies [87]. This is used to cut the most obvious backgrounds while retaining as much of the signal as possible. A semi-leptonic W pair decay is characterised by a highly energetic isolated lepton, two jets and missing energy and momentum due to the undetected neutrino.

Only good charged tracks are used in the analysis. A good charged track has at least four 3-dimensional points in the TPC and originates from within a cylinder with a radius of 2 cm and a length of 20 cm centred around the interaction point. In the pre-selection only charged tracks with $|\cos\theta| < 0.95$ are used to ensure a good coverage by the TPC.

To estimate the four vector of the neutrino the following definitions are used. The missing momentum $\not{p}$ is defined as the momentum opposite to the total momentum of all energy flow objects in the event. The transverse missing momentum $\not{p}_T$ is the component of this vector perpendicular to the beam axis. The missing energy $\not{E}$ is defined as the beam energy minus the energy of all energy flow objects in the event.

Beam-gas interactions and $\gamma\gamma$ events are characterised by few low energy tracks. A cut on the total energy of all charged tracks removes most of these events. Cosmic ray events are removed because the charged tracks are required to originate from the interaction point.

Radiative Z events are similar to signal events if the photon escapes along the beam pipe resulting in missing energy and momentum. These events are cut by requiring that the missing momentum along the beam direction is small. The cut value is derived from Monte Carlo studies. Assume that the photon is produced along the beam axis. The energy of the photon E_γ is equal to the three-momentum of the produced Z (times c) and it can therefore be shown that:

$$\mathrm{E}_\gamma = \frac{\mathrm{E_{cms}}}{2}\left(1 - \frac{\mathrm{M_Z}^2}{\mathrm{E_{cms}}^2}\right). \tag{4.1}$$

The missing momentum in the beam direction is required to be smaller than expected for a radiative return event, or small with respect to the total missing energy:

$$\not{p}_z < \max(\{2\mathrm{E}_\gamma - \sqrt{|\not{E}^2 - \not{p}_T^2|} - 6.0\}, \{\mathrm{E}_\gamma - 27.5\}), \tag{4.2}$$

where the second expression makes use of the non-zero transverse momentum in case of a semi-leptonic W pair decay.

Background from events that are completely contained in the detector is eliminated by requiring the missing energy and momentum to be non-zero.

To summarise, in the preselection most background is eliminated by requiring the following:

- the event has more than five good charged tracks,
- the energy of all good charged tracks is more than 10% of the beam energy,
- $\not{E}$ and $\not{p}$ are greater than zero and $\not{p} > 35 - \not{E}$,
- $\not{p}_z$ is not compatible with a radiative Z topology (equation 4.2).

Studies at $\mathrm{E_{cms}}$= 172.1 and 182.7 GeV show that most processes with a $l\bar{l}(\gamma)$ final state are eliminated from the sample after the pre-selection [87]. Processes with a hadronic final state are more difficult to exclude and more cuts are needed to increase the purity ρ: the fraction of the selected events that originates from a signal process (ρ= 6% at 172.1 and 9% at 182.7 GeV).

At E_{cms}= 188.6 GeV, the efficiency for $(e/\mu)\nu q\bar{q}$ events is 97.9% after the pre-selection. Cuts on the charged tracks cut 0.5% of the $e\nu q\bar{q}$ signal and 0.2% of the $\mu\nu q\bar{q}$ signal. The total missing energy and momentum cuts reduce the signal efficiency by another 1.3% and 1.4% respectively. The cut on the missing momentum along the beam pipe is responsible for 0.5% reduction in the $e\nu q\bar{q}$ channel and 0.3% in the $\mu\nu q\bar{q}$ channel.

4.1.2 Lepton selection and identification

The new lepton selection is based on its momentum and the isolation of the lepton with respect to other particles in the event. For each charged track in the event, the discriminating value V_d is calculated, where [88]

$$V_d = P_l \cdot \sin(\alpha/2). \tag{4.3}$$

P_l is the momentum of the track in the TPC, and α is the isolation angle of the track. All remaining good charged tracks with $|\cos\theta| < 0.975$ are clustered into jets, and the angle between the lepton and the nearest jet is defined as the isolation angle α if two or more jets are found. If less than two jets are found, the lepton track is not selected.

For the clustering, a DURHAM [89] jet finding algorithm is used. Define two tracks a and b. The *jet resolution*, y_{ab}, is defined as:

$$y_{ab} = 2\left(\frac{\min\{E_a, E_b\}}{E_{cms}}\right)^2 (1 - \cos\theta_{ab}), \tag{4.4}$$

where $E_{a,b}$ are the energies of the tracks and θ_{ab} is the angle between the two tracks. The algorithm evaluates y_{ab} for each pair of tracks in the event, ignoring the lepton candidate, and combines the pair with the lowest y value to create a new track. This procedure is repeated until the minimum y value in the event is larger than a cut value, in this case 3.0×10^{-4}. The remaining objects are called jets. If a small y cut is used, more jets will be found than in case of a large y cut.

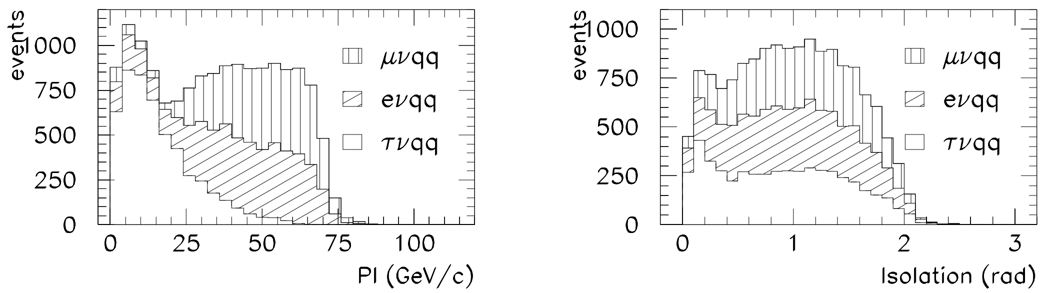

Figure 4.2: Momentum P_l and isolation of the selected lepton candidate for generated $l\nu q\bar{q}$ events. The different contributions of the three channels are superimposed. The bin size is 4 GeV/c for the lepton momentum and 0.1 rad for the isolation.

The charged track with the largest discriminating value V_d is chosen as the lepton candidate. Only good charged tracks with $|\cos\theta| < 0.95$ and a momentum above 200 MeV/c are considered as lepton candidates.

The momentum and the isolation of the lepton candidate for $l\nu q\bar{q}$ events are shown in figure 4.2. The momenta of the leptons selected from $\tau\nu q\bar{q}$ events is small because, after the τ lepton decayed, only one track in the jet is chosen as the lepton candidate and any neutrino energy is lost. For $\tau\nu q\bar{q}$ events a peak is seen at low values of the lepton isolation due to other charged tracks in the τ jet. In the case of $\mu\nu q\bar{q}$ events, less low energy leptons are selected than in case of $e\nu q\bar{q}$ decays. This is due to radiation effects such as Bremsstrahlung and final state radiation that are more important for electrons than for muons.

Identification of the muon

After a lepton candidate is selected, it is identified as either a muon or an electron. Information from the calorimeters and the muon chambers is used. The contribution of each of the sub-detectors is described below.

The first step is to identify the good muons. If the track can be extrapolated to one or more hits in the muon chambers, or a good digital pattern in HCAL, it is identified as a muon. Of the true $\mu\nu q\bar{q}$ events 89.7% are identified in this way and only 0.2% of the true $e\nu q\bar{q}$ events are misidentified as $\mu\nu q\bar{q}$ events.

Some muons do not satisfy this criterion because they escape through cracks in HCAL and the muon chambers. If the track points to a dead zone in HCAL a muon is recovered if:

- its ECAL energy is less than 1 GeV and less than 10% of the track energy,
- its HCAL energy is less than 5 GeV and less than 10% of the track energy.

A further 1.3% of the true $\mu\nu q\bar{q}$ decays are recovered this way, resulting in an efficiency in the $\mu\nu q\bar{q}$ channel of 91.1%. Less than 0.03% of the $e\nu q\bar{q}$ events are misidentified in this way. Events that pass the muon identification are flagged as $\mu\nu q\bar{q}$ events and the remaining sample is used for the identification of $e\nu q\bar{q}$ events.

Identification of the electron

ECAL information is used to identify the electrons. Unlike muon and hadron showers, the electro-magnetic shower of an electron originating from the leptonic W decay is fully contained in ECAL. To determine if the ECAL shower associated to the track is electro-magnetic or hadronic, three quantities are used to describe its topology: the pull of the compactness, R_T, of the shower, of its longitudinal profile, R_l, and of the ionisation, R_i, defined in section 3.3.1 and 3.3.2.

The track is extrapolated into ECAL, where R_T and R_l are determined. A good electron is defined as a track that does not point in the direction of a crack region and for which R_i and R_l are both larger than -2.5 and R_T is larger than -8. An upper cut at 100 is used in case of R_T and R_l to cut events with a wrong momentum measurement in the TPC [88]. In this way 83.5% of the $e\nu q\bar{q}$ events are identified and only 0.2% of the $\mu\nu q\bar{q}$ events are wrongly identified as $e\nu q\bar{q}$ events.

Since the cuts on the shower profile also remove $e\nu q\bar{q}$ events in which the electron escapes through an ECAL crack these events are recovered using HCAL information. If the ionisation in the TPC is in agreement with the electron hypothesis ($R_i > -2.5$) and the track points towards a crack region in ECAL, the digital pattern of HCAL is read out. If less than 10 HCAL planes are hit the lepton is assumed to be an electron. This procedure recovers a further 3.0% of the $e\nu q\bar{q}$ events while misidentifying 0.07% of the $\mu\nu q\bar{q}$ events as electrons. In total 86.5% of the $e\nu q\bar{q}$ events pass the electron identification criteria.

4.1.3 Selection comparison with previous years

The topology of a semi-leptonic W pair decay changes with centre-of-mass energy. At threshold, the two W bosons are produced at rest in the laboratory frame, and the decay products from each W are produced back-to-back. At higher energies, the W bosons are boosted. In particular, at E_{cms}= 188.6 GeV, the W velocity is approximately given by:

$$\beta = \sqrt{1 - (M_W/E_W)^2} \approx 0.5. \tag{4.5}$$

At lower centre-of-mass energies, the lepton with the largest momentum component anti-parallel to the missing momentum was chosen as candidate for the lepton originating from the $W \to l\nu$ decay. Since the W bosons are boosted at higher LEP energies a new algorithm is implemented based on the lepton momentum and the isolation of the lepton with respect to other particles in the event as described above. The recovery of leptons in cracks is improved by looking in ECAL for possible muon tracks and in HCAL for $e\nu q\bar{q}$ candidate events.

Before the implementation of these changes, the CC03 selection efficiency was found to decrease with energy. Studies at E_{cms}= 172.1 GeV and 182.7 GeV show a decrease in the efficiency for $e\nu q\bar{q}$ events from 87.8% to 85.3% and for $\mu\nu q\bar{q}$ events from 91.4% to 86.5% [87].

At E_{cms}= 188.6 GeV the lepton selection and identification efficiency for the old algorithms is evaluated on 36k generated $4f$ events and is found to be 80.9±0.5% for $e\nu q\bar{q}$ events and 86.1±0.5% for $\mu\nu q\bar{q}$ events. With the implementation of these new algorithms the trend is reversed and the efficiency increases to 86.5±0.1% in the $e\nu q\bar{q}$ channel and 91.1±0.1% in the $\mu\nu q\bar{q}$ channel as mentioned in the previous section.

4.1.4 Radiative corrections

The final state of the leptonically decaying W can contain additional final state particles. Radiated photons affect the momentum of the final state lepton and are taken into account if they are detected.

Most Bremsstrahlung occurs at the boundaries of the VDET and the ITC or the ITC and the TPC and Bremsstrahlung photons are usually found near the lepton track. Since high energy electrons have a small mass they are likely to radiate a Bremsstrahlung photon in ALEPH, while these effects are negligible in case of muons. According to Monte Carlo simulations at E_{cms}= 188.6 GeV, the electron loses more than 500 MeV of its energy due to Bremsstrahlung in 43% of $e\nu q\bar{q}$ decays.

Final state radiation occurs at the interaction point in both the $e\nu q\bar{q}$ and $\mu\nu q\bar{q}$ channels. In total 16% of electrons and 9% of muons lose more than 500 MeV due to final state radiation. The energy spectra for losses due to FSR and Bremsstrahlung of more than 500 MeV are shown in figure 4.3.

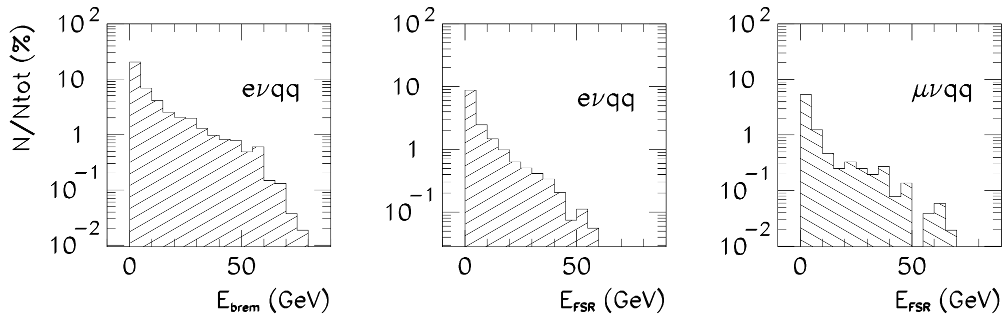

Figure 4.3: Energy loss due to Bremsstrahlung and final state radiation in generated $e\nu q\bar{q}$ and $\mu\nu q\bar{q}$ events. The fraction of the total generated sample per 5 GeV is shown as a function of energy.

Photons originating from final state radiation appear at large angles to the lepton track. Energy from both Bremsstrahlung and final state radiation is added to the jets if the lepton is not corrected. This results in a worsening of the resolution of the lepton four vector and a bias in the jet angles which can cause problems in the kinematic fit described in section 4.2. The method to look for these photons and add them to the leptons before creating the jets is described in this section.

Bremsstrahlung off the electron

In the $e\nu q\bar{q}$ channel an algorithm is implemented to look and correct for Bremsstrahlung photons. If the correction to the lepton energy is less than 300 MeV, or if more than 5 GeV of good charged energy is found in a 6° cone around the lepton, the original lepton measurement is kept. The correction to the electron track is described in detail in [87] and consists of the following steps.

Energy deposits in ECAL within a cone of 2.5° around the point of impact of the lepton track with ECAL are added if in total they exceed 500 MeV. The same is done within the "ellipse" that combines two such cones for hypothetical photons originating from the VDET/ITC and ITC/TPC walls respectively at the point where the track passes these boundaries.

For high energy tracks the cone (associated with the lepton) and the ellipse (associated with the photons) will overlap but in case of a low energy electron the regions can be very different: the photons will always travel along a straight line from their origin to ECAL, while low energy tracks are bent by the magnetic field. Three energy deposits E_e, E_c and E_{ec} are defined as the energy in the ellipse only, the energy in the cone only and the energy in the overlap region. Two possible scenarios are then distinguished.

- $E_e > E_{ec}$: the ECAL showers of the electron and the photon are separable. The photon energy E_γ is equal to:

$$E_\gamma = \left(\frac{E_e}{E_e + E_c}\right) E_{ec} + E_e. \tag{4.6}$$

  In this case the electron and photon are reconstructed and their four-vectors are added to create the corrected lepton.

- $E_e \leq E_{ec}$: the ECAL showers are not separable. In order to use the calorimeter and the tracking information in the most optimal way two weights $w_{\text{cal}}(x)$ and $w_{\text{tr}}(x)$ are calculated where:

$$x = \frac{E_{\text{cal}} - E_{\text{tr}}}{\sqrt{\sigma_{\text{cal}}^2 + \sigma_{\text{tr}}^2}}, \tag{4.7}$$

  in which σ_{cal} is the energy resolution of the calorimeter and σ_{tr} is the energy resolution of the TPC, ITC and VDET combined. The energy of the corrected lepton is then set equal to a weighted sum of these two different energy measurements and the momentum is changed accordingly, forcing the mass of the track to be equal to the electron mass.

  As a result, the energy is measured by ECAL if E_{cal} is more than three standard deviations larger than E_{tr}, by ECAL and the tracking detectors if E_{cal} is less than three standard deviations larger than E_{tr} and by the tracking only if $E_{\text{cal}} < E_{\text{tr}}$.

Final state radiation

If a final state photon is produced in the same direction as the lepton track, it will be identified as Bremsstrahlung in case of the $e\nu q\bar{q}$ selection and added to the electron automatically. To ensure that high energy photons near the lepton are not missed in the $\mu\nu q\bar{q}$ channel the method described in the previous section is applied to the muons as well but energy is only added if the correction exceeds 2 GeV.

The GAMPECK [90] program is used to look for FSR candidates. Photons that are not identified by the Bremsstrahlung routine, have an energy of more than 500 MeV and do not originate from π^0 decay are selected as candidates. Photons are rejected if they are likely to be:

- Part of a hadronic jet: The photon must be closer to the lepton than to any other charged track and the angle between the photon and the closest other tracks has to exceed $40°$.
- Initial state radiation: The photon has to be closer to the lepton than to the beam pipe.

The four vector of photons that pass this selection are added to the track four vector.

4.1.5 Finding the jets

When the lepton is identified and the associated neutral energy is added to the track, the remaining objects are assumed to originate from the hadronically decayed W. The two quarks that are initially produced both create a jet of particles because of the confinement of the strong interaction.

The jets are reconstructed using the DURHAM [89] jet finding algorithm. Define two objects a and b. The jet resolution y_{ab} defined in equation 4.4 is evaluated for each pair of objects in the event and the pair with the lowest y value is combined to create a new object c. This procedure is repeated until only two objects are left, that are defined to be the two hadronic jets.

The combination of all the original objects can be done in various ways. Monte Carlo studies are done to optimise the algorithm for both the association of objects to the jets and the evaluation of the four-vectors of the two final jets [91].

The DURHAM-P scheme is used to associate the objects to the jets, which forces the new object c to have zero invariant mass:

$$\begin{aligned} \vec{p}_c &= \vec{p}_a + \vec{p}_b \\ \mathrm{E}_c &= |\vec{p}_a + \vec{p}_b|. \end{aligned} \tag{4.8}$$

When all objects are associated to one of the two jets, the DURHAM-E scheme is used to approximate the four-vectors p^μ of the original quarks $q = 1, 2$:

$$p_q^\mu = \sum_{n=1}^{N} p_n^\mu, \tag{4.9}$$

where n runs over all N particles associated to jet q.

4.1.6 Lepton momentum cut

The energy of leptons originating from the leptonically decaying W is typically between 20 and 75 GeV/c. Distributions of the lepton momenta for different centre-of-mass energies are shown in chapter 7, figure 7.1. The lepton selected as candidate in background events will often have a momentum of less than 20 GeV/c, especially if it originates from a hadronic jet.

The most dominant background is due to $\mathrm{q\bar{q}}$ final states. Of all events in which two jets are found as well as an identified lepton, 56% of the $e\nu\mathrm{q\bar{q}}$ background and 68% of the $\mu\nu\mathrm{q\bar{q}}$ background is due to $\mathrm{q\bar{q}}(\gamma)$ events. A cut on the lepton momentum is used to reduce this background significantly.

The cut value is chosen in order to lose not more than 1% of the semi-leptomic decays of CC03 processes in which the lepton is correctly identified. A sample of 5×10^4 CC03 events is used to optimise the cut. The result is shown in figure 4.4. At a cut value of $\mathrm{P_l} > 22$ GeV/c, 98.8 % of $e\nu\mathrm{q\bar{q}}$ decays and 99.0% of $\mu\nu\mathrm{q\bar{q}}$ decays in which the lepton is properly identified pass the cut, while 74% of the $\mathrm{q\bar{q}}$ background is removed in the $e\nu\mathrm{q\bar{q}}$ channel and 78% is removed in the $\mu\nu\mathrm{q\bar{q}}$ channel.

Events in which the lepton has an energy larger than the centre-of-mass energy, due to problems in the reconstruction of the track, are removed as well in order to improve the convergence of the kinematic fit described in section 4.2. At $\mathrm{E_{cms}} = 188.6$ GeV, 3 such events are expected in the background to the $e\nu\mathrm{q\bar{q}}$ channel and 0.2 in the $\mu\nu\mathrm{q\bar{q}}$ channel. The effects of the cuts on the lepton momentum for the various background processes and the $4f$ sample are shown in table 4.2.

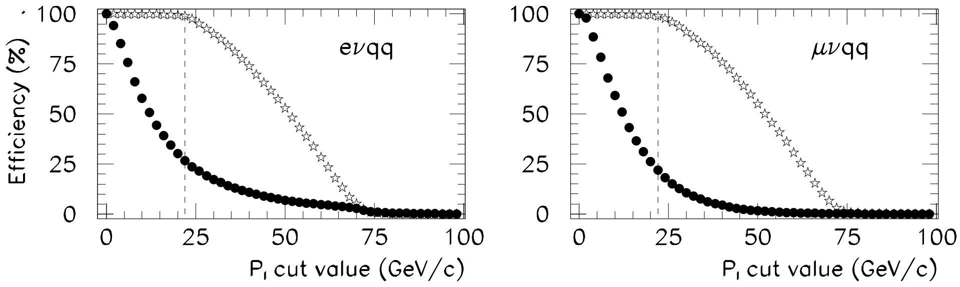

Figure 4.4: Optimisation of the cut on the lepton momentum. The stars represent correctly identified WW signal, the solid circles represent $\mathrm{q\bar{q}}$ background. All events with a lepton momentum below $\mathrm{P_l}$ = 22 GeV/c are rejected.

	$e\nu\mathrm{q\bar{q}}$		$\mu\nu\mathrm{q\bar{q}}$	
Process	$\mathrm{N_{exp}}$	$\Delta\mathrm{N_{exp}}$	$\mathrm{N_{exp}}$	$\Delta\mathrm{N_{exp}}$
$\mathrm{WW} \rightarrow (e/\mu)\nu\mathrm{q\bar{q}}$	376.9	(7.5)	378.5	(3.8)
WW background	33.2	(50.5)	32.0	(45.7)
$\mathrm{q\bar{q}}(\gamma)$	95.0	(266.9)	58.6	(208.4)
Zee	46.2	(51.7)	0.8	(4.2)
ZZ	7.3	(11.1)	7.6	(10.9)
W$e\nu$	3.3	(3.2)	0.2	(1.5)
$\tau\tau$	5.6	(4.3)	3.4	(2.6)
$\gamma\gamma \rightarrow \mathrm{q\bar{q}}$	28.4	(17.6)	0.8	(11.8)
$\gamma\gamma \rightarrow \tau\tau$	5.5	(3.0)	0.3	(2.8)
Total $\mathrm{N_{exp}}$	601.4	(415.9)	482.2	(291.6)

Table 4.2: Effect of the lepton momentum cut on the expected number of selected events at $\mathrm{E_{cms}}$= 188.6 GeV. $\mathrm{N_{exp}}$ is the number of expected events after the cut, $\Delta\mathrm{N_{exp}}$ is the number of events removed by the cut. The first column only incorporates events in which the lepton type is properly identified.

4.1.7 Bhabha cut

In the data sample at $\mathrm{E_{cms}}$= 188.6 GeV, 672 events pass the lepton momentum cut in the $e\nu\mathrm{q\bar{q}}$ channel and 503 events pass the cut in the $\mu\nu\mathrm{q\bar{q}}$ channel. The number of expected events at this stage is shown in table 4.2 to be 601 and 482 events respectively. This excess of events is not significant in the $\mu\nu\mathrm{q\bar{q}}$ channel but corresponds to 2.7 standard deviations in the $e\nu\mathrm{q\bar{q}}$ channel.

A discrepancy between data and Monte Carlo in this channel is found in the number of charged tracks and the missing momentum in the event perpendicular to the beam direction. The distributions of these two variables are shown in figure 4.5.

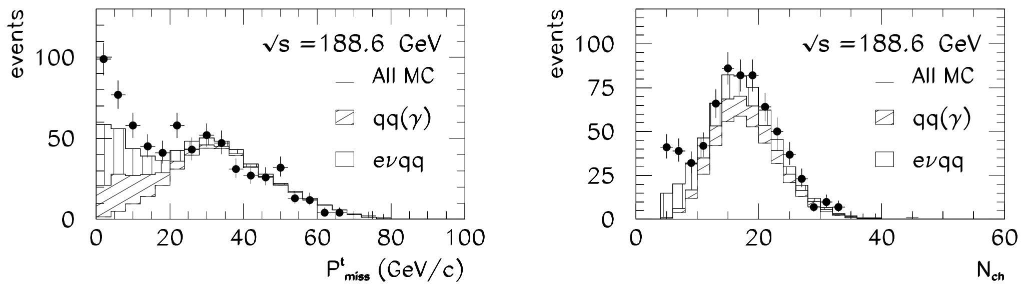

Figure 4.5: Discrepancy between data and Monte Carlo in the transverse missing momentum $\mathrm{P}^{\mathrm{t}}_{\mathrm{miss}}$ and the number of charged tracks N_{ch} before the Bhabha cut. Bhabha Monte Carlo is not included in this figure. The number of events in each distribution are shown per 4 GeV/c and per 2 tracks respectively.

The region in the number of charged tracks and the missing momentum, in which the excess of data events occurs, is scanned. A significant number of events are observed that are likely to be radiative Bhabha events, where the two beam leptons scatter off one another, after which the final state leptons radiate one or more photons. These photons can pair produce and create a number of charged tracks in the detector. The probability for the electrons to radiate more than one photon is relatively small, but due to the high Bhabha cross section this process can add significantly to the background to W pair decays.

Events with less than 5 charged tracks are removed in the pre-selection. A sample of 4×10^5 Bhabha events was generated as shown in table 4.1. A number of events corresponding to 11.8 expected events in the data sample are selected by the $e\nu\mathrm{q\bar{q}}$ selection. No events with more than 9 charged tracks are observed in the selected sample and no events pass the $\mu\nu\mathrm{q\bar{q}}$ selection.

Of the CC03 $e\nu\mathrm{q\bar{q}}$ events in which the correct lepton track is identified, 2.6% have less than 9 charged tracks in the detector. In order to lose as little efficiency as possible, while rejecting all the Bhabha events, a two dimensional cut is defined. The transverse missing momentum of Bhabha and signal events with less than 9 charged tracks is shown in figure 4.6. Events with less than 9 charged tracks are removed only if their transverse missing momentum is less than 20 GeV/c. As a result of this cut, all Bhabha events are removed from the selected sample. From the CC03 $e\nu\mathrm{q\bar{q}}$ events in which the correct lepton track is identified, 99.7% pass this cut.

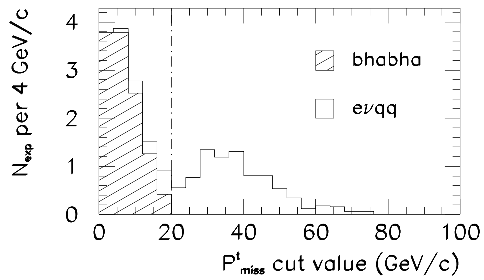

Figure 4.6: Missing transverse momentum for events with less than 9 charged tracks. Bhabha events are shown, as well as CC03 signal events in which the right electron track is selected.

The result of this cut for the number of expected signal and background events in the $e\nu q\bar{q}$ selection at E_{cms}= 188.6 GeV is shown in table 4.3.

Process	N_{exp}	ΔN_{exp}
$WW \rightarrow e\nu q\bar{q}$	375.9	(1.0)
WW background	32.5	(0.7)
$q\bar{q}(\gamma)$	90.8	(4.2)
Zee	37.7	(8.5)
ZZ	6.3	(1.0)
$We\nu$	3.3	(0.0)
$\tau\tau$	2.4	(3.2)
$\gamma\gamma \rightarrow q\bar{q}$	17.1	(11.3)
$\gamma\gamma \rightarrow \tau\tau$	1.3	(4.2)
Total N_{exp}	567.4	(34.0)

Table 4.3: Effect of the Bhabha cut on the expected number of selected $e\nu q\bar{q}$ events at E_{cms} = 188.6 GeV. N_{exp} is the number of expected events after the cut, ΔN_{exp} is the number of events removed by the cut. The first column only incorporates events in which the identified lepton is indeed an electron.

The number of expected Bhabha events removed by this cut is 11.8. This results in a total of 45.9 events expected to be removed by this cut. A total of 80 events are removed from the data sample at E_{cms}= 188.6 GeV, but cuts in the generation of Bhabha and $\gamma\gamma$ event samples can cause the backgrounds in the region of low transverse missing momentum to be underestimated (e.g.[92]). It is therefore important to remove any such background from the sample before the W mass is fitted.

A total of 592 events pass this cut in the data. This is in agreement with the number of expected events in table 4.3 within less than one standard deviation. Almost all remaining backgrounds are removed, as described in the next section.

4.1.8 Parameterisation of the signal probabilities

The final step in the selection is a cut on the *signal probability* of the event. This probability is parameterised in a three dimensional space, spanned by:

- the momentum $\mathrm{P_l}$ of the charged lepton from the $\mathrm{W} \to l\nu$ decay,
- the missing momentum perpendicular to the beam direction $\mathrm{P^t_{miss}}$,
- the isolation I of the lepton with respect to the jets and the charged tracks in the event, defined as:

$$I = \ln\left[\tan\left(\frac{\phi_{\mathrm{ch}}}{2}\right)\right] + \ln\left[\tan\left(\frac{\phi_{\mathrm{jet}}}{2}\right)\right], \tag{4.10}$$

  where ϕ_{ch} is the angle between the lepton and the nearest good charged track and ϕ_{jet} is the angle between the lepton and the nearest hadronic jet. As one of the angles in equation 4.10 tends to zero, the lepton isolation tends to $-\infty$. Leptons that are part of a jet will therefore have a negative value for I.

The distributions of these three variables for the $e\nu\mathrm{q\bar{q}}$ and $\mu\nu\mathrm{q\bar{q}}$ selections are shown in figure 4.7.

A multiquadric radial basis function [93] is fitted to both the signal and the background distributions as a function of the discriminating variables defined above. Define $\vec{v} \equiv (\mathrm{P_l}, \mathrm{P^t_{miss}}, I)$. The fitted probability density functions define the probability for an event to be found at coordinates $\vec{v}$, given that it originated from a signal final state s or background final state b: $p(\vec{v}|s)$ and $p(\vec{v}|b)$ respectively.

Take an event sample of which a fraction f_s originated from signal processes and a fraction f_b $(= 1 - f_s)$ is background. Bayes' theorem is used to define the probability $\mathcal{P}$ for an event to originate from a signal rather than a background process, given its coordinates $\vec{v}$:

$$\mathcal{P}(s|\vec{v}) = \frac{f_s p(\vec{v}|s)}{f_s p(\vec{v}|s) + f_b p(\vec{v}|b)}. \tag{4.11}$$

Two samples of 750 selected CC03 events are used as signal in both the $e\nu\mathrm{q\bar{q}}$ and $\mu\nu\mathrm{q\bar{q}}$ channels to parameterise the probabilities $p(\vec{v}|s)$ and $p(\vec{v}|b)$, with the appropriate number of background events. In the $e\nu\mathrm{q\bar{q}}$ channel, $(\gamma\gamma \to \mathrm{u\bar{u}/d\bar{d}/c\bar{c}}/\tau\tau)$ events are included in the parameterisation. The distributions of $\mathcal{P}$ for both the

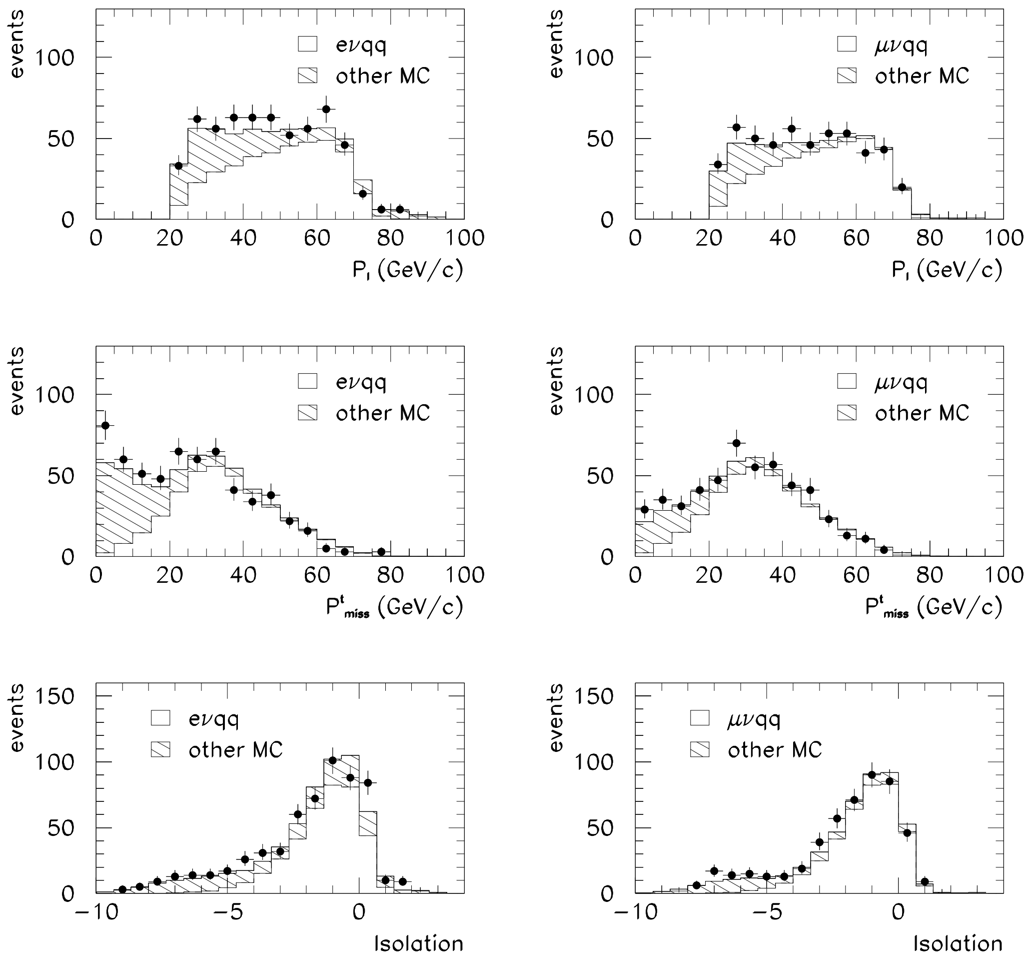

Figure 4.7: Distributions of P_l, P^t_{miss} and I for the $e\nu q\bar{q}$ (left-hand side) and the $\mu\nu q\bar{q}$ (right-hand side) selections respectively. The dots represent the data at E_{cms}=188.6 GeV. The background is shown as the hatched area on top of the signal. All semi-leptonic WW decays that are selected in the proper (e/μ) decay channel are counted as signal. The bin size is 4 GeV/c per bin for the momenta, and 3 bins per 2 units of isolation.

$e\nu q\bar{q}$ and $\mu\nu q\bar{q}$ channels are shown in figure 4.8 for both data and Monte Carlo events. In this figure, all $4f$ final states are included.

The cut on the probability is optimised with respect to the selection quality $Q = \sqrt{\epsilon\rho}$, where the efficiency ϵ and the purity ρ are defined using CC03 events and non-WW background. The efficiency, purity and quality for both channels as a function of the cut value are shown in figure 4.9. The quality of the selection is constant over a large range of cut values. The cut is chosen at $\mathcal{P} > 0.4$ for both channels.

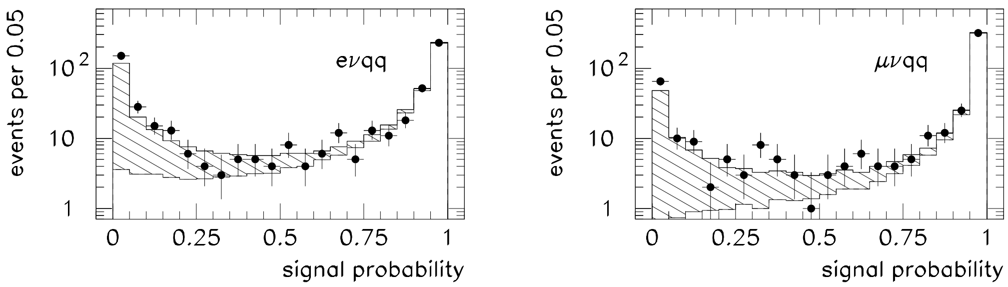

Figure 4.8: Probability distributions for both channels. The background is shown as the hatched area on top of the signal. All semi-leptonic WW decays that are selected in the proper (e/μ) decay channel are counted as signal.

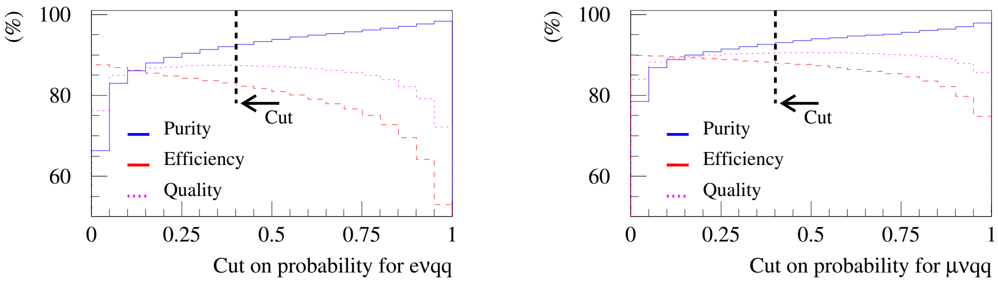

Figure 4.9: Selection efficiency, purity and quality as a function of the probability cut value for both the $e\nu q\bar{q}$ and $\mu\nu q\bar{q}$ samples. Only CC03 decays of the WW pairs are used for the optimisation.

4.1.9 Final statistics and conclusions

The efficiency and purity of the selection are determined on CC03 and non-WW background samples only in order to be independent of the cuts in the generation of events from non-CC03 diagrams. A signal event is defined as a semi-leptonic W pair decay that is selected in the correct (e/μ) decay channel. The results for E_{cms} = 188.6 GeV are shown in table 4.4.

The selection quality that results from table 4.4 is equal to the quality at E_{cms}= 172.1 GeV within the statistical uncertainty and better than the quality at E_{cms}= 182.7 GeV by 1.1%, averaged over both channels [87]. This improvement is due to the new algorithms for the lepton identification, the new cuts and the re-parameterisation of the probabilities.

In this thesis, the analyses of data at five different centre-of-mass energies are described. For the energies above E_{cms}= 188.6 GeV, preliminary results are evaluated,

	$e\nu q\bar{q}$		$\mu\nu q\bar{q}$	
ϵ (%)	82.0	(87.2)	88.1	(89.9)
ρ (%)	92.4	(66.1)	93.3	(78.5)

Table 4.4: CC03 selection efficiencies and purities for both channels, for the final selection at E_{cms}= 188.6 GeV. In brackets the efficiency and purity before the probability cut are shown. The final purity of the sample used to fit the mass and width of the W increases due to a cut on the reconstructed mass value described in the next section, resulting in ρ =97.2% in the $e\nu q\bar{q}$ channel and 99.2% in the $\mu\nu q\bar{q}$ channel.

using the same analysis as at 188.6 GeV.

At E_{cms}= 191.6 GeV, CC03 samples are generated as well as $4f$ samples. The selection efficiency decreases by 1.1±0.4% in the $e\nu q\bar{q}$ and 0.3±0.3% in the $\mu\nu q\bar{q}$ channel with respect to the efficiencies at E_{cms}= 188.6 GeV.

At each of the energies described in this thesis, large samples of Monte Carlo were generated of both W pair events and event types that add to the selected background. The size of these samples is shown in table 4.5.

	$4f$		$q\bar{q}$		ZZ		$We\nu$		Zee	
E_{cms}	N	σ	N	σ	N	σ	N	σ	N	σ
188.6	1039	16.93	490	99.41	100	2.759	15	0.6607	1957	99.11
191.6	200	17.27	500	95.82	50	2.823	0		100	6.897
195.5	200	17.59	500	91.01	50	2.855	20	0.7565	250	99.04
199.5	200	17.81	1000	86.58	50	2.847	20	0.8110	100	7.072
201.6	200	17.89	1000	84.53	100	2.847	20	0.8351	1792	98.95

Table 4.5: Size of the generated event samples, where N = $N_{gen}/1000$ and the cross section is σ(pb). The centre-of-mass energy is E_{cms}(GeV). Missing in the table are the $\tau\tau$ final states, of which 1.9×10^5 events were generated at E_{cms}= 188.6 GeV only. The cross section at this energy is $\sigma_{\tau\tau}$ = 8.182 pb. The different values for σ_{Zee} are due to different values of the input parameter C_{kin} [37].

In the 10 GeV range between E_{cms}= 191.6 and 201.6 GeV, the $4f$ efficiency decreases by 2.4% in the $e\nu q\bar{q}$ channel and by 1.6% in the $\mu\nu q\bar{q}$ channel. In both channels the purity decreases by about 1.3%. For the final analysis, the selection cuts need to be optimised for each of the energies separately and the probabilities need to be re-parameterised to improve the quality of the selection.

The luminosity of the samples varies and the number of expected events, for all the samples used to fit the mass and width of the W, are shown in table 4.6. The number of events observed in the data, N_d, is shown in the same table. A total of 1866 events are expected to pass the selection and 1847 events are observed in the data samples, both in good agreement.

	N_{exp} $e\nu q\bar{q}$				
E_{cms}(GeV)	188.6	191.6	195.5	199.5	201.6
$\mathcal{L}$ (pb^{-1})	174.2	28.9	79.9	86.3	41.9
$e\nu q\bar{q}$	352.3	58.4	162.2	178.6	85.4
WW bkg	13.6	2.5	7.6	9.2	4.5
$q\bar{q}(\gamma)$	7.1	0.9	2.8	3.0	1.5
Zee	2.9	0.5	1.7	2.0	0.9
ZZ	1.0	0.2	0.6	0.8	0.4
$We\nu$	2.1	0.5	1.2	1.3	0.7
$\tau\tau$	0.4	-	-	-	-
N_{exp} total	381	63	176	195	93
N_d	367	64	178	192	106

	N_{exp} $\mu\nu q\bar{q}$				
$\mu\nu q\bar{q}$	370.8	62.6	174.6	187.8	91.9
WW bkg	17.5	3.0	9.4	10.9	5.5
$q\bar{q}(\gamma)$	5.2	1.0	3.1	3.0	1.6
Zee	0.1	0.0	0.1	0.1	0.0
ZZ	3.3	0.6	1.7	2.1	1.1
$We\nu$	0.1	0.0	0.1	0.1	0.0
$\tau\tau$	0.7	-	-	-	-
N_{exp} total	398	67	189	204	100
N_d	396	66	172	212	94

Table 4.6: Number of expected signal and background events after the probability cut. Large samples of each event type were generated and used to fit the mass and width of the W. A $\tau\tau$ sample was only generated at E_{cms}= 188.6 GeV.

The data distributions for various variables are compared to Monte Carlo simulations. Examples are shown in figures 4.10, 4.11 and 4.12. The $\tau\tau$ background is not included in energies above E_{cms} = 188.6 GeV. About one $\gamma\gamma$ event is expected to survive the $e\nu q\bar{q}$ selection before any cuts on the W mass are imposed at E_{cms} = 188.6 GeV. This background is not included in the fit but the effect of this sample on the mass and width of the W is negligible, as shown in chapter 7.

The main uncertainty in the background is due to the normalisation of the background with respect to the signal. To evaluate this effect, the discrepancy between

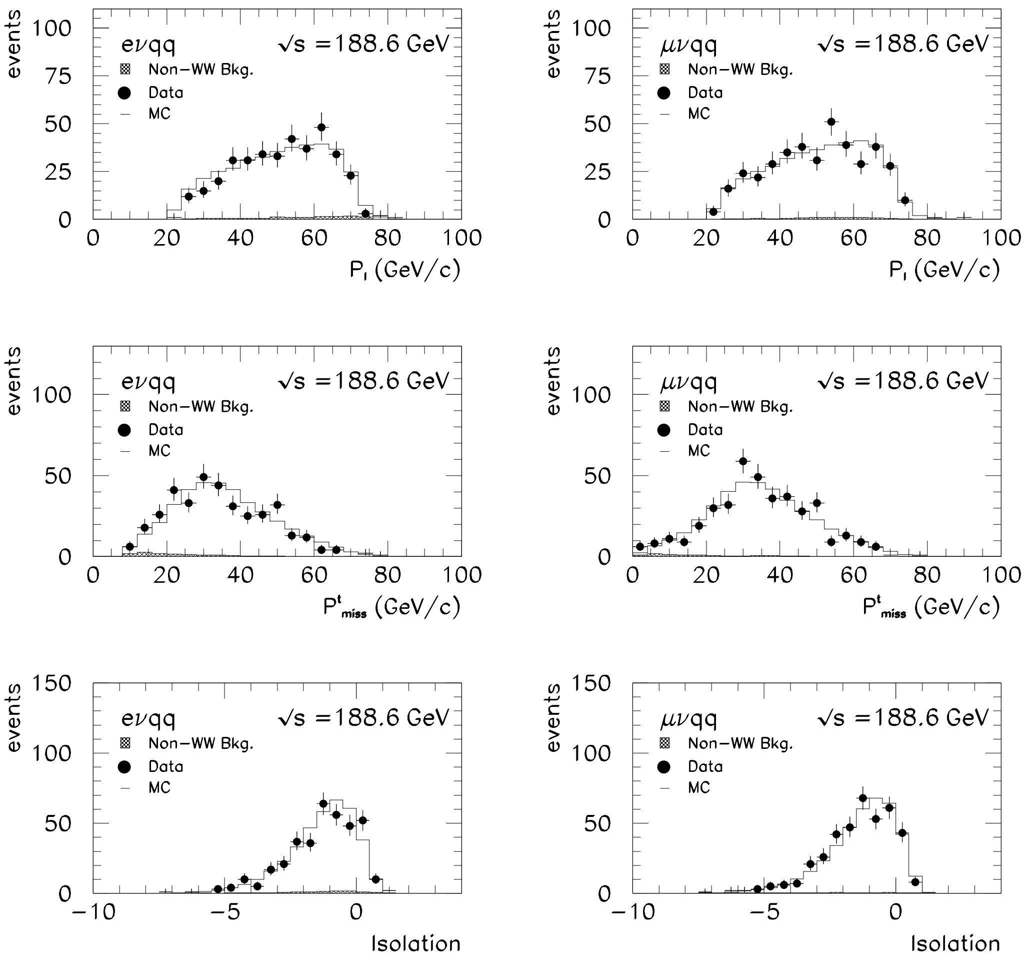

Figure 4.10: Distributions of P_l, P^t_{miss} and I after all $e\nu q\bar{q}$ (left-hand side) and the $\mu\nu q\bar{q}$ (right-hand side) selection cuts respectively. The bin sizes are 4 GeV/c in case of P_l and P^t_{miss} and 0.5 in case of I. These variables are used to define the signal probability described in section 4.1.8. A χ^2 is evaluated for all plots, taking into account bins with more than 4 expected events only. All fluctuations are compatible with statistics, the largest value of χ^2/n is 1.8, for 10 degrees of freedom.

data and Monte Carlo in the background region is estimated from the distributions in figure 4.8. The number of data events with a signal probability below 5% exceeds the number of expected events in both channels. Even though this discrepant region is rejected in the final selection, the difference in the number of events is used to estimate the uncertainty due to the background normalisation as will be discussed in section 6.2.

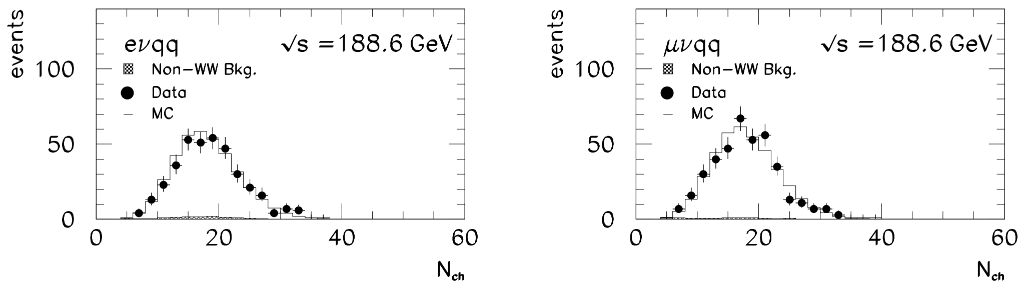

Figure 4.11: Distributions of the number of charged tracks N_{ch} after all $e\nu q\bar{q}$ (left-hand side) and the $\mu\nu q\bar{q}$ (right-hand side) selection cuts respectively, with 4 tracks per bin. N_{ch} is used to define the Bhabha cut described in section 4.1.7. The χ^2/n is 0.6 in the $e\nu q\bar{q}$ channel and 1.1 in the $\mu\nu q\bar{q}$ channel, for 12 degrees of freedom.

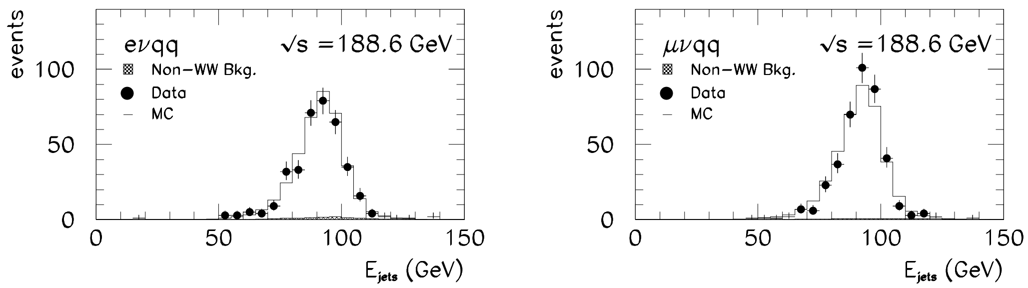

Figure 4.12: Distributions of the total energy of the jets after all $e\nu q\bar{q}$ (left-hand side) and the $\mu\nu q\bar{q}$ (right-hand side) selection cuts respectively. The bin size is 5 GeV. The χ^2/n is 1.0 in the $e\nu q\bar{q}$ channel and 1.5 in the $\mu\nu q\bar{q}$ channel, for 9 degrees of freedom.

4.2 Reconstruction of the W mass

The mass of the two W bosons can be computed from the measured four vectors in the event. However, because the beam energy of LEP is known with high precision, this result can be improved by a *kinematic fit*. The procedure is similar to the one used at E_{cms}= 182.7 GeV [87], apart from some minor improvements [94].

The first step in the procedure is to evaluate the offset and the resolution of the measured four-vectors on a large sample of Monte Carlo generated W pair decays. This is done for both channels separately, in a two dimensional space spanned by the energy and the polar angle at which the final state lepton or quark was generated. The parameterisation is redone for E_{cms}= 188.6 GeV [96].

A data or Monte Carlo event that is used to fit the mass and width of the W is then treated as follows. The four-vectors of the lepton and the two jets are reconstructed from the measured energy flow as described in the selection. These four-vectors are corrected for the offset as defined by the Monte Carlo parameterisation.

To approximate the original four-vectors of the event, a χ^2 is minimised while the four-vectors of the event are varied within their resolutions. In the evaluation of this χ^2, the energy in the event is forced to be equal to the LEP energy. A second constraint imposes that the two masses in the event are equal. The four-vector of the neutrino is evaluated by imposing conservation of momentum in the event.

For the minimisation procedure, the software packages MIGRAD and MINUIT are used [97]. The χ^2 is defined as:

$$\chi^2 = [Y_f - Y_m]^T \mathrm{V}^{-1} [Y_f - Y_m] + \lambda f(Y), \tag{4.12}$$

where Y_f is the vector of fitted variables, Y_m is the vector of measured variables and $\mathrm{V}_{ij} (=< Y_i Y_j > - < Y_i >< Y_j >)$ is the covariance matrix. $f(Y)$ contains the energy and mass constraints discussed below and λ are the Lagrange multipliers [95].

The Cartesian coordinates are transformed to variables that are minimally correlated, but close to the measured quantities to ensure their Gaussian behaviour. The 11 variables used to define χ^2 are:

- the velocities of the jets, β,
- the energies, E, of the jets and the lepton,
- two components, $p_{T\theta}$ and $p_{T\phi}$, of the transverse momentum of the jets and the lepton.

If the energy of the lepton is not corrected in any way in the selection, it is fully defined by the result of track fit. In this case, the lepton variables defined above are replaced by:

- the inverse radius of curvature, $1/r$, of the lepton track,
- its dip angle, $\tan\lambda$,

- the azimuthal direction of the track at the event vertex, ϕ_0.

Since the offset and the resolution of these variables are defined as a function of the energy and the polar angle of the original rather than the measured fermions, they are redefined at each step in the minimisation process. When the minimum is reached, the covariance matrix V in equation 4.12 returns the upper χ^2 probability of the fit and the error on the W mass.

Before any constraints are imposed, the neutrino four-vector can be evaluated from momentum conservation only because it is assumed to be massless. If the two masses are allowed to be different, energy conservation imposes one constraint on the event kinematics. This fit is therefore known as a 1C fit and results in two (hadronic and leptonic) mass estimators per event. If the masses are forced to be equal, two constraints define the χ^2. This is referred to as a 2C fit and results in one mass estimator per event. This second constraint is acceptable to impose because the resolution of the mass estimator is comparable to the W width, Γ_{W}. The 2C mass estimator contains most information and is therefore used for the analysis in this thesis.

The W mass from events with energy escaping through the beam pipe, such as background events with an escaping beam lepton, or events with a high energy ISR photon, is overestimated. Energy conservation forces the total energy to equal the LEP beam energy causing some of the escaping energy to be absorbed in the W mass. Some of these events are found at or near the kinematic limit ($\mathrm{M_W} = \mathrm{E_{cms}}/2$). Bins with few or no events in the Monte Carlo reference cause statistical fluctuations in the expected distribution of the mass estimator used in the parameter fits described in chapter 5. A mass window is therefore imposed before the mass and width are fitted. Many windows have been investigated and only events with a fitted mass in the range $70 < \mathrm{M_{2C}} < 90$ GeV/c^2 are used in the analysis. Studies on data and Monte Carlo are discussed in chapter 7.

Data distributions of the fitted four-vectors are compared to Monte Carlo predictions. Examples are shown in figures 4.13, 4.14 and 4.15.

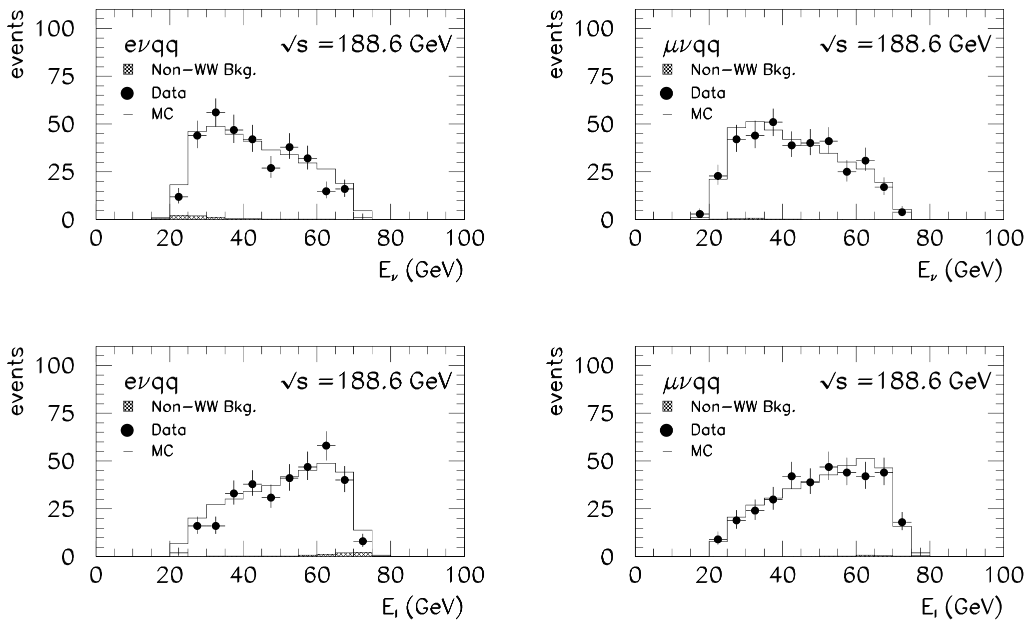

Figure 4.13: Distributions of the neutrino and the lepton energies after the kinematic fit for the $e\nu q\bar{q}$ (left-hand side) and the $\mu\nu q\bar{q}$ (right-hand side) selections respectively. Events within the 70 - 90 GeV/c^2 mass window are included. The bin size is 5 GeV. A χ^2 is evaluated taking into account bins with at least 4 expected events. The largest value of χ^2/n is 1.8, for 10 degrees of freedom.

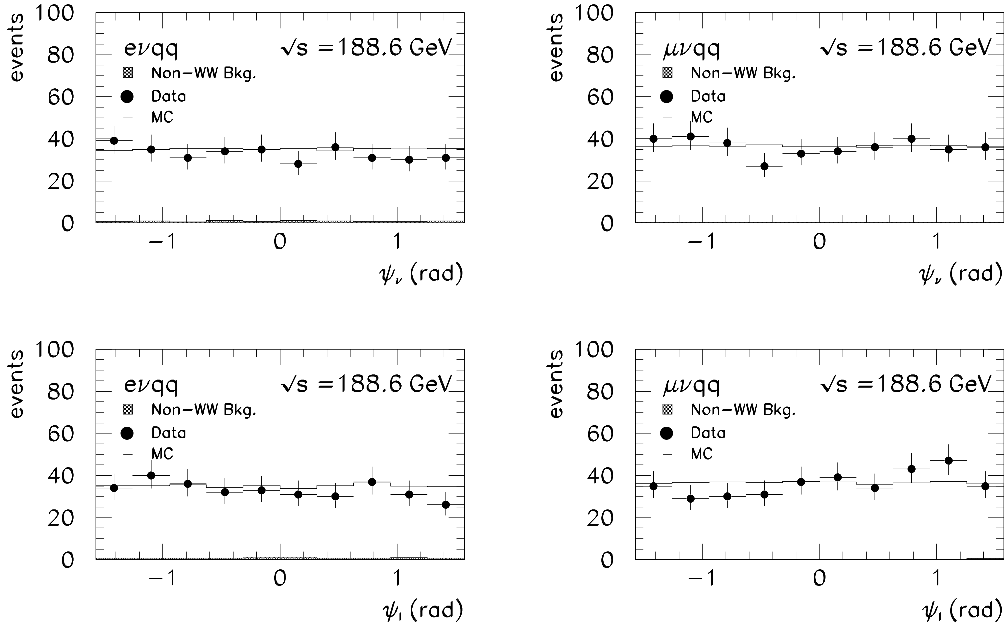

Figure 4.14: Distributions of the azimuthal angle of the neutrino and the lepton after the kinematic fit for the $e\nu q\bar{q}$ (left-hand side) and the $\mu\nu q\bar{q}$ (right-hand side) selections respectively. The bin size is $\pi/10$ and the sign depends on the x coordinate of the track. Positive and negative y values are combined. The largest value of χ^2/n is 0.9, for 9 degrees of freedom.

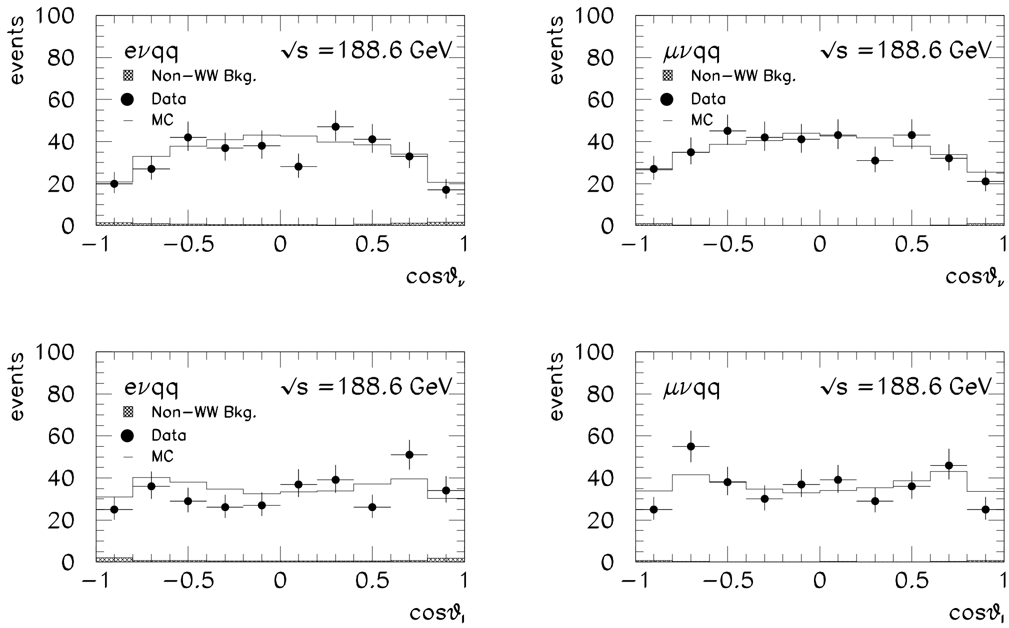

Figure 4.15: Distributions of the polar angle of the neutrino and the lepton after the kinematic fit for the $e\nu q\bar{q}$ (left-hand side) and the $\mu\nu q\bar{q}$ (right-hand side) selections respectively. The bin size is 0.1. The largest value of χ^2/n is 1.7, for 9 degrees of freedom.

Chapter 5

Extraction of the mass and width of the W

The method to extract the mass and the width of the W from the reconstructed mass of the selected events is outlined in this chapter. Section 5.1 describes a reweighting method which is used to limit the sample of Monte Carlo events that is needed for the measurement. The fit procedure is explained in section 5.2. Expectations for the statistical uncertainty on M_W and Γ_W from this method are shown in section 5.3.

Results of linearity checks are shown in section 5.4 and 5.6. In section 5.5, the correlation between the two parameters is commented on.

5.1 The reweighting method

The mass and width of the W are obtained from the distribution of the 2C mass estimator defined in section 4.2. The measured distribution is compared to simulated distributions for various values of M_W and Γ_W. A likelihood fit is used to obtain the values for which the simulated distribution gives the best fit to the data distribution.

A sample of approximately 10^6 W pair events with final states containing four fermions were generated using the Monte Carlo simulation procedure described in section 2.3. For this sample, the W mass is fixed to $M_W = 80.35$ GeV/c^2 and Γ_W is calculated to be $\Gamma_W = 2.09$ GeV/c^2 (see section 2.2.2).

In order to simulate mass distributions for any other values of $\mathrm{M_W}$ and Γ_W, the 2C mass distribution is reweighted. The event weight, w_s, is calculated from the Standard Model CC03 matrix element $\mathcal{M}$ [98]:

$$w_s(\mathrm{M_W}, \Gamma_\mathrm{W}) = \frac{|\mathcal{M}(\mathrm{M_W}, \Gamma_\mathrm{W}, (p^\mu)_{i=1,4})|^2}{|\mathcal{M}(\mathrm{M_W}^{\mathrm{ref}}, \Gamma_\mathrm{W}^{\mathrm{ref}}, (p^\mu)_{i=1,4})|^2}, \tag{5.1}$$

where $\mathrm{M_W}^{\mathrm{ref}}$=80.35 GeV/$c^2$, $\Gamma_\mathrm{W}^{\mathrm{ref}} = 2.09$ GeV/c^2 and $(p^\mu)_i$ are the 4 four-vectors of the fermions in the event. Examples of reweighted mass distributions are shown in figure 5.1. The sensitivity of the reweighting method to the mass and the width is illustrated in figure 5.2, where the change in the event density, $\rho_i = (\sigma_i/\sigma_{\mathrm{tot}})$, in a specific mass range Δm_i, is shown for a change in Γ_W and $\mathrm{M_W}$ of 500 and 50 MeV/c^2 respectively.

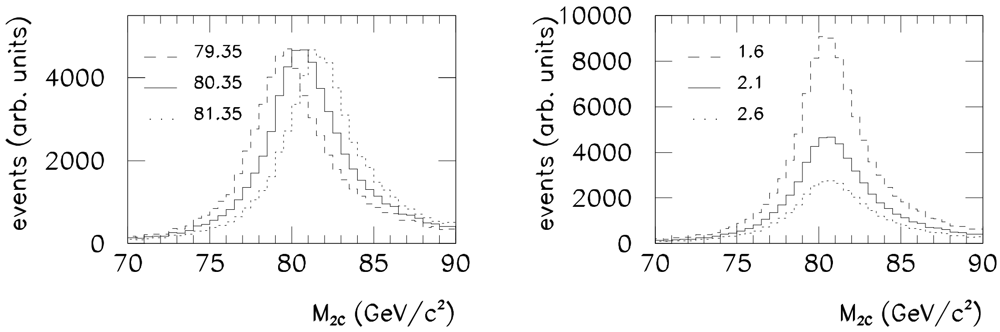

Figure 5.1: Reweighted mass distributions for simulated W pair decays, selected as $\mu\nu q\bar{q}$ decays. Left: reweighting to two different W masses, with Γ_W calculated according to the Standard Model relation. Right: reweighting to two different W widths, with $\mathrm{M_W} = 80.35$ GeV/c^2.

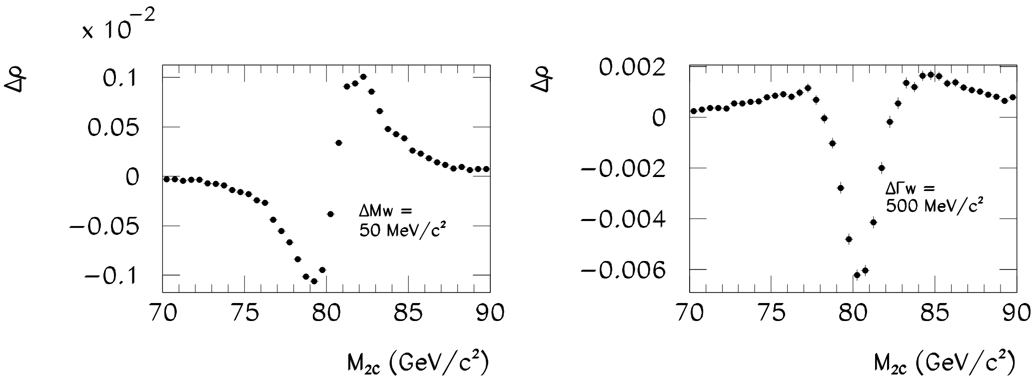

Figure 5.2: Sensitivity distributions for a change in $\mathrm{M_W}$ of 50 MeV/c^2 (left-hand side) and a change in Γ_W of 500 MeV/c^2 (right-hand side).

5.2 The fit procedure

The mass and width are fitted by varying them both independently during the fit procedure. For each set of values, (M_W,Γ_W), the 2C mass distribution is normalised to the number of observed data events. The additional Monte Carlo background samples ($q\bar{q}$, Zee, ZZ, $We\nu$ and $\tau\tau$) are added to the distribution. The dependence of the backgrounds on M_W and Γ_W is assumed to be negligible and background events are given a constant weight $w_b = 1$ during the fit. The total number of generated events for each of the samples is listed in table 4.5. The fit is performed for each energy and both decay channels separately but, at centre-of-mass energies exceeding 188.6 GeV, the $e\nu q\bar{q}$ and $\mu\nu q\bar{q}$ decay channels are combined (see chapter 7).

The W pair cross section is needed as an input parameter in the fit in order to properly normalise the signal with respect to the background and is mass dependent. It is calculated from M_W according to a parameterisation derived with the GENTLE [37] package:

$$\sigma(M_W) = \sigma({M_W}^{ref}) \cdot (1 + a\ \Delta M_W + b\ (\Delta M_W)^2), \tag{5.2}$$

where $\Delta M_W = M_W - {M_W}^{ref}$. The resulting parameterisations are shown in figure 5.3. A new version of the GENTLE package has shown that the version used for this parameterisation has a 2% normalisation uncertainty due to electroweak next-to-leading order corrections [99], but this is negligible compared to the 35% variation in the normalisation used to determine the systematic uncertainty on the measurement (see section 6.2).

Due to the use of a mass window in the selection, the selection efficiency is a function of Γ_W (and M_W). Only events with a 2C mass reconstructed between 70 and 90 GeV/c^2 are accepted. The effect on the efficiency $\epsilon(\Gamma_W)$ is determined from the sum of the event weights before and after the mass window cut. The following parameterisation is used:

$$\epsilon(\Gamma_W) = \epsilon({\Gamma_W}^{ref}) \cdot (1 + c \cdot ({\Gamma_W}^{ref} - \Gamma_W)) \tag{5.3}$$

and similar for M_W. Event samples generated at different values of M_W and Γ_W are used as a cross check. The dependency on the mass is found to be negligible and the

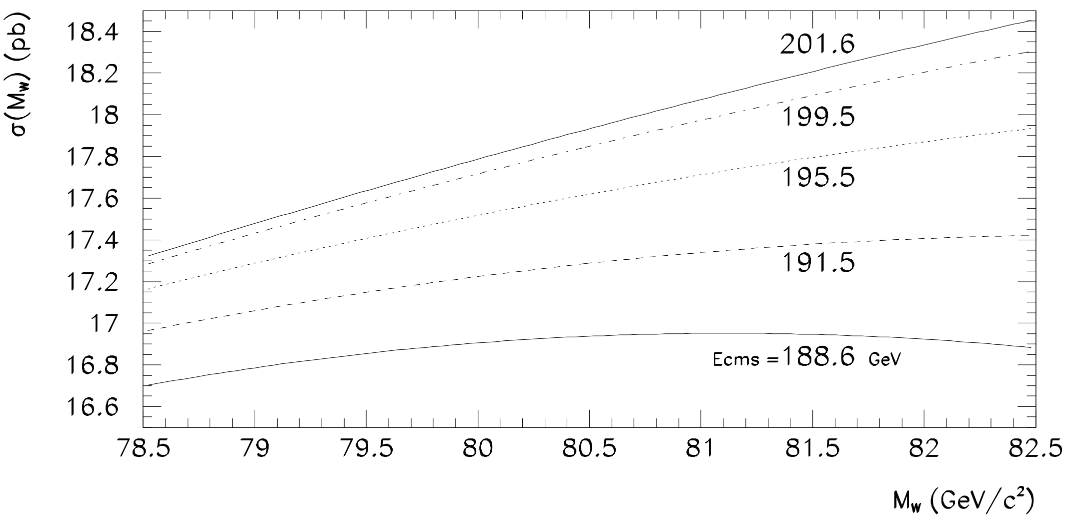

Figure 5.3: GENTLE parameterisations for the cross section dependence on $\mathrm{M_W}$, for various centre-of-mass energies.

small $\mathcal{O}(1\%)$ effect due to $\epsilon(\Gamma_\mathrm{W})$ is taken into account during the fit. The values for $c(\mathrm{GeV}^{-1})$ in equation 5.3 are given in table 5.1. The uncertainty in these values is estimated by evaluating the coefficients at $\mathrm{E_{cms}}=$ 188.6 GeV from 8 different samples of 100k generated $4f$ events and scaling the RMS of this distribution to the total number of events in the reference. It is found to be of the order of 0.03% for the 188.6 GeV samples and 0.06% for the samples at higher energies because of the reduced statistics of the reference. The value of c increases with increasing centre-of-mass energy because the kinematic limit on the reconstructed mass shifts upwards, while the upper mass window cut is kept constant for the preliminary result.

$\mathrm{E_{cms}}$(GeV)	188.6($e\nu\mathrm{q\bar{q}}$)	188.6($\mu\nu\mathrm{q\bar{q}}$)	191.6	195.5	199.5	201.6
$c(\times 10^2)$	1.24	1.14	1.52	1.71	1.85	1.96

Table 5.1: Values for $c(\mathrm{GeV}^{-1})$ in equation 5.3 at various centre-of-mass energies in GeV. For the energies above 188.6 GeV, the two decay channels are combined.

For each calculated distribution, a likelihood $\mathcal{L}$ is calculated:

$$-2\log\mathcal{L} = -2\sum_{i=1}^{\mathrm{N_{evt}}} \log\mathcal{P}_i, \tag{5.4}$$

where $\mathcal{P}_i$ is the probability for event i to be found in the mass range (bin) that it was observed in. The value of $\mathcal{P}$ corresponding to a certain mass range is simply the contents of this bin in the 2C mass distribution if the integral over the distribution is normalised to unity.

The 2C distribution corresponding to the likelihood maximum is selected, and the input values for $\mathrm{M_W}$ and Γ_W used to obtain this distribution are the output values of the fit. The CERN software package MINUIT [97] is used for the minimisation.

The statistical error is determined using the MINOS package. The function $y(\mathrm{M_W}, \Gamma_\mathrm{W}) = -2\log\mathcal{L}$ is sampled until the 2-dimensional contour in the $(\mathrm{M_W},\Gamma_\mathrm{W})$ plane corresponding to $y(\mathrm{M_W}, \Gamma_\mathrm{W}) = (y_{\min} + 1)$ is found. The extreme points of the projection of the contour on each of the parameter axes are used to define the positive and negative errors. The assumption of symmetrical parabolic behaviour is not made and the positive and negative fit errors can therefore differ. Due to the asymptote at $\Gamma_\mathrm{W} = 0$ GeV/c^2, the negative error on Γ_W will be smaller than the positive error. Since $\mathrm{M_W} = 0$ GeV/c^2 is hundreds of standard deviations away from the minimum, the effect of this asymptote is negligible and the statistical errors on $\mathrm{M_W}$ are symmetric. An example of this likelihood is shown on figure 5.4.

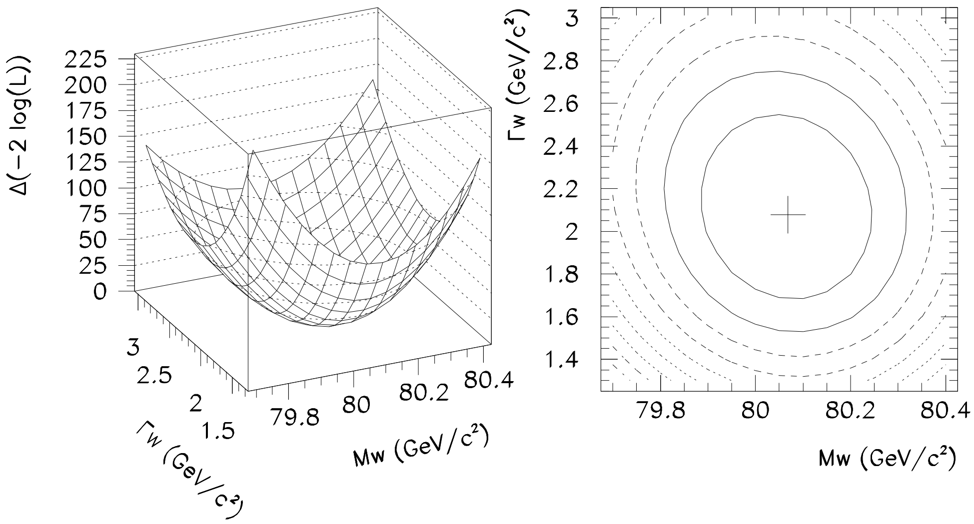

Figure 5.4: Likelihood function for a two dimensional fit to a large sample of Monte Carlo events generated at $\mathrm{M_W}$= 80.10 GeV/c^2 and selected as $e\nu\mathrm{q\bar{q}}$ decays. The result of the fit is shown in the right-hand contour plot. The cross indicates the size of the fit errors.

In addition to the two parameter fit described above, a second fit is done to determine $\mathrm{M_W}$. During this fit, the Standard Model width is calculated from the mass according to equation 2.39 before the event weight is evaluated and not varied during the fit.

5.3 Expected statistical errors

The expected statistical uncertainty is evaluated using the event samples in table 4.5. First, the observed number of data events that pass the selection is determined. Samples of this size are selected from the Monte Carlo events. The probability for each type of event is read from table 4.6. The actual number of selected events for each type at E_{cms}= 188.6 GeV is determined at random according to Poisson statistics. Events are taken from the files until 100 $\mu\nu q\bar{q}$ samples and 94 $e\nu q\bar{q}$ samples are constructed. Signal events can only be selected once, but background events can be selected twice if the generated sample is too small. Each sample is fitted to the full reference sample. The fit results are used to determine the mean and pull of the fitted value of M_W and Γ_W , their RMS, and the mean of the fit errors. The pull is defined as the difference between the fitted value and the reference value, divided by the average of the upper and lower fit errors. The results are shown in figure 5.5 for M_W and figure 5.6 for Γ_W. The numerical results are summarised in table 5.2. A fit is performed to ensure that the distributions in the figures are Gaussian and the χ^2/n for each of the fitted distributions is in agreement with this assumption ($0.3 \leq \chi^2/n \leq 1.6$).

Channel	M_W(GeV/c^2)	σ_- (GeV/c^2)	σ_+ (GeV/c^2)	Pull
$e\nu q\bar{q}$	80.337 ± 0.020	0.172 ± 0.001	0.170 ± 0.001	-0.05 ± 0.11
$\mu\nu q\bar{q}$	80.361 ± 0.017	0.155 ± 0.001	0.154 ± 0.001	0.08 ± 0.10

Channel	Γ_W(GeV/c^2)	σ_- (GeV/c^2)	σ_+ (GeV/c^2)	Pull
$e\nu q\bar{q}$	2.08 ± 0.04	0.385 ± 0.004	0.429 ± 0.004	-0.15 ± 0.09
$\mu\nu q\bar{q}$	2.11 ± 0.04	0.355 ± 0.004	0.394 ± 0.004	-0.12 ± 0.10

Table 5.2: Mean expected fit values and statistical uncertainties. The expected errors are valid for 330 selected $e\nu q\bar{q}$ events and 360 selected $\mu\nu q\bar{q}$ events at E_{cms}= 188.6 GeV. The values for M_W and Γ_W should be compared to the reference values M_W = 80.35 GeV/c^2 and Γ_W = 2.09 GeV/c^2.

The expected statistical uncertainties at higher energies are estimated according to equation 6.18. The combined statistical uncertainty for the data taken at centre-of-mass energies from 191.6 to 201.6 GeV is found to be 0.24 GeV/c^2 for Γ_W and

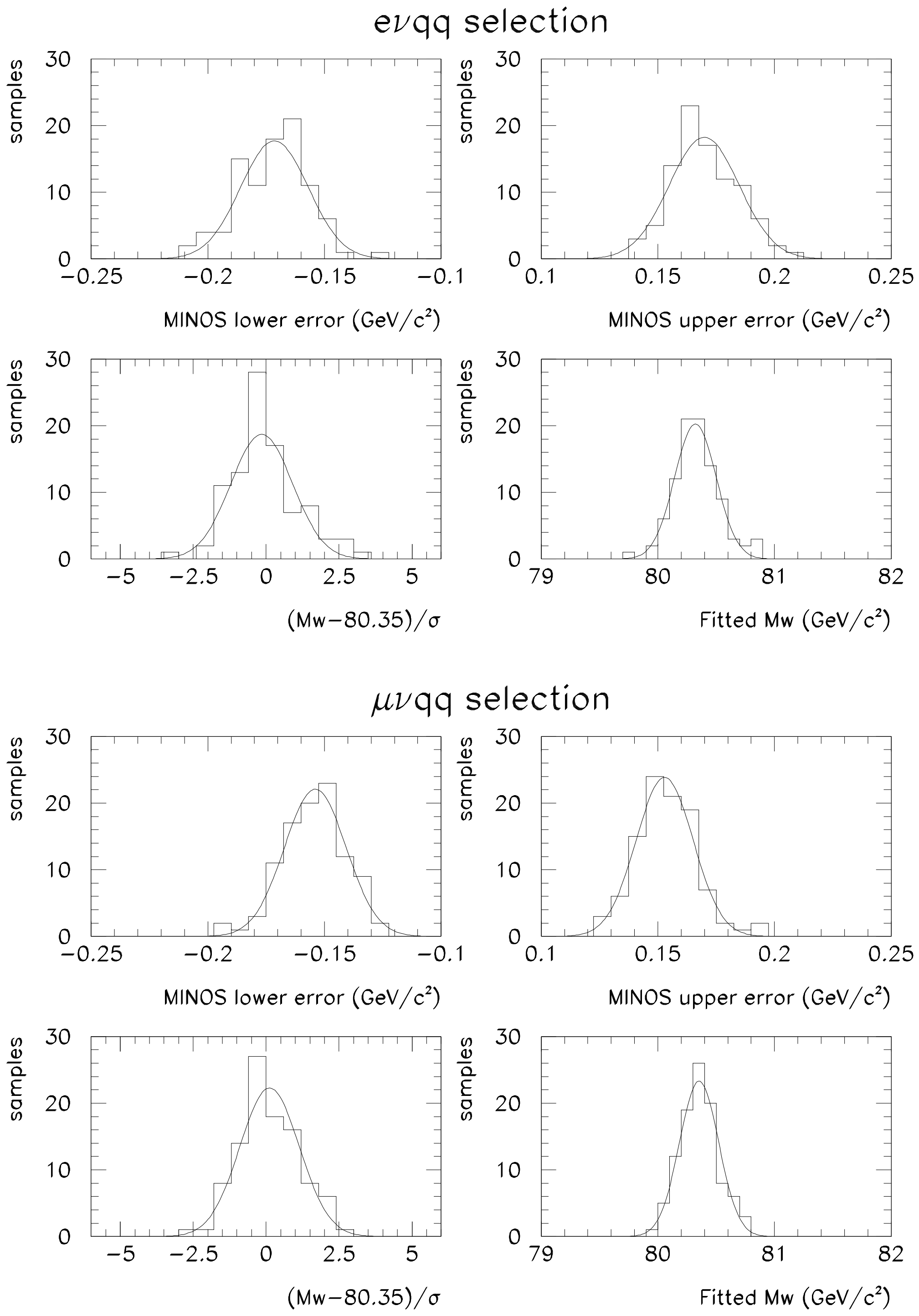

Figure 5.5: Expected errors and pull distributions for M_W. All distributions are at E_{cms} = 188.6 GeV, where 330 $e\nu q\bar{q}$ and 360 $\mu\nu q\bar{q}$ events were selected from the ALEPH data sample. The fitted means of the Gaussian distributions agree with the averages in table 5.2.

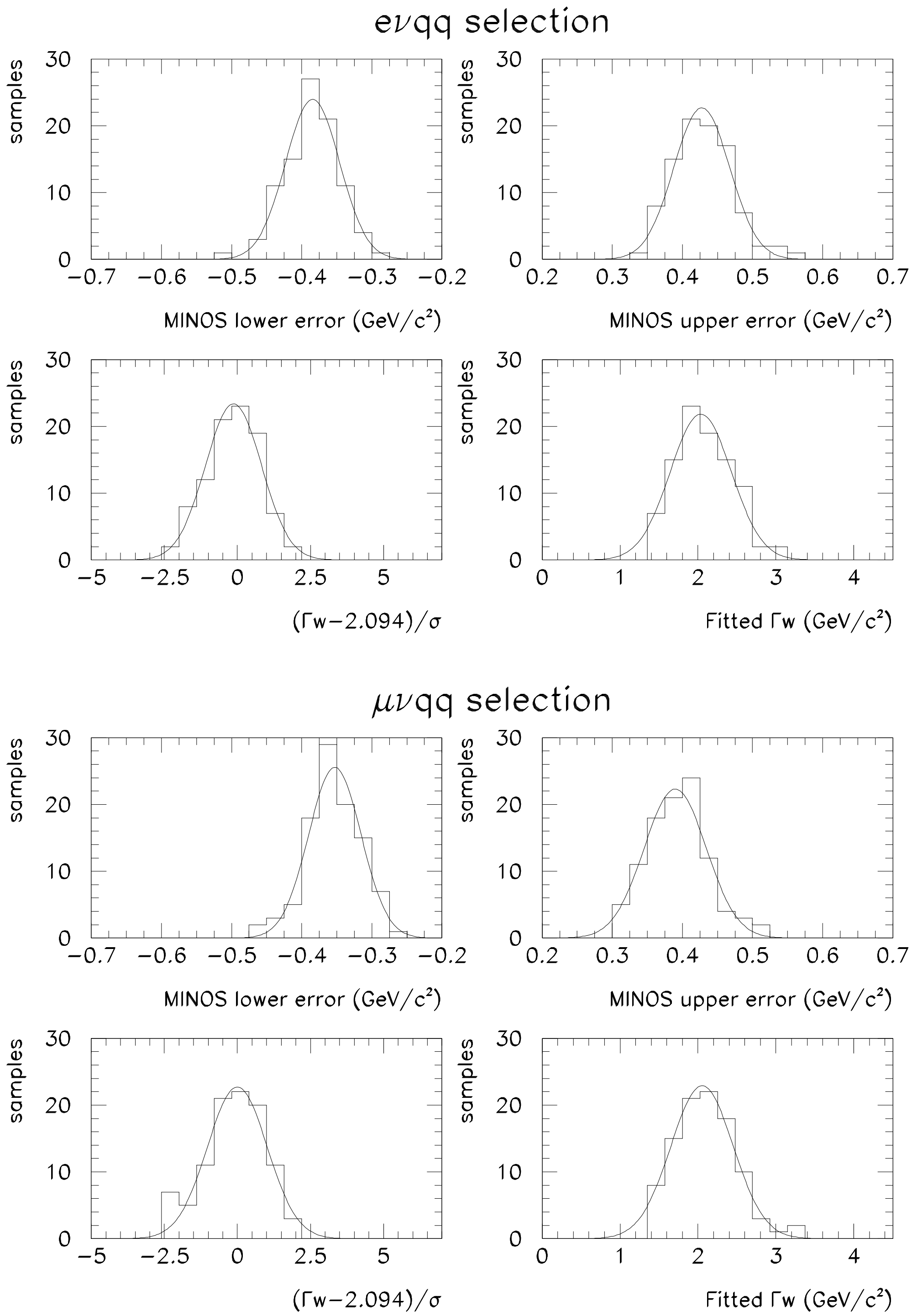

Figure 5.6: Expected errors and pull distributions for Γ_W. All distributions are at E_{cms} = 188.6 GeV, where 330 $e\nu q\bar{q}$ and 360 $\mu\nu q\bar{q}$ events are selected from the ALEPH data sample. The fitted means of the Gaussian distributions agree with the averages in table 5.2.

0.104 GeV/c^2 for $\mathrm{M_W}$. At these energies, the $(e/\mu)\nu q\bar{q}$ channels are combined in the same fit, but this does not significantly worsen the expected statistical uncertainty (less than 5 MeV/c^2 in case of Γ_W and 1 MeV/c^2 in case of $\mathrm{M_W}$). Equation 6.18 is valid in the high statistics limit and the upper and lower expected errors calculated with this method are symmetrical.

5.4 Linearity checks

Samples of $4f$ final states are generated away from the reference values $\mathrm{M_W} = 80.35$ GeV/c^2 and $\Gamma_W = 2.09$ GeV/c^2 to investigate the linearity of the fit (the fitted parameters versus the parameters used in the generation). Many Standard Model samples are generated at various W masses. For these samples, the W width is calculated according to equation 2.39. The statistics of the samples are shown in the right-hand column of table 5.3.

In the Monte Carlo generator KORALW [76], one has the option to set Γ_W in the propagator to a different value, violating the Standard Model relation between the mass and the width in equation 2.39 and changing the shape of the resonance. The actual value of the cross section is in this case no longer meaningful because the decay channels of the W have not changed. However, these non-Standard Model samples can be used as a cross check for the method because only the shape of the mass distribution is relevant. These samples are shown in the left-hand column of table 5.3.

The results of fits of all samples to the full $4f$ reference sample are shown in figures 5.7, 5.8 and 5.9. A straight line is fitted to these points:

$$Y(X) = a(X - X^{\mathrm{ref}}) + b, \tag{5.5}$$

where X is either $\mathrm{M_W}$ or Γ_W and X^{ref} is the corresponding reference value. In this fit, the statistical component due to finite Monte Carlo statistics of the reference sample is not taken into account. The results of the fit are shown in table 5.4.

The offset of $\mathrm{M_W}$ in the $\mu\nu q\bar{q}$ channel at $\mathrm{E_{cms}} = 188.6$ GeV has been studied extensively. A better calculation of the error on each point, taking into account the uncertainty due to finite statistics of the reference sample has been performed

Non-Standard Model				Standard Model			
M_W	Γ_W	E_{cms}	N	M_W	E_{cms}	N	σ(pb)
				79.35	188.6	60	16.81
				79.70	188.6	50	16.85
				79.85	188.6	60	16.88
				80.10	188.6	58	16.90
80.35	1.8	188.6	30	80.25	188.6	50	16.92
80.35	2.4	188.6	30	80.45	188.6	50	16.92
80.60	1.5	188.6	45	80.60	188.6	60	16.93
80.60	2.7	188.6	30	80.85	188.6	60	16.96
				81.00	188.6	50	16.96
				81.35	188.6	60	16.97
80.35	1.5	199.5	50	79.85	199.5	50	17.65
80.35	2.7	199.5	50	80.85	199.5	50	17.97

Table 5.3: Size of the generated event samples, where M_W and Γ_W are quoted in GeV/c^2 and E_{cms} is quoted in GeV. The number of generated events N = $N_{gen}/1000$. For the Non-Standard model samples, the Standard Model cross section $\sigma(M_W)$ is used. Γ_W in case of the Standard Model samples varies between $\Gamma_W(M_W{=}79.35)$ = 2.02 GeV/c^2 and $\Gamma_W(M_W{=}81.35)$ = 2.17 GeV/c^2, according to equation 2.39.

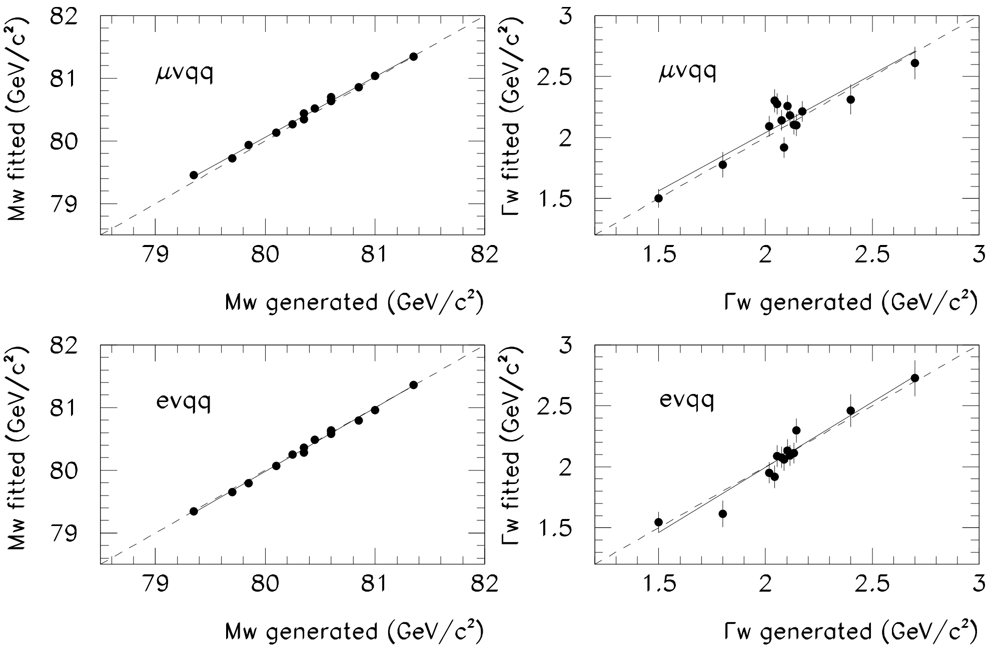

Figure 5.7: Linear fits for both decay channels at E_{cms} = 188.6 GeV. The offset and slope of the fits are listed in table 5.4.

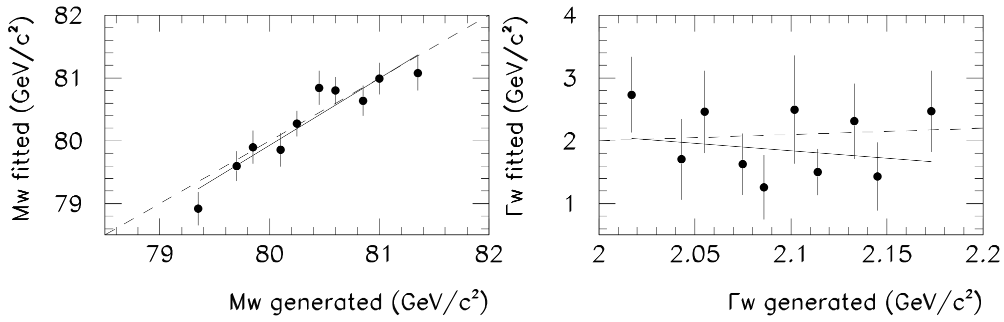

Figure 5.8: Linear fits for both decay channels combined at E_{cms} = 188.6 GeV. Only events with problems in the kinematic fit (zero mass error) are selected. The offset and slope of the fits are listed in table 5.4.

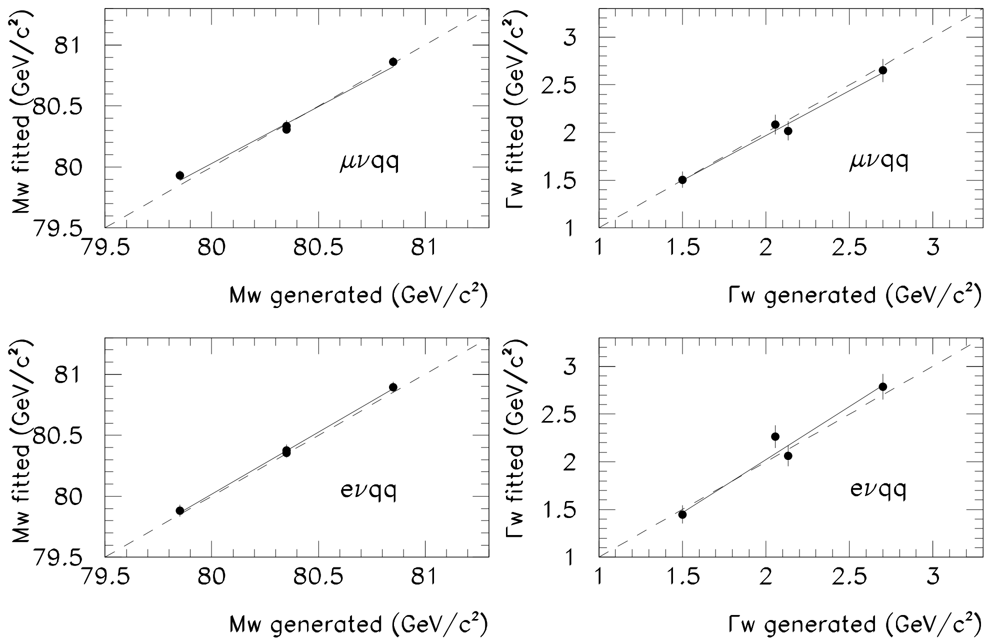

Figure 5.9: Linear fits for both decay channels at E_{cms} = 199.5 GeV. The offset and slope of the fits are listed in table 5.4.

[100]. Two additional contributions add to the uncertainty in the offset (and slope) of the line. Firstly, an additional 8 MeV has to be taken into account due to the finite statistics of the reference. Secondly, an additional 2 MeV originates from the decrease in reference statistics when the sample is reweighted to values away from the

		a			b		(GeV/c^2)	χ^2/n
$e\nu q\bar{q}$	M_W	1.015	$\pm$	0.020	80.335	$\pm$	0.011	0.8
(188.6 GeV)	Γ_W	1.07	$\pm$	0.11	2.097	$\pm$	0.026	0.8
$\mu\nu q\bar{q}$	M_W	0.965	$\pm$	0.018	80.397	$\pm$	0.010	0.8
(188.6 GeV)	Γ_W	0.95	$\pm$	0.10	2.129	$\pm$	0.025	1.8
$(e/\mu)\nu q\bar{q}$	M_W	1.07	$\pm$	0.14	80.302	$\pm$	0.078	1.0
$(\sigma_{M_W} = 0)$	Γ_W	-2	$\pm$	4	1.86	$\pm$	0.18	1.0
$e\nu q\bar{q}$	M_W	1.013	$\pm$	0.065	80.374	$\pm$	0.022	1.6
(199.5 GeV)	Γ_W	1.11	$\pm$	0.13	2.128	$\pm$	0.057	1.7
$\mu\nu q\bar{q}$	M_W	0.934	$\pm$	0.058	80.356	$\pm$	0.021	2.0
(199.5 GeV)	Γ_W	0.94	$\pm$	0.12	2.059	$\pm$	0.052	0.5

Table 5.4: Slope and offset of the fits in figure 5.7. The errors on the fitted values are underestimated as the uncertainty due to finite reference statistics has not been taken into account, see [100]. At E_{cms} = 188.6 GeV, these effects add a total of 8 MeV/c^2 to the uncertainty on the offset on M_W, and 0.6% ($\mu\nu q\bar{q}$) or 0.7% ($e\nu q\bar{q}$) on the slope. At E_{cms} = 199.5 GeV, these numbers are a factor 2.2 larger due to less statistics. For events with convergence problems in the kinematic fit ($\sigma_{M_W} = 0$) the linearity is also investigated, combining both decay channels to increase the statistics.

reference mass. Therefore, the actual uncertainty in the offset is 13 MeV/c^2 rather than the 10 MeV/c^2 quoted in table 5.4. For the slope, the additional uncertainty due to finite reference statistics is 0.2% and the additional uncertainty due to the reweighting is 0.6%.

The event samples at E_{cms}= 199.5 GeV are fitted to a reference of only 2×10^5 events. The uncertainties due to the finite statistics of the reference are therefore of the order of $\sqrt{5} \approx 2.2$ times larger, resulting in an additional contribution of 17 MeV/c^2 on the offset, and 1.4% on the slope.

Many classes of events are investigated. Events with leptons in the barrel were compared to events with leptons in the endcaps, and events with leptons parallel or anti-parallel to the e^- beam direction were separated. No significant difference was observed.

Linear fits can be performed where the mass distribution in both the reweighting reference sample and the samples being fitted to are taken from generator level rather than reconstruction level. This is a useful test to isolate any problems to either one of the two levels [101]. Such a test found that fitting the leptonic W mass distribution of the sample at M_W = 79.35 GeV/c^2 resulted in a fit value approximately 3σ higher than the input parameter. This correlates to the observation that the fit at the standard reconstructed level also has a significant offset in figure 5.7 ($M_W = 79.453 \pm 0.034$ GeV/c^2). A new sample at $M_W = 79.35$ GeV/c^2 was generated. The fit to this sample results in a value less then 1σ below the input mass. The difference between the first and the second generated sample is 121 ± 51 MeV/c^2.

To investigate the linearity of the width fit in the $\mu\nu q\bar{q}$ channel from the Standard Model samples only (Γ_W= 2.02 to 2.17 GeV/c^2), the distribution of the mean of the two generated W masses before the reconstruction is used. A straight line is fitted to the results of reweighting fits to this distribution for each of the ten samples. The slope and offset agree with the expectations within one standard deviation, with an uncertainty of 12 MeV/c^2 and 25% respectively, if the effects due to the finite reference statistics are not taken into account.

To investigate events with convergence problems in the kinematic fit separately, the function in equation 5.5 is fitted to the Standard Model samples for this class events ($\sigma_{M_W} = 0$). The $e\nu q\bar{q}$ and $\mu\nu q\bar{q}$ decay channels are combined in order to increase the statistical significance of the fit. The results are shown in table 5.4 and figure 5.8 respectively. No significant offset, or slope different from one, is observed. The uncertainty in the fitted offset and slope is large and the events carry little weight in the actual data fit.

If the results from both decay channels at $E_{cms} = 188.6$ GeV are included in the same fit, the result from these 28 points is M_W= $80.368 \pm 0.007 \pm 0.006$ GeV/c^2, consistent with the reference mass within 1.9σ. The slope of the line is consistent with one within less than a standard deviation: $0.989 \pm 0.013 \pm 0.006$. At $E_{cms} = 199.5$ GeV, no significant offset is observed.

Apart from the offset of the $\mu\nu q\bar{q}$ mass no significant discrepancies are observed. After many studies the shift could not be associated with a problem in the analysis. Significant fluctuations are observed in the Monte Carlo used to fit the straight line. If there is an effect on the measurement it should be of the order of 18 MeV/c^2 on the combined result which is small compared to the statistical and systematic uncertainties of the data fit.

5.5 Correlation between $\mathrm{M_W}$ and Γ_W

The fit is not sensitive to the theoretical correlation between the $\mathrm{M_W}$ and Γ_W. The observed correlation is a superposition of various effects, including efficiency dependencies and detector acceptance. The expected correlation is determined using the samples described in the discussion of the expected statistical uncertainty. The results are $\rho_{e\nu\mathrm{q\bar{q}}}$ = -16 $\pm$ 10 % and $\rho_{\mu\nu\mathrm{q\bar{q}}}$ = -8 $\pm$ 10 %. The corresponding distributions are shown in figure 5.10.

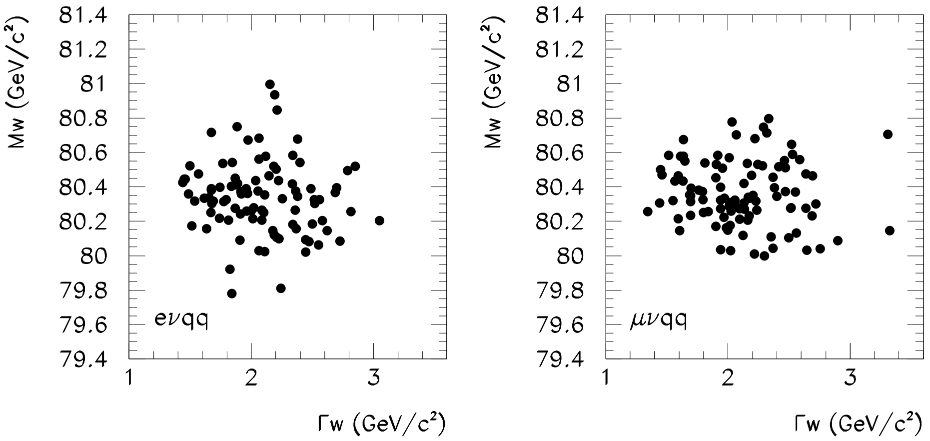

Figure 5.10: Correlation between $\mathrm{M_W}$ and Γ_W at $\mathrm{E_{cms}}$ =188.6 GeV, from the subsamples described in section 5.3.

Since the correlation between $\mathrm{M_W}$ and Γ_W is small, it is possible to fit the width while fixing the mass to a well chosen value. However, if $\mathrm{M_W}$ is fixed to a value away from the value that would be the result of the two parameter fit, the fitted width is always overestimated. To avoid a positive bias in the measurement of Γ_W, the mass has to vary freely while the width is being extracted.

5.6 Additional checks for Γ_W

No significant offset, or slope different from one, is observed in the linear fits for Γ_W. If all samples are combined at $\mathrm{E_{cms}}$= 188.6 GeV, the slope is +0.5 and -0.6 standard deviations away from unity in the $e\nu\mathrm{q\bar{q}}$ and $\mu\nu\mathrm{q\bar{q}}$ channels respectively. The offset is +1.4 and +0.1 standard deviations away from the reference value.

The standard ALEPH mass analysis does not use events with an upper χ^2 probability, from the kinematic fit, $P(\chi^2)$, below 1% because these events are badly reconstructed. The distributions of $P(\chi^2)$ for events that pass the two selections are shown in figure 5.11. In chapter 7 the fit error on M_W will be shown to be stable for various cuts on the χ^2 probability.

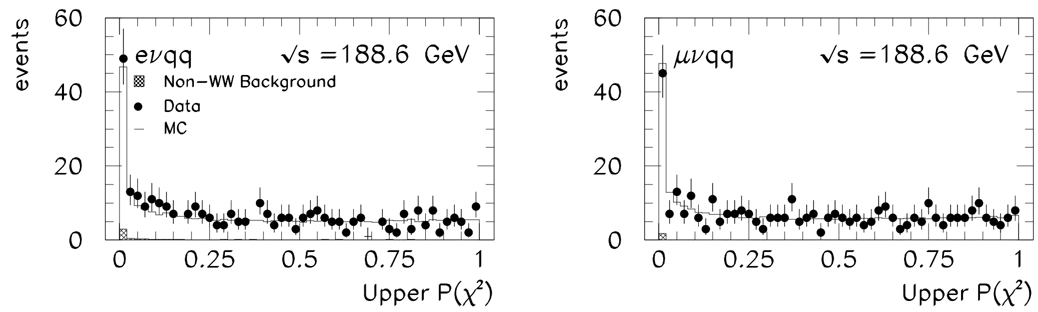

Figure 5.11: Upper χ^2 probability of the kinematic fit for $e\nu q\bar{q}$ and $\mu\nu q\bar{q}$ events respectively, with a bin size of 2%.

To investigate if these events are sensitive to the W width additional checks are done. The effects on the slope and the offset of only the three samples with $M_W = 80.35$ GeV/c^2 are studied for different selection cuts. The five different analyses are listed in table 5.5. Apart from two cuts on the upper χ^2 probability of the kinematic fit, a cut on a proper convergence of the kinematic fit, 'KF conv', and a cut on the signal probability at 30% instead of 40% to look for biases due to $4f$ background, are investigated.

Subsample studies are done to investigate the pull and the expected errors for each of these analyses. A total of 100 subsamples with the size of the data are used, including all WW and non-WW backgrounds. The means of the fit values are stable and are in good agreement with the reference value. The expected error on Γ_W increases significantly if a cut on the χ^2 probability is added to the selection. With an uncertainty in each expected error of the order of 4 MeV/c^2 the positive and negative errors increase by $^{+26}_{-17}$ MeV/c^2 in case of the $e\nu q\bar{q}$ channel and $^{+12}_{-9}$ MeV/c^2 in case of the $\mu\nu q\bar{q}$ channel. This corresponds to a change in the mean fit error of 5% in the $e\nu q\bar{q}$ and 3% in the $\mu\nu q\bar{q}$ channel. Events with a low kinematic fit probability are therefore sensitive to the W width.

	$e\nu q\bar{q}$			
Cut	a	b (GeV/c^2)	χ^2/n	N_d
Default	1.45 ± 0.29	2.07 ± 0.07	1.1	330
$P(\chi^2)$ >0.01	1.41 ± 0.31	2.09 ± 0.07	0.4	290
$P(\chi^2)$ >0.02	1.28 ± 0.30	2.09 ± 0.07	0.6	281
Prob>30%	1.43 ± 0.28	2.06 ± 0.07	1.2	336
KF conv	1.49 ± 0.29	2.06 ± 0.07	1.2	327

	$\mu\nu q\bar{q}$			
Cut	a	b (GeV/c^2)	χ^2/n	N_d
Default	0.95 ± 0.28	2.05 ± 0.07	0.6	360
$P(\chi^2)$ >0.01	0.99 ± 0.28	2.08 ± 0.07	1.2	330
$P(\chi^2)$ >0.02	0.96 ± 0.29	2.08 ± 0.07	0.6	315
Prob>30%	0.97 ± 0.27	2.05 ± 0.06	0.5	366
KF conv	0.92 ± 0.28	2.05 ± 0.07	0.5	322

Table 5.5: Slope and offset of the linear fits for Γ_W if only the three samples with widths between 1.8 and 2.4 GeV/c^2 are used.

The same study is done using a theoretical calculation of the expected error described in section 6.4.3. The expected statistical uncertainty on the W width for the combined $(e/\mu)\nu q\bar{q}$ data samples at centre-of-mass energies between 191.6 and 201.6 GeV increases from 0.24 to 0.26 GeV/c^2, confirming the trend observed at 188.6 GeV. Since the slope and offset of the linear fits are stable within their uncertainty no cut is used for the analysis of the data.

5.7 Summary

In this chapter, the method to extract the mass and width of the W from the distribution of the 2C mass estimator by means of a reweighting method is described. A large sample of Monte Carlo events is generated at a fixed value of both M_W and Γ_W and reweighted to different values according to a CC03 matrix element. Large Monte Carlo samples of the significant background processes are simulated as well. The measured data distribution is compared to the reweighted Monte Carlo reference distributions to which the background processes have been added.

The Monte Carlo distributions are normalised to the number of observed data events while performing a maximum likelihood fit. The signal and background contributions are normalised taking into account the change in the signal cross section as a function of the W mass, as well as the change in the efficiency of the mass window cut as a function of the W width. To extract the mass and width of the W, M_W and Γ_W are varied independently during the fit.

The expected statistical uncertainties on the measurements are determined from a large number of Monte Carlo samples with the same size as the selected data sample. The expected correlation between M_W and Γ_W is found to be small. Monte Carlo samples at different values of M_W and Γ_W are generated to investigate the performance of the method away from the values of M_W and Γ_W at which the reference Monte Carlo event sample is generated. Many studies are done to find the cause of a possible offset of the W mass in the $\mu\nu q\bar{q}$ channel. If the samples for both channels are included in the same straight line fit (measured M_W versus generated M_W), the offset is found to be $\Delta M_W = +18\pm7\pm6$ MeV/c^2. No systematic cause is found and the shift is assumed to be due to a statistical fluctuation.

Events with a low value (below 1%) for the upper χ^2 probability from the kinematic fit do not change the expected statistical uncertainty on M_W, but are sensitive to the W width. The expected error on Γ_W increases significantly if events with a low probability are rejected. Therefore, no cut on the upper χ^2 probability is used in the analysis.

Chapter 6

Systematic errors

Apart from the statistical errors evaluated in the previous chapter, systematic errors are a significant source of uncertainties in the measurement of both $\mathrm{M_W}$ and Γ_W. The various contributions to the systematic error are described in this chapter.

Uncertainties due to the characteristics of the ALEPH detector are described in section 6.1. The estimation of the background is not perfect, as will be discussed in section 6.2. In section 6.3 the significance of the uncertainties in the LEP beam energy will be discussed.

The theoretical model used for the analysis is not perfect. Discrepancies between the data sample and the Monte Carlo generated events cause a systematic error on the mass and width. Three uncertainties in the prediction of the reference distributions are investigated; errors due to fragmentation of the $q\bar{q}$ system, initial state radiation off the beam leptons and the finite statistics of the generated reference sample. These contributions to the systematic error are all described in section 6.4.

The different systematic uncertainties are summarised at the end of the chapter in table 6.9.

6.1 Detector uncertainties

The characteristics of the ALEPH detector are not known with infinite precision. The best estimate for, or calculation of, the detector resolutions and the position of the detector modules are input to the Monte Carlo simulation. The differences between the actual apparatus and the detector description used in the Monte Carlo simulation cause a systematic change in the predicted mass distribution as a function of M_W and Γ_W and are therefore sources of systematic uncertainties. Possible differences have been studied and the results of these studies are described in this section.

The high energy lepton originating from the leptonically decaying W is measured with good resolution [84] (e.g. for $E_e \simeq 47$ GeV, $\Delta E/E \simeq 3.5\%$) and small uncertainties in the measurement of the lepton, due to errors in the tracking such as a wrong magnetic field map in the TPC, or a miscalculation of the drift velocity in the TPC, can therefore have a large impact on the measurement. Uncertainties in the lepton angle, its momentum and their resolutions are investigated as well as uncertainties in the measurement of the jets. An additional uncertainty enters due to the calibration of the calorimeters. The angles θ and ϕ, and the positive x, y and z axes, are defined in figure 6.1.

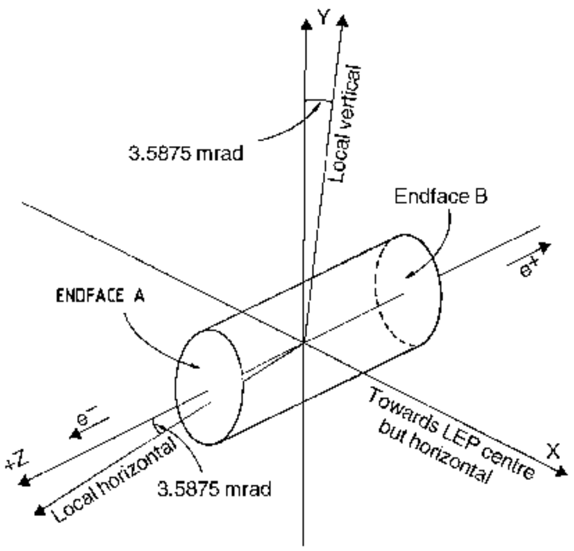

Figure 6.1: Position of the ALEPH detector in the LEP ring and definition of the ALEPH coordinate system. The angle θ is defined as the angle of a track with the positive z axis. ϕ is the angle between the projection of a track in the $x - y$ plane and the positive x axis.

6.1.1 Lepton angles

Uncertainties in the bias of the lepton angle θ_l have been investigated in three independent ways. The first method uses the calibration data taken at the Z resonance (E_{cms}= 91.2 GeV) in 1999. The second method is the same technique applied to the high energy data (E_{cms}= 188.6 GeV) on events that are selected by the selection described in chapter 4. The third method measures the angle between muon tracks from Z decays that should be back-to-back. In this section these three studies are described first, followed by studies related to the resolution of θ_l . At the end of the section, the bias and resolution of ϕ_l will be discussed.

A charged particle track is reconstructed in ALEPH from three of the sub-detectors: the VDET, the ITC and the TPC. The VDET coordinates are well known and the position of the faces is stable to less than 5 μm [85]. However, a misalignment between the VDET and the other sub-detectors can cause a bias in the measurement of the lepton angles. To investigate this bias, the lepton angle is measured in three different ways and the discrepancy between data and Monte Carlo is evaluated as follows:

- measure the lepton angle from the VDET only (θ_1), from the ITC and the TPC (θ_2) or from all detectors (θ_3),
- define the angular bias as the difference between the three measurements, $\Delta\theta_{ij} = \theta_i - \theta_j$, for both data and Monte Carlo events as a function of cosθ,
- determine the largest difference between data and Monte Carlo on this bias.

Only events with at least two VDET coordinates can be used, which limits the acceptance to $|\cos\theta| < 0.9$. This method is first applied to events collected at the Z resonance in 1999 [102]. Cuts are applied to obtain a clean sample of Z decays and tracks are selected if their momentum exceeds 3 GeV/c. The mean misalignment is determined in 50 bins of equal size in cosθ and no difference between data and Monte Carlo of more than 0.2 mrad is observed. The Monte Carlo distribution reaches maxima of $\Delta\theta_{13} \approx 0.06$ mrad near the end caps and the TPC membrane.

This method is repeated at E_{cms} = 188.6 GeV on the semi-leptonic W pair selection. No mass window is imposed, but the requirement of a good VDET reconstruction reduces the number of selected $(e/\mu)\nu q\bar{q}$ data events to 497. Since the positive W is produced mainly in the direction of the e^+ beam and the negative W in the direction of the e^- beam, the distribution as a function of polar angle indirectly separates positively and negatively charged leptons. The difference between data and Monte Carlo in the polar angle of the lepton is shown in figure 6.2. For each bin, the distribution of $\Delta\theta_{13}$ is found to be Gaussian. No effects of more than 0.5 mrad are observed. The distribution of $\Delta\theta_{12}$ is determined as well, leading to the same conclusion.

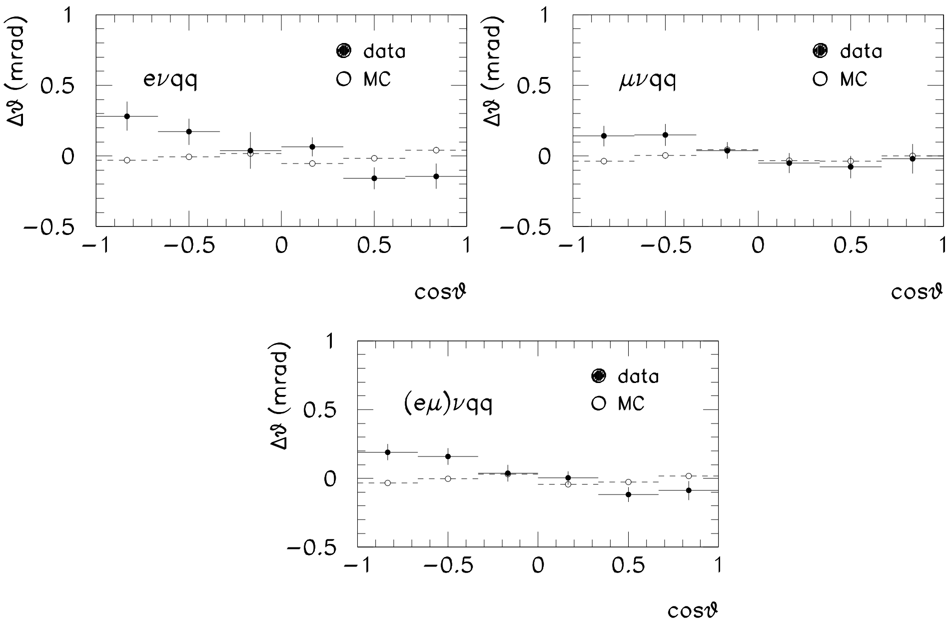

Figure 6.2: Misalignment in the polar angle of the track, $\Delta\theta_{13}$, for data and Monte Carlo events as a function of cosθ.

To cross check this method, the angle between the two muons originating from a $Z \rightarrow \mu^+\mu^-$ decay at the Z peak is measured in both data and Monte Carlo [103], using data taken at 1999. The difference between the angles of the muons is defined as:

$$\Delta\theta_\mu = \theta_{(\mu^+)} - \theta_{(\mu^-)} - \pi \tag{6.1}$$

and is ideally described by a δ-function centred around zero ($\theta_{(\mu^+)} - \theta_{(\mu^-)} = \pi$) because the muons are produced back-to-back. If the two LEP beams collide at a slight angle or if the e^+e^- pair collides away from the assumed interaction point, an offset and a worsening of the resolution will be observed that is not related to a wrong reconstruction of the track. The offset and the resolution of θ_l will therefore be overestimated and only muons with an energy of E = 45.6 GeV can be investigated. The difference between data and Monte Carlo in the distribution of $\Delta\theta_\mu$ is determined in 20 bins in both cosθ and ϕ. No effect of more than 0.5 mrad is observed.

To determine the uncertainty in the resolution of θ_l , the width of the distribution of θ_{13} is compared between data and Monte Carlo. This width is found to be of the order of 0.5 mrad using the 497 selected W pair decays mentioned above. No discrepancy between data and Monte Carlo of more than 0.3 mrad is observed, if 6 bins in cosθ_l are analysed separately. The distribution of $\Delta\theta_{13}$ for all events combined is shown in figure 6.3.

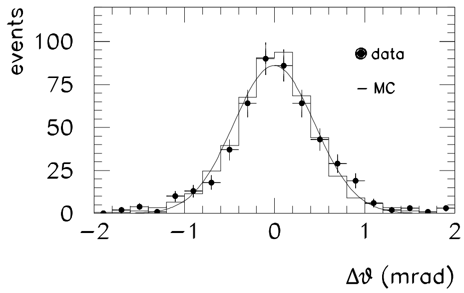

Figure 6.3: Misalignment in the polar angle of the lepton, $\Delta\theta_{13}$, for selected semi-leptonic WW data and Monte Carlo events. A Gaussian is fitted to the Monte Carlo distribution.

The distribution of $\Delta\theta_\mu$ in equation 6.1 from events taken at the Z resonance contains similar information. A perfect detector and ideal event kinematics would result in a δ-function centred around zero, as explained above. The mean and the RMS of the observed data and Monte Carlo distributions are shown in table 6.1. The differences between data and Monte Carlo are an overestimation of the uncertainties in θ_l. The mean value of $\Delta\phi_\mu = \phi_{(\mu^+)} - \phi_{(\mu^-)} - \pi$ as a function of cosθ and ϕ is also obtained from Z events as well as the resolution on $\Delta\phi_\mu$. The results are shown in table 6.1.

To obtain the systematic shift in $\mathrm{M_W}$ and Γ_W due to errors in the bias and the resolution of the lepton angles ϕ_l and θ_l, a large sample of Monte Carlo events is

	μ_{data} (mrad)	μ_{MC} (mrad)	σ_{data} (mrad)	σ_{MC} (mrad)
$\Delta\theta$	0.05 $\pm$ 0.03	0.008 $\pm$ 0.005	1.50 $\pm$ 0.02	0.638 $\pm$ 0.004
$\Delta\phi$	-0.025 $\pm$ 0.008	0.006 $\pm$ 0.003	0.452 $\pm$ 0.008	0.334 $\pm$ 0.003

Table 6.1: Mean μ and resolution σ of the difference between the ϕ and θ angles of the two muons originating from a decaying Z at E_{cms} = 91.2 GeV. The two leptons are expected to be back to back, neglecting small effects mentioned in the text.

analysed. A conservative approach is adopted in the first instance, assuming that the systematic shifts will be small. All observed discrepancies are less than 1 mrad and six different analyses are compared to the standard analysis: For all selected leptons, θ_l and ϕ_l are shifted both up and down by 1 mrad, and the resolution of each of the angles is worsened by an additional smearing with an RMS of 1 mrad.

A positive bias in θ_l is defined as:

$$\begin{aligned} \theta_l &\to \theta_l + 1 \text{ mrad} & \cos\theta_l &> 0 \\ \theta_l &\to \theta_l - 1 \text{ mrad} & \cos\theta_l &< 0. \end{aligned}$$

The lepton is therefore always moved away from the beam pipe. A negative bias is defined in such a way that the lepton is moved closer to the beam pipe. A Monte Carlo sample of 36k $4f$ decays is analysed four times to investigate each bias separately. After the shift, events that are selected in both the shifted sample and the original sample are used to determine the systematic uncertainty. Typically 0.1% of the events is present in only one of the two samples. These are removed to reduce statistical fluctuations. A total of 4.3k $\mu\nu q\bar{q}$ and 4.2k $e\nu q\bar{q}$ events are fitted to the standard reference sample, both with and without the bias. The difference between the fitted values is used as an estimate for the systematic uncertainty in M_W and Γ_W .

The uncertainty in this shift is obtained from subsample studies. The common events are cut into samples of 350 events. For each of these samples, the shift is determined and the RMS of this shift is calculated. The error on the shift of the full sample is obtained by multiplying this RMS by a scale factor $f = \sqrt{350/N_{\text{tot}}}$, where N_{tot} is the total size of the Monte Carlo sample. The shifts (bias - original) and their uncertainties are shown in table 6.2.

The resolution of θ_l is worsened by applying an additional smearing with an RMS of 1 mrad. To illustrate this, the difference between θ_l before and after the smearing is shown in figure 6.4. The mass and width are again determined from 4.2k $e\nu q\bar{q}$ and 4.3k common $\mu\nu q\bar{q}$ events. The uncertainty on the shift is determined from subsample studies and the results are shown in table 6.2.

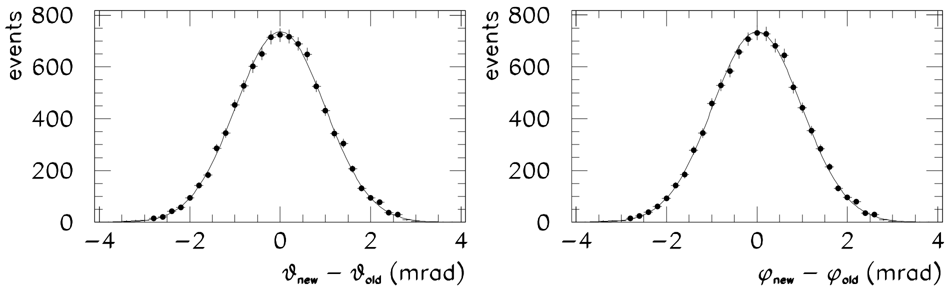

Figure 6.4: Additional smearing in Monte Carlo events of the lepton angles θ_l and ϕ_l . A Gaussian is fitted to the shift. The mean is compatible with zero, and the RMS is compatible with 1 mrad for both angles.

A positive (negative) bias in ϕ_l is simulated by adding (subtracting) 1 mrad from ϕ of the lepton track. After the negative bias or after the smearing, 4.2k $e\nu q\bar{q}$ events and 4.3k $\mu\nu q\bar{q}$ events remain. A smaller sample of $4f$ events is used to determine the effect of a positive bias from which 3.8 and 3.9k events are selected in the $e\nu q\bar{q}$ and $\mu\nu q\bar{q}$ channels respectively.

Finally, a Gaussian smearing is applied to ϕ_l as illustrated in figure 6.4. Again 4.2k and 4.3k events are used to determine the shift. The results are shown in table 6.2.

The shifts in table 6.2 are small compared to the expected statistical uncertainty in the measurement and all shifts in Γ_W are compatible with zero within 1.5 σ. The negative effect on the width due to additional smearing in ϕ_l is caused by a statistical fluctuation. Some shifts in M_W could be significant, but the uncertainty in the error is large (only 10 subsamples were used to find the RMS of the shift).

The shifts are relatively small and a conservative approach is adopted. For the final systematic due to uncertainties in the lepton angles, four components are added in quadrature: the largest shift due to a bias in θ_l , the shift due to the smearing of θ_l , the largest shift due to a bias in ϕ_l and the shift due to the smearing in ϕ_l .

Systematic change	$\Delta M_W(\mathrm{MeV}/c^2)$ $e\nu q\bar{q}$	$\Delta M_W(\mathrm{MeV}/c^2)$ $\mu\nu q\bar{q}$	$\Delta\Gamma_W(\mathrm{MeV}/c^2)$ $e\nu q\bar{q}$	$\Delta\Gamma_W(\mathrm{MeV}/c^2)$ $\mu\nu q\bar{q}$
θ_l + 1 mrad	-7 $\pm$ 3	6 $\pm$ 5	5 $\pm$ 4	0 $\pm$ 10
θ_l - 1 mrad	-4 $\pm$ 3	7 $\pm$ 4	2 $\pm$ 8	10 $\pm$ 9
θ_l smeared	-6 $\pm$ 4	5 $\pm$ 2	3 $\pm$ 8	4 $\pm$ 9
ϕ_l + 1 mrad	-4 $\pm$ 1	10 $\pm$ 4	-2 $\pm$ 5	-3 $\pm$ 4
ϕ_l - 1 mrad	-4 $\pm$ 4	-3 $\pm$ 5	10 $\pm$ 10	4 $\pm$ 11
ϕ_l smeared	-7 $\pm$ 4	4 $\pm$ 4	-8 $\pm$ 6	-4 $\pm$ 7

Table 6.2: Systematic shifts in the mass and width as a result of a simulated bias or a simulated smearing of 1 mrad. All numbers are a fit to the systematically shifted or smeared sample, minus the original fit.

The uncertainty in the shifts is used if it is larger than the shift itself. The final result is a systematic uncertainty in M_W of 12 MeV/c^2 in the $e\nu q\bar{q}$ channel and 14 MeV/c^2 in the $\mu\nu q\bar{q}$ channel and an uncertainty in Γ_W of less than 17 MeV/c^2 and 19 MeV/c^2 respectively.

6.1.2 Lepton momentum

Due to small errors in the alignment of the tracking detectors, the lepton momentum measurement suffers from a bias. This bias is measured from $Z \to \mu^+\mu^-$ events [104]. Measurements show that the momentum of negative tracks is overestimated, while the momentum of positive tracks is underestimated. Muon tracks with a momentum of ~45.6 GeV/c are used to parameterise the shift between the beam energy and the momentum of the muon as a function of the polar angle of the track. This shift reaches a maximum of 6% near the beam pipe ($|\cos\theta| > 0.9$). The momentum of tracks for which $|\cos\theta| < 0.9$ is equal to the beam energy within 1% uncertainty. A correction function is parameterised as a function of polar angle and taken into account in the measurement of M_W and Γ_W.

The difference between the fit values obtained with or without this correction is used to estimate the systematic uncertainty in M_W and Γ_W. A sample of 60k $4f$ events is used to determine the shift in the fitted values if the correction is switched off. This corresponds to 5.7k selected $e\nu q\bar{q}$ and 6.2k selected $\mu\nu q\bar{q}$ decays in common with the original sample. Subsamples are used to estimate the uncertainty in the shift. The results are shown in table 6.3.

To determine the uncertainty in the resolution of the lepton momentum, the momentum pull distributions are compared between data and Monte Carlo. The distributions are obtained from the track fit algorithm, used to reconstruct charged particles in ALEPH, applied to muons at $E_{cms} = 91.2$ GeV [103] originating from $Z \rightarrow \mu^+\mu^-$ decay. The momentum pull for these tracks is defined as:

$$\text{pull} = \frac{E_b - p}{\sigma_p}. \tag{6.2}$$

For 15 equal bins in $\cos\theta$, the mean and the RMS of the pull distribution is determined using a Gaussian fit. Effects due to a shift in the mean of the Gaussian are taken into account by the bias correction explained above. A difference in the width of the pull distribution is a direct measurement of a discrepancy in the momentum resolution between data and Monte Carlo, because the error on the track fit (σ_p) is defined to be equal in both samples. The width observed in data and Monte Carlo is shown as a function of the polar angle of the track in figure 6.5.

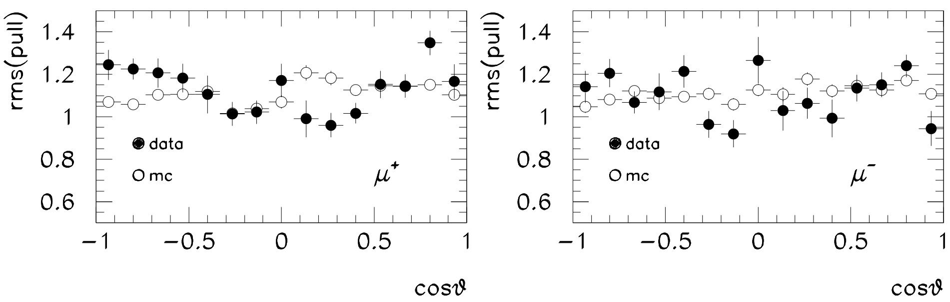

Figure 6.5: Width of the pull distributions for the momentum of muons with an energy of E = 45.6 GeV. Positive and negative muons are treated separately.

To estimate the systematic shift in M_W and Γ_W due to the uncertainty in the momentum resolution of the lepton, a Monte Carlo sample of 36k $4f$ events is reanalysed. The momentum of the selected lepton is smeared with a Gaussian to simulate the data better. In this way, the momentum resolution can obviously only be increased. The width of the Gaussian used in the smearing, σ_{smear}, can be defined in various ways. Two different methods are discussed here.

Firstly, the error weighted mean of the points in figure 6.5 is calculated for both data and Monte Carlo. The difference in the mean RMS in quadrature, multiplied by the error on the momentum, is used for the width of the Gaussian:

$$\sigma_{\mathrm{smear}} = \sqrt{(\mathrm{RMS})_{\mathrm{data}}{}^2 - (\mathrm{RMS})_{\mathrm{MC}}{}^2} \cdot \sigma_p. \tag{6.3}$$

For all positive tracks combined, this difference is found to be $\Delta(\mathrm{RMS}) = 0.21$. For negative tracks, the difference is 0.18 in the opposite direction, and the difference is 0.08 for all tracks combined. To be conservative, the lepton momentum is smeared by adding a Gaussian distributed number with an RMS of:

$$\sigma_{\mathrm{smear}} = 0.25\ \sigma_p. \tag{6.4}$$

However, this method can be an underestimation of the systematic uncertainty if bins in which the data and the Monte Carlo differ significantly carry more weight in the analysis.

The second method to estimate the systematic uncertainty uses the actual points in figure 6.5. The charge and the polar angle of each selected lepton originating from a W pair decay is determined. Its momentum is then smeared with an additional width given by the actual difference between two points in the distribution:

$$\sigma_{\mathrm{smear}} = \Delta\mathrm{RMS}(\mathrm{C}, \cos\theta) \cdot \sigma_p. \tag{6.5}$$

where $\Delta\mathrm{RMS}(\mathrm{C}, \cos\theta)$ is defined by equation 6.3 with an additional dependence on the lepton charge C and its polar angle θ. The RMS is defined as the fit value plus its uncertainty in case of the data, and the fit value minus its uncertainty in case of Monte Carlo, in order to be conservative. If the RMS in the data is still less than the RMS in the Monte Carlo, the momentum is not changed. This method can overestimate the systematic shift, because the width is artificially increased while compensating effects are not taken into account, as is illustrated in figure 6.6. If all the events for which the momentum is smeared are added in a single histogram, the width of the distribution of $(\mathrm{p_{new}} - \mathrm{p_{old}})/\mathrm{p_{old}}$ is found to be of the order of 1%.

The shift corresponding to the first method is evaluated on 4.2k $e\nu\mathrm{q\bar{q}}$ and 4.3k $\mu\nu\mathrm{q\bar{q}}$ events respectively. To obtain a negligible uncertainty on the shift in Γ_{W}, 86k $4f$ events are used for method 2, corresponding to 9.9k and 11k selected events. In case of method 2, the uncertainty in the shift is estimated for each channel from the

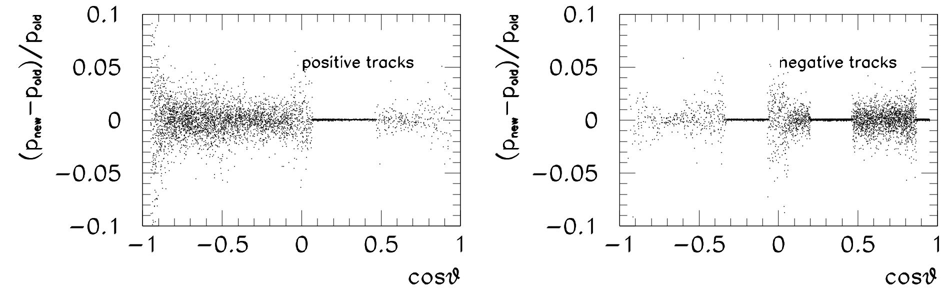

Figure 6.6: Fraction of the momentum added or subtracted from the total lepton momentum as a function of polar angle, for positive and negative tracks. The lines correspond to areas where the expected resolution is larger than the measured resolution from $Z \rightarrow \mu^+\mu^-$ events.

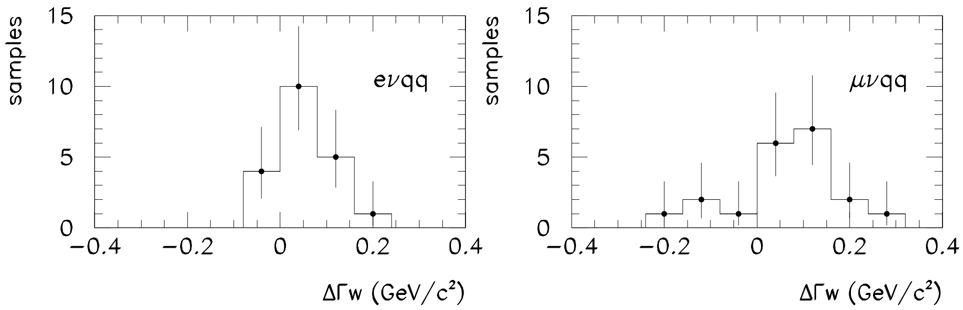

Figure 6.7: Shift in Γ_W as a result of a worsening of the resolution of the lepton momentum, according to method 2 (see text). The RMS of each of the distributions is calculated and scaled to the total number of events used in the fit to obtain the uncertainty in the systematic shift.

Systematic change	$\Delta M_W(\mathrm{MeV}/c^2)$ $e\nu q\bar{q}$	$\Delta M_W(\mathrm{MeV}/c^2)$ $\mu\nu q\bar{q}$	$\Delta\Gamma_W(\mathrm{MeV}/c^2)$ $e\nu q\bar{q}$	$\Delta\Gamma_W(\mathrm{MeV}/c^2)$ $\mu\nu q\bar{q}$
P_l bias	1 ± 8	-7 ± 6	-11 ± 15	-10 ± 10
P_l smearing 1	-9 ± 7	0 ± 8	6 ± 18	0 ± 14
P_l smearing 2	-5 ± 6	-7 ± 7	47 ± 11	56 ± 19

Table 6.3: Systematic shifts in the mass and width as a result of a simulated bias or a simulated smearing of the lepton momentum. All numbers are the systematically shifted or smeared fit minus the original fit.

RMS of 20 subsamples, each containing 350 selected events. The distribution of the shift in Γ_W for each of the samples is shown in figure 6.7.

The systematic shifts in M_W are consistent with zero and both methods are in agreement. The second method results in a significant systematic shift in Γ_W and is therefore used as the uncertainty in the measurement. The additional smearing causes the width to increase as expected, and the results are shown in table 6.3. The total systematic uncertainty on M_W due to the lepton momentum is found to be 10 MeV/c^2 in both channels. For Γ_W this uncertainty is 49 MeV/c^2 in the $e\nu q\bar{q}$ channel and 57 MeV/c^2 in the $\mu\nu q\bar{q}$ channel.

6.1.3 Jet angle

To evaluate the uncertainty due to the angular bias of the jets, $Z \to q\bar{q}$ events collected at E_{cms}= 91.2 GeV in 1994, 1998 and 1999 are used [105]. The jets are separated into two independently measured components, one containing the charged tracks and one containing the photons. The difference in the polar angles of these components is measured as a function of $\cos\theta_{jet}$ both in data and in Monte Carlo. A total of 40 equally sized bins are used. The large sample of $Z \to q\bar{q}$ events taken in 1994 is used to find a function that describes the difference between data and Monte Carlo. This difference is consistent with zero apart from the region where the barrel and the end caps of the calorimeter overlap ($0.7 < \cos\theta_{jet} < 0.9$). In this region, discrepancies of less than 2 mrad are observed. When Z data collected in 1999 is used to cross check this parameterisation, no significant difference is observed. A study which incorporates the neutral hadron component of the jets yields similar results. The function derived from the Z data taken in 1994 is used to estimate the systematic uncertainty in M_W and Γ_W due to jet angular biases.

The same three data samples, from 1994, 1998 and 1999, are used to measure the angular resolution of the jets. The resolution is found to be slightly worse in the data than in the Monte Carlo. The angles of the jets in a large sample of Monte Carlo events originating from the hadronically decaying W are smeared with a Gaussian to determine the effect on M_W and Γ_W . The additional smearing needed to simulate the data properly is found to be 3.5 mrad in θ_{jet} and $(2.6/\sin\theta_{jet})$ mrad in ϕ_{jet} , which is of the order of 10% of the jet resolution [106].

A sample of 50k $4f$ events (5.8k and 6.2k selected events) is used to determine the shift in M_W and Γ_W due to an angular bias and 86k $4f$ events are used to determine the uncertainty due to the angular resolution. The results are shown in table 6.4. The shifts are small compared to the total systematic uncertainty and all shifts are compatible with zero within two standard deviations. To be conservative, the uncertainty in the shift is used if it exceeds the size of the shift itself. This results in a total systematic uncertainty in the mass of ΔM_W= 4 MeV/c^2 in the $e\nu q\bar{q}$ and 9 MeV/c^2 in the $\mu\nu q\bar{q}$ channel respectively. For the width, $\Delta\Gamma_W$ equals 13 and 14 MeV/c^2 for the two channels separately.

Systematic change	ΔM_W(MeV/c^2) $e\nu q\bar{q}$	ΔM_W(MeV/c^2) $\mu\nu q\bar{q}$	$\Delta\Gamma_W$(MeV/c^2) $e\nu q\bar{q}$	$\Delta\Gamma_W$(MeV/c^2) $\mu\nu q\bar{q}$
Jet angular bias	2 ± 2	8 ± 4	6 ± 6	-8 ± 6
Jet angular smearing	-1 ± 4	5 ± 3	-4 ± 11	3 ± 11

Table 6.4: Systematic shifts in the mass and width as a result of a simulated bias or a simulated smearing of the jet angles. All numbers are the systematically shifted fit minus the original fit.

6.1.4 Jet energy

The energy of a jet in ALEPH is equal to the sum of the energies of all associated objects. To ensure a good agreement in the jet energy between data and Monte Carlo, Z data collected in 1998 is used to compare the measured and simulated energy of jets with E_{jet} = 45.6 GeV as a function of cosθ_{jet} [107]. The discrepancy between data and Monte Carlo is about 0.5% in the barrel but increases to 3.5% for $|\cos\theta| > 0.95$. This difference is applied as a correction to the Monte Carlo, and the uncertainty in this correction is used to evaluate the systematic error on the measurement due to a jet energy bias.

To determine the uncertainty in the jet energy resolution, the same data sample is used. The jet energy is mainly measured by the calorimeters, and the resolution is therefore proportional to $\sqrt{E}$. An additional angular dependent term, parameterised using $Z \to q\bar{q}$ events at the Z peak, is added to equation 3.17 to describe the worsening of the jet energy resolution at low angles [108]:

$$\sigma_E = (0.6\sqrt{E} + 0.6) \cdot (1 + \cos^2\theta_{jet}). \tag{6.6}$$

In the barrel region, data and Monte Carlo are in agreement to less than 2%. Near the beam pipe ($|\cos\theta_{jet}| > 0.95$) discrepancies around 10% are observed. To estimate the systematic uncertainty, the energy of the jets in a large Monte Carlo sample is smeared with a Gaussian with an RMS of $\sqrt{(1.02)^2 - 1} = 20\%$ of the resolution for jets with $|\cos\theta_{jet}| < 0.95$ and $\sqrt{(1.1)^2 - 1} = 46\%$ for jets with $|\cos\theta_{jet}| > 0.95$.

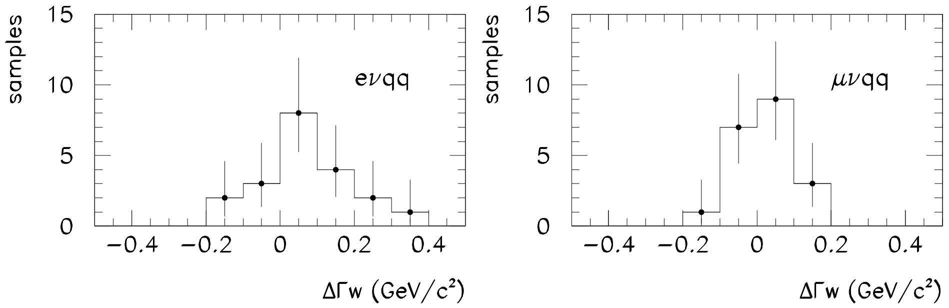

Figure 6.8: Shift in Γ_W as a result of a worsening of the resolution of the jet energy. The RMS of each of the distributions is calculated and scaled to the total number of events used in the fit to obtain the uncertainty in the systematic shift.

To determine the systematic shift in $\mathrm{M_W}$ and Γ_W due to a jet energy bias, 5.8k $e\nu q\bar{q}$ and 6.2k $\mu\nu q\bar{q}$ events are used. The shift due to the jet energy resolution has a larger RMS and to determine its mean, larger samples are needed (9.9k and 11k events).

The change in the jet energy resolution shifts Γ_W significantly. A worsening of the resolution causes the width to increase as expected. The uncertainty on the shift is derived from the RMS of 20 samples shown in figure 6.8. The results are shown in table 6.5. The total systematic uncertainty due to the jet energy measurement is $\Delta\mathrm{M_W}$= 19 MeV/c^2 in the $e\nu q\bar{q}$ channel and 8 MeV/c^2 in the $\mu\nu q\bar{q}$ channel. For the width, $\Delta\Gamma_\mathrm{W}$ equals 62 and 45 MeV/c^2 for the two channels respectively.

Systematic change	$\Delta\mathrm{M_W}$(MeV/c^2) $e\nu q\bar{q}$	$\Delta\mathrm{M_W}$(MeV/c^2) $\mu\nu q\bar{q}$	$\Delta\Gamma_\mathrm{W}$(MeV/c^2) $e\nu q\bar{q}$	$\Delta\Gamma_\mathrm{W}$(MeV/c^2) $\mu\nu q\bar{q}$
$\mathrm{E_{jet}}$ positive bias	5 ± 2	0 ± 3	7 ± 7	-1 ± 6
$\mathrm{E_{jet}}$ negative bias	1 ± 2	1 ± 1	1 ± 3	-2 ± 4
$\mathrm{E_{jet}}$ resolution	-18 ± 7	-7 ± 6	62 ± 22	45 ± 14

Table 6.5: Systematic shifts in the mass and width as a result of a bias or Gaussian smearing of the jet energies. All numbers are a fit to the shifted or smeared sample minus the original fit.

6.1.5 Calorimeter simulation

Discrepancies in the jet energies are corrected for as mentioned above, but these corrections are valid for the 1998 Z data only. Time fluctuations when running at higher energies are not taken into account. These fluctuations were evaluated on 1998 data and found to be at the level of 0.4% and 1.3% for ECAL and HCAL respectively [109]. To determine the uncertainty due to these fluctuations, the energy depositions in the calorimeters are rescaled by these amounts.

This rescaling affects all calorimeter objects in the event and the RMS of the shift is large. To reduce the uncertainty in the mean of the shift, samples of 11k $e\nu q\bar{q}$ events and 12k $\mu\nu q\bar{q}$ events are used. The uncertainty in the shift is derived from a total of 27 and 32 samples of each 350 selected events in the two channels respectively, as illustrated in figure 6.9. The results are shown in table 6.6.

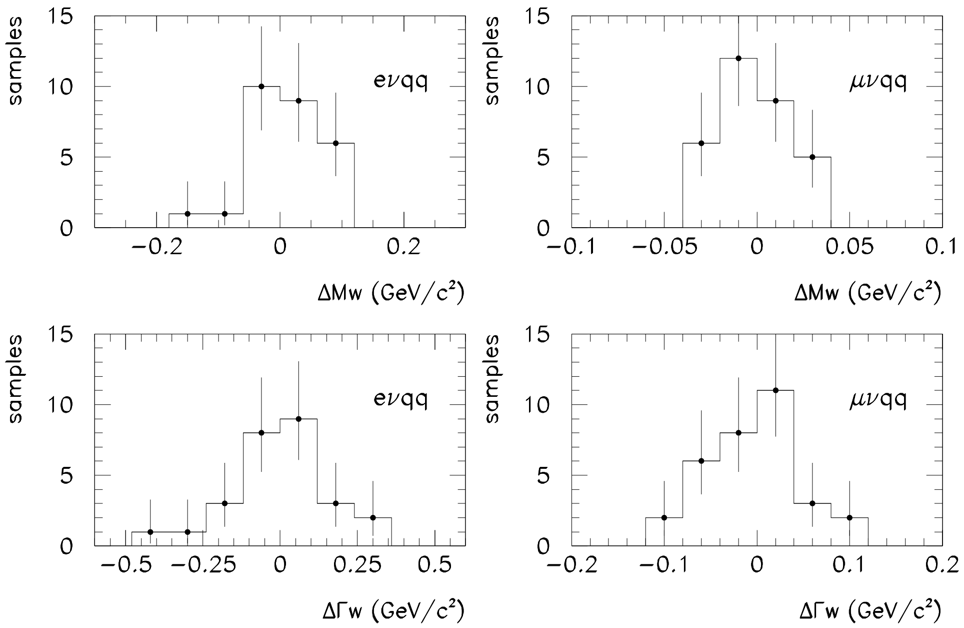

Figure 6.9: Shift in M_W and Γ_W as a result of calorimeter rescaling. The RMS of each of the distributions is calculated and scaled to the total number of events used in the fit to obtain the uncertainty in the systematic shift. Note that the scale of the shift is a factor 3 larger for the $e\nu q\bar{q}$ samples than for the $\mu\nu q\bar{q}$ samples. This directly affects the uncertainty in the shift quoted in table 6.6.

Discrepancies between data and Monte Carlo in the energy of Bremsstrahlung and FSR photons are not corrected for. These photons are ECAL objects and the uncertainty in their energy is evaluated by rescaling the ECAL energy with its full uncertainty of $\pm 0.7\%$ (0.4% absolute calibration, 0.6% intermodule and time variation). Samples of 4.2k and 4.3k selected events were used to determine the uncertainty and the results are shown in table 6.6. For the W mass, the systematic uncertainty due to uncertainties in the calorimeter calibration is estimated to be

ΔM_W= 31 MeV/c^2 and 14 MeV/c^2 for the $e\nu q\bar{q}$ and $\mu\nu q\bar{q}$ channels respectively. For the width, $\Delta\Gamma_W$ equals 52 and 16 MeV/c^2 for the two channels respectively.

Systematic change	ΔM_W(MeV/c^2) $e\nu q\bar{q}$	ΔM_W(MeV/c^2) $\mu\nu q\bar{q}$	$\Delta\Gamma_W$(MeV/c^2) $e\nu q\bar{q}$	$\Delta\Gamma_W$(MeV/c^2) $\mu\nu q\bar{q}$
Time variations	7 ± 10	-2 ± 3	13 ± 27	-4 ± 9
Positive ECAL bias	16 ± 5	-3 ± 5	-25 ± 16	3 ± 13
Negative ECAL bias	-29 ± 8	-14 ± 5	44 ± 20	10 ± 6

Table 6.6: Systematic shifts in the mass and width as a result of uncertainties in the calorimeter calibrations. All numbers are the systematically shifted fit minus the original fit.

6.2 Background uncertainties

To determine the uncertainty due to the normalisation of the background, the discrepancy between data and Monte Carlo in the background region in figure 4.8 is used. In the region below a signal probability of 5%, only 4 $e\nu q\bar{q}$ events and less than 1 $\mu\nu q\bar{q}$ event is expected. Additionally, 112 background events are expected in the $e\nu q\bar{q}$ channel and 48 in the $\mu\nu q\bar{q}$ channel, predominantly originating from hadronically decaying neutral current events ($e^+e^-\rightarrow q\bar{q}(\gamma)$). In the data taken at E_{cms}= 188.6 GeV, 151 events are selected in the $e\nu q\bar{q}$ channel and 65 in the $\mu\nu q\bar{q}$ channel. This corresponds to a discrepancy between data and Monte Carlo of 29% in the $e\nu q\bar{q}$ channel and 34% in the $\mu\nu q\bar{q}$ channel.

After the probability cut, no significant discrepancies between data and Monte Carlo are observed. For the evaluation of the uncertainty however, the assumption is made that the background is underestimated by up to 35%. The background is increased by 35% during the fit, and the mean shift of a large number of subsamples each containing 350 selected events is added to the systematic uncertainty.

This shift is expected to be less in the $\mu\nu q\bar{q}$ channel than in the $e\nu q\bar{q}$ channel, because of the higher $\mu\nu q\bar{q}$ selection purity. The background distribution is broader than the signal, therefore the fitted width is expected to decrease if the background is enhanced during the fit. These expected trends are observed and the mass goes up if the background is increased as is illustrated for the $e\nu q\bar{q}$ channel in figure 6.10.

The uncertainty in the shifts is less than 1 MeV/c^2 due to the small RMS of the shift and the large number of samples. The results are $\Delta M_W = 7$ MeV/c^2 in the $e\nu q\bar{q}$ and 2 MeV/c^2 in the $\mu\nu q\bar{q}$ channel and $\Delta\Gamma_W = 41$ and 15 MeV/c^2 respectively.

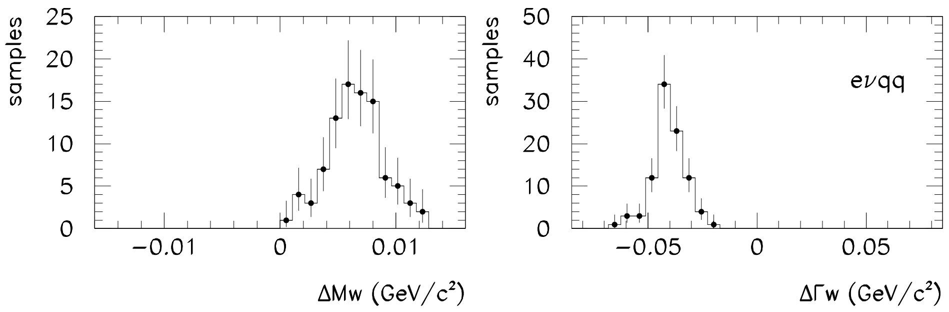

Figure 6.10: Shift in M_W and Γ_W as a result of a 35% enhancement of the background during the fit, for events selected in the $e\nu q\bar{q}$ channel.

6.3 Beam energy uncertainties

At LEP1, a method based on *resonant depolarisation* [110] was used to determine the LEP energy with a precision better than 1 MeV. The transverse polarisation of the LEP beam [111] can be destroyed by an oscillating magnetic field if the oscillation frequency equals the spin precession frequency, or spin tune ν_s, related to the beam energy E_b as:

$$\nu_s = \frac{g_e - 2}{2}\frac{E_b}{m_e}, \tag{6.7}$$

where m_e is the electron mass and $(g_e - 2)/2$ is the anomalous part of its giromagnetic ratio, originating from renormalisation (see section 2.1.6). This transverse polarisation is measured from the angular distribution of polarised laser light after Compton-scattering and E_b is derived from a measurement of ν_s at energies up to $E_{cms} = 61$ GeV . The method breaks down at higher beam energies, because depolarisation effects increase rapidly with energy.

Relation 6.7 holds for ideal storage rings and is corrected for small imperfections. The beam energy is proportional to the integrated magnetic field around the beam trajectory l:

$$E_b = \frac{e}{2\pi c}\oint_{\mathrm{LEP}} B \cdot dl. \tag{6.8}$$

The energy of the LEP2 beams is measured mainly from the magnetic field in the dipoles around the ring. A total of 16 nuclear magnetic resonance (NMR) probes are used to sample the magnetic field in some of the bend dipoles [112]. This method is used above centre-of-mass energies of 41 GeV. Since the probes only sample some of the LEP magnets, a calibration is needed. The relation between the measured field and the beam energy is assumed to be linear and in the region between 41 and 61 GeV resonant depolarisation is used to calibrate the NMR measurement and confirm the linear dependence between the NMR field and the beam energy. Various methods are used to cross check the absolute calibration and the linear dependence.

A flux loop is installed in all dipole magnets around the ring. When there is no beam in LEP this loop is used to measure 96.5% of the field integral [112]. The NMR probes are read out simultaneously. Again, the linear dependence between the NMR field and the beam energy is confirmed.

The beam energy is not constant over the ring, but is reduced due to synchrotron radiation in the arcs and increased in the RF accelerating sections. The actual beam energy therefore depends on the position of the experiment in the ring and is calculated separately at each interaction point. For example, at $\mathrm{E_{cms}}$ = 182.7 GeV, the ALEPH centre-of-mass energy was on average 11 MeV below the mean LEP energy, with a difference between the e^+ and the e^- beam of less than 100 MeV [112]. Small effects due to temperature variations or the passage of electric trains (e.g. TGV) nearby can cause leakage currents in the dipoles. Movements of the ring due to earth tides or other geological forces can cause the beam to be slightly out of central orbit. When this happens, the quadrupoles add to the field integral as well. These effects are all taken into account in the beam energy measurement.

The main uncertainty originates from the linear extrapolation of the relation between the NMR field and the beam energy. The difference between the NMR and the spin tune measurement is extrapolated, resulting in an uncertainty of $\Delta\mathrm{E_b}$ = 15 MeV at $\mathrm{E_{cms}}$= 188.6 GeV. The total uncertainty is estimated to be 20 MeVat 188.6 GeV [113] and 21 MeV at energies up to 201.6 GeV [114].

This uncertainty enters in the measurement because of the use of a kinematic fit in which the total energy of an event is forced to be equal to the measured centre-of-mass energy (see section 4.2). If the events were all isotropic, one could use the equation [115]:

$$\frac{\Delta \mathrm{M_W}}{\mathrm{M_W}} = \frac{\Delta \mathrm{E}}{\mathrm{E}}, \tag{6.9}$$

where E is the energy of the beam, to determine the uncertainty in $\mathrm{M_W}$. This results in $\Delta \mathrm{M_W} = 17$ MeV$/c^2$ for a centre-of-mass energy of 188.6 GeV. To cross check this evaluation and to determine the uncertainty in Γ_W, the beam energies in a large sample of Monte Carlo events is shifted by ± 20 MeV and the systematic shift is determined directly. A comparison of event-by-event mass shifts for various centre-of-mass energies is shown in figure 6.11 and agrees with this estimate within 1.5 MeV$/c^2$.

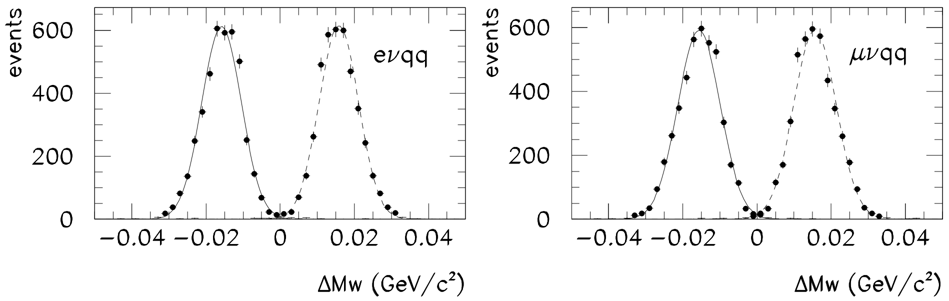

Figure 6.11: Shift in the event-by-event mass of common events if the beam energy is shifted up or down by 20 MeV. A Gaussian is fitted to each of the distributions but does not fit the peak region well. The mean shift is found to be less than 16 MeV$/c^2$ for all fits. The correlation between the shifted mass and the original mass of the event is found to be more than 99.5% for each of the four samples.

The spread in the beam energy $\sigma_{\mathrm{E_b}}$ can be derived from the measured longitudinal bunch size σ_z [116]:

$$\sigma_{\mathrm{E_b}} = \frac{\sqrt{2}\ \mathrm{E_b}\ Q_s}{\alpha\ R_{\mathrm{LEP}}}\ \sigma_z, \tag{6.10}$$

where R_{LEP} is the average LEP radius, and α and Q_s are related to the optics and the RF frequency. The assumption is made that the energy dispersion of both beams is identical and therefore [116]:

$$\sigma_{\mathrm{E_{cms}}} \approx \sqrt{2}\ \sigma_{\mathrm{E_b}}. \tag{6.11}$$

The total spread in the event-by-event centre-of-mass energy is estimated to be 237 MeV at $\mathrm{E_{cms}}$= 188.6 GeV and ranges from 254 to 265 MeV at higher centre-of-mass energies [114]. The uncertainty in this spread is of the order of 5%. This spread is used to determine the systematic shift. E_{cms} is measured by the NMR method every 15 minutes during data taking and the resolution on an individual NMR measurement is only 1-2 MeV and therefore negligible with respect to the event-by-event spread [117].

A spread in the beam energy will add in quadrature to the width of the mass distribution and therefore to the measured width of the W. For example, an additional spread of 168 MeV in the beam energy (237 MeV in the centre-of-mass energy) will only shift Γ_W by 7 MeV/c^2 if Γ_W= 2.09 GeV/c^2. Two samples are analysed, one with an additional smearing of 20 MeV and one with an additional smearing of 200 MeV. The two smeared samples are used to cross check the above argument. In one individual event both beams are shifted by the same amount. Effects due to a boost of the centre-of-mass frame are not included. The results are shown in table 6.7.

All studies are performed with a sample of 36k $4f$ events, resulting in 4.2k selected $e\nu q\bar{q}$ and 4.3k selected $\mu\nu q\bar{q}$ events in common with the original sample. A mean decrease of the width due to an additional smearing of the beam energy is caused by a statistical fluctuation. Assuming that the uncertainty in each of the shifts is equal, the mean shift on the mass due to a bias in the beam energy is 19 ± 3 MeV/c^2 for $e\nu q\bar{q}$ channel and 14 ± 3 MeV/c^2 for the $\mu\nu q\bar{q}$ channel, both compatible with 17 MeV/c^2 derived from equation 6.9. This value is therefore used.

Systematic change	ΔM_W(MeV/c^2) $e\nu q\bar{q}$	ΔM_W(MeV/c^2) $\mu\nu q\bar{q}$	$\Delta\Gamma_W$(MeV/c^2) $e\nu q\bar{q}$	$\Delta\Gamma_W$(MeV/c^2) $\mu\nu q\bar{q}$
E_b positive bias	15 ± 4	17 ± 6	2 ± 6	14 ± 10
E_b negative bias	-23 ± 3	-10 ± 3	-13 ± 8	-6 ± 8
E_b smearing 20 MeV	-9 ± 4	-1 ± 3	-12 ± 6	8 ± 11
E_b smearing 200 MeV	-6 ± 11	-18 ± 9	-4 ± 15	11 ± 12

Table 6.7: Systematic shifts in the mass and width as a result of uncertainties in the energy of the LEP beams. All numbers are the systematically shifted or smeared fit minus the original fit.

The uncertainty on M_W due to an additional smearing is taken from table 6.7. The value for a smearing of 200 MeV is used because the beam energy smearing varies from 168 MeV at E_{cms}= 188.6 GeV to 180-187 MeV at higher centre-of-mass energies. This results in a total uncertainty ΔM_W of 20 MeV/c^2 in the $e\nu q\bar{q}$ channel, and 25 MeV/c^2 in the $\mu\nu q\bar{q}$ channel.

No large shift in Γ_W is observed due to an additional smearing even if a spread of 200 MeV is added. The above argument is therefore assumed to be valid and 7 MeV/c^2 is taken into account in both channels at E_{cms}= 188.6 GeV, resulting in a total uncertainty due to the beam energy measurement of $\Delta\Gamma_W$= 15 MeV/c^2 in the $e\nu q\bar{q}$ channel and 16 MeV/c^2 in the $\mu\nu q\bar{q}$ channel. At higher energies, 8 MeV/c^2 is used as an estimate for the systematic uncertainty due to beam energy smearing.

6.4 Theoretical problems

The simulation of the mass distribution as a function of M_W and Γ_W is based on a theoretical model that is not perfect and also not the only possible one. Uncertainties in the choice of the model and limitations of the calculation itself affect the measurement. The resulting systematic shifts in M_W and Γ_W are described in this section. The methods used to determine the uncertainties are described first and the shifts are summarised at the end of the section in table 6.8.

6.4.1 Fragmentation uncertainties

The hadronically decaying W produces two quarks. The direction of the quarks is defined by the kinematics of the event ranging from back-to-back at the W pair threshold to smaller angles (of the order of 2.2 rad at E_{cms}= 188.6 GeV) if the W is boosted. Due to the confinement of the strong interaction, the quarks are not observed separately but as the origin of two jets of particles. Since the jet fragmentation process is governed mainly by the strong interaction it cannot be calculated analytically. Different fragmentation algorithms are known that approximate a full calculation to predict the particle and energy densities in the final state. The JETSET [77] and HERWIG [78] models have had their model parameters tuned, using event-shape variables and charged particle inclusive distributions, to best fit the ALEPH LEP1 data [118]. Depending on which distribution is under study, one model can give a better distribution than the other. The difference between these two models in W pair simulations is used to evaluate the uncertainty due to fragmentation.

Other studies are ongoing to find which observables in the WW Monte Carlo show differences between the two fragmentation models [119] and to find how to propagate these differences to a shift on the W mass and width [120]. The goal of such study is to be able to evaluate a difference, in terms of a W mass and width shift, between only one model (JETSET) and the data. The method can be tested by replacing the data with the second model (HERWIG). Attempts in this direction [121] have so far resulted in smaller parameter shifts than for the direct comparison of the fit results between the two fragmentation models. Until this is fully understood, the conservative approach of the direct comparison is preferred.

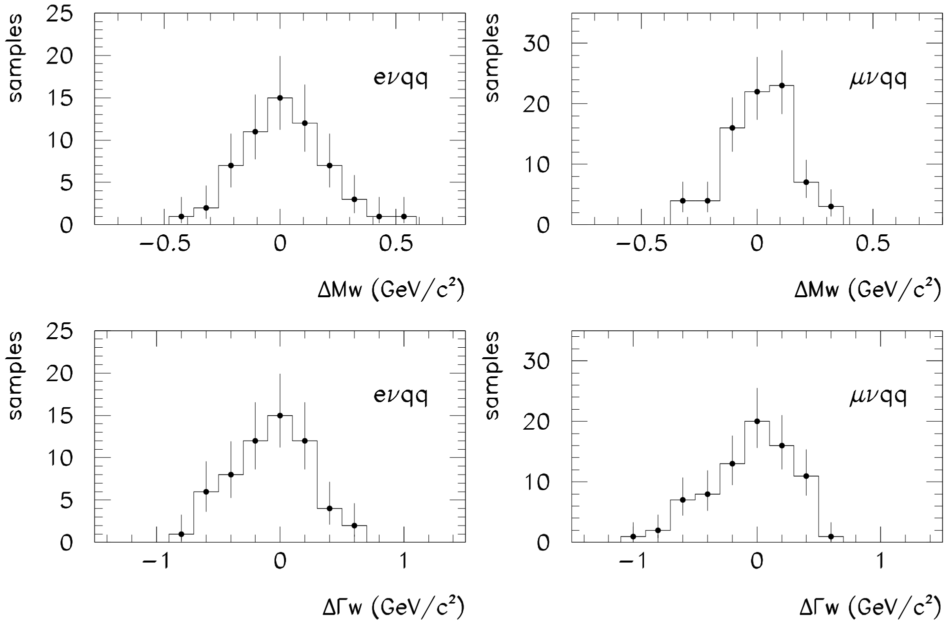

Figure 6.12: Shift in M_W and Γ_W as a result of a change in the fragmentation model (HERWIG-JETSET). The total number of events used to determine the mean is approximately twice larger, the samples are used to determine the uncertainty in the systematic shift.

Since the spread of the mass and width shifts between the two models is large, a sample of 382k $4f$ events is used to determine the mean. Each event with an identical primary $4f$ topology [122] is fragmented with both the JETSET and the HERWIG algorithms. The common events in 8 samples of equal size are fitted to the standard reference. The difference in the error-weighted mean of these 8 samples is used as an estimate for the systematic uncertainty in the measurement. A total of 60 $e\nu q\bar{q}$ and 79 $\mu\nu q\bar{q}$ samples of 350 events each are used to determine the RMS of the shift, as shown in figure 6.12. This RMS, scaled to the number of selected events, is used to determine the uncertainty in the mean. The results for the $e\nu q\bar{q}$ and $\mu\nu q\bar{q}$ channels respectively are 51 and 20 MeV/c^2 for the mass and 62 and 48 MeV/c^2 for the width, see table 6.8.

Recent ALEPH studies have shown that the HERWIG jets are thinner than the JETSET jets in both the hadronic [123] and the semi-leptonic [119] decay channels. However, it is known from studies at the Z that the relative broadness is opposite for JETSET and HERWIG, so this has been investigated further in ALEPH. The origin of the problem has been identified [124]. In the HERWIG program, the hard matrix element correction to the first gluon or photon emission is restricted to the process $e^+e^- \rightarrow Z/\gamma \rightarrow q\bar{q}$ and deep inelastic lepton-nucleon scattering, but is *not* executed for W pair events, as it should have been. A future comparison of JETSET and HERWIG cannot be made until a solution from the HERWIG authors has been provided.

6.4.2 Initial state radiation

The beam leptons can radiate a photon before colliding. This process is known as initial state radiation and can affect the measurement. Most likely the photon will not be detected but disappear into the beam pipe. When this happens the actual collision energy is less than the LEP centre-of-mass energy. If the photon is detected, it will interfere with the final state topology as it will either be added to one of the jets, or to the lepton as final state radiation or even Bremsstrahlung. If initial state radiation were described perfectly in the Monte Carlo simulation, the fit method would automatically correct for any misidentification. Differences between the data and the Monte Carlo can however affect the measurement.

In the reference Monte Carlo, the initial state radiation is simulated up to order α^2 [76]. To determine the effect of the higher order diagrams, the assumption is made that the series converges, i.e. the difference between a first and second order calculation is larger than between the second order and the full calculation. This first difference is evaluated and taken into account as a systematic uncertainty.

A large sample of Monte Carlo events is used. A Standard Model calculation is performed to evaluate for each simulated event the weight that translates the $\mathcal{O}(\alpha^2)$ Monte Carlo distribution of the W mass estimator to a $\mathcal{O}(\alpha)$ distribution. During the fit, the likelihood is corrected by weighting the logarithm of the probability for each event accordingly. A sample of 100k generated $4f$ events (12k and 13k selected $e\nu q\bar{q}$ and $\mu\nu q\bar{q}$ events respectively) is used to determine the shift on M_W and Γ_W . The shifts are small in comparison to other sources of systematic uncertainties. The mass changes by less than 1 MeV/c^2 in both channels. The width changes by 2 MeV/c^2.

6.4.3 Finite Monte Carlo reference statistics

The finite statistics of the reference sample results in a systematic uncertainty in M_W and Γ_W . The uncertainty in the mass $(\Delta M_W)_{tot}$ can be evaluated as follows. Each bin i in the mass distribution reduces the uncertainty according to:

$$\frac{1}{(\Delta M_W)^2_{tot}} = \left(\sum_{i=1}^{N}(\Delta M_W)_i^2\right)^{-1} . \tag{6.12}$$

Define the cross section in bin i as $\sigma_i = N_i/\mathcal{L}$, where N_i is the number of selected events and $\mathcal{L}$ is the luminosity. Since the cross section and its derivative are finite, it can be shown that:

$$(\Delta M_W)_i \simeq \Delta\sigma_i \left(\frac{\partial\sigma_i}{\partial M_W}\right)^{-1} . \tag{6.13}$$

Define the density of bin i as $\rho_i = \sigma_i/\sigma_{tot}$. The change of the density if the mass is reweighted away from the reference is then given by:

$$\frac{\partial\rho_i}{\partial M_W} = \frac{1}{\sigma_{tot}}\frac{\partial\sigma_i}{\partial M_W} = \frac{\mathcal{L}}{N_{tot}}\frac{\partial\sigma_i}{\partial M_W} \tag{6.14}$$

and therefore, if the uncertainty in σ_i is assumed to be Poisson-like ($\Delta\sigma_i = \sqrt{N_i}/\mathcal{L}$):

$$(\Delta M_W)_i \simeq \frac{\sqrt{N_i}}{N_{tot}}\left(\frac{\partial\rho_i}{\partial M_W}\right)^{-1} . \tag{6.15}$$

Similarly, for the width follows:

$$(\Delta\Gamma_W)_i \simeq \frac{\sqrt{N_i}}{N_{tot}}\left(\frac{\partial\rho_i}{\partial\Gamma_W}\right)^{-1} . \tag{6.16}$$

These relations are used to determine the uncertainty due to finite Monte Carlo statistics in both M_W and Γ_W. The reference Monte Carlo sample is reweighted 50 MeV/c^2 away from the reference mass and width independently to approximate $\partial\rho_i/\partial M_W$ and $\partial\rho_i/\partial\Gamma_W$ respectively.

If the data fit value is far away from the reference value, the effective number of reference events decreases according to [125]:

$$N_{\text{eff}} = \frac{(\sum w_i)^2}{\sum w_i^2}, \tag{6.17}$$

where i runs over all selected events in the Monte Carlo reference and w_i is the weight of a reference event when it is reweighted to the data fit value of M_W and Γ_W. This difference between the selected and the effective number of events increases this evalaution of the systematic uncertainty and is taken into account.

The final systematic uncertainty depends on the size of the reference sample at each energy and the data fit value of the sample. At E_{cms}= 188.6 GeV the reference consists of over one million generated $4f$ events, while the reference at higher energies consists of only 200k events per energy point. At the higher energies, the $e\nu q\bar{q}$ and $\mu\nu q\bar{q}$ channels are combined as will be discussed in chapter 7. If the data fit values for M_W and Γ_W are assumed to be equal to the reference values, the uncertainty increases with increasing centre-of-mass energy. This is expected because the selection is not optimised for energies above 188.6 GeV. For energies between 191.6 and 201.6 GeV and a reference sample of 200k events, the uncertainty in the mass increases from 14.3 to 15.6 MeV/c^2 and the uncertainty in the width from 34.7 to 39.4 MeV/c^2.

When the data fit values in chapter 7 are used, the results vary between 16 and 20 MeV/c^2 for the mass, and 38 and 51 MeV/c^2 for the width. At E_{cms} = 188.6 GeV the uncertainties are ΔM_W = 9 MeV/c^2 in the $e\nu q\bar{q}$ channel and 8 MeV/c^2 in the $\mu\nu q\bar{q}$ channel and $\Delta\Gamma_W$ equals 21 and 20 MeV/c^2 for each channel respectively.

Equations 6.15 and 6.16 are also equal to the statistical uncertainty on the data fit for a data sample containing N_{tot} events, if N_{tot} is large. The uncertainty on the data fit is Gaussian as shown in the sub-sample studies in section 5.3 and equations 6.15 and 6.16 can be used to estimate the expected statistical uncertainty of the data fit by multiplying the expressions by a scale factor $\sqrt{\mathrm{N_{tot}/N_d}}$:

$$
\begin{aligned}
(\Delta \mathrm{M_W})_i &\simeq \frac{\sqrt{\mathrm{N}_i}}{\sqrt{\mathrm{N_{tot} N_d}}} \left(\frac{\partial \rho_i}{\partial \mathrm{M_W}} \right)^{-1} \\
(\Delta \Gamma_\mathrm{W})_i &\simeq \frac{\sqrt{\mathrm{N}_i}}{\sqrt{\mathrm{N_{tot} N_d}}} \left(\frac{\partial \rho_i}{\partial \Gamma_\mathrm{W}} \right)^{-1} .
\end{aligned}
\tag{6.18}
$$

The background is included in this calculation. The expected statistical uncertainties are found to be in agreement with the mean of the upper and lower statistical uncertainties from the sub-sample studies at $\mathrm{E_{cms}}$= 188.6 GeV described in section 5.3.

Systematic change	$\Delta\mathrm{M_W}(\mathrm{MeV}/c^2)$ $e\nu\mathrm{q\bar{q}}$	$\Delta\mathrm{M_W}(\mathrm{MeV}/c^2)$ $\mu\nu\mathrm{q\bar{q}}$	$\Delta\Gamma_\mathrm{W}(\mathrm{MeV}/c^2)$ $e\nu\mathrm{q\bar{q}}$	$\Delta\Gamma_\mathrm{W}(\mathrm{MeV}/c^2)$ $\mu\nu\mathrm{q\bar{q}}$
Fragmentation	51 ± 17	20 ± 13	-62 ± 30	-48 ± 30
ISR	<1	<1	2	2
Finite ref 188.6	9	8	21	20
Finite ref 191.6	16		38	
Finite ref 195.5	16		40	
Finite ref 199.5	16		38	
Finite ref 201.6	20		51	

Table 6.8: Systematic shifts in the mass and width as a result of theoretical uncertainties. The uncertainty due to finite reference statistics is evaluated at each centre-of-mass energy separately. At the four higher energies, the $e\nu\mathrm{q\bar{q}}$ and $\mu\nu\mathrm{q\bar{q}}$ channels are combined, as will be described in chapter 7.

	$\Delta M_W (MeV/c^2)$		$\Delta \Gamma_W (MeV/c^2)$	
Source	$e\nu q\bar{q}$	$\mu\nu q\bar{q}$	$e\nu q\bar{q}$	$\mu\nu q\bar{q}$
Detector	**39**	**25**	**97**	**78**
Lepton angles	**12**	**14**	**17**	**19**
Bias θ_l	7 ± 3	7 ± 4	2 ± 8	10 ± 9
Resolution θ_l	6 ± 4	5 ± 2	3 ± 8	4 ± 9
Bias ϕ_l	4 ± 4	10 ± 4	10 ± 10	4 ± 11
Resolution ϕ_l	7 ± 4	4 ± 4	8 ± 6	4 ± 7
Lepton momentum	**10**	**10**	**49**	**57**
Bias	1 ± 8	7 ± 6	11 ± 15	10 ± 10
Resolution	5 ± 6	7 ± 7	47 ± 11	56 ± 19
Jet angles	**4**	**9**	**13**	**14**
Bias	2 ± 2	8 ± 4	6 ± 6	8 ± 6
Resolution	1 ± 4	5 ± 3	4 ± 11	3 ± 11
Jet energies	**19**	**8**	**62**	**45**
Bias	5 ± 2	0 ± 3	7 ± 7	1 ± 6
Resolution	18 ± 7	7 ± 6	62 ± 22	45 ± 14
Calorimeters	**31**	**14**	**52**	**16**
ECAL bias	29 ± 8	14 ± 5	44 ± 20	3 ± 13
Time variations	7 ± 10	2 ± 3	13 ± 27	4 ± 9
Background	**7**	**2**	**41**	**15**
Beam energy	**20**	**25**	**14**	**15**
Bias	17	17	13 ± 8	14 ± 10
Spread	6 ± 11	18 ± 9	7	7
Theory	**52**	**22**	**65**	**52**
Fragmentation	51 ± 17	20 ± 13	62 ± 30	48 ± 30
ISR	<1	<1	2	2
Finite ref 188.6	9	8	21	20
Total	**69**	**41**	**125**	**96**

Table 6.9: Summary of all systematic uncertainties. For each study, the largest values are shown and added in quadrature to obtain the total systematic error at E_{cms}= 188.6 GeV. For the other centre-of-mass energies, the same table is used except for the systematic due to finite Monte Carlo reference and the beam energy spread. These uncertainties are evaluated for each centre-of-mass energy separately, taking the into account the actual data fit value in case of the finite statistics systematic described in the previous section.

Chapter 7

Results from the data

In the previous chapters the method to extract the mass and width, and the expected uncertainties are described. In this chapter the actual result of the fits are quoted for the various energies as well as the measured statistical uncertainties.

In section 7.1 the data samples that are analysed are described. Comparisons between these samples and Monte Carlo predictions for some of the variables used in the analysis are shown in section 7.2. The results from the fit to Monte Carlo reference distributions at the different centre-of-mass energies are listed in section 7.3. Many checks are done to ensure the stability of the fit result as a function of cuts in the selection. In section 7.4 the results of these checks are shown.

7.1 The data samples

In 1998, at E_{cms}= 188.6 GeV, ALEPH recorded a data sample with an integrated luminosity of 174.2 pb^{-1} that is used for the W analysis. A preliminary analysis of data taken at energies between 191.6 and 201.6 GeV in 1999 is described as well. The sizes of these samples are shown in table 7.1. The mean beam energy is measured for each nominal energy point by the LEP energy group.

Monte Carlo studies at E_{cms}= 188.6 GeV show that 398 $e\nu q\bar{q}$ and 382 $\mu\nu q\bar{q}$ candidates are expected to pass the selection before any constraints on the W mass are imposed. A total of 396 $e\nu q\bar{q}$ and 367 $\mu\nu q\bar{q}$ candidates are selected from the data sample, in agreement with the expected number of events within less than one

		$e\nu q\bar{q}$		$\mu\nu q\bar{q}$	
E_{cms}	$\mathcal{L}$ (pb^{-1})	N_d	N_{exp}	N_d	N_{exp}
188.6	174.2	330	351	360	366
191.6	28.9	55	57	62	60
195.5	79.9	151	154	157	165
199.5	86.3	157	167	180	176
201.6	41.9	93	79	83	86
total	411.2	786	808	842	852

Table 7.1: Number of selected events, N_d, and number of expected events, N_{exp}, in both channels for each data sample and after all cuts. The total number of selected events is in good agreement with the expectation. A total of 1661 events are expected and 1628 events are observed in the data.

standard deviation. After the mass window cut ($70 < M_{2C} < 90$ GeV/c^2) the number of expected and selected events for each data sample is shown in table 7.1. The selection is optimised at E_{cms}= 188.6 GeV as described in chapter 4. As a result, the number of expected $(e/\mu)\nu q\bar{q}$ candidate events per 100 pb^{-1} decreases with increasing centre-of-mass energy from 411 to 393 due to a decrease in selection efficiency. In total, 1628 $(e/\mu)\nu q\bar{q}$ events are analysed, in agreement with the expected total number of events within one standard deviation.

7.2 Data distributions at different energies

Comparisons between data and Monte Carlo predictions for various variables are shown in chapter 4 where the selection of the $(e/\mu)\nu q\bar{q}$ candidates was introduced. In this section, distributions of the events that are used in the fit are described. All figures contain the number of events shown in table 7.1. The Monte Carlo prediction is normalised to the number of observed data events to be able to compare only the shape of the distribution. This is allowed if the assumption is made that the small differences between the numbers of observed and the numbers of expected events are due to statistical fluctuations.

In figure 7.1, the distribution of the momentum of the isolated lepton before the kinematic fit is shown at each energy and for both channels. Final state radiation and Bremsstrahlung have been added to the lepton track measured by the TPC. The lower boundary at $P_l = 22$ GeV/c is caused by a cut in the selection described

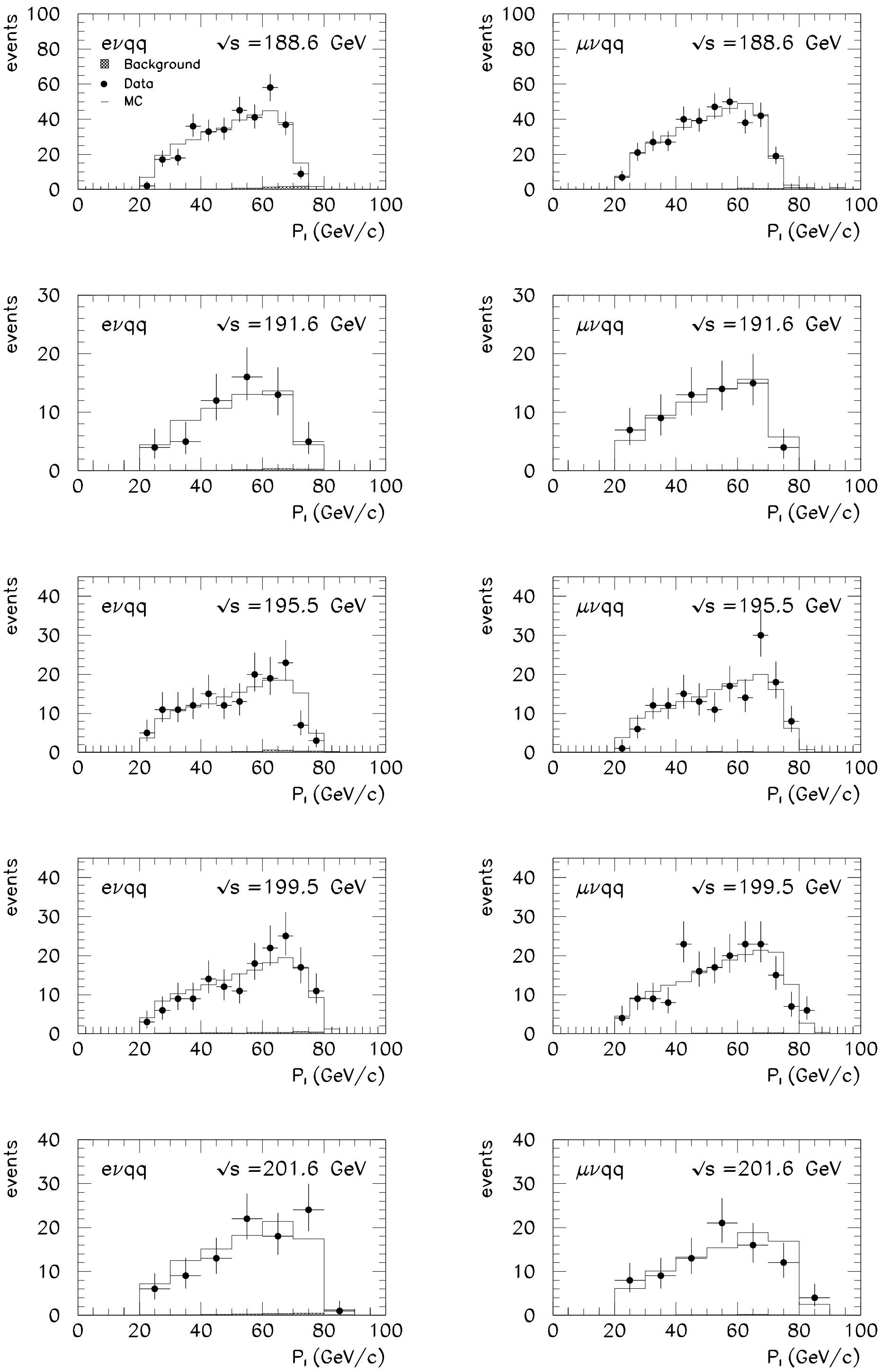

Figure 7.1: Distribution of the momentum of the lepton originating from the leptonically decayed W before the kinematic fit, for data and Monte Carlo. The bin size is 5 GeV/c for E_{cms}= 188.6, 195.5 and 199.5 GeV, and 10 GeV/c per bin for the smaller samples at E_{cms}= 191.6 and 201.6 GeV.

in section 4.1.6. The upper kinematic limit shifts upwards with increasing centre-of-mass energy. For each distribution a χ^2 estimator is calculated and the differences between data and Monte Carlo are in agreement with a statistical fluctuation (the mean value of χ^2/n is 1.1, the largest value is 1.9).

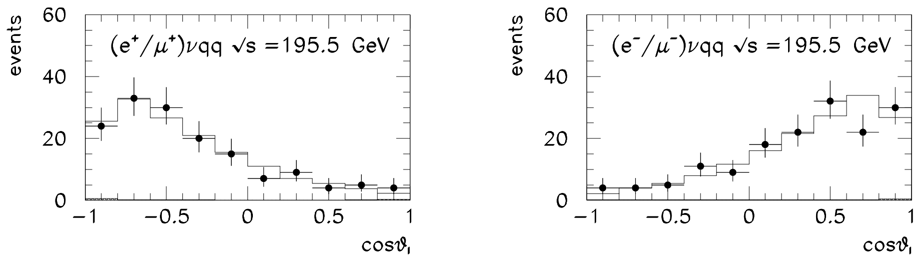

Figure 7.2: Distribution of the polar angle P_l of the positive and negative leptons as measured in the TPC at E_{cms}= 195.5 GeV, for data and Monte Carlo. No correction for Bremsstrahlung of FSR is applied.

The positively charged lepton originates from a leptonically decaying W^+ and the negative lepton from a W^-. Since the cross section depends on the scattering angle, the positive W is predominantly created in the direction of the e^+ beam. This is illustrated in figure 7.2 by the $\cos\theta_l$ distributions for positive and negative tracks at a centre-of-mass energy of E_{cms}= 195.5 GeV. The reduction in the number of events in the outer bins is due to a cut at $|\cos\theta_l| = 0.95$ that is introduced because the acceptance of the tracking detectors is limited by the beam pipe.

The 2C mass estimator M_{2C} from the kinematic fit is shown in figures 7.3 and 7.4. For the preliminary result at the four highest energies the $e\nu q\bar{q}$ and $\mu\nu q\bar{q}$ channels are combined to obtain sufficient statistics for a stable fit.

The kinematic limit of the 2C mass estimator is half the centre-of-mass energy and ranges from 94.3 to 100.8 GeV/c^2 for the energies in figures 7.3 and 7.4. The mass window cut is set to 90 GeV/c^2 at E_{cms}= 188.6 GeV and is not changed for the preliminary high energy results. Due to this shift of the kinematic limit, studies are done for an upper mass window cut of 94 GeV/c^2.

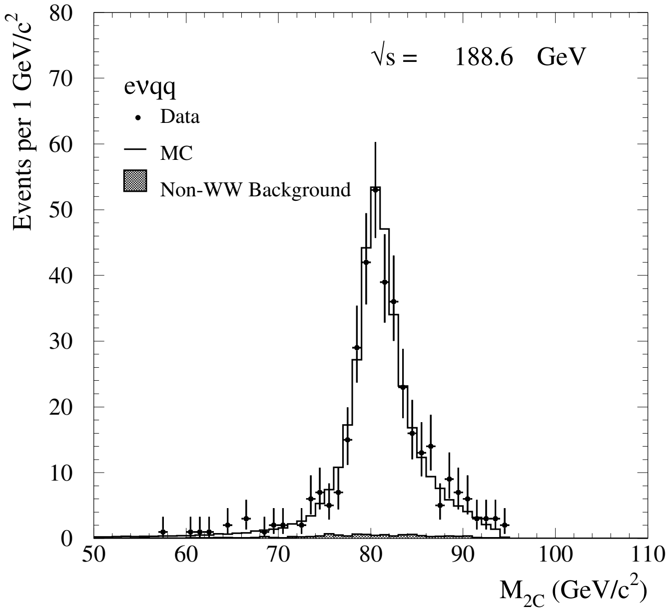

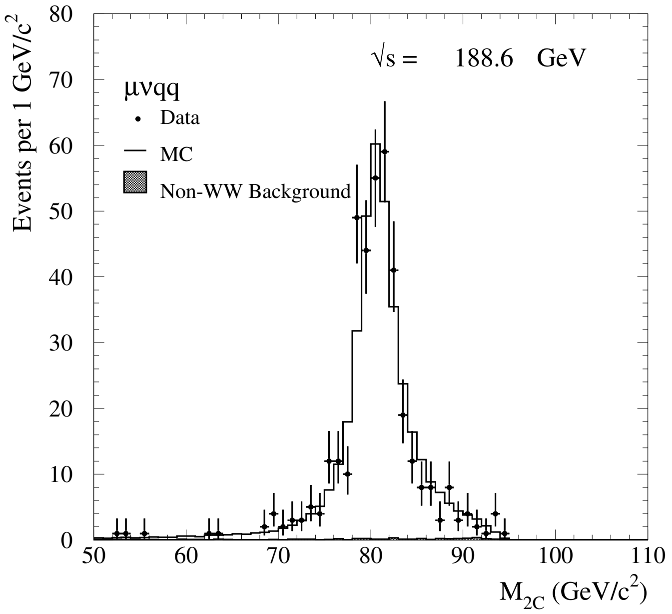

Figure 7.3: Distribution of the mass estimator from a 2C kinematic fit at E_{cms} = 188.6 GeV, for the $e\nu q\bar{q}$ and $\mu\nu q\bar{q}$ channels separately.

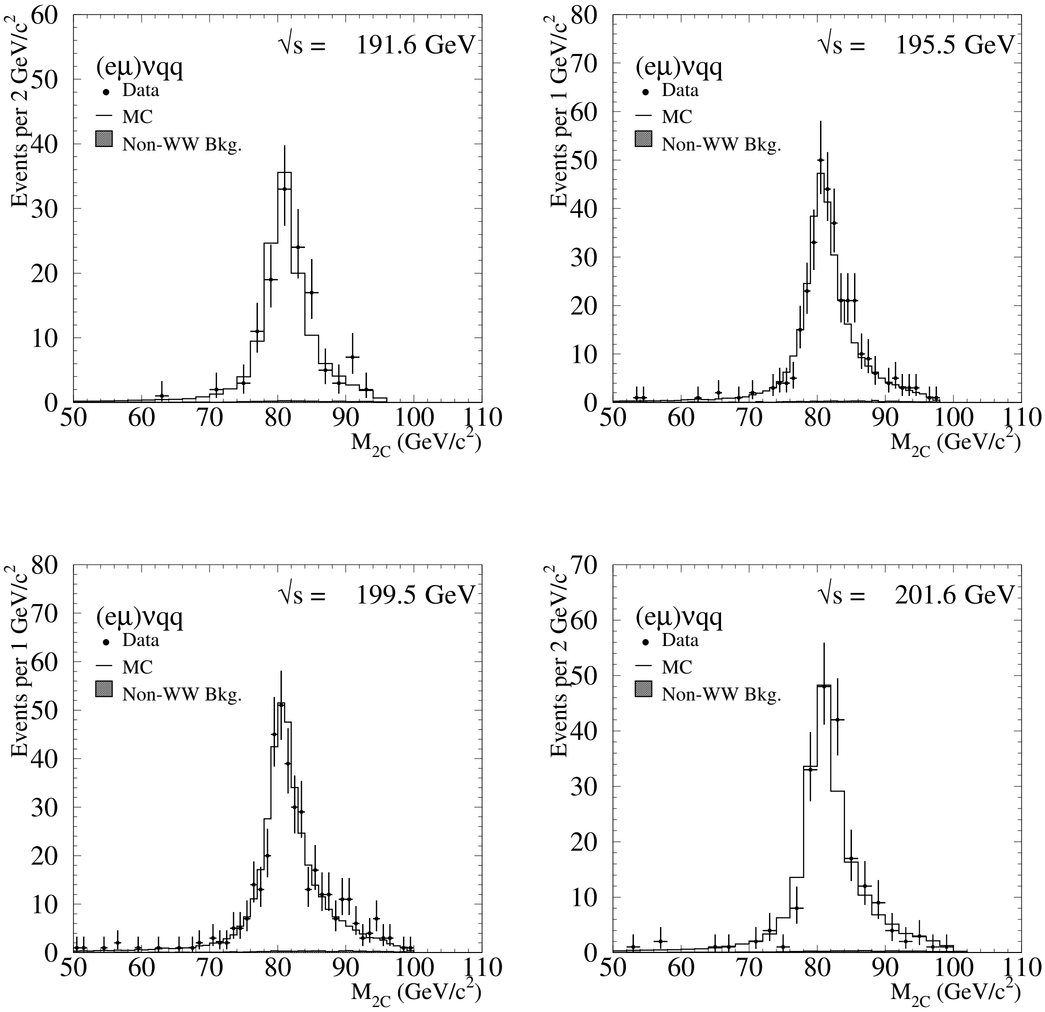

Figure 7.4: Distribution of the mass estimator from a 2C kinematic fit for E_{cms} between 191.6 and 201.6 GeV. For the preliminary results the $(e/\mu)\nu q\bar{q}$ channels are combined to increase the statistics of the samples.

7.3 Results from the fit

The data samples in table 7.1 are fitted to the Monte Carlo reference samples in table 4.5. No $\mathrm{W}e\nu$ events are generated at E_{cms}= 191.6 GeV and the sample at 195.5 GeV is used instead. The expected fraction of events in the mass distribution originating from $\mathrm{W}e\nu$ events is of the order of 0.3% corresponding to approximately 0.4 expected events at E_{cms}= 191.6 GeV.

The likelihood is a function of M_W and Γ_W and can therefore be illustrated by a 2-

dimensional surface. An example of this surface in case of a $4f$ sample at M_W= 80.10 GeV/c^2 is shown in figure 5.4. Since the correlation between M_W and Γ_W is small, the dependence of the likelihood on M_W and Γ_W can be shown as a cross section of this surface, starting at the minimum and parallel to the M_W and Γ_W axes respectively. These functions are shown in figure 7.5 for the data at E_{cms} = 188.6 GeV and figure 7.6 at higher energies. The dashed vertical lines show the upper and lower MINOS errors, corresponding to 1 unit in -2log$\mathcal{L}$.

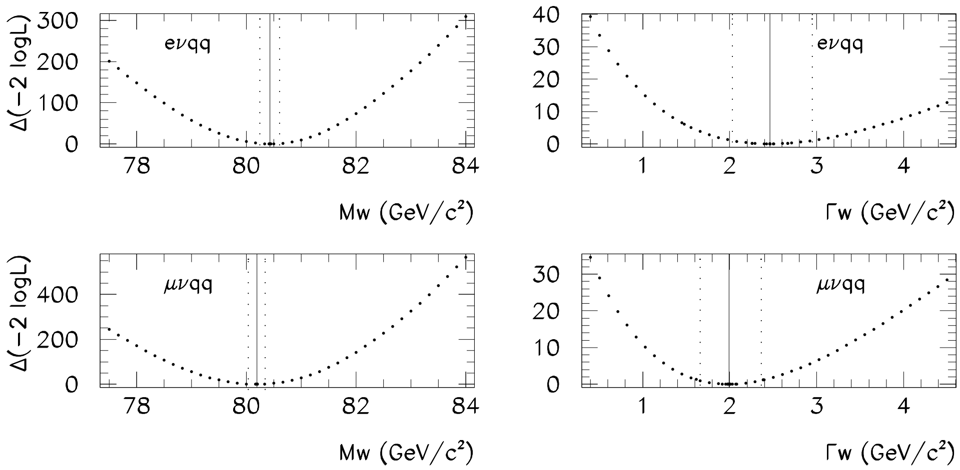

Figure 7.5: Variation of the likelihood at E_{cms}= 188.6 GeV as a function of M_W (for constant Γ_W) and as a function of Γ_W (for constant M_W) for the fits to the data samples. The statistical uncertainty of the fit is represented by the vertical dashed lines on both sides of the minimum and corresponds to 1 unit in -2log$\mathcal{L}$.

The results of the two-parameter fits are shown in table 7.2. In case of the width, the likelihood is not symmetrical around the minimum due to the asymptote at Γ_W = 0 GeV/c^2. This results in asymmetric plus and minus errors. In the case of M_W the likelihood is symmetrical and so are the statistical uncertainties, within 2 MeV/c^2.

At E_{cms}= 188.6 GeV, a one parameter fit to M_W is done as well, fixing Γ_W to the Standard Model value according to equation 2.39. In the $e\nu q\bar{q}$ channel, the result is M_W = 80.440 ± 0.174 GeV/c^2, in the $\mu\nu q\bar{q}$ channel M_W= 80.189 ± 0.156 GeV/c^2, in good agreement with the results in table 7.2.

The expected statistical uncertainty on M_W at E_{cms}= 188.6 GeV from sub-sample studies is ±171 MeV/c^2 in the $e\nu q\bar{q}$ channel and ±155 MeV/c^2 in the $\mu\nu q\bar{q}$ channel, with the RMS of the fit errors of the order of 15 MeV/c^2, in good agreement

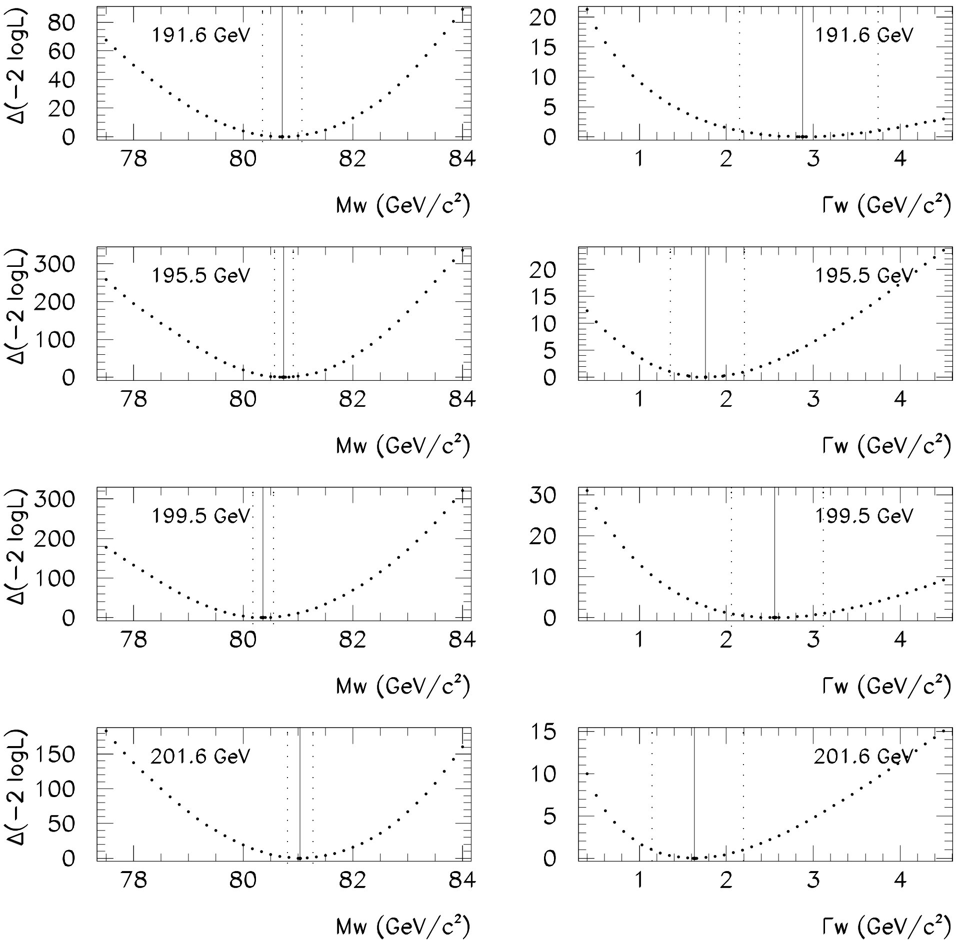

Figure 7.6: Variation of the likelihood at higher energies as a function of M_W (for constant Γ_W) and as a function of Γ_W (for constant M_W) for the fits to the data samples. The statistical uncertainty of the fit is represented by the dashed lines on both sides of the minimum, and corresponds to 1 unit in -2log$\mathcal{L}$. At each energy the $e\nu q\bar{q}$ and $\mu\nu q\bar{q}$ channels are combined in the reweighting fit.

E_{cms}(GeV)	Channel	N_d	M_W(GeV/c^2)	Γ_W(GeV/c^2)	ρ(%)
188.6	$e\nu q\bar{q}$	330	80.430 -0.182 +0.181	2.47 -0.43 +0.48	-5
	$\mu\nu q\bar{q}$	360	80.193 -0.155 +0.155	1.99 -0.33 +0.37	-6
191.6	$(e/\mu)\nu q\bar{q}$	117	80.716 -0.359 +0.357	2.88 -0.73 +0.87	-2
195.5		308	80.742 -0.168 +0.170	1.76 -0.41 +0.44	6
199.5		337	80.363 -0.190 +0.190	2.56 -0.50 +0.56	-1
201.6		176	81.036 -0.230 +0.233	1.63 -0.49 +0.57	2

Table 7.2: Results of the fit to all data samples for M_W and Γ_W. The corresponding mass distributions are shown in figures 7.3 and 7.4 and the likelihood functions in figures 7.5 and 7.6. The correlation ρ between M_W and Γ_W is derived by MINOS [97] from the shape of the likelihood.

with the measured uncertainties. For Γ_W, these uncertainties are $^{+0.43}_{-0.39}$ GeV/c^2 and $^{+0.40}_{-0.36}$ GeV/c^2 respectively, with the RMS of the fit errors of the order of 40 MeV/c^2.

A combination of the results in table 7.2, taking into account all statistical and systematic sources of uncertainties, is described in chapter 8.

7.4 Stability checks

7.4.1 Data taken at E_{cms}= 188.6 GeV

The stability of the fit result is checked as a function of the bin size in the reweighting fit, the signal probability cut, a cut on the upper χ^2 probability from the kinematic fit and the mass window cuts. Table 7.3 shows the values of these parameters used in the checks at E_{cms}= 188.6 GeV.

Bin size (MeV/c^2)	Prob (%)	N_d $e\nu q\bar{q}$	N_d $\mu\nu q\bar{q}$	$P(\chi^2)$ (%)	N_d $e\nu q\bar{q}$	N_d $\mu\nu q\bar{q}$	Window (GeV/c^2)	N_d $e\nu q\bar{q}$	N_d $\mu\nu q\bar{q}$
500	40	330	360	0.0	330	360	70-90	330	360
100	30	336	366	0.5	297	340	60-90	341	368
250	50	323	357	1.0	290	330	74-90	320	347
400	60	314	355	2.0	281	315	70-86	295	338
800	80	288	344				70-94	345	371
1000							60-94	356	379
							74-86	285	325

Table 7.3: The different fits performed to investigate the stability of the result at E_{cms}= 188.6 GeV. In the first row the default fit parameters are shown. The number of data events, N_d, varies if the cuts are changed. The bin size is changed without changing the data sample.

For each of the analyses the selection is performed on the data sample and on the reference sample and a 2 parameter fit is done to extract the new values for M_W and Γ_W. The shift between the new and the default fit result is calculated and the statistical significance of this shift is estimated, defining σ_Δ according to:

$$\sigma_\Delta = \sqrt{|\sigma^2_{\rm new} - \sigma^2_{\rm nom}|}, \tag{7.1}$$

where $\sigma_{\rm nom}$ is the default fit error and $\sigma_{\rm new}$ is the new fit error. σ_Δ corresponds to a significance of one standard deviation if the fit errors are equal to the expected fit error for that analysis and the shift is Gaussian, in which case the probability that the shift is due to a systematic effect can be evaluated. The upper and lower fit errors are averaged to minimise the statistical fluctuations. However, the nominal and the new analyses are not fully correlated and the RMS of the expected fit error is large: typically 40 MeV/c^2 for Γ_W and 15 MeV/c^2 for M_W at 188.6 GeV/c^2, for the subsamples in section 5.3. σ_{nom} in equation 7.1 can therefore only be used to obtain a rough estimate of the actual significance of the shift.

The significance is overestimated because only one feature in the analysis is changed and corrections such as the selection efficiency as a function of Γ_W due to the mass window cuts, or the types of background included in the fit, are not changed. These corrections will cause small systematic shifts that do not affect the default measurement.

For these reasons any shift of less than two standard deviations is assumed to be due to a statistical fluctuation unless the absolute shift is large with respect to the statistical fit error. Where necessary, subsample studies are done to determine the real significance of the shift, in which case the correlation between the two different results is automatically taken into account. The results for the $e\nu q\bar{q}$ and $\mu\nu q\bar{q}$ samples are compared to look for possible trends in the fit result and some of the checks are repeated at higher energies as will be described in section 7.4.2.

For each channel and each analysis the fit results are shown in the following sections, as well as the shift between the new fit result and the default analysis and its uncertainty, defined in equation 7.1.

The stability of the data is also investigated by changing the parameter c defined in section 5.2. c describes the dependence of the mass window efficiency on the width. When it is set to zero, or doubled in size, the shifts in M_W and Γ_W are less or equal to 1MeV/c^2 in each of the channels. To cross check that any remaining $\gamma\gamma$ events have a negligible effect on the result, the available Monte Carlo was included, resulting in the same fit values.

Size of the M_{2C} bins

For the default analysis a bin size of 500 MeV/c^2 is used. If the chosen bin size is too large, information is lost and the statistical uncertainty is expected to increase. If the bin size is chosen much smaller than the resolution on the W mass, no information

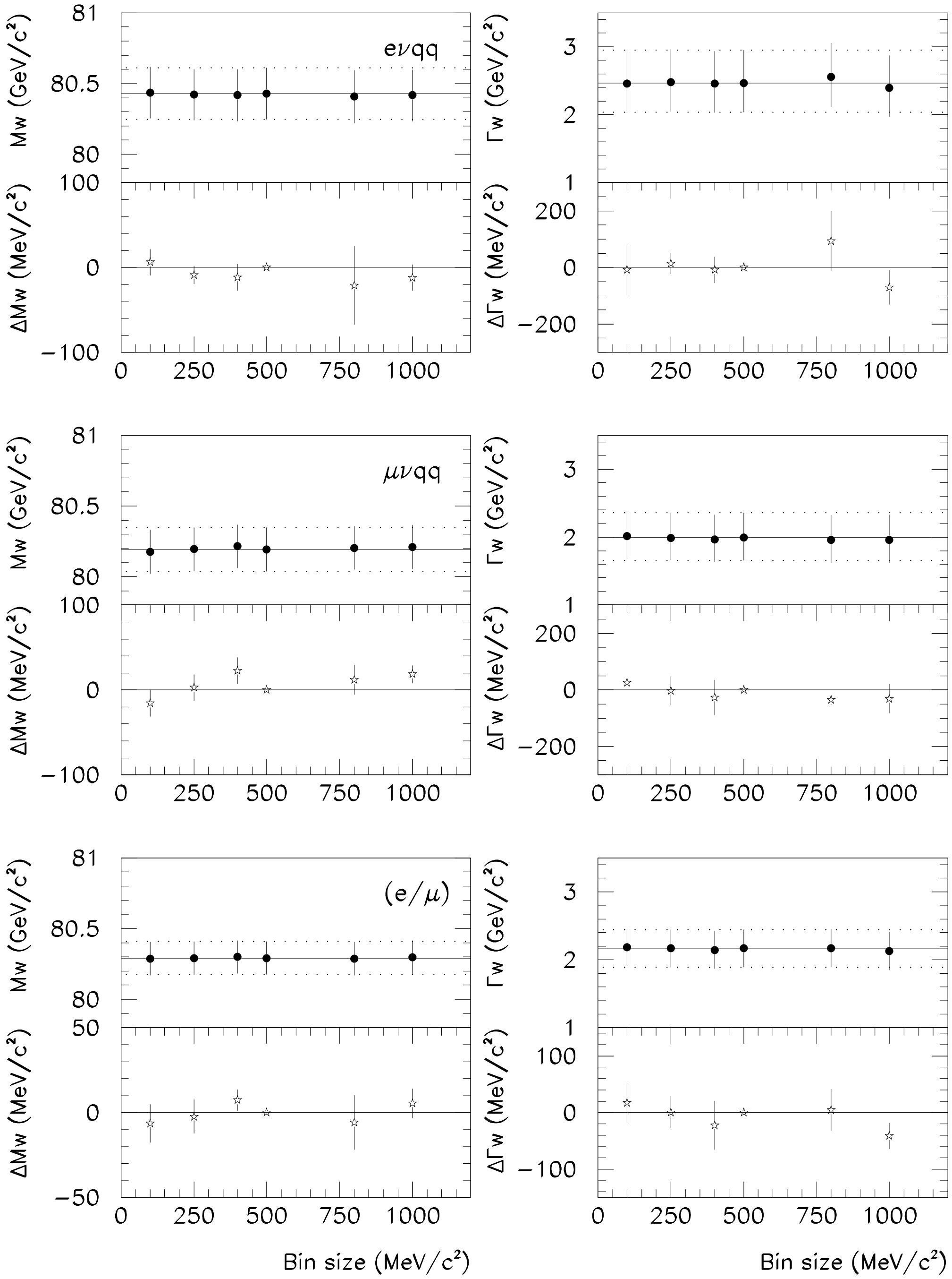

Figure 7.7: Stability of the data fit results for M_W and Γ_W in the $e\nu q\bar{q}$ channel (top), the $\mu\nu q\bar{q}$ channel (middle) and the combination (bottom) at E_{cms}= 188.6 GeV for different values of the bin size. The standard selection cuts are used resulting in 330 selected events. The fit results (upper) and the difference with the standard fit with a bin size of 500 MeV/c^2 (lower) are shown for both M_W (left) and Γ_W (right). The uncertainty in the standard fit result is shown by the dashed lines.

is gained. In this last scenario, systematic uncertainties can cause non-Gaussian shifts.

Bin sizes between 100 and 1000 MeV/c^2 are investigated. The mean of the upper and lower fit errors, for the $e\nu q\bar{q}$ and $\mu\nu q\bar{q}$ channels combined, is shown in figure 7.8. The error bars correspond to the RMS of the parabolic fit error from subsample studies shown in figure 5.5 and 5.6 combined for both channels, 28 MeV/c^2 for Γ_W and 10 MeV/c^2 for M_W, corrected for the change in the fit error. No significant increase in the error as a function of the bin size is observed.

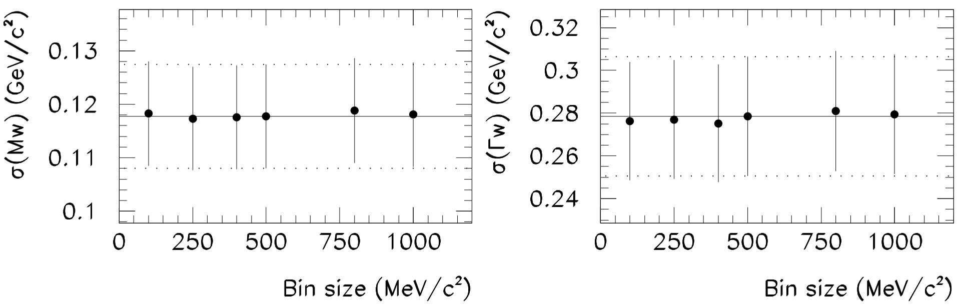

Figure 7.8: Average fit error for both channels combined as a function of the bin size for M_W on the left and Γ_W on the right. The errors are correlated and equal to the full RMS of the fit error.

The fit results for the different bin sizes are shown in figure 7.7. On the left-hand side the results for M_W and on the right-hand side the results for Γ_W are shown. The $e\nu q\bar{q}$ and $\mu\nu q\bar{q}$ channels are fitted separately and the two fit results are combined taking only the statistical uncertainty into account. To determine the weight of each sample the positive and negative fit errors are averaged. All shifts are less than 21% of the statistical uncertainty of the fit and no significant shifts are observed.

Signal probability cut

The default cut on the signal probability is 40%. Four other cuts are investigated, 30, 50, 60 and 80% respectively. There are 48 $e\nu q\bar{q}$ and 22 $\mu\nu q\bar{q}$ events with a signal probability between 30 and 80%.

Since the number of events and the quality of the selection are reduced, the fit error is expected to increase away from a probability cut of 40%. The combined result for both channels is shown in figure 7.10. In the $e\nu q\bar{q}$ channel the fit error increases for each step in signal probability. In the $\mu\nu q\bar{q}$ channel the difference in

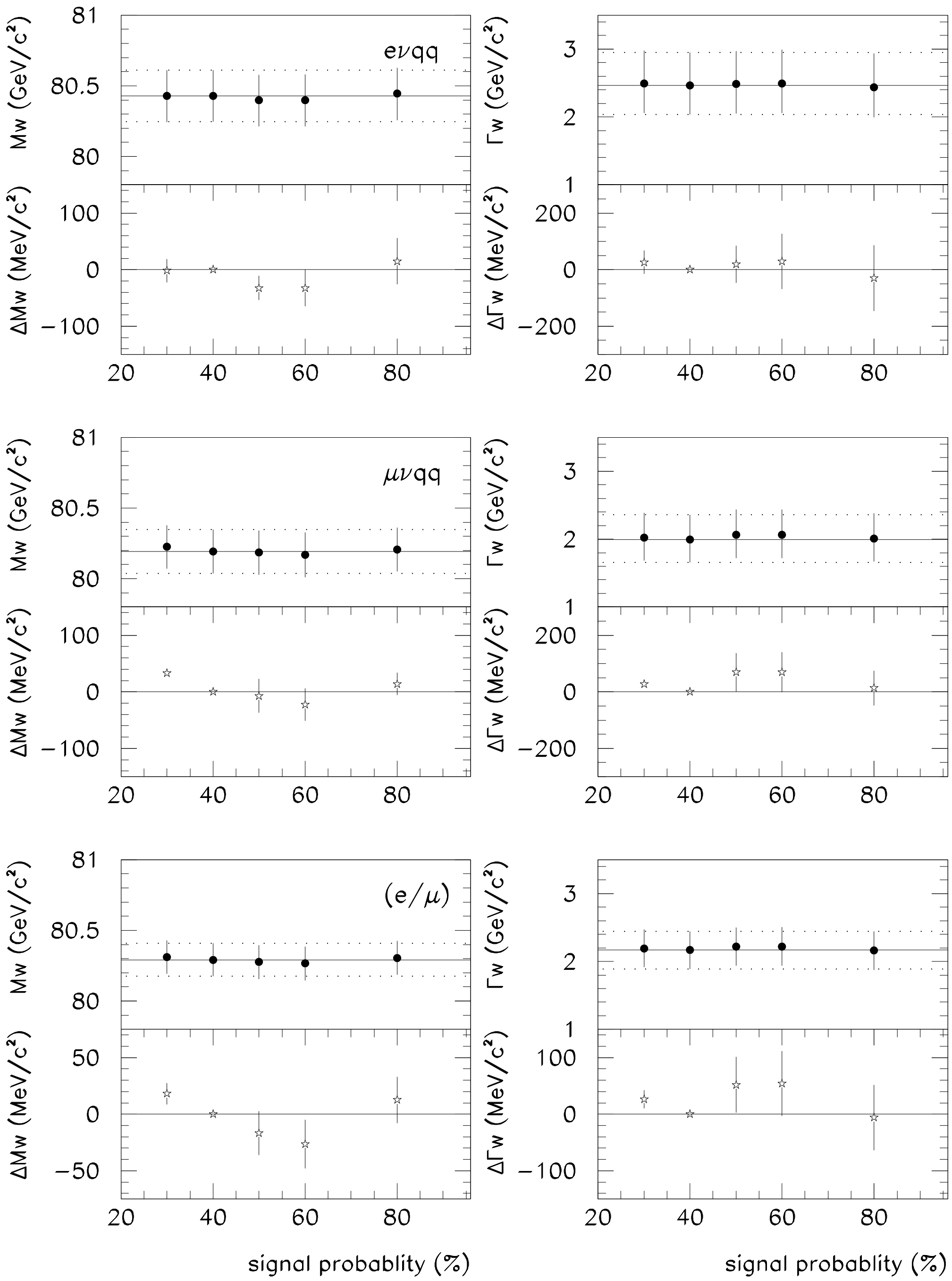

Figure 7.9: Stability of the data fit results for M_W and Γ_W in the $e\nu q\bar{q}$ channel (top), the $\mu\nu q\bar{q}$ channel (middle) and the combination (bottom) at E_{cms}= 188.6 GeV for different signal probability cuts. The nominal sample with a signal probability cut of 40 % is the standard selection and the other samples are described in table 7.3.

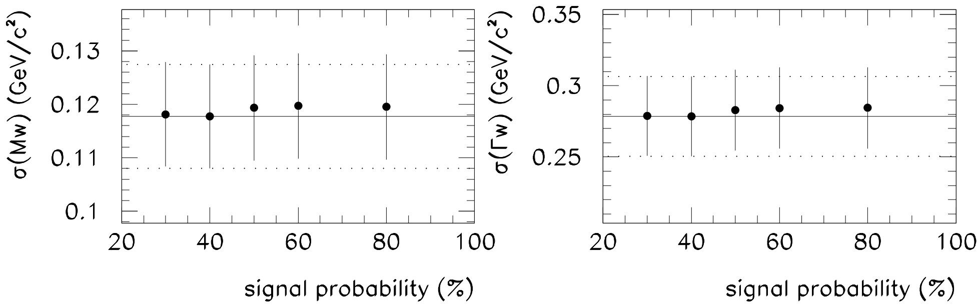

Figure 7.10: Average fit error for both channels combined as a function of the probability cut. The errors are correlated and equal to the full RMS of the fit error.

the selection is smaller and the error does not show a clear trend. The combined result does however illustrate the increase in the fit error as a function of the cut value. The error on the points is the (scaled) full RMS of the default fit error.

The results of the fits are shown in figure 7.9. A trend in the points as a function of the probability is not per definition a sign of a systematic problem, because the points are correlated. The uncertainty on the shift is expected to increase as a function of the probability cut for the same reason. The fit with a probability cut at 30% can be systematically shifted because of new backgrounds entering in the selection (see chapter 4).

All shifts are less than 22% of the statistical uncertainty in the default fit and no significant shifts are observed.

$P(\chi^2)$ cut

In the default analysis no cut is added for the quality of the kinematic fit because no significant discrepancies between data and Monte Carlo are observed and the events with a low upper χ^2 probability are sensitive to the W width. The expected error increases as a function of the cut value (see chapter 4) and the same trend is seen in the data fit error shown in figure 7.12.

To exclude a possible bias in the data due to bad events, the stability of the data is checked as a function of a cut on the upper χ^2 probability. An excess of events is present in the low probability region due to a bad reconstruction in the detector or an inconsistency between the event topology and the assumptions made in the kinematic fit (for instance in the case of ISR events).

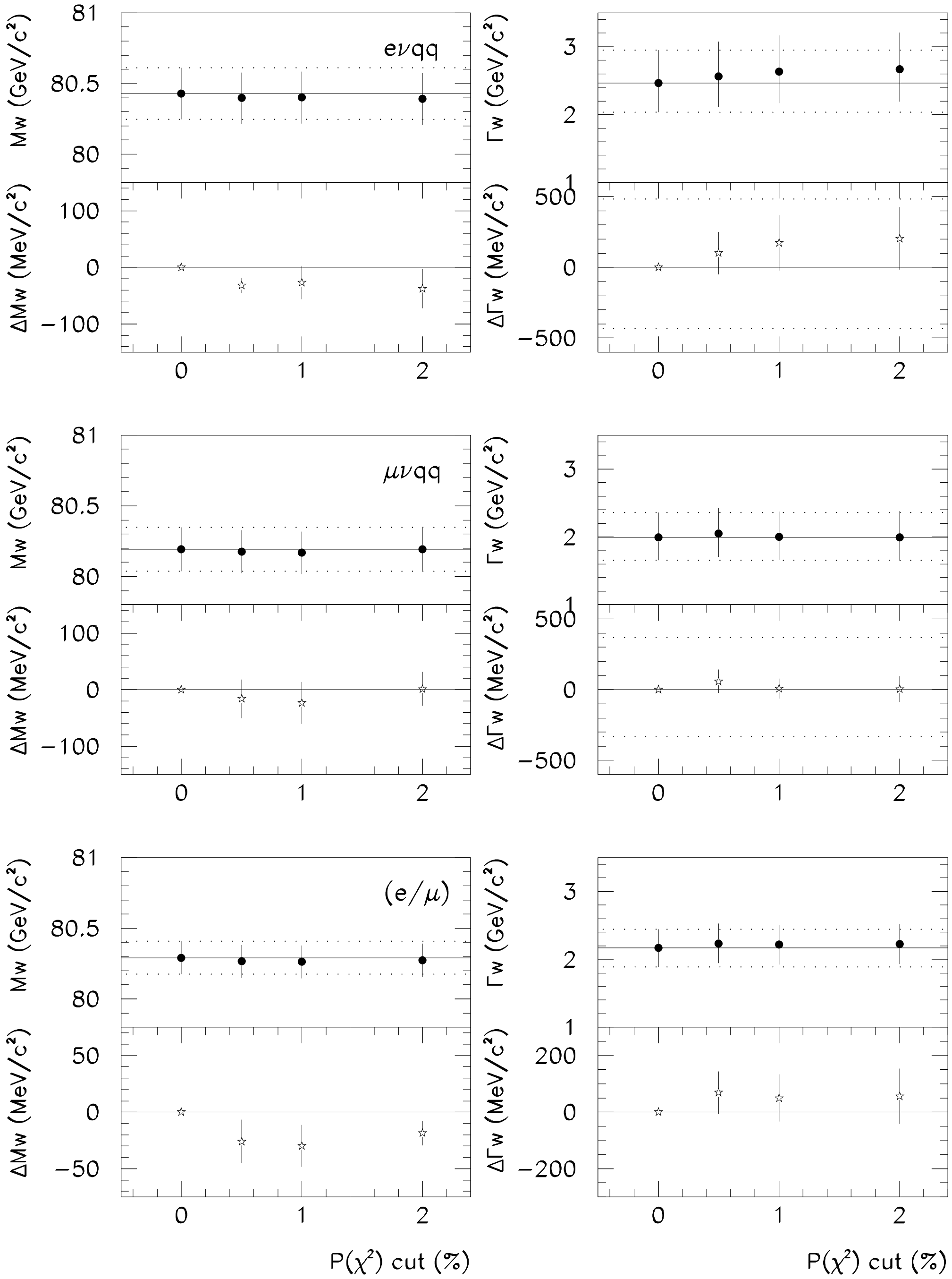

Figure 7.11: Stability of the data fit results for M_W and Γ_W in the $e\nu q\bar{q}$ channel (top), the $\mu\nu q\bar{q}$ channel (middle) and the combination (bottom) at E_{cms}= 188.6 GeV for different cuts on the upper χ^2 probability from the kinematic fit. The first sample is the standard selection and the other samples are described in table 7.3.

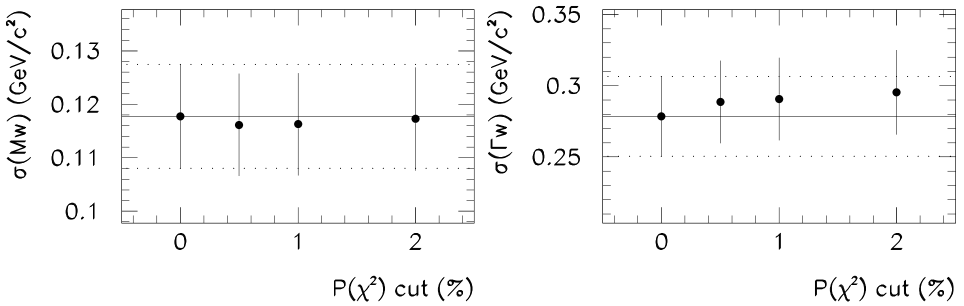

Figure 7.12: Average fit error for both channels combined as a function of a cut on the upper χ^2 probability of the kinematic fit. The errors are correlated and equal to the full RMS of the fit error.

If all events with a probability below 2% are removed, the distribution is flat as is illustrated in figure 5.11. Three cuts are used at a probability of 0.5%, 1% and 2% respectively. The number of events that do not pass this cut agrees between data and Monte Carlo and is shown in table 7.3. At a cut at 2% a total of 51 $e\nu q\bar{q}$ and 45 $\mu\nu q\bar{q}$ events are rejected from the original sample. The results of the fits are shown in figure 7.11. The trend in the fit result as a function of the cut is expected because the points are correlated.

A total of 12 $(e/\mu)\nu q\bar{q}$ Monte Carlo subsamples with the same luminosity of the data and without background are used to determine the actual significance of the shifts. The RMS of the sample by sample shift is found to be 106 MeV/c^2 in case of Γ_W and 35 MeV/c^2 in case of M_W. The observed shifts are all less than 22% of the statistical uncertainty in the default analysis and compatible with zero within one standard deviation.

Mass window cuts

The mass window chosen for the default fit is $70 < M_{2C} < 90$ GeV/c^2. The low mass region is populated by background events while the high mass region is obscured by badly reconstructed events that have a reconstructed mass near the kinematic limit ($\sim$94.3 GeV/c^2) or events with missing energy from sources other than the neutrino, such as ISR. The sensitivity to M_W and Γ_W decreases rapidly for events away from the peak region as illustrated in the sensitivity functions in figure 5.2.

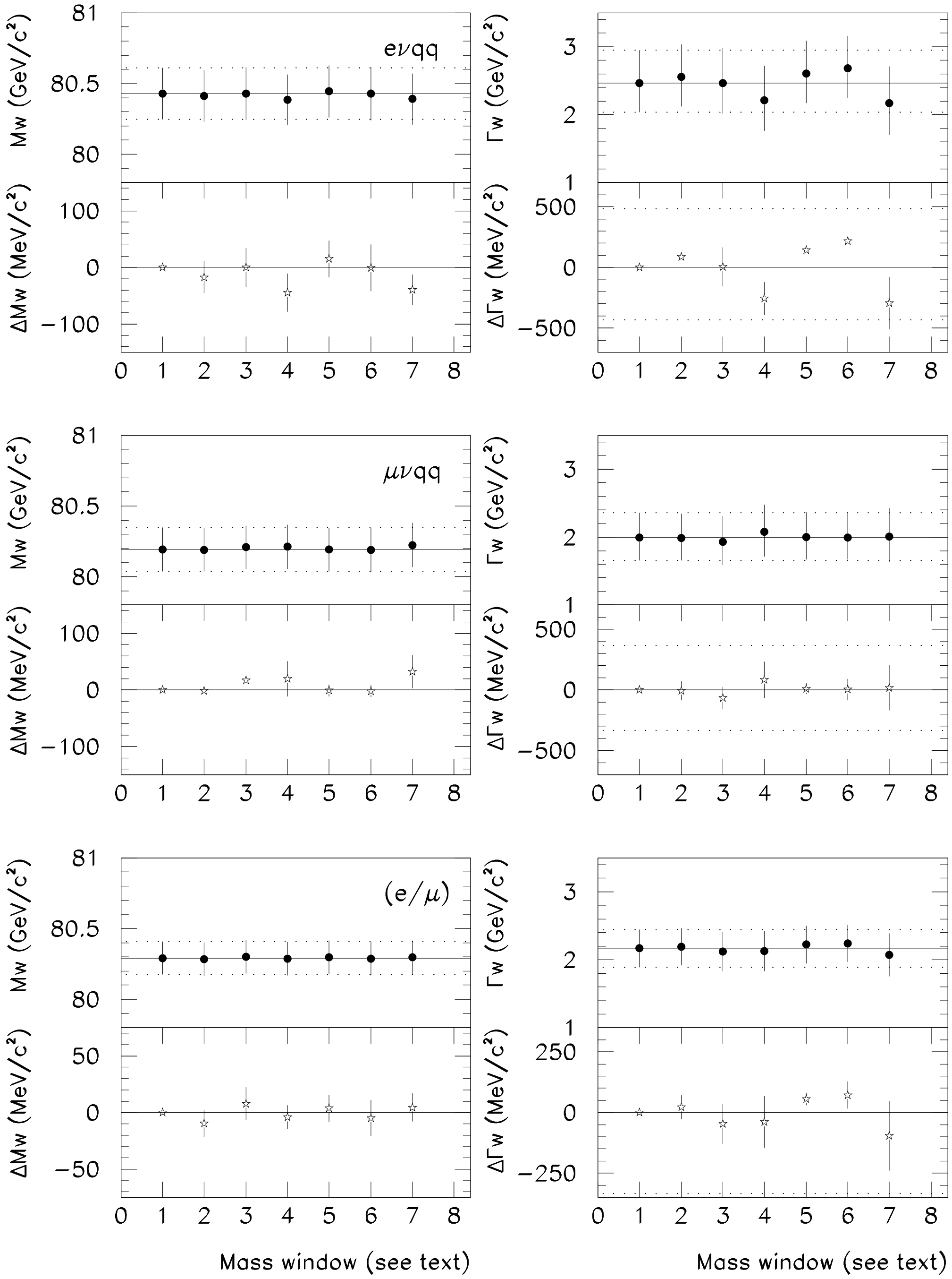

Figure 7.13: Stability of the data fit results for M_W and Γ_W in the $e\nu q\bar{q}$ channel (top), the $\mu\nu q\bar{q}$ channel (middle) and the combination (bottom) at E_{cms}= 188.6 GeV for different mass window cuts. The first sample is the standard selection and the other samples are described in table 7.3. The numbers on the horizontal axes correspond to the rows in the table.

The fit result should be stable if the tails are included in the fit and the background and ISR events are well described by the Monte Carlo calculations. Seven different mass windows are investigated as listed in table 7.3.

The results for different mass windows are shown in figure 7.13. In the $e\nu q\bar{q}$ channel large shifts in Γ_W are observed if the upper window cut is moved from 86 (fit numbers 4 and 7) to 94 GeV/c^2(fit numbers 5 and 6). If the lower mass window cut is kept constant and the upper mass window is changed to 86 GeV/c^2 the fitted width decreases by 256 MeV/c^2 or 59% of the fit error. If the cut is changed to 94 GeV/c^2, the width increases by 142 MeV/c^2 or 29% of the fit error.

In the upper tail of the data distribution of M_{2C} in the $e\nu q\bar{q}$ channel an excess of events is present between M_{2C} = 86 and 94 GeV/c^2. In this range 50 events are observed in the data sample while only 40.2 events are expected, consisting of 38.1 W pair events and 2.0 background events. This fluctuation of the order of 1.4 standard deviations in the number of events can have a significant effect on the mass. Various other mass windows are investigated and the largest shifts are found between mass windows with a lower mass cut at M_{2C} = 74 GeV/c^2 and upper window cuts at M_{2C} = 86, 90 and 94 GeV respectively. The shifts in the data fit value are shown in table 7.4.

A subsample study is done to determine the significance of these shifts. The three mass windows are investigated using 12 Monte Carlo samples of $4f$ events with the same luminosity as the data sample. The allowed shift due to a change in the number of signal events is determined and no background is included in the fits. Each of the 12 samples is fitted with the three different mass window cuts and the RMS of difference between the fitted value of Γ_W is determined, as well as the mean of the positive and negative fit errors. To estimate the shift in the fit value for Γ_W, the mean fit errors for both analyses are subtracted in quadrature. The results are shown in table 7.4. The RMS of the sample-by-sample shift in the fit value should be equal to the mean of these positive and negative fit errors and is shown in the same table. The effect of the background is small and can only increase this RMS.

The shift of 459 MeV/c^2, observed on the data sample, has a significance of 1.6 standard deviations if the RMS of the expected shift is used and 2.0 standard deviations if the change in the fit errors is used. The probability that an effect of

Change in upper M_W cut (GeV/c^2)	Monte Carlo $\sqrt{\lvert\sigma_a^2 - \sigma_b^2\rvert}$ (MeV/c^2)	Monte Carlo RMS($\Delta\Gamma_W$) (MeV/c^2)	Data $\Delta\Gamma_W$ (MeV/c^2)
86-94	+259 -207	296	459
86-90	+201 -155	246	299
90-94	+163 -136	106	160

Table 7.4: Data shift and expected shift in Γ_W as a result of a change in the upper mass window cut, estimated from 12 sub-samples with the same luminosity as the data. Events that pass the $e\nu q\bar{q}$ selection are fitted and non-WW background is excluded.

2 standard deviations is observed in the data is more than 5% and thus likely to occur in one of the 18 different analyses that are compared.

At higher energies the shift in Γ_W between an upper mass cut of 90 and 94 GeV/c^2 is 45 MeV/c^2 or 17% of the mean fit error. In total, 90 $e\nu q\bar{q}$ events are observed between 86 and 94 GeV/c^2 while only 72 are expected. Between 86 and 90 GeV/c^2 4 more events are observed, corresponding to a discrepancy of 0.5 standard deviations. The other 14 additional events have a reconstructed mass between 90 and 94 GeV/c^2. This discrepancy corresponds to 2.3 standard deviations. At E_{cms} = 188.6 GeV, the discrepancy in the number of events with a mass between 86 and 90 GeV/c^2 corresponds to one standard deviation.

To conclude, there is no evidence for any systematic discrepancy in the number of reconstructed events with a mass between 86 and 90 GeV/c^2. For a window from 90 to 94 GeV/c^2 a discrepancy cannot yet be proven but if this range will be used for the final result at high energies more studies need to be done. If a discrepancy is present however, the effect on the width result is small as the shift is only 17% of the mean fit error. The large shifts observed at E_{cms}= 188.6 GeV are likely to be due to a statistical fluctuation.

7.4.2 Data taken at higher energies

For the high energy data (E_{cms} from 191.6 to 201.6 GeV) the $e\nu q\bar{q}$ and $\mu\nu q\bar{q}$ channels are combined to give a preliminary result. The different analyses are listed in table 7.5. The upper mass window cut is changed to 94 GeV/c^2 and a P(χ^2) cut is introduced at 1%. In addition, the bin size is changed to 250 and 1000 MeV/c^2. The results for all separate energies are shown in figure 7.14.

Analysis cut	E_{cms} (GeV) 191.6	195.5	199.5	201.6	All
Default	117	308	337	176	938
70-94	126	323	361	182	992
$P(\chi^2)>0.01$	103	268	289	154	814

Table 7.5: Number of events for the different fits performed to investigate the stability of the result at the higher energies. In the first row the default fit parameters are shown. The number of data events varies if the cuts are changed. The bin size is changed without changing the data sample.

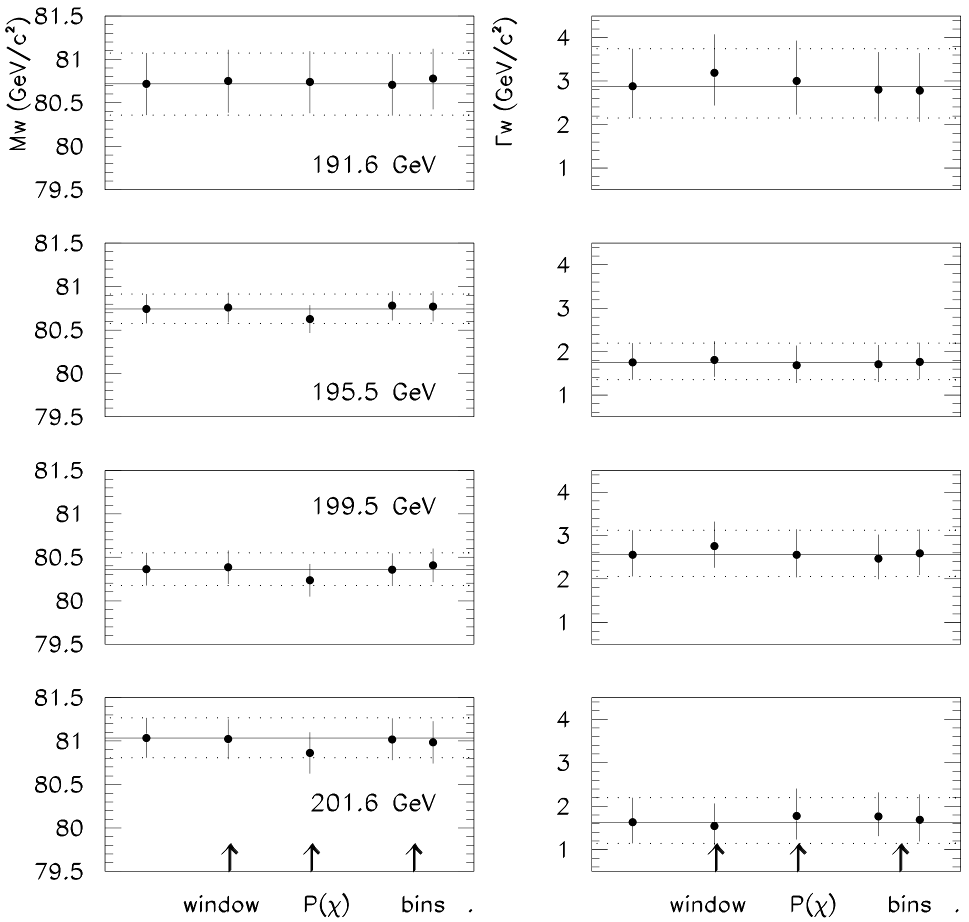

Figure 7.14: Stability of the data fit results for M_W and Γ_W at high energies. The first point corresponds to the standard fit. The upper mass window cut is changed to 94 GeV/c^2, a $P(\chi^2)$ cut is introduced at 1% and the bin size is halved (fourth point) and doubled (fifth point).

The result for the combination is shown in figure 7.15. The mean of the upper and lower errors is used to combine the results and compute the final uncertainties. The uncertainties in the figure are therefore symmetrical for both M_W and Γ_W.

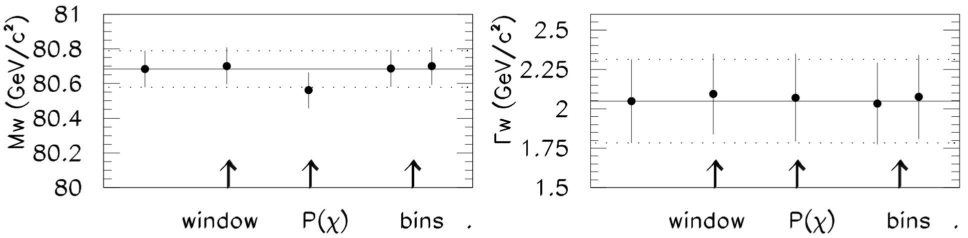

Figure 7.15: Stability of the data fit results for M_W and Γ_W, for all high energies combined. The errors are symmetrised and systematic uncertainties are neglected. The first point corresponds to the standard fit. The upper mass window cut is changed to 94 GeV/c^2, a $P(\chi^2)$ cut is introduced at 1% and the bin size is halved (fourth point) and doubled (fifth point).

If the upper mass window cut is changed to 94 GeV/c^2, the fitted width increases at three of the four energies but decreases at E_{cms}= 201.6 GeV. The combined result changes by only 45 MeV/c^2 or 17% of the mean fit error. The effect on the fit result if the bin size is doubled or halved is small for all samples. The results at the various centre-of-mass energies are combined, taking only statistical uncertainties into account. The combined width result varies from 2.03 to 2.07 GeV/c^2 and the mass result from 80.684 to 80.701 GeV/c^2, in both cases a fluctuation of 16% of the mean fit error.

A large shift in the mass is observed when the $P(\chi^2)$ cut is imposed. However, the total data sample is reduced from 938 to 814 events, a reduction of 13%. This significantly reduces the correlation between the two results. If all events were equally important in the fit, the correlation between the samples is estimated to be $\rho = \sqrt{N_a/N_b} \simeq 93\%$ and the shift in M_W with a significance of one standard deviation can be estimated to be: $\Delta M_W = \sqrt{\sigma_a^2 + \sigma_b^2 - 2\rho\ \sigma_a \sigma_b} \simeq 39$ MeV/c^2.

At E_{cms}= 188.6 GeV/c^2 the shift corresponding to one standard deviation is determined from 12 Monte Carlo subsamples with the same luminosity as the data. The difference in the mean fit error in quadrature for these samples with and without the cut is equal to 18 MeV/c^2 but the RMS of the distribution of ΔM_W is 35 MeV/c^2. If these numbers are corrected for the difference in the total luminosity of the high energy samples ($\mathcal{L}$ = 237 pb^{-1}) compared to the sample at 188.6 GeV, the results are ΔM_W= 16 and 30 MeV/c^2 for the change in the error and the RMS respectively. Since the expected fraction of events removed by the χ^2 cut is larger at high energies

(12.0% compared to 11.2%) this should be an underestimation of the RMS of the shift. The difference in the fit error is also an underestimation if the change is due to a superposition of effects that shift the result in opposite directions.

The actual shift of the combined result at high energies is 123 MeV/c^2, if systematic uncertainties are not taken into account in the combination. According to the above arguments, this corresponds to more than three standard deviations. In total 124 events are rejected in the data and 113 are expected according to the Monte Carlo, in agreement within one standard deviation. At E_{cms}= 188.6 GeV/c^2, 70 events are rejected by a cut at 1% in data and 80 are expected, in agreement within 1.2 standard deviations and, because the discrepancy is in the opposite direction to the higher energy samples, it is likely to be a statistical fluctuation.

The four different data fits shift in the same direction apart from the sample at E_{cms}= 191.6 GeV. At E_{cms}= 188.6 GeV, the shift in the combined mass result is 30 MeV/c^2 or 25% of the mean fit error. The changes at 188.6 GeV are not significant but at the higher energies a systematic effect can, although not proven, not be excluded. For the final result the parameterisation of the kinematic fit needs to be redone and the stability re-investigated.

7.4.3 Concluding remarks

All fit results are stable if the bin size is changed and the size of the fit error does not change significantly in the tested range of bin sizes between 100 and 1000 MeV/c^2. The signal probability cut is chosen to optimise the quality of the selection and a change in this cut worsens the data fit error. The fit value is stable in the tested range of 30 to 80%.

The numbers of events in the five different data samples used for the fit are in agreement with the Monte Carlo predictions. In the high mass region, that is not used in the fit ($M_{2C} > 90$ GeV/c^2), a discrepancy with a significance of 2.3 standard deviations is observed at energies above 188.6 GeV and if this region is included in the future more studies need to be done. Apart from this observation, no evidence for instabilities due to the mass window cut is found.

A cut on the upper χ^2 probability from the kinematic fit worsens the error on Γ_W and at E_{cms}= 188.6 GeV there are no indications that badly reconstructed events corrupt the measurement. At higher energies, the result for Γ_W is stable but the shift in M_W has a significance of at least 3 standard deviations. The parameterisation of the kinematic fit needs to be redone for the final result.

Chapter 8

Combination and comparison of results

In the first section of this chapter, the results for the mass and the width obtained in chapter 7 are combined. The official ALEPH results for the width in the $(e/\mu)\nu q\bar{q}$ channels are described in this thesis. The official mass measurements at energies from 188.6 GeV use the same selections but a different fit technique. The ALEPH results from data up to 201.6 GeV are shown in section 8.2. In section 8.3, the measurements described in this thesis are compared to the official ALEPH results.

In section 8.4, the origin of the world average W mass is explained and the most recent preliminary world average from the ICHEP 2000 summer conferences is shown [63]. This most recent combination is interpreted in the framework of the Standard Model in section 8.4.4. In section 8.5, the origin of the world average width is explained and compared to the Standard Model prediction.

8.1 Combination of the results for $\mathrm{M_W}$ and Γ_W

In this section, the results for the 2-parameter mass and width fits described in this thesis, from the $\mathrm{E_{cms}}$= 188.6 GeV and $\mathrm{E_{cms}}$= 191.6 - 201.6 GeV data, are combined taking into account all systematic and statistical uncertainties.

The χ^2 of the combination is defined as:

$$\chi^2 = \sum_{n=1}^{\mathrm{N}} \left(\frac{< \mathrm{M_W} > - {\mathrm{M_W}}^n}{\sigma^n_{\mathrm{tot}}} \right)^2 , \tag{8.1}$$

where the statistical and systematic uncertainties in the measurement are added in quadrature to obtain σ^n_{tot} and $< \mathrm{M_W} >$ is the error weighted mean of the measurements $\mathrm{M_W}^n$. σ^n_{tot} is used to weight the fit values in the determination of this mean.

Only the systematic contribution due to finite Monte Carlo statistics is assumed to be uncorrelated between energies and decay channels. The other systematic errors are assumed to be fully correlated to ensure that the final uncertainty is not underestimated. The uncorrelated uncertainties are added in quadrature, while the total correlated uncertainty, σ_{corr}, is the error weighted mean of the contributions σ^n_{corr} from all N measurements.

Since the RMS of many of the systematic uncertainties is large, this estimator does not follow an ideal χ^2 distribution and can only be used to approximate the significance of discrepancies between results.

The combination of the results in chapter 7 at $\mathrm{E_{cms}}$= 188.6 GeV yields:

$$\begin{aligned} \mathrm{M_W} &= 80.313 \pm 0.119(\mathrm{stat.}) \pm 0.052(\mathrm{syst.})\ \mathrm{GeV}/c^2 \\ \Gamma_\mathrm{W} &= 2.17^{+0.29}_{-0.26}(\mathrm{stat.}) \pm 0.11(\mathrm{syst.})\ \mathrm{GeV}/c^2, \end{aligned}$$

where 27 MeV/c^2 is added to the mass, and 0.7 MeV/c^2 to the width with respect to the results in chapter 7 to translate to the running width scheme (see section 2.2.3). The χ^2/n of these combinations are 0.9 and 0.6 for the mass and the width respectively, for one degree of freedom.

For the preliminary 1999 results, most of the contributions to the systematic uncertainty are taken from the measurement at $\mathrm{E_{cms}}$= 188.6 GeV. The systematics due to finite reference statistics and beam energy smearing in case of Γ_W are re-evaluated for each measurement as described in sections 6.4.3 and 6.3. The preliminary results are combined with the results above, yielding:

$$\begin{aligned} \mathrm{M_W} &= 80.537 \pm 0.079(\mathrm{stat.}) \pm 0.052(\mathrm{syst.})\ \mathrm{GeV}/c^2 \\ \Gamma_\mathrm{W} &= 2.11^{+0.20}_{-0.18}(\mathrm{stat.}) \pm 0.11(\mathrm{syst.})\ \mathrm{GeV}/c^2. \end{aligned}$$

The χ^2/n for this combination is 2.3 for the mass and 0.7 for the width respectively, for 5 degrees of freedom. For the final measurement at energies from 191.6 GeV, the kinematic fit should be re-parameterised. The cut on the upper χ^2 probability decreases the fit result at higher energies (see section 7.4.2).

8.2 Official ALEPH M_W and Γ_W results

The width of the W is measured by ALEPH from direct reconstruction of the W mass for the first time at E_{cms}= 188.6 GeV [2]. The preliminary measurements at higher energies were presented at the ICHEP 2000 summer conferences [3]. All the official ALEPH results for Γ_W from the direct reconstruction of the W in the $e\nu q\bar{q}$ and $\mu\nu q\bar{q}$ channels are a result of the work presented in this thesis.

The ALEPH measurements of M_W, from 188.6 GeV, use the selection described in this thesis. The official ALEPH mass results differ from the measurements described in this thesis and the fit method that was used to extract M_W for the ALEPH publication at E_{cms}= 188.6 GeV is introduced in this section.

The official ALEPH results are presented below, starting with the final results at E_{cms}= 188.6 GeV in section 8.2.1, followed by the preliminary results at higher energies in section 8.2.2. The final and preliminary results are combined in section 8.2.3.

8.2.1 Official results at E_{cms}= 188.6 GeV

Mass results

The published W mass results from the 188.6 GeV ALEPH data are obtained from a one parameter fit. To minimise the statistical uncertainty on the mass, this fit is performed in a three dimensional space spanned by the 2C mass estimator, the 1C hadronic mass estimator and the error on the mass from the kinematic fit. The published results for the $(e/\mu)\nu q\bar{q}$ decay channels are [2]:

$$\begin{aligned} e\nu q\bar{q}: \quad M_W =& \quad 80.319 \pm 0.154(\text{stat.}) \pm 0.061(\text{syst.})\ \text{GeV}/c^2 \\ \mu\nu q\bar{q}: \quad M_W =& \quad 80.272 \pm 0.141(\text{stat.}) \pm 0.047(\text{syst.})\ \text{GeV}/c^2. \end{aligned}$$

Apart from these measurements, the W mass is measured by ALEPH at E_{cms}= 188.6 GeV/c^2 from a one parameter fit in the other W pair decay channels [2]:

$$\begin{aligned} \tau\nu q\bar{q}: \quad M_W =& \quad 80.385 \pm 0.287(\text{stat.}) \pm 0.047(\text{syst.})\ \text{GeV}/c^2 \\ q\bar{q}q\bar{q}: \quad M_W =& \quad 80.551 \pm 0.108(\text{stat.}) \pm 0.037(\text{syst.}) \pm 0.042(\text{FSI})\ \text{GeV}/c^2 \\ l\nu l\nu: \quad M_W =& \quad 81.81 \pm 0.67(\text{stat.}) \pm 0.20(\text{syst.})\ \text{GeV}/c^2. \end{aligned}$$

The additional final state interaction (FSI) contribution to the uncertainty is due to colour reconnection [38] and Bose-Einstein effects [39] in the ($WW \rightarrow q\bar{q}q\bar{q}$) decay channel. Various models are used to describe these two effects. ALEPH estimates the additional uncertainty in the hadronic mass measurement to be 30 MeV/c^2 for each of these effects, but estimates vary widely between collaborations. If these effects bias the hadronic mass measurement significantly, the mass measurement from the $q\bar{q}q\bar{q}$ and $l\nu q\bar{q}$ decay channels will differ. Combined results for these two channels are compared in section 8.4.4.

The official ALEPH results for the $(e/\mu)\nu q\bar{q}$ channels are combined with the measurements above and yield the ALEPH W mass at E_{cms}= 188.6 GeV/c^2:

$$M_W = 80.432 \pm 0.072(\text{stat.}) \pm 0.041(\text{syst.}) \pm 0.019(\text{FSI}) \pm 0.017(\text{LEP})\ \text{GeV}/c^2.$$

Width results

The width in the $(e/\mu)\nu q\bar{q}$ channels is combined with a measurement in the $q\bar{q}q\bar{q}$ channel [2]:

$$\begin{aligned} e\nu q\bar{q}: \quad \Gamma_W = &\quad 2.47 \pm 0.46(\text{stat.}) \pm 0.12(\text{syst.})\ \text{GeV}/c^2 \\ \mu\nu q\bar{q}: \quad \Gamma_W = &\quad 1.99 \pm 0.35(\text{stat.}) \pm 0.10(\text{syst.})\ \text{GeV}/c^2 \\ q\bar{q}q\bar{q}: \quad \Gamma_W = &\quad 2.34 \pm 0.28(\text{stat.}) \pm 0.17(\text{syst.})\ \text{GeV}/c^2. \end{aligned}$$

The combined width result from each of the two $l\nu q\bar{q}$ channels gives:

$$\Gamma_W = 2.17 \pm 0.28(\text{stat.}) \pm 0.10(\text{syst.})\ \text{GeV}/c^2.$$

The combination of all three decay channels yields:

$$\Gamma_W = 2.24 \pm 0.20(\text{stat.}) \pm 0.13(\text{syst.})\ \text{GeV}/c^2.$$

8.2.2 Preliminary results at E_{cms}= 191.6 - 201.6 GeV

The official ALEPH preliminary 1999 results, submitted to the ICHEP 2000 summer conference, for the channels studied in this thesis are derived from a 1 parameter fit in three dimensions as explained in the previous section. The results are [3]:

$$\begin{aligned} e\nu q\bar{q}: \quad M_W = &\quad 80.596 \pm 0.155(\text{stat.}) \pm 0.061(\text{syst.})\ \text{GeV}/c^2 \\ \mu\nu q\bar{q}: \quad M_W = &\quad 80.600 \pm 0.138(\text{stat.}) \pm 0.046(\text{syst.})\ \text{GeV}/c^2. \end{aligned}$$

Fits to the other decay channels yield:

$$\tau\nu\mathrm{q\bar{q}}: \quad \mathrm{M_W} = \quad 80.408 \pm 0.236(\mathrm{stat.}) \pm 0.048(\mathrm{syst.})\ \mathrm{GeV}/c^2$$
$$\mathrm{q\bar{q}q\bar{q}}: \quad \mathrm{M_W} = \quad 80.384 \pm 0.091(\mathrm{stat.}) \pm 0.037(\mathrm{syst.}) \pm 0.042(\mathrm{FSI})\ \mathrm{GeV}/c^2.$$

Due to limited Monte Carlo statistics, only a one dimensional reweighting fit was used for the W mass extraction, rather than the three dimensional fit used for the results at $\mathrm{E_{cms}}$= 188.6 GeV. The combination of the results for the all four decay channels yields:

$$\mathrm{M_W} = 80.476 \pm 0.065(\mathrm{stat.}) \pm 0.039(\mathrm{syst.}) \pm 0.022(\mathrm{FSI}) \pm 0.017(\mathrm{LEP})\ \mathrm{GeV}/c^2.$$

The preliminary measurement of the W width is obtained from the $(e/\mu)\nu\mathrm{q\bar{q}}$ channels. The two channels are combined in the fit as explained in chapter 7 and the combined result for the four different energies is:

$$\Gamma_\mathrm{W} = 2.05 \pm 0.26(\mathrm{stat.}) \pm 0.11(\mathrm{syst.})\ \mathrm{GeV}/c^2.$$

8.2.3 Combined results for all data

In this section the official combination of results from all ALEPH data is described, starting with the published results up to $\mathrm{E_{cms}}$= 182.7 GeV. The preliminary combination of all ALEPH data up to energies of 201.6 GeV is shown at the end of this section.

The mass of the W has been measured directly by ALEPH since the LEP beam energy passed the threshold for W pair production in 1996. At production threshold, the cross section is very sensitive to the mass because it is proportional to β according to equation 2.35. The event rate is measured and the GENTLE [37] simulation program is used to derive the mass [126]:

$$\mathrm{M_W} = 80.14 \pm 0.34(\mathrm{stat.}) \pm 0.09(\mathrm{syst.}) \pm 0.03(\mathrm{LEP})\ \mathrm{GeV}/c^2,$$

where the systematic uncertainty due to the error on the LEP beam energy is quoted separately.

At energies above production threshold, the mass has been determined from the direct reconstruction of the W bosons in the event. Two samples at $\mathrm{E_{cms}}$= 172.1

and 182.7 GeV/c^2 are analysed [127, 98]. The results are combined for all decay channels of the W, except the fully leptonic decay channel and with the cross section result at threshold to obtain the published ALEPH W mass:

$$\mathrm{M_W} = 80.423 \pm 0.112(\mathrm{stat.}) \pm 0.044(\mathrm{syst.}) \pm 0.021(\mathrm{FSI}) \pm 0.023(\mathrm{LEP})\ \mathrm{GeV}/c^2.$$

This result is used in the derivation of the final world average as explained in section 8.4.

The measurement of $\mathrm{M_W}$ at 188.6 GeV described in the previous section is combined with the results at $\mathrm{E_{cms}}$= 161.3 - 182.7 GeV and with the preliminary ALEPH results at $\mathrm{E_{cms}}$= 191.6 - 201.6 GeV to obtain the preliminary ALEPH mass result:

$$\mathrm{M_W} = 80.440 \pm 0.044(\mathrm{stat.}) \pm 0.040(\mathrm{syst.}) \pm 0.020(\mathrm{FSI}) \pm 0.017(\mathrm{LEP})\ \mathrm{GeV}/c^2.$$

The width is measured from the W mass distribution for the first time by ALEPH at $\mathrm{E_{cms}}$= 188.6 GeV. This measurement is combined with the preliminary measurements at higher energies to obtain the preliminary ALEPH measurement for the ICHEP 2000 summer conferences [3]:

$$\Gamma_\mathrm{W} = 2.17 \pm 0.16(\mathrm{stat.}) \pm 0.12(\mathrm{syst.})\ \mathrm{GeV}/c^2.$$

8.3 Comparison to official ALEPH results

The official ALEPH results at $\mathrm{E_{cms}}$= 188.6 GeV shown in section 8.2.1 are to be compared to the results in this thesis:

$$\begin{aligned}
e\nu\mathrm{q\bar{q}}:\quad \mathrm{M_W} &= 80.457 \pm 0.182(\mathrm{stat.}) \pm 0.069(\mathrm{syst.})\ \mathrm{GeV}/c^2\\
\Gamma_\mathrm{W} &= 2.47^{+0.48}_{-0.43}(\mathrm{stat.}) \pm 0.13(\mathrm{syst.})\ \mathrm{GeV}/c^2\\
\mu\nu\mathrm{q\bar{q}}:\quad \mathrm{M_W} &= 80.220 \pm 0.155(\mathrm{stat.}) \pm 0.041(\mathrm{syst.})\ \mathrm{GeV}/c^2\\
\Gamma_\mathrm{W} &= 1.99^{+0.37}_{-0.33}(\mathrm{stat.}) \pm 0.10(\mathrm{syst.})\ \mathrm{GeV}/c^2.
\end{aligned}$$

The results for $\mathrm{M_W}$ in this thesis differ from the official ALEPH results for the following reasons. Firstly, the 2C mass estimator does not contain all the relevant kinematic information of the event. The use of two other variables in the fit recovers some of the lost information and therefore results in a reduction of the statistical uncertainty on the measurement and a statistical shift in the mean value. The expected rather than the fitted statistical uncertainties should be compared and studies have shown that the improvement is of the order of 10% for the combined $(e/\mu)\nu q\bar{q}$ results [128]. ALEPH measurements of the mass at lower beam energies ($E_{cms} \leq 182.7$ GeV) were obtained from a one dimensional fit to the 2C mass estimator. For a future combined measurement of the mass and the width, the use of more dimensions in the fit will reduce the statistical uncertainty in M_W. The effect of a multi-dimensional reweighting fit on the width measurement is to be investigated.

Secondly, the official result is obtained from events with an upper χ^2 probability from the kinematic fit of more than 99% only. The sample with very low χ^2 probability is not sensitive to the mass, but is sensitive to the width. Since the expected uncertainty in the width increases significantly if these events are rejected, this cut is not applied in the analysis described in this thesis.

Finally, the result described in this thesis is obtained from a two parameter fit to both the mass and the width. The small correlation between the two variables can change the result of the fit.

The difference between the methods means the results are not fully statistically correlated. The systematic uncertainties differ as well. Since some of the systematic uncertainties have a large RMS, e.g. the uncertainties due to calorimeter fluctuations (figure 6.9) and the fragmentation model (figure 6.12), statistical shifts in the mean value can be large.

The systematic uncertainties in the ALEPH results differ from the results quoted above. In the ALEPH publication, all the contributions to the systematic uncertainty are rounded to the nearest 5 MeV/c^2 before they are combined, the uncertainty due to the beam energy spread is not included and, in the combination, the background systematic in the different channels is assumed to be uncorrelated. This systematic uncertainty is due to a normalisation uncertainty in the background that is of the same order in both channels and is therefore assumed to be correlated in this thesis. As a result, the ALEPH systematic uncertainty on Γ_W is 0.12 GeV/c^2 and not 0.13 GeV/c^2 as quoted above. The $\mu\nu q\bar{q}$ result does not change significantly. Finally, the positive and negative fit errors are not averaged in this thesis because of the expected asymmetry in the likelihood.

The combined result for the preliminary 2-parameter fits at energies between 191.6 and 201.6 GeV described in this thesis is:

$$\begin{aligned}\mathrm{M_W} = &\quad 80.712 \pm 0.106(\mathrm{stat.}) \pm 0.052(\mathrm{syst.})\mathrm{GeV}/c^2 \\ \Gamma_\mathrm{W} = &\quad 2.06^{+0.28}_{-0.25}(\mathrm{stat.}) \pm 0.11(\mathrm{syst.})\ \mathrm{GeV}/c^2.\end{aligned}$$

The χ^2/n for this combination is 1.6 in case of the mass and 1.0 in case of the width for three degrees of freedom.

This result for $\mathrm{M_W}$ differs from the official ALEPH result in section 8.2.2. Studies were done to find the cause of the discrepancy and the only significant contribution is found to be the effect of the cut on the probability from the kinematic fit described in section 7.4.2. At $\mathrm{E_{cms}}$= 188.6 GeV the fit result is stable for different cut values and for the final measurement at higher energies this discrepancy is to be investigated further. The systematic uncertainties differ with and without this selection cut and because the RMS of many of the systematics is large, shifts can be expected.

The official ALEPH width result differs from this result due to the differences in the treatment of the systematic uncertainties mentioned above and because the positive and negative fit errors are averaged. The fit values and the statistical uncertainties that are used for the ALEPH combination are equal to the values in chapter 7.

8.4 Combination of world results for $\mathrm{M_W}$

All the published LEP results are combined with results from $p\bar{p}$ colliders to obtain a final world average W mass. This average includes ALEPH measurements up to $\mathrm{E_{cms}}$ = 182.7 GeV. Preliminary ALEPH results up to 201.6 GeV are used to obtain a preliminary world average.

In section 8.4.1, the combined results from the four LEP collaborations are given, followed by the results from $p\bar{p}$ colliders in section 8.4.2. The two (final and preliminary) world averages for $\mathrm{M_W}$ are shown in section 8.4.3 and implications of the most recent combination for the ICHEP 2000 summer conferences are discussed in section 8.4.4.

8.4.1 LEP experiments M_W combination

All four LEP experiments have measured the mass from the W pair production threshold. For the final world average W mass, published results (up to E_{cms}= 182.7 GeV) are included in the combination:

$$\begin{aligned}
OPAL\ [134]: \quad M_W =& \quad 80.38 \pm 0.12(\text{stat.}) \pm 0.05(\text{syst.})\ \text{GeV}/c^2 \\
DELPHI\ [135]: \quad M_W =& \quad 80.270 \pm 0.137(\text{stat.}) \pm 0.048(\text{syst.})\ \text{GeV}/c^2 \\
L3\ [136]: \quad M_W =& \quad 80.61 \pm 0.15\ \text{GeV}/c^2 \\
ALEPH\ [127]: \quad M_W =& \quad 80.423 \pm 0.112(\text{stat.}) \pm 0.054(\text{syst.})\ \text{GeV}/c^2.
\end{aligned}$$

At threshold, all collaborations derive the mass from the cross section as explained in section 8.2.3. At higher energies, the mass is extracted by direct reconstruction of the W bosons. DELPHI measures the mass from an event-by-event maximum likelihood fit to a relativistic Breit-Wigner convoluted with a Gaussian, to which a simulated background distribution is added. The result is corrected for a bias due to events with ISR photons. The other collaborations use a binned likelihood derived from Monte Carlo simulated event samples similar to the one described in this thesis.

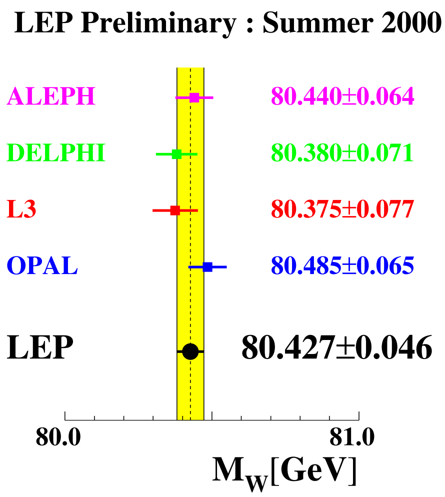

Figure 8.1: Preliminary LEP results for M_W [63].

The preliminary measurements of the LEP collaborations up to 201.6 GeV that are used to obtain the preliminary LEP W mass for the ICHEP 2000 summer conferences are shown in figure 8.1. The preliminary LEP W mass is [129]:

$$\mathrm{M_W} = 80.427 \pm 0.046\ \mathrm{GeV}/c^2.$$

8.4.2 $\mathrm{M_W}$ results from $p\bar{p}$ colliders

The mass is also measured at Fermilab, by the D0 and the CDF collaborations. The Tevatron accelerator produces p and $\bar{p}$ beams that collide with a centre-of-mass energy of 1.8 TeV. W bosons that are created in these collisions and decay to either an $e\nu$ or a $\mu\nu$ pair are analysed. The measured *transverse mass* of the W, m_T, defined as:

$$m_\mathrm{T} = \sqrt{2\mathrm{P}_\mathrm{T}^{\nu}\mathrm{P}_\mathrm{T}^{l}(1-\cos\Delta\phi)}, \tag{8.2}$$

is compared to Monte Carlo predictions at various assumptions for the W mass. $\mathrm{P}_\mathrm{T}^{l}$ is the transverse momentum of the lepton with respect to the beam pipe. The transverse momentum of the neutrino $\mathrm{P}_\mathrm{T}^{\nu}$ is derived from momentum conservation in the event. $\Delta\phi$ is the azimuthal separation of the two leptons. The results are:

$$\begin{aligned} D0\ [130]: &\quad \mathrm{M_W} = 80.482 \pm 0.091\ \mathrm{GeV}/c^2 \\ CDF\ [131]: &\quad \mathrm{M_W} = 79.91 \pm 0.39\ \mathrm{GeV}/c^2 \\ CDF\ [132]: &\quad \mathrm{M_W} = 80.41 \pm 0.18\ \mathrm{GeV}/c^2. \end{aligned}$$

The two CDF results are independent measurements from data samples obtained in 1988-89 and 1992-93 respectively.

An additional result from the UA2 collaboration in 1992 is included in averages by the LEP electroweak working group [133]:

$$\mathrm{M_W} = 80.84 \pm 0.22 \pm 0.83\ \mathrm{GeV}/c^2,$$

that is derived from a measurement of the ratio $\mathrm{M_W}/\mathrm{M_Z}$ from $(\mathrm{W} \to e\nu)$ and $(\mathrm{Z} \to e^+e^-)$ events and the LEP measurement of the Z mass. Preliminary measurements presented at the ICHEP 2000 conference are combined with the measurements above to obtain the preliminary result from $p\bar{p}$ colliders [129]:

$$\mathrm{M_W} = 80.448 \pm 0.062\ \mathrm{GeV}/c^2.$$

8.4.3 The world average W mass

The final LEP and Tevatron measurements listed above are used to obtain the final direct world average W mass [45]:

$$\mathrm{M_W} = 80.419 \pm 0.056\ \mathrm{GeV}/c^2.$$

At the time of the summer conferences, preliminary LEP and Tevatron measurements are combined to obtain the preliminary world average mass. The different contributions to this measurement are discussed above and the result of the combination is [129]:

$$\mathrm{M_W} = 80.434 \pm 0.037\ \mathrm{GeV}/c^2.$$

8.4.4 Implications of the world average W mass

In this section, the preliminary world average mass result is interpreted in the context of the Standard Model. Implications for the significance of final state interactions between two hadronically decaying W bosons and conclusions for the mass of the Higgs boson are mentioned.

Final state interactions

As mentioned above, a difference between the mass measurements in the $l\nu\mathrm{q\bar{q}}$ and the $\mathrm{q\bar{q}q\bar{q}}$ decay channels can indicate biases due to colour reconnection or Bose-Einstein effects. The combined preliminary measurement from all four LEP collaborations is [129]:

$$\begin{aligned} l\nu\mathrm{q\bar{q}}: \quad \mathrm{M_W} = &\ 80.427 \pm 0.051\ \mathrm{GeV}/c^2 \\ \mathrm{q\bar{q}q\bar{q}}: \quad \mathrm{M_W} = &\ 80.432 \pm 0.073\ \mathrm{GeV}/c^2. \end{aligned}$$

The difference between these measurements, $\Delta\mathrm{M_W} = 5 \pm 51\ \mathrm{MeV}/c^2$, is to be compared to the estimated systematic uncertainty, which is of the order of 30 MeV/c^2 for each of the two final state interaction processes. At present, there are no indications for large FSI biases.

The mass of the Higgs boson and the top quark

As explained in chapter 1, the mass of the W can be derived from a precise measurement of a chosen set of at least 18 Standard Model observables. The LEP electroweak working group performed Standard Model fits to the most recent experimental results excluding the W mass. The most recent Standard Model prediction for $\mathrm{M_W}$ from the LEP1, Tevatron and neutrino scattering data, including measurements of the top quark mass, is [129]:

$$\mathrm{M_W} = 80.387 \pm 0.025 \ \mathrm{GeV}/c^2.$$

The preliminary direct measurements of $\mathrm{M_W}$ and the mass of the top quark at the time of ICHEP 2000 are compared to the indirect measurements in figure 8.2. These masses are the main uncertainties in the prediction of the mass of the Higgs boson, that is included in the figure. The left-hand boundary at $\mathrm{M_H} = 113.3$ GeV/c^2 corresponds to the 95% CL limit from direct Standard Model Higgs searches at LEP [137].

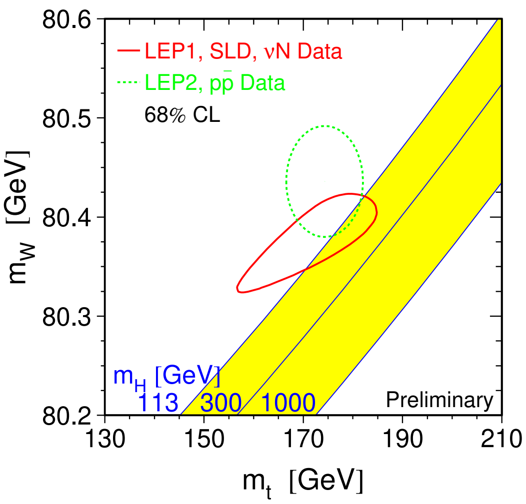

Figure 8.2: Preliminary comparison between the direct and the indirect measurements of the mass of the W and the top quark. At present, the measurements are in good agreement.

The Standard Model prediction for the mass of the Higgs is derived as well from Standard Model fits by the LEP electroweak working group. The most recent publication uses the contributions of LEP and Tevatron measurements to the

1999 summer conferences [34]. The combined LEP result for M_W at this time had an uncertainty of 56 MeV/c^2, to be compared to 46 MeV/c^2 at the time of the 2000 summer conferences. Including the mass of the W in the fit to the available experimental data improves the indirect measurement of the higgs mass from $M_H = 81^{+77}_{-42}$ GeV/c^2 to $M_H = 77^{+69}_{-39}$ GeV/c^2. The result of the fits is derived in terms of $\log M_H$ and the uncertainty in this prediction is therefore only Gaussian if the mass is expressed accordingly. The most recent upper limit from Standard Model fits presented at ICHEP 2000 is [129]:

$$M_H \leq 170 \text{ GeV}/c^2 \quad (95\% \text{ CL}).$$

8.5 Combination of the world results for Γ_W

The LEP, SPS and Tevatron measurements of Γ_W are listed in sections 8.5.1 and 8.5.2 and the evaluation of the world average measurement of the W width is described in 8.5.3.

8.5.1 LEP experiments Γ_W combination

All four LEP collaborations have measured the width from the direct reconstruction of the W bosons in the event, by generalising their mass fit method to a two parameter fit in which M_W and Γ_W vary freely.

The LEP results that are used in the combination for the final world average width use data up to a centre-of-mass energy of ~183 GeV:

$$\begin{aligned} OPAL\ [134]: \quad \Gamma_W = &\quad 1.84 \pm 0.32(\text{stat.}) \pm 0.20(\text{syst.}) \text{ GeV}/c^2 \\ DELPHI\ [135]: \quad \Gamma_W = &\quad 2.38 \pm 0.40(\text{stat.}) \pm 0.10(\text{syst.}) \text{ GeV}/c^2 \\ L3\ [136]: \quad \Gamma_W = &\quad 1.97 \pm 0.38 \text{ GeV}/c^2. \end{aligned}$$

The results used in the preliminary combination at the time of the ICHEP 2000 conference are shown in figure 8.3.

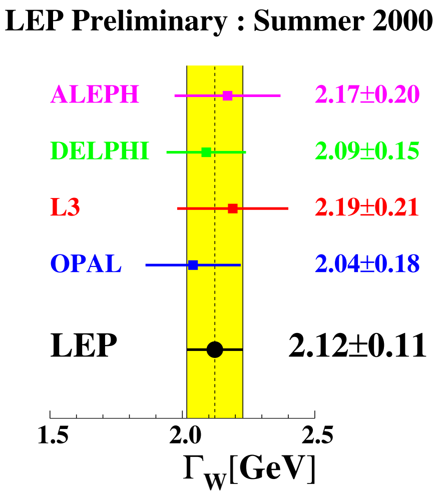

Figure 8.3: Preliminary combination of LEP results for Γ_W.

8.5.2 Γ_W results from $p\bar{p}$ colliders

The other measurements of the width are performed by the DO, the CDF, the UA1 and the UA2 collaborations. The UA1 and UA2 measurements are obtained from collisions in the CERN $p\bar{p}$ collider at a centre-of-mass energy of 630 GeV. The Tevatron operates at E_{cms}= 1.8 TeV as mentioned in section 8.4.2. The results are:

$$
\begin{aligned}
CDF\ [138]: \quad \Gamma_W &= \quad 2.11 \pm 0.28(\text{stat.}) \pm 0.16(\text{syst.})\ \text{GeV}/c^2 \\
CDF\ [139]: \quad \Gamma_W &= \quad 2.064 \pm 0.060(\text{stat.}) \pm 0.059(\text{syst.})\ \text{GeV}/c^2 \\
D0\ [140,\ 141]: \quad \Gamma_W &= \quad 2.152 \pm 0.066\ \text{GeV}/c^2 \\
UA1\ [142]: \quad \Gamma_W &= \quad 2.10 \pm 0.14(\text{stat.}) \pm 0.09(\text{syst.})\ \text{GeV}/c^2 \\
UA2\ [143]: \quad \Gamma_W &= \quad 2.18 \pm 0.25(\text{stat.}) \pm 0.04(\text{syst.})\ \text{GeV}/c^2,
\end{aligned}
$$

where only the first measurement is obtained from the direct reconstruction of W bosons. The high-mass tail of the transverse mass spectrum of W $\rightarrow e\nu$ decays is compared with Monte Carlo predictions to find the best fitting value for Γ_W.

The indirect Tevatron measurements are obtained from the ratio of Z $\rightarrow ll$ to W $\rightarrow l\nu$ decays. Experimental LEP results for the cross sections and the Z $\rightarrow ll$ branching ratio are used to extract the full width of the W.

8.5.3 The world average W width

The published LEP measurements (up to 183 GeV) are combined with the results from $p\bar{p}$ colliders listed in section 8.5.2 to obtain the present world average value for Γ_W [45]:

$$\Gamma_W = 2.12 \pm 0.05 \text{ GeV}/c^2.$$

The Standard Model prediction for the width is [45, 70]:

$$\Gamma_W = 2.067 \pm 0.021 \text{ GeV}/c^2,$$

in good agreement with both the final world average and the preliminary LEP measurement quoted in figure 8.3 in section 8.5.1.

Chapter 9

Summary and conclusions

In this thesis, a measurement of the mass and width of the W from the direct reconstruction of W bosons in the ALEPH detector is described. A precise measurement of the mass of the W is of importance because it is not predicted by the Standard Model and it can be used as input for the prediction of other Standard Model parameters, such as the mass of the Higgs boson. Since the Standard Model is over constrained, the result of a direct measurement of the W mass can be compared to a Standard Model prediction that is derived from a fit to a well chosen set of measured Standard Model observables. This allows a cross check of the internal consistency of the Standard Model.

The width of the W can be calculated from the Standard Model, and a comparison between a measurement and the Standard Model prediction allows a test of the model. Discrepancies can be due to the presence of non-Standard Model particles, but theoretical implications of a discrepancy are not straight forward and the aim of the measurement described in this thesis is to allow a cross check of the Standard Model width and not to obtain a model independent measurement of Γ_{W}. Since the Standard Model is used for the calculation of the cross section and the branching ratios and for the generation of the expected distributions for the mass estimator, as well as the background distributions, the results in this thesis are to be interpreted within the framework of the Standard Model only.

If the resolution of the ALEPH detector is not simulated correctly, the width measurement is affected. These effects are taken into account as systematic uncertainties on both the mass and the width measurements. If the Standard Model is assumed to be valid, good agreement between the prediction and the measurement of the W width confirms that this uncertainty is not underestimated and that the detector resolutions are understood.

The selection of the W pairs used in the analysis is an improvement of the selection used for previously published ALEPH results. Previously, the selection was based on the assumption that the neutrino and the lepton that originate from the W $\rightarrow l\nu$ decay are produced back-to-back. This assumption holds at threshold ($E_{cms} \simeq$ 161 GeV). For the higher centre-of-mass energies analysed in this thesis, a new algorithm is implemented for the selection of the lepton, based on its high momentum and its isolation with respect to the other charged tracks in the event.

Leptons escaping through cracks in the calorimeters or the muon chambers are recovered by combining the information from both ECAL and HCAL. These two independent improvements in the selection of the high energy lepton improve the $4f$ efficiency of the selection by 5.6±0.5% in the $e\nu\mathrm{q\bar{q}}$ and 5.0±0.5% in the $\mu\nu\mathrm{q\bar{q}}$ channel respectively, before any additional selection cuts are applied.

Events with a low momentum lepton candidate are removed to reduce the background, most importantly due to $\mathrm{q\bar{q}}(\gamma)$ events. A new cut is introduced to remove Bhabha and $\gamma\gamma$ events that pass this cut in the $e\nu\mathrm{q\bar{q}}$ channel.

The probability for an event to be a signal event is parameterised as a function of the lepton momentum, the transverse missing momentum in the event and the isolation of the lepton. This parameterisation is derived from Monte Carlo samples of signal and background processes. In the $e\nu\mathrm{q\bar{q}}$ channel, $\gamma\gamma$ events are added to the background simulation to ensure the removal of these events from the final sample. A cut on this signal probability is optimised as a function of the quality of the selection.

The selection efficiency for events originating from the three dominant W pair production (CC03) processes is 82.0% in the $e\nu\mathrm{q\bar{q}}$ channel and 88.1% in the $\mu\nu\mathrm{q\bar{q}}$ channel, with purities of 92.4% and 93.3% respectively. A total of 367 events pass the $e\nu\mathrm{q\bar{q}}$ selection and 398 events pass the $\mu\nu\mathrm{q\bar{q}}$ selection at E_{cms}= 188.6 GeV, in good agreement with the expected number of events. Many comparisons between data and Monte Carlo are done to ensure no discrepancies are present in the selected sample.

For the preliminary measurements at higher energies, the selection is not optimised. A total of 1084 events are selected, in good agreement with the expectation. If the number of events are compared in each channel and for each energy separately they are also in good agreement.

The mass of the W is reconstructed from a kinematic fit that uses the measured LEP beam energy to impose energy and momentum conservation in the event. The masses are forced to be equal to improve the resolution on the mass estimator, referred to as the 2C event mass. Only events with a fitted mass between 70 and 90 GeV/c^2 are used in the analysis.

The measured 2C mass distribution is compared to Monte Carlo distributions for different values of $\mathrm{M_W}$ and Γ_W. The background consists of $\mathrm{q\bar{q}}$, $\mathrm{Z}ee$, ZZ, $\mathrm{W}e\nu$ and $\tau\tau$ events. Large Monte Carlo samples of these background processes are simulated and added to the reconstructed mass distribution. A shape fit is used to extract the mass and width, normalising the distribution to the number of observed data events at each step during the fit. The best fit is determined by maximising a binned likelihood with a bin size of $\Delta\mathrm{M_{2C}} = 500$ MeV/c^2. Corrections for the cross section as a function of the mass and the efficiency as a function of the width are implemented to ensure a proper normalisation of the signal with respect to the background.

Large sets of Monte Carlo samples with the same size as the data are used to determine the expected statistical uncertainty on the measurements. The distributions of the fitted mass and width and their uncertainties are found to be Gaussian.

Samples are generated at various mass and width values to check the linearity of the fit as a function of the two parameters. A possible offset of the W mass linearity fit in the $\mu\nu\mathrm{q\bar{q}}$ channel is thoroughly investigated. After many studies, no systematic cause is found and the shift is assumed to be due to a statistical fluctuation. If the samples for both channels are included in the same fit, the offset is found to be $\Delta\mathrm{M_W} = +18\pm7\pm6$ MeV/c^2. If this were taken into account as an additional systematic uncertainty on the combined result, the total systematic error increases from 52 to 55 MeV/c^2.

The systematic uncertainties are evaluated for the two channels separately. For each contribution, a large sample of Monte Carlo events is systematically altered and fitted using the standard fit method. The shift in the fit result with respect to the standard sample is taken into account as systematic uncertainty on the measurement.

New systematic studies are introduced with respect to previous years because of the sensitivity of the width to the detector resolutions. Uncertainties in the resolution and bias of the lepton and jet angles are investigated, as well as uncertainties in the energy and momentum resolutions and the calibration of the calorimeters.

Uncertainties due to the background and the beam energy are evaluated as well as theoretical uncertainties due to the choice of the jet fragmentation model, higher order initial state radiation and the limited statistics of the reference sample.

The combined systematic uncertainty for the mass is found to be 69 MeV/c^2 in the $e\nu\mathrm{q\bar{q}}$ and 41 MeV/c^2 in the $\mu\nu\mathrm{q\bar{q}}$ channel respectively. For the width, these values are 0.13 GeV/c^2 and 0.10 GeV/c^2.

The systematic uncertainties in the electron channel exceed the uncertainties in the muon channel. Firstly, most high energy muons pass through the detector without losing significant amounts of energy. Bremsstrahlung and final state radiation affect the measurement of the electron. The momentum of the muon is therefore better reconstructed than the momentum of the electron and the $e\nu\mathrm{q\bar{q}}$ channel is therefore more sensitive to systematic uncertainties in the jets. Secondly, electrons are found in many background processes. Therefore, the electron selection is of lesser quality than the muon selection and uncertainty due to the background is larger.

For both the mass and the width measurement, the detector uncertainties and the uncertainty in the jet fragmentation model are the main contributions. The systematic uncertainty on the width is mainly due to three contributions; the resolution on both the lepton momentum and the jet energy, and the fragmentation uncertainty.

The uncertainty on the fragmentation is estimated from the difference between two theoretical models. The cause of the shift in the fitted values for these two models is presently under investigation. The aim is to identify the variables that are causing the shift and to use discrepancies between the data and the default theoretical model rather than the difference between two models to evaluate the uncertainty.

Fit results

After all cuts, 330 $e\nu q\bar{q}$ and 360 $\mu\nu q\bar{q}$ events remain at E_{cms}= 188.6 GeV, in good agreement with expectations. Comparisons between data and Monte Carlo distributions show good agreement. The fit to the data at E_{cms}= 188.6 GeV yields:

$$\begin{aligned} M_W &= 80.313 \pm 0.119(\text{stat.}) \pm 0.052(\text{syst.}) \text{ GeV}/c^2 \\ \Gamma_W &= 2.17^{+0.29}_{-0.26}(\text{stat.}) \pm 0.11(\text{syst.}) \text{ GeV}/c^2. \end{aligned}$$

If the preliminary measurements at higher energies are combined with these results, the fitted values are:

$$\begin{aligned} M_W &= 80.537 \pm 0.079(\text{stat.}) \pm 0.052(\text{syst.}) \text{ GeV}/c^2 \\ \Gamma_W &= 2.11^{+0.20}_{-0.18}(\text{stat.}) \pm 0.11(\text{syst.}) \text{ GeV}/c^2. \end{aligned}$$

Both results are in agreement with the ALEPH mass results published previously. The data described in this thesis is not included in the final world average mass [45]:

$$M_W = 80.419 \pm 0.056 \text{ GeV}/c^2.$$

If all uncertainties are added in quadrature, the mass measurement at 188.6 GeV agrees with this result within 0.7 standard deviation and the preliminary measurement up to 201.6 GeV agrees within 1.1 standard deviation.

The width is in agreement with the world average: $\Gamma_W = 2.12 \pm 0.05$ GeV/c^2 and with the theoretical Standard Model calculation [45, 70]:

$$\Gamma_W = 2.067 \pm 0.021 \text{ GeV}/c^2.$$

However, this thesis describes a measurement of the broadness of the distribution of the W mass assuming the Standard Model to be valid. It is therefore to be used as a cross check of the Standard Model width only, and not as a model independent measurement of the W width.

The stability of the results is investigated for different sizes of the bins used in the fit, cuts on the signal probability, cuts on the upper χ^2 probability of the kinematic fit and definitions of the upper mass window. The results at E_{cms}= 188.6 GeV are found to be stable. For the preliminary measurements at higher energies, a shift of the order of 3 standard deviations is found if a cut on the upper χ^2 probability is imposed. However, this significance can be overestimated because the fit methods are not fully correlated and many systematic uncertainties have a large RMS. For the final result at these energies, this shift is to be investigated further.

The official ALEPH measurement for $\mathrm{M_W}$ is combined with measurements of the other LEP collaborations and measurements from Fermilab to obtain the preliminary mass measurement [129]:

$$\mathrm{M_W} = 80.434 \pm 0.037 \ \mathrm{GeV}/c^2.$$

This result is in good agreement with the Standard Model prediction, obtained from Standard Model fits to LEP1, Tevatron data and and neutrino scattering experiments. Multi-parameter fits to Standard Model observables, including the mass of the W, predict the mass of the Higgs to be less than 170 GeV/c^2, at 95% CL [129].

Preliminary mass measurements from the $l\nu\mathrm{q\bar{q}}$ and $\mathrm{q\bar{q}q\bar{q}}$ channels are in good agreement, indicating that final state interactions do not significantly bias the mass measurement in the $\mathrm{q\bar{q}q\bar{q}}$ channel.

Appendix A

Definitions and derivations

A.1 Renormalisation

The running coupling is defined as a function of the exchanged momentum q^2. When the theory is defined in this way, the series of Feynman diagrams contributing to a certain observable process converges again, but a cutoff momentum μ needs to be defined up to which scale the parameterisation is valid.

The running coupling constant for the electromagnetic interaction is defined as:

$$\alpha(q^2) = \frac{\alpha^0}{1 - \frac{\alpha^0}{3\pi}\ln\left(\frac{q^2}{\mu^2}\right)}, \tag{A.1}$$

where $\alpha^0 = \alpha(\mu^2)$. As q^2 increases, the coupling increases. This is observed experimentally as the effective charge of a particle increases with decreasing distance. This effect is known as electromagnetic charge screening.

The running coupling for the strong interaction is defined as:

$$\alpha_s(q^2) = \frac{\alpha_s^0}{1 + \frac{\alpha_s^0}{12\pi}(11n - 2f)\ln\left(\frac{q^2}{\mu^2}\right)} \tag{A.2}$$

$$\approx \frac{12\pi}{(11n - 2f)\log\left(\frac{q^2}{\Lambda^2}\right)}, \tag{A.3}$$

where Λ^2 is the scale at which the second term in the denominator dominates and the coupling becomes large. n is the number of colours, and f the number of flavours in the theory. In case of the Standard Model there are three colours and six flavours $(11n - 2f = 19)$.

Since $11n > 2f$, the strength of the strong interaction increases with decreasing q^2 or increasing distance between the interacting particles. At large values of q^2, or very short distances, quarks behave as free particles. This is known as *asymptotic freedom*. At small values of q^2, or long distances, the coupling of the strong interaction increases. As a result, strong interacting particles are not observed separately but always part of a bigger structure. This characteristic is known as the *confinement* of the strong interaction.

As a result of the long range of the interaction, QCD calculations cannot be done analytically. A solution is to use a lattice in space and time to approximate observables numerically, but *lattice* QCD calculations still result in significant uncertainties in predictions for the strong interaction.

A.2 The lowest order W pair cross section

Define the momenta of the in-going electron and positron as p and q, and the momentum of the outgoing W^- and W^+ as k and l. The Mandelstam variables are used to define the momentum exchanged by the propagators:

$$\begin{aligned} s &= (p+q)^2 = (k+l)^2 \\ t &= (p-k)^2 = (q-l)^2. \end{aligned} \tag{A.4}$$

If $\mathrm{m}_e = 0$, the electron and positron have opposite helicities ($\equiv \pm h$). The helicities of the $\mathrm{W}^\pm$ bosons are defined as h_+ and h_- respectively.

The differential cross section for W pair production of unpolarised Ws and electrons is given by (equation 2.33):

$$\begin{aligned} \frac{d\sigma}{d\Omega} &= \frac{\beta}{64\pi^2 s} \times \frac{1}{2} \sum_{h,h_+,h_-} |\mathcal{M}(h,h_+,h_-,s,t)|^2 \\ &\equiv \frac{\beta}{64\pi^2 s} |\mathcal{M}(s,t)|^2. \end{aligned} \tag{A.5}$$

Introduce the abbreviated notation $\gamma^\mu p_\mu \equiv \not{p}$. Define $\mathcal{M} \equiv \mathcal{M}(h,h_-,h_+,s,t)$ and $\epsilon^*(v) \equiv \epsilon^*(v,h_\pm)$, for a W with momentum v. According to the Feynman rules, the matrix element for the neutrino exchange process is given by:

$$-i\mathcal{M}_\nu = \bar{v}(q) \left(\frac{-ig}{\sqrt{2}} \gamma^\mu \frac{1}{2}(1-\gamma_5) \right) \epsilon^*_\mu(l) \left(\frac{i(\not{p}-\not{k})}{|p-k|^2} \right) \epsilon^*_\nu(k) \left(\frac{-ig}{\sqrt{2}} \gamma^\nu \frac{1}{2}(1-\gamma_5) \right) u(p)$$

$$\begin{aligned}
\mathcal{M}_\nu &= \frac{e^2}{2\sin^2\theta_\mathrm{W} t}\ \bar{v}(q)\ \gamma^\mu \frac{1}{2}(1-\gamma_5)\ \epsilon^*_\mu(l)\ (\not{p}-\not{k})\ \epsilon^*_\nu(k)\ \gamma^\nu \frac{1}{2}(1-\gamma_5)\ u(p) \\
&= \frac{e^2}{4\sin^2\theta_\mathrm{W} t}\ \bar{v}(q)\ \not{\epsilon}^*(l)\ (\not{p}-\not{k})\ \not{\epsilon}^*(k)\ (1-\gamma_5)\ u(p) \\
&= \frac{e^2}{2\sin^2\theta_\mathrm{W} t}\ \bar{v}(q)\ \not{\epsilon}^*(l)\ (\not{p}-\not{k})\ \not{\epsilon}^*(k)\ u_L(p) \\
&\equiv \frac{e^2}{2\sin^2\theta_\mathrm{W} t}\ \bar{v}(q)\ S\ u_L(p), \qquad \text{(A.6)}
\end{aligned}$$

where

$$S = \not{\epsilon}^*(l)\ (\not{p}-\not{k})\ \not{\epsilon}^*(k). \qquad \text{(A.7)}$$

The matrix element for the photon annihilation process is given by:

$$\begin{aligned}
-i\mathcal{M}_\gamma &= \bar{v}(q)(ie\gamma^\mu)u(p)\left(\frac{-ig_{\mu\nu}}{|p+q|^2}\right) \times \\
&\quad \epsilon^*_\tau(k)(-ie[g^{\nu\sigma}(p+q+l)^\tau + g^{\sigma\tau}(k-l)^\nu + g^{\nu\tau}(-k-p-q)^\sigma])\epsilon^*_\sigma(l) \\
\mathcal{M}_\gamma &= \frac{e^2}{s}\bar{v}(q)\gamma^\mu u(p) g_{\mu\nu}\epsilon^*_\tau(k)[g^{\nu\sigma}(k+2l)^\tau + g^{\sigma\tau}(k-l)^\nu + g^{\nu\tau}(-2k-l)^\sigma]\epsilon^*_\sigma(l) \\
&\equiv \frac{e^2}{s}\ \bar{v}(q)\ T\ u(p), \qquad \text{(A.8)}
\end{aligned}$$

where

$$\begin{aligned}
T &= \gamma^\mu g_{\mu\nu}\epsilon^*_\tau(k)[g^{\nu\sigma}(k+2l)^\tau + g^{\sigma\tau}(k-l)^\nu + g^{\nu\tau}(-2k-l)^\sigma]\epsilon^*_\sigma(l) \\
&= \gamma^\mu g_{\mu\nu}[\epsilon^*(k)\cdot(k+2l)(\epsilon^*(l))^\nu + (k-l)^\nu(\epsilon^*(k)\cdot\epsilon^*(l)) - (\epsilon^*(k))^\nu(2k+l)\cdot\epsilon^*(l)] \\
&= 2(\epsilon^*(k)\cdot l)\ \not{\epsilon}^*(l) - 2\not{\epsilon}^*(k)\ (k\cdot\epsilon^*(l)) + (\epsilon^*(k)\cdot\epsilon^*(l))\ (\not{k}-\not{l}). \qquad \text{(A.9)}
\end{aligned}$$

For the Z annihilation process follows:

$$\begin{aligned}
-i\mathcal{M}_\mathrm{Z} &= \bar{v}(q)\left(\frac{-ig\gamma^\mu}{2\cos\theta_\mathrm{W}}\right)(c_v^e - c_A^e\gamma^5)u(p)\left(\frac{-ig_{\mu\nu}}{|p+q|^2 - \mathrm{M_Z}^2}\right) \times \\
&\quad \epsilon^*_\tau(k)(-ig\cos\theta_\mathrm{W}[g^{\nu\sigma}(p+q+l)^\tau + g^{\sigma\tau}(k-l)^\nu + g^{\nu\tau}(-k-p-q)^\sigma])\epsilon^*_\sigma(l) \\
\mathcal{M}_\mathrm{Z} &= \frac{e^2}{2\sin^2\theta_\mathrm{W}(s-\mathrm{M_Z}^2)}\ \bar{v}(q)\ T\ \left(\frac{1}{2} - \frac{1}{2}\gamma^5 - 2\sin^2\theta_\mathrm{W}\right)\ u(p) \\
&= \frac{e^2}{s-\mathrm{M_Z}^2}\ \bar{v}(q)\ T\ \left(\frac{1}{2\sin^2\theta_\mathrm{W}}\ u_L(p) - u(p)\right). \qquad \text{(A.10)}
\end{aligned}$$

The total amplitude is therefore given by:

$$\mathcal{M}_{\nu\gamma\mathrm{Z}} = \bar{v}(q)\ (c_\nu S + c_{\gamma\mathrm{Z}} T)\ u(p), \qquad \text{(A.11)}$$

where, if $\delta_L u(p) = u_L(p)$,

$$\begin{aligned} c_\nu &= \frac{e^2\delta_L}{2\sin^2\theta_{\mathrm{W}} t} \\ c_{\gamma\mathrm{Z}} &= \frac{e^2}{s} + \frac{e^2}{s-\mathrm{M_Z}^2}\left(\frac{1}{2\sin^2\theta_{\mathrm{W}}}\delta_L - 1\right). \end{aligned} \tag{A.12}$$

To obtain the cross section, one needs to calculate $|\mathcal{M}(s,t)|^2$ in equation A.5 and therefore the terms $\mathcal{M}(h, h_+, h_-, s, t)$ for each of the possible combinations of the W polarisations. If the beam direction is chosen along the z-axis, the momenta $p,\ q,\ k$ and l are defined by the beam energy E, the W velocity $\beta = \sqrt{1-\mathrm{M_W}^2/E^2}$ and the scattering angle between the positron and the W^+, θ. For the Mandelstam variables in equation A.4 this results in:

$$\begin{aligned} s &= E^2 \\ t &= E^2(1+\beta^2-2\beta\cos\theta). \end{aligned} \tag{A.13}$$

The three possible polarisation vectors $\epsilon^*(v, h_\pm)$ for $\mathrm{W}^\pm$ can be defined in the centre-of-mass frame as a function of the kinematic variables E, β and θ. As a result, the total amplitude $\mathcal{M}_{\nu\gamma\mathrm{Z}}(h_+, h_-) \equiv \mathcal{M}_{\nu\gamma\mathrm{Z}}(h, h_+, h_-, s, t)$ can be evaluated for each of the W polarisations [62], if $\delta \equiv 1$ for left-handed electrons and $\delta \equiv 0$ for right-handed electrons:

$$\begin{aligned} \mathcal{M}_{\nu\gamma\mathrm{Z}}(\pm1,\mp1) &= \frac{e^2 s}{4\sin^2\theta_{\mathrm{W}} t}(\cos\theta \mp 2h)\delta\sin\theta \qquad \text{(A.14)} \\ \mathcal{M}_{\nu\gamma\mathrm{Z}}(1,1) &= 4\mathrm{M_W}^2 e^2\left[\frac{\delta}{2\beta\sin^2\theta_{\mathrm{W}}}\left(\frac{1}{s}+\frac{1}{4t}\right) - a\beta\right]\sin\theta \\ \mathcal{M}_{\nu\gamma\mathrm{Z}}(0,\pm1) &= 2\sqrt{2s}e^2\mathrm{M_W}\left[a\beta - \frac{\delta}{2\sin^2\theta_{\mathrm{W}}}\left(\frac{1}{s\beta}+\frac{1\mp 2h\beta}{4\beta t}\right)\right](\cos\theta \pm 2h) \\ \mathcal{M}_{\nu\gamma\mathrm{Z}}(0,0) &= 2e^2\left[\frac{\delta}{2\sin^2\theta_{\mathrm{W}}}\left(\frac{\beta}{2} - \frac{1}{\beta}\left\{\frac{\mathrm{M_W}^2}{t}+1\right\}\right) + a\beta(s+2\mathrm{M_W}^2)\right]\sin\theta, \end{aligned}$$

where

$$a = \frac{1}{4\cos^2\theta_{\mathrm{W}}(s-\mathrm{M_Z}^2)}\left(\frac{\delta}{2\sin^2\theta_{\mathrm{W}}} - 1\right) \tag{A.15}$$

The other amplitudes are given by $\mathcal{M}_{\nu\gamma\mathrm{Z}}(\mp1,0) = \mathcal{M}_{\nu\gamma\mathrm{Z}}(0,\pm1)$ and $\mathcal{M}_{\nu\gamma\mathrm{Z}}(-1,-1) = \mathcal{M}_{\nu\gamma\mathrm{Z}}(1,1)$, as long as the CP violating contributions are neglected.

A.3 The decay width of the W

The partial width of the W, $\Gamma_{\mathrm{W}}(\mathrm{W} \to f_1 f_2)$, is related to the amplitude $\mathcal{M}$ according to equation 2.37. Because the W decay does not have a preferred direction, the integration over Ω results in a multiplication factor of 4π:

$$\Gamma_{\mathrm{W}}(\mathrm{W} \to f_1 f_2) = \frac{|p|}{8\pi {\mathrm{M_W}}^2} |\mathcal{M}|^2, \tag{A.16}$$

where p is the momentum of one of the fermions.

The lowest order width for the leptonic decay channel ($\mathrm{W} \to l\nu$) is derived from the matrix element :

$$\mathcal{M} = \epsilon_\mu \bar{u}(p) \left(\frac{-ie\gamma^\mu (1-\gamma^5)}{2\sqrt{2}\sin\theta_{\mathrm{W}}} \right) v(q), \tag{A.17}$$

where p and q are the momenta of the lepton and the anti-lepton respectively. The hadronic decay ($\mathrm{W} \to \mathrm{q}\bar{\mathrm{q}}$) is described by the same expression, except for an additional multiplication factor $V_{\mathrm{q}\bar{\mathrm{q}}}$ that enters in the vertex. $V_{\mathrm{q}\bar{\mathrm{q}}}$ is the element of the CKM matrix corresponding to the final state quark pair.

For the decay of an unpolarised sample of W bosons, the width is derived by taking the average over the three W polarisations λ and the sum over the fermion spins states s. The square of the amplitude equals:

$$|\mathcal{M}|^2 = \frac{1}{3} \sum_\lambda \sum_s \mathcal{M}^*(s,\lambda)\mathcal{M}(s,\lambda). \tag{A.18}$$

The sum over the W polarisation states and the fermion spins is as in equation 2.27. If the momentum of the W equals k, the result is:

$$|\mathcal{M}|^2 = \frac{e^2 V_{f\bar{f}}^2}{12\sin^2\theta_{\mathrm{W}}} \mathrm{tr}[(\not{p} + m_{f1})\gamma^\mu(\not{q} + m_{f2})\gamma^\nu(1-\gamma^5)](-g_{\mu\nu} + k_\mu k_\nu/{\mathrm{M_W}}^2). \tag{A.19}$$

The anti-symmetric γ^5 term disappears when multiplied with the symmetric term $(-g_{\mu\nu} + k_\mu k_\nu/{\mathrm{M_W}}^2)$. If the fermion masses m_{f1} and m_{f2} are small compared to $\mathrm{M_W}$ (and therefore small compared to p and q), the trace theorems, in for example [41], can be used to derive:

$$\begin{aligned} |\mathcal{M}|^2 &= \frac{e^2 V_{f\bar{f}}^2}{3\sin^2\theta_{\mathrm{W}}} [p^\mu q^\nu + q^\mu p^\nu - g^{\mu\nu}(p\cdot q)](-g_{\mu\nu} + k_\mu k_\nu/{\mathrm{M_W}}^2) \\ &= \frac{e^2 V_{f\bar{f}}^2}{3\sin^2\theta_{\mathrm{W}}} [(p\cdot q) + 2(k\cdot p)(k\cdot q)/{\mathrm{M_W}}^2] \\ &= \frac{e^2 V_{f\bar{f}}^2 {\mathrm{M_W}}^2}{3\sin^2\theta_{\mathrm{W}}}, \end{aligned} \tag{A.20}$$

where $V_{f\bar{f}}^2 = 1$ if f_1 and f_2 are leptons. The last step follows since $2(p \cdot q) = 2(k \cdot p) = 2(k \cdot q) = \mathrm{M_W}^2$ if the masses of the fermions are neglected. Also, $p_f = \mathrm{M_W}/2$ and according to equation A.16:

$$\Gamma_{\mathrm{W}}(\mathrm{W} \rightarrow f_1 f_2) = \frac{|\mathcal{M}|^2}{16\pi \mathrm{M_W}} = \frac{e^2 V_{f\bar{f}}^2 \mathrm{M_W}}{48\pi \sin^2\theta_{\mathrm{W}}}, \tag{A.21}$$

The muon is an unstable particle and decays according to $(\mu^- \rightarrow e^- \bar{\nu}_e \nu_\mu)$ with a lifetime of $\tau_\mu = 2.20 \times 10^{-6}$ s, measured to a precision of about 0.002% [45]. The coupling strength of the μ to the W is set by the Fermi coupling constant G_{F} [41]:

$$G_{\mathrm{F}} = \frac{\sqrt{2}e^2}{8\sin^2\theta_{\mathrm{W}} \mathrm{M_W}^2}. \tag{A.22}$$

Since this constant is known with high precision, the width of the W is expressed in terms of G_{F}:

$$\Gamma_{\mathrm{W}}(\mathrm{W} \rightarrow f_1 f_2) = \frac{G_{\mathrm{F}} V_{f\bar{f}}^2 \mathrm{M_W}^3}{6\sqrt{2}\pi}. \tag{A.23}$$

To obtain the full width of the W, the expression in equation A.23 has to be summed over all possible lepton and quark pairs N_l and N_q, and the number of quark colours N_c. Strong higher order corrections result in an additional multiplication factor in case of hadronic W decay [62, 69]. The final result is:

$$\begin{aligned}\Gamma_{\mathrm{W}} &= \frac{G_{\mathrm{F}} \mathrm{M_W}^3}{6\sqrt{2}\pi} \left\{ N_l + N_c \sum_{ij} V_{ij}^2 \left[1 + \frac{\alpha_s}{\pi} + \mathcal{O}\left(\frac{\alpha_s^2}{\pi^2}\right) \right] \right\} \\ &= \frac{G_{\mathrm{F}} \mathrm{M_W}^3}{2\sqrt{2}\pi} \left[3 + 2\frac{\alpha_s}{\pi} + \mathcal{O}\left(\frac{\alpha_s^2}{\pi^2}\right) \right]. \end{aligned} \tag{A.24}$$

The sum over the CKM matrix elements $\sum_{ij} V_{ij}^2 \approx 2$ because the W is too light to produce a top quark in the final state. The elements $V_{u\bar{d}}$ and $V_{c\bar{s}}$ (in the case of a W^+) add up to about 1.9 of the total, the off-diagonal terms contribute a further 0.1.

Most electroweak corrections have already been absorbed in the definition of G_{F} and/or the physical value of $\mathrm{M_W}$. As a result, virtual electroweak and soft photonic corrections add only a small ($\mathcal{O}(0.1-1\%)$) correction δ^{SM} to the expression in equation A.24 [70]:

$$\Gamma_{\mathrm{W}} = \frac{G_{\mathrm{F}} \mathrm{M_W}^3}{2\sqrt{2}\pi} \left[3 + 2\frac{\alpha_s}{\pi} + \mathcal{O}\left(\frac{\alpha_s^2}{\pi^2}\right) \right] (1 + \delta^{SM}), \tag{A.25}$$

where δ^{SM} depends on assumptions on the mass of the top quark and the Higgs boson.

References

[1] J. C. Thompson *et al.* (The ALEPH collaboration), *Measurement of the W Mass in e^+e^- Collisions from 161 GeV to 189 GeV*, ALEPH 99-017, presented at the Int. Eur. Conf. on High-Energy Physics (EPS-HEP99), Tampere, Finland, 15-21 July (1999).

[2] R. Barate *et al.* (The ALEPH collaboration), *Measurement of the W Mass and Width in e^+e^- Collisions at 189 GeV*, CERN-EP-2000-052, submitted to Phys. Lett. **B**.

[3] R. Barate *et al.* (The ALEPH collaboration), *Measurement of the W Mass and Width in e^+e^- Collisions at $\sqrt{s} \simeq$ 192 - 202* GeV, ALEPH 2000-018, CONF2000-015 (2000).

[4] J. Dalton, *A new System of Chemical Philosophy, Vol.I(I)*, 1808, reprinted by William Dawson and Sons Ltd., London, UK (1953).

[5] W. C. Röntgen, *A New Kind of Rays*, Nature **53**, 274 (1896).

[6] A. Einstein, *On a Heuristic Point of View about the Creation and Conversion of Light*, Ann. Phys. Chem. **17**, 132 (1905).

[7] A. Einstein, *On Electrodynamics of Moving Bodies*, Ann. Phys. Chem. **17**, 891 (1905).

[8] J. J. Thomson, *Cathode Rays*, Phil. Mag. **44**, 293 (1897).

[9] E. Rutherford, *The Scattering of the Alpha and Beta Particles by Matter and the Structure of the Atom*, Phil. Mag. VI **21**, 669 (1911).

[10] N. Bohr, *On the Constitution of Atoms and Molecules*, Phil. Mag. **26**, 1 (1913).

[11] E. Rutherford, *Collision of Alpha Particles with Light Atoms IV; An Anomalous Effect in Nitrogen*, Phil. Mag. VI, **37**, 581 (1919).

[12] P. A. M. Dirac, *The Quantum Theory of the Electron*, Proc. Roy. Soc. Lond. **A117**, 610 (1928).

[13] P. A. M. Dirac, *Quantized Singularities in the Electromagnetic Field*, Proc. Roy. Soc. Lond. **A133**, 60 (1931).

[14] C. D. Anderson, *The Apparent Existence of Easily Deflectable Positives*, Science **76**, 238 (1932).

[15] J. D. Jackson, *Classical Electrodynamics*, 2nd ed., John Wiley & Sons, New-York, USA (1975).

[16] W. Heisenberg and W. Pauli, *On Quantum Field Theory 1 and 2*, Z. Phys. **56**, 1 (1929) and **59**, 168 (1930).

[17] E. Fermi, *An Attempt of a Theory of Beta Radiation 1*, Z. Phys. **88**, 161 (1934).

[18] T. D. Lee, M. Rosenbluth and C. N. Yang, *Interaction of Mesons with Nucleons and Light Particles*, Phys. Rev. **75**, 905 (1949).

[19] S. Glashow, *Partial Symmetries of Weak Interactions*, Nucl. Phys. **22**, 579 (1961).

[20] S. Weinberg, *A Model of Leptons*, Phys. Rev. Lett. **19**, 1264 (1967).

[21] A. Salam, in: *Elementary Particle Theory*, 367 (1968), Proc. Nob. Symp. 1968, Lerum, Sweden; Ed. N. Svaratholm, Almquiat and Forlag, Stockholm, Sweden.

[22] F. Hasert *et al.* (The Gargamelle neutrino collaboration), *Observation of Neutrino like Interactions without Muon or Electron in the Gargamelle Neutrino Experiment*, Phys. Lett. **B46**, 138 (1973).

[23] G. Arnison *et al.* (The UA1 collaboration), *Experimental Observation of Lepton Pairs of Invariant Mass around 95 GeV/c^2 at the CERN SPS Collider*, Phys. Lett. **B126**, 398 (1983).

[24] P. Bagnaia *et al.* (The UA2 collaboration), *Evidence for $Z^0 \to e^+e^-$ at the CERN $\bar{p}p$ Collider*, Phys. Lett. **B129**, 130 (1983).

[25] G. Arnison *et al.* (The UA1 collaboration), *Experimental Observation of Isolated Large Transverse Energy Electrons With Associated Missing Energy at $\sqrt{s}$ = 540 GeV*, Phys. Lett. **B122**, 103 (1983).

[26] M. Banner *et al.* (The UA2 collaborartion), *Observation of Single Isolated Electrons of High Transverse Momentum in Events with Missing Transverse Energy at the CERN $\bar{p}p$ Collider*, Phys. Lett. **B122**, 476 (1983).

[27] General meeting of the American Physical Society (APS), New York, USA, Jan 24-27 (1983).

[28] J. Chadwick, *Possible Existence of a Neutron*, Nature **129**, 312 (1932).

[29] J. C. Street and E. C. Stevenson, *New Evidence for the Existence of a Particle of Mass Intermediate between the Proton and the Electron*, Phys. Rev. **52**, 1003 (1937).

[30] G. P. S. Occhialini and C. F. Powell, *Nuclear disintegration produced by slow charged particles of small mass*, Nature **159**, 186 (1947).

[31] M. Gell-Mann, *A Schematic Model of Baryons and Mesons*, Phys. Lett. **8**, 214 (1964).

[32] J. D. Bjorken and E. A. Paschos, *Inelastic Electron-Proton and γ-Proton Scattering and the Structure of the Nucleon*, Phys. Rev. **185**, 1975 (1969).

[33] P. W. Higgs, *Spontaneous Symmetry Breakdown Without Massless Bosons*, Phys. Rev. **145**, 1156 (1966).

[34] The LEP collaborations *et al.*, *A Combination of Preliminary Electroweak Measurements and Constraints on the Standard Model*, CERN-EP-2000-016 (2000).

[35] R. Barate *et al.* (The ALEPH collaboration), *Measurement of the Z Resonance Parameters at LEP*, Eur. Phys. Journ. **C14**, 1 (2000).

[36] The LEP collaborations *et al.*, *A Combination of Preliminary Electroweak Measurements and Constraints on the Standard Model*, CERN-PPE-96-183 (1996).

[37] D. Bardin and R. Kleiss *et al.*, *Event Generators for WW Physics*, in: *Physics at LEP2, Vol.2*, 3 (1996), CERN96-01, CERN, Geneva, Switzerland.

[38] T. Sjöstrand and V. A. Khoze, *On Colour Rearrangement in Hadronic W^+W^- Events*, Z. Phys. **C62**, 281 (1994).

[39] D. Decamp *et al.* (The ALEPH collaboration), *A Study of Bose-Einstein Correlations in e^+e^- Annihilation at 91 GeV*, Z. Phys. **C54**, 75 (1992).

[40] D. Griffiths, *Introduction to Elementary Particles*, John Wiley & Sons, Braun-Brumfield Inc., USA (1987).

[41] F. Halzen and A. D. Martin, *Quarks and Leptons*, John Wiley & Sons, Singapore, Malaysia (1984).

[42] M. Veltman, *Diagrammatica*, Cambridge Univ. Press, Cambridge, UK (1994).

[43] P. Renton, *Electroweak Interactions*, Cambridge Univ. Press, Cambridge, UK (1990).

[44] E. J. Eichten, K. D. Lane and M. E. Peskin, *New Tests for Quark and Lepton Substructure*, Phys. Rev. Lett. **50**, 811 (1983).

[45] D.E. Groom *et al.*, *2000 Review of Particle Physics*, Eur. Phys. Jour. **C15**, 1 (2000).

[46] C. W. Misner, K. S. Thorne and J. A. Wheeler, *Gravitation*, W. H. Freeman and co., San Fransisco, USA (1973).

[47] W. Pauli, *Relation between the Closing In of Electron-Groups in the Atom and the Structure of Complexes in the Spectrum*, Z. Phys. **31**, 765 (1925).

[48] U. Amaldi, W. de Boer and H. Fürstenau, *Comparison of Grand Unification Theories with Electroweak and Strong Coupling Constants Measured at LEP*, Phys. Lett. **B260**, 447 (1991).

[49] M. Goldhaber, L. Grodzins and A. W. Sunyar, *Helicity of Neutrinos*, Phys. Rev. **109**, 1015 (1958).

[50] H. Abramowicz *et al.*, *Limit on Righthanded Weak Coupling Parameters from Inelastic Neutrino Interactions*, Z. Phys. **C12**, 225 (1982).

[51] T. Bowcock *et al.*, *Search for the Production of Fractionally Charged Particles in e^+e^- Annihilations at $\sqrt{s}$ = 10.5 GeV*, Phys. Rev. **D40**, 263 (1989).

[52] A. Brignole, J. Ellis, G. Ridolfi and F. Zwirner, *The Supersymmetric Charged Higgs Boson Mass and LEP Phenomenology*, Phys. Lett. **B271**, 123 (1991).

[53] Y. Fukuda *et al.* (The Super-Kamiokande collaboration), *Evidence for Oscillation of Atmospheric Neutrinos*, Phys. Rev. Lett. **81**, 1562 (1998).

[54] R. P. Feynman, *Space-Time Approach to Nonrelativistic Quantum Electrodynamics*, Rev. Mod. Phys. **20**, 367 (1948).

[55] M. Kobayashi and K. Maskawa, *CP-violation in the Renormalisable Theory of the Weak Interaction*, Prog. Theor. Phys. **49**, 652 (1973).

[56] G. 't Hooft, *Renormalizable Lagrangians for Massive Yang-Mills Fields*, Nucl. Phys. **B35**, 167 (1971).

[57] R. P. Feynman, *The Theory of Positrons*, Phys. Rev. **76**, 749 (1949).

[58] S. Tomonaga, *On Infinite Field Reactions in Quantum Field Theory*, Phys. Rev. **74**, 224 (1948).

[59] J. Schwinger, *Quantum Electrodynamics, II and III*, Phys. Rev. **75**, 651 (1949) and **76**, 790 (1949).

[60] C. N. Yang and R. L. Mills, *Conservation of Isotopic Spin and Isotopic Gauge Invariance*, Phys. Rev. **96**, 191 (1954).

[61] K. R. Dienes, E. Dudas and T. Gherghetta, *TeV-Scale GUTs*, CERN-TH-98-245, hep-ph/9807522 (1998).

[62] W. Beenakker and A. Denner, *Standard-Model Predictions for W-Pair Production in Electron-Positron Collisions*, Int. J. Mod. Phys. **A9**, 4837 (1994).

[63] ICHEP 2000, *XXXth International Conference on High Energy Physics*, http://ichep2000.hep.sci.osaka-u.ac.jp/, Osaka, Japan, Jul 27 - Aug 2 (2000).

[64] A. Denner, S. Dittmaier, M. Roth and D. Wackeroth, *Four-Fermion Production with RacoonWW*, J. Phys. **G26**, 593 (2000).

[65] S. Jadach, W. Płacek, M. Skrzypek, B. F. L. Ward and Z. Wąs, *Exact $\mathcal{O}(\alpha)$ Gauge Invariant YFS Exponentiated Monte Carlo for (Un)stable W^+W^- Production at and beyond LEP2 Energies*, Phys. Lett. **B417**, 326 (1998).

[66] The LEP Collaborations *et al.*, *LEP W-pair, Z-pair and Single W Cross Section Results for the Summer 2000 Conferences*, LEPEWWG/XSEC/2000-01 (2000).

[67] J. Alitti *et al.* (The UA2 collaboration), *Experimental Limit on the Decay* $W^{\pm} \to \pi^{\pm}\gamma$ *at the CERN* $\bar{p}p$ *Collider*, Phys. Lett. **B277**, 203 (1992).

[68] G. Degrassi and A. Sirlin, *Comparative Analysis of Electroweak Corrections to* $e^+e^- \to f\bar{f}$ *in On-Shell and (MS) Frameworks*, Nucl. Phys. **B352**,342 (1991).

[69] K. G. Chetyrkin, J. H. Kühn and A. Kwiatkowski, *QCD Corrections to the* e^+e^- *Cross Section and the* Z *Boson Decay Rate: Concepts and Results*, Phys. Rept. **277**, 189 (1996).

[70] J. L. Rosner, M. P. Worah and T. Takeuchi, *Oblique Corrections to the W Width*, Phys. Rev. **D49**, 1363 (1994).

[71] G. Altarelli *et al.*, *Physics at LEP2, Vol.1*, CERN96-01, CERN, Geneva, Switzerland.

[72] R. G. Stuart, *Gauge Invariance, Analyticity and Physical Observables at the* Z^0 *Resonance*, Phys. Lett. **B262**, 113 (1991).

[73] A. Sirlin, *Theoretical Considerations Concerning the* Z^0 *Mass*, Phys. Rev. Lett. **67**, 2127 (1991).

[74] W. Press, S. Teukolsky, W. Vetterling and B. Flannery, *Numerical Recipies*, 2nd ed., Cambridge Univ. Press, Cambridge, UK (1992).

[75] S. Jadach, B. F. L. Ward and Z. Wąs, *The Monte Carlo Program KORALZ, Version 4.0, for the Lepton or Quark Pair Production at LEP/SLC Energies*, Comp. Phys. Comm. **79**, 503 (1994).

[76] M. Skrzypek, S. Jadach, W. Płaczek and Z. Wąs, *Monte Carlo Program KORALW 1.02 for W-Pair Production at LEP2/NLC Energies with Yennie-Frautschi-Suura Exponentiation*, Comp. Phys. Comm. **94**, 216 (1996).

[77] T. Sjöstrand, *High-Energy-Physics Event Generation with PYTHIA 5.7 and JETSET 7.4*, Comp. Phys. Comm. **82**, 74 (1994).

[78] G. Marchesini *et al.*, *HERWIG: A Monte Carlo Event Generator for Simulating Hadron Emission Reactions with Interfering Gluons Version 5.1*, Comp. Phys. Comm. **67**, 465 (1992).

[79] R. Brun, R. Hagelberg, M. Hansroul and J. C. Lassalle, *GEANT: Simulation Program for Particle Physics Experiments. User Guide and Reference Manual*, CERN-DD-78-2 (1978).

[80] R. Fernow, *Introduction to Experimental Particle Physics*, Cambridge Univ. Press, New York, USA (1986).

[81] W. W. Armstrong *et al.* (The ATLAS collaboration), *ATLAS: Technical Proposal for a General-Purpose pp Experiment at the Large Hadron Collider*, CERN-LHCC-94-43 (1994).

[82] J. P. Delahaye and I. Wilson *et al.* (The CLIC study team), *CLIC - A Two-Beam Multi-TeV* $e^{\pm}$ *Linear Collider*, CERN-PS-2000-047-RF, presented at Linac 2000, Monterey, California, USA, 21-25 Aug (2000).

[83] C. Bowdery ed. (The ALEPH collaboration), *The ALEPH Handbook 1995, Vol. 1 and 2*, CERN, Geneva, Switzerland, (1995 and 1997).

[84] D. Buskulic *et al.* (The ALEPH collaboration), *Performance of the ALEPH Detector at LEP*, Nucl. Instr. Meth. **360**, 481 (1995).

[85] D. Schlatter, P. Perrodo, O. Schneider and A. Wagner, $\aleph$ *in Numbers*, internal ALEPH note (1996).

[86] E. J. Wolin and L. L. Ho, *Covariance Matrices for Track Fitting with the Kalman Filter*, Nucl. Instr. Meth. **A329**, 493 (1993).

[87] E. J. Thomson, *Measurements of the W boson Mass from* $e^+e^- \rightarrow W^+W^- \rightarrow l\bar{\nu}q\bar{q}$ *Events with the ALEPH Detector*, Ph.D. thesis, Univ. of Glasgow, Glasgow, UK (1998).

[88] R. Barate *et al.* (The ALEPH collaboration), *Measurement of W-Pair Production in* e^+e^- *Collisions at 189 GeV*, Phys. Lett. **B484**, 205 (2000).

[89] S. Catani *et al.*, *New Jet Clustering Algorithm for Multi-Jet Cross-Sections in* e^+e^- *Annihilation*, Phys. Lett. **B269**, 432 (1991).

[90] H. Albrecht, E. Blucher and J. Boucrot *et al.*, *ALPHA Physics Analysis Package Versions $\geq$ 124*, 61, and references therein, ALEPH 99-087, CERN, Geneva, Switzerland (1999).

[91] M. Chalmers, *Measurements of the Mass of the W Boson in the $W^+W^- \rightarrow qqqq$ Channel with the ALEPH Detector*, Ph. D. thesis, University of Glasgow, Glasgow, UK, Dec (1999).

[92] B. W. Kennedy, *Radiative Backgrounds to the Tagged Two-Photon Process $e^+e^- \rightarrow e^+e^-$ + Hadrons*, OPAL-TN-164 (1993).

[93] J. Allison, *Multiquadric Radial Basis Functions for Representing Multidimensional High Energy Physics Data*, Comp. Phys. Comm. **77**, 377 (1993).

[94] E. Thomson, private communication.

[95] M. L. Boas, *Mathematical Methods in the Physical Sciences*, 2nd Ed., John Wiley & Sons, 172.

[96] H. Przysieniak, private communication.

[97] F. James and M. Roos, *MINUIT, a System for Function Minimization and Analysis if the Parameter Errors and Correlations*, Comp. Phys. Comm. **10**, 343 (1975).

[98] R. Barate *et al.* (The ALEPH collaboration), *Measurement of the W Mass by Direct Reconstruction in e^+e^- Collisions at 172 GeV*, Phys. Lett. **B422**, 384 (1998).

[99] B. F. L. Ward, S. Jadach, W. Płacek, M. Skrzypek and Z. Wąs, *Coherent Exclusive Exponentiation for Precision Monte Carlo Calculations of Fermion Pair Production / Precision Predictions for (Un)stable W^+W^- Pairs*, hep-ph/0009352, presented at ICHEP2000, Osaka, Japan, Sept. (2000).

[100] A. Blondel and H. Przysieniak, *Estimate of the Full Statistical Error for the Reweighting Technique*, ALEPH internal note, ALEPH 99-113 (1999).

[101] J. J. Ward, *M_W Studies for the $l\nu q\bar{q}$ Channel*, presented at the ALEPH semi-leptonic W meeting, Aug 3 (1999), CERN, Geneva, Switzerland.

[102] A. Bonnisent, private communication.

[103] W. Wiedenmann, private comunication.

[104] J. Carr, private communication.

[105] R. Tenchini, *Jet Angular Studies*, presented during the ALEPH W meeting, CERN, Geneva, Switzerland, 12 Dec (1999).

[106] M. Kado, *Recherche du Boson de Higgs dans le Canal à Énergie Manquante avec le Détecteur ALEPH á LEP2*, LAL99-16, 158 (1999).

[107] F. Ligabue, private communication.

[108] R. Tenchini, private communication.

[109] A. Venturi, *Increasing the Entropy of the Simulation Systematics*, presented during the ALEPH W meeting, CERN, Geneva, 12 Dec (1999).

[110] R. Assmann *et al.* (The LEP energy working group), *Calibration of Centre-of-Mass Energies at LEP1 for Precise Measurement of Z Properties*, Eur. Phys. J. **C6**, 2 (1999).

[111] A. Sokolov and I. Ternov, *On Polarisation and Spin Effects in the Theory of Synchrotron Radiation*, Sov. Phys. Dokl. **8**, 1203 (1964).

[112] A. Blondel *et al.* (The LEP energy working group), *Evaluation of the LEP Centre-of-Mass Energy above the W-Pair Production Threshold*, Eur. Phys. J. **C11**, 573 (1999).

[113] R. Assmann *et al.* (The LEP energy working group), *Evaluation of the LEP Centre-of-Mass Energy for Data taken in 1998*, 99/01 (1999).

[114] R. Assmann *et al.* (The LEP energy working group), *Evaluation of the LEP Centre-of-Mass Energy for Data taken in 1999*, 00/01 (2000).

[115] A. Venturi, *Analytical Study of* $\Delta M/M$ *versus* $\Delta E/E$, presented at the ALEPH W meeting, Dec 15 (1999).

[116] E. Lancon and A. Blondel, *Determination of the LEP Energy Spread using Experimental Constraints*, ALEPH 96-136 (1997).

[117] J. Wenninger, private communication.

[118] R. Barate *et al.* (The ALEPH collaboration), *Studies of Quantum Chromodynamics with the ALEPH Detector*, Phys. Rep. **294**, 1 (1998).

[119] J. J. Ward, *Jet Structure in $(e/\mu)\nu q\bar{q}$ Events*, presented at ALEPH W meeting, CERN, Geneva, Switzerland, June 28 (2000).

[120] A. Blondel and J. J. Ward, *An Estimate of the Fragmentation Systematic Error on* $\mathrm{M_W}$ *in the* $\mathrm{WW}\rightarrow(e/\mu)\nu q\bar{q}$ *Channels at* $\sqrt{s}$*=189 GeV by comparing Distributions in Data and MC*, ALEPH 2000-056 (2000).

[121] J. J. Ward, *Comparing MC with Data to Estimate* ΔM_W, presented at WW00 meeting, CERN, Geneva, Switzerland, Apr 18-19 (2000).

[122] B. Bloch-Devaux, *KINAGAIN: A Facility to Restart Hadronization including Final State Interactions (FSI)*, ALEPH 2000-034, SOFTWR2000-001 (2000).

[123] E. Lancon, *JETSET versus HERWIG*, presented at ALEPH W meeting, CERN, Geneva, Switzerland, June 14 (2000).

[124] G. Rudolph, private communication, Sept 7 (2000).

[125] E. Lancon et. al., *W Mass Measurement in the Semileptonic Channel using a Monte Carlo Reweighting Technique*, ALEPH internal note, ALEPH 97-073 (1997).

[126] R. Barate *et al.* (The ALEPH collaboration), *Measurement of the W Mass in* e^+e^- *Collisions at Production Threshold*, Phys. Lett. **B401**, 347 (1997).

[127] R. Barate *et al.* (The ALEPH collaboration), *Measurement of the W Mass in* e^+e^- *Collisions at 183 GeV*, Phys. Lett. **B453**, 121 (1999).

[128] O. Buchmüller *et al.*, *Measurement of the W-Boson Mass in the Semileptonic Channel using a Multi-Dimensional Reweighting Technique*, ALEPH internal note, ALEPH 99-107 (1999).

[129] A. Gurtu, *Precision Tests of the EW Gauge Theory*, presented at ICHEP2000, Osaka, Japan, Jul 27 - Aug 2 (2000).

[130] B. Abbott *et al.* (The D0 collaboration), *A Measurement of the W Boson Mass using Electrons at Large Rapidities*, Phys. Rev. Lett. **84**, 222 (2000).

[131] F. Abe at al. (The CDF collaboration), *Measurement of the W Boson Mass*, Phys. Rev. Lett. **65**, 2243 (1990).

[132] F. Abe at al. (The CDF collaboration), *A Measurement of the W Boson Mass*, Phys. Rev Lett. **75**, 11 (1995).

[133] J. Alitti *et al.*, *An Improved Determination of the Ratio of W and Z Masses at the CERN $\bar{p}p$ Collider*, Phys. Lett. **B276**, 354 (1992).

[134] G. Abbiendi *et al.* (The OPAL collaboration), *Measurement of the W Mass and Width in e^+e^- Collisions at 183 GeV*, Phys. Lett. **B453**, 138 (1999).

[135] P. Abreu *et al.* (The DELPHI collaboration), *Measurement of the Mass of the W Boson Using Direct Reconstruction at $\sqrt{s}$ = 183 GeV*, Phys. Lett. **B462**, 410 (1999).

[136] M. Acciarri *et al.* (The L3 collaboration), *Measurement of Mass and Width of the W Boson at LEP*, Phys. Lett. **B454**, 386 (1999).

[137] P. Igo-Kemenes, *Search for New Particles and New Phenomena: Results from e^+e^- Colliders*, presented at ICHEP2000, Osaka, Japan, July 27 - Aug 2 (2000).

[138] F. Abe at al. (The CDF collaboration), *Direct Measurement of the W Boson Width*, Phys. Rev. Lett. **74**, 341 (1995).

[139] F. Abe at al. (The CDF collaboration), *Measurement of the Ratio $\sigma{\cdot}B(p\bar{p} \to W \to e\nu)/\sigma \cdot B(p\bar{p} \to Z^0 \to ee)$ in $p\bar{p}$ Collisions at $\sqrt{s}$=1800 GeV*, Phys. Rev. **D52**, 2624 (1995).

[140] B. Abbott *et al.* (The D0 collaboration), *Measurement of W and Z Boson Production Cross Sections*, Phys. Rev. **D60**, 52003 (1999).

[141] B. Abbott *et al.* (The D0 collaboration), *Extraction of the Width of the W Boson from Measurements of $\sigma(p\bar{p} \to W + X)B(W \to e\nu)$ and $\sigma(p\bar{p} \to Z + X)B(Z \to ee)$ and their Ratio*, Phys. Rev. **D61**, 72001 (2000).

[142] C. Albajar *et al.* (The UA1 collaboration), *Measurement of the Ratio $R = \sigma_W Br(W \to \mu\nu)/\sigma_Z Br(Z \to \mu\mu)$ and $\Gamma_W^{\rm tot}$ at the CERN Proton-Antiproton Collider*, Phys. Lett. **B253**, 503 (1991).

[143] J. Alitti *et al.* (The UA2 collaboration), *A Measurement of the W and Z Production Cross Sections and a Determination of Γ_W at the CERN $\bar{p}p$ Collider*, Phys. Lett. **B276**, 365 (1992).